

# The dynamics of chemically active droplets

DISSERTATION

zur Erlangung des akademischen Grades

Doctor rerum naturalium  
(Dr. rer. nat)

vorgelegt

dem Bereich Mathematik und Naturwissenschaften  
der Technischen Universität Dresden

von

Rabea Seyboldt,  
geboren am 21. Februar 1988 in Friedrichshafen.

Die Dissertation wurde am

Max Planck Institute for the Physics of Complex Systems  
*Department of Biological Physics*

angefertigt.



Eingereicht im April 2019,  
verteidigt am 21. Juni 2019.

Betreuer:

**Prof. Frank Jülicher**

Gutachter:

Prof. Frank Jülicher

Prof. Karsten Kruse

Prof. Stefan Grill

Promotionskommission:

Prof. Sebastian Reineke

Prof. Frank Jülicher

Prof. Holger Kantz

Dr. habil. Benjamin Friedrich







## Zusammenfassung

In unserem täglichen Leben begegnen wir Tropfen oft in physikalischen Systems, beispielsweise als Öltropfen in Salatsoße. Diese Tropfen sind meist chemisch inaktiv. In biologischen Zellen bilden Proteine und RNA zusammen Tropfen. Zellen sind chemisch aktiv, so dass die Tropfenkomponenten neu gebildet, abgebaut und modifiziert werden können.

In dieser Doktorarbeit wird das dynamische Verhalten von chemisch aktiven Tropfen mit analytischen und numerischen Methoden untersucht. Um das dynamische Verhalten von solchen aktiven Tropfen zu untersuchen, benutzen wir ein Minimalmodell mit zwei Komponenten, die zwei Phasen bilden und durch chemische Reaktionen ineinander umgewandelt werden. Die chemischen Reaktionen werden durch das Brechen von Detailed Balance aus dem Gleichgewicht gehalten, so dass die Tropfen chemisch aktiv sind. Wir konzentrieren uns auf den Fall, in dem Tropfenmaterial im Tropfen in die äußere Komponente umgewandelt wird, und in der äußeren Phase erzeugt wird.

Wir finden ein vielfältiges dynamisches Phasendiagramm mit Regionen, in denen Tropfen schrumpfen und verschwinden, Regionen, in denen Tropfen eine stabile stationäre Größe besitzen, und Regionen, in denen eine Forminstabilität zu komplexer Tropfen-Dynamik führt. In der letzten Region deformieren sich Tropfen typischerweise prolat, verformen sich zu einer Hantel, und teilen sich in zwei Tochtertropfen, die wieder anwachsen. Dies kann zu Zyklen von Wachstum und Teilung von Tropfen führen, bis die Tropfen das gesamte Volumen füllen. Während sphärische Tropfen durch die chemischen Reaktionen entgegen ihrer Oberflächenspannung deformiert werden, können Tropfen-Zylinder und Platten durch chemische Reaktionen stabilisiert werden.

Generell ist die Dynamik von Tropfen ein hydrodynamisches Problem, da die Oberflächenspannung von deformierten Tropfen hydrodynamische Flüsse erzeugt. Wir finden, dass chemische Reaktionen entgegen die Oberflächenspannung Arbeit verrichten können, so dass die Tropfenteilung auch unter Berücksichtigung hydrodynamischer Flüsse möglich ist.

Diese Doktorarbeit zeigt, dass die Kombination von chemische Reaktionen und Phasenseparation unter Nichtgleichgewichtsbedingungen zu neuem dynamischen Verhalten führen kann. Die Ergebnisse zeigen die Relevanz von chemischen Reaktionen zum Verständnis von Phasenseparation in biologischen Systemen auf, und können bei der Umsetzung der diskutierten Phänomene in experimentellen Systemen helfen. Die Tropfenteilung, die in dieser Doktorarbeit diskutiert wird, erinnert an die Teilung von biologischen Zellen. Davon motiviert schlagen wir vor, dass die Teilung von chemisch aktiven Tropfen ein Mechanismus für die Replikation von Tropfen-artigen Protozellen am Ursprung des Lebens gewesen sein könnte.



## Abstract

In our everyday environment, we regularly encounter liquid-liquid phase separation in physical systems such as oil droplets in vinegar. These droplets tend to be chemically inert. In biological cells, protein and RNA may together form liquid droplets. Cells are chemically active, so that droplet components can be created, degraded and modified.

In this thesis we study the influence of nonequilibrium chemical reactions on the shape dynamics of a droplet theoretically, using analytical and numerical methods. To discuss the dynamical behavior that results from combining phase separation and chemical reactions in sustained nonequilibrium conditions, we introduce a minimal model with only two components that separate into distinct phases. These two components are converted into each other by chemical reactions. The reactions are kept out of equilibrium by breaking of detailed balance, so that the droplet becomes active. We concentrate on the case where the reaction inside the droplet degrades droplet material into the outer component, and where the reaction outside creates new droplet material.

We find that chemically active droplets have a rich dynamic phase space, with regions where droplets shrink and vanish, regions where droplets have a stable stationary size, and regions where the flux-driven instability leads to complex dynamic behavior of droplets. In the latter, droplets typically elongate into a dumbbell shape and then split into two symmetrical daughter droplets. These droplets then grow until they have the same size as the initial droplet. This can lead to cycles of growth and division, so that an initial droplet divides until droplets fill the simulation volume. We analyze the stationary spherical state of the droplet, which is created by a balance of the fluxes driven by the chemical reactions. We find that stationary droplets may have a shape instability, which is driven by the continuous fluxes across the droplet interface and which may trigger the division. We also find that while reactions may destabilize spherical droplet shapes despite the surface tension of the droplet, they can have stabilizing effects on cylindrical droplets and droplet plates.

Generally, the shape dynamics of droplets is a hydrodynamic problem because surface tension in non-spherical droplets drives hydrodynamic flows that redistribute material and deform the droplet shape. We therefore study the influence of hydrodynamic flows on the shape changes of chemically active droplets. We find that chemical reactions in active droplets can perform work against surface tension and flows, so that the droplet division is possible even in the presence of hydrodynamic flows.

The present thesis highlights how the combination of basic physical behaviors – phase separation and chemical reactions – may create novel dynamic behavior under sustained nonequilibrium conditions. The results demonstrate the importance of considering chemical reactions for understanding the dynamics of droplets in biological systems, as well as proposes a minimalist model for experimentalists that are interested in creating a system of dividing droplets. Finally, the division of chemically active droplets is reminiscent of the division of biological cells, and it motivates us to propose that chemically active droplets could have provided a simple mechanism for the self-replication of droplet-like protocells at the origin of life.



# Contents

<b>1</b>	<b>Introduction</b>	<b>1</b>
1.1	Phase separation and droplets . . . . .	1
1.2	Chemical reactions . . . . .	6
1.3	Droplets in biological systems . . . . .	7
1.4	Origin and evolution of life . . . . .	8
1.5	Dynamical behavior of active systems . . . . .	10
1.6	Overview of the thesis . . . . .	12
<b>2</b>	<b>Theory of multi-component phase-separating systems with chemical reactions</b>	<b>13</b>
2.1	Dynamic description with linear response . . . . .	14
2.2	Detailed balance of chemical reactions . . . . .	21
2.3	Summary . . . . .	24
<b>3</b>	<b>Minimal model for chemically active droplets in two formulations</b>	<b>27</b>
3.1	Continuum model for chemically active droplets . . . . .	27
3.2	Effective droplet model for chemically active droplets . . . . .	32
3.3	Outlook . . . . .	36
<b>4</b>	<b>Shape instability of spherical droplets with chemical reactions</b>	<b>39</b>
4.1	Stability of spherical droplets with chemical reactions . . . . .	39
4.2	Physical mechanism driving the shape instability . . . . .	47
4.3	Relationship to Mullins-Sekerka instability . . . . .	49
4.4	Droplet shape stability in the limit of a small reaction amplitude . . . . .	52
4.5	Summary . . . . .	58
<b>5</b>	<b>Dynamical behavior of chemically active droplets</b>	<b>61</b>
5.1	Numerical solution of droplet dynamics in the continuum model . . . . .	61
5.2	Dynamics of the homogeneous state . . . . .	63
5.3	Volume growth of chemically active droplets . . . . .	64
5.4	Division of chemically active droplets . . . . .	65
5.5	Cycles of growth and division . . . . .	68
5.6	Summary . . . . .	69

<b>6</b>	<b>Shape instability of droplets with various geometries</b>	<b>71</b>
6.1	Droplet shapes with a flat interface in 1d, 2d and 3d: Line-segments, bands and plates . . . . .	72
6.2	Stationary droplet disks in 2d . . . . .	77
6.3	Stationary droplet cylinders in 3d . . . . .	79
6.4	Summary . . . . .	84
<b>7</b>	<b>Role of hydrodynamic flows in chemically driven droplet division</b>	<b>87</b>
7.1	Stability of droplets with hydrodynamic flows . . . . .	87
7.2	Scaling of the hydrodynamic stability diagram . . . . .	93
7.3	Droplet division with hydrodynamic flows . . . . .	94
7.4	Summary . . . . .	96
<b>8</b>	<b>Chemically active droplets as a model for protocells at the origin of life</b>	<b>97</b>
8.1	Protocells – simple precursors of biological cells . . . . .	97
8.2	Discussion of chemically active droplets as protocells . . . . .	98
8.3	Examples of parameter values for dividing droplets . . . . .	102
8.4	Summary . . . . .	104
<b>9</b>	<b>Conclusion</b>	<b>105</b>
	<b>Appendices</b>	<b>109</b>
<b>A</b>	<b>Reaction rates with broken detailed balance</b>	<b>111</b>
<b>B</b>	<b>Relation between the continuum model and the effective droplet model</b>	<b>117</b>
B.1	Derivation of jump conditions for equilibrium phase separation . . .	117
B.2	Stress balance across the interface . . . . .	118
B.3	Dynamics of the effective droplet model . . . . .	120
<b>C</b>	<b>Details on the effective droplet model</b>	<b>123</b>
C.1	Stationary states of spherical droplets . . . . .	123
C.2	Stability analysis of a spherical droplet without hydrodynamic flows .	124
C.3	Scaling behavior of stationary radius and instability in the effective droplet model . . . . .	130
<b>D</b>	<b>Details on the continuum droplet model</b>	<b>137</b>
D.1	Linear stability of the homogeneous state in the continuum droplet model . . . . .	137
D.2	Numerical solution of the continuum model . . . . .	138
D.3	Comparison of droplet deformation in the continuum model and the effective droplet model . . . . .	141
<b>E</b>	<b>Stability analysis of different geometrical droplet shapes</b>	<b>143</b>
E.1	Effective droplet model for active droplets . . . . .	143



E.2	Stationary line segments in 1d . . . . .	144
E.3	Stationary bands in 2d . . . . .	146
E.4	Stationary plates in 3d . . . . .	148
E.5	Stationary cylinders in 3d . . . . .	148
E.6	Stationary disks in 2d . . . . .	153
<b>F</b>	<b>Stability analysis of chemically active droplets with hydrodynamic flows</b>	<b>155</b>
F.1	Linear stability analysis with hydrodynamic flows . . . . .	155
F.2	Scaling relations in the limit of small reaction fluxes . . . . .	160
<b>G</b>	<b>Parameter examples</b>	<b>165</b>
G.1	Chemical turnover time of stationary droplets . . . . .	165
G.2	Examples of parameter values for dividing droplets without hydrodynamics . . . . .	166
G.3	Estimation of the influence of hydrodynamic flows . . . . .	166
	<b>Bibliography</b>	<b>171</b>



In this thesis, we consider the combination of phase separation and chemical reactions. Phase separation, such as the separation of water and oil in vinaigrette, is a well-studied physical phenomena. Chemical reactions, the conversion of molecules into other molecules, is a common behavior as well, for example the burning of wood in a camp fire. The combination of both effects seems rare, judging by our everyday environment. However, both phase separation and chemical reactions occur together in biological systems, inside living cells. Nonequilibrium conditions are common in our world, but they are especially important in living systems, which are alive only as long as they are out of equilibrium. This motivates the theoretical study of the dynamical shape changes a droplet can undergo if it is driven out of equilibrium by chemical reactions.

In this chapter the background concepts are introduced. We start with phase separation which leads to liquid droplets, including different models to describe it. We briefly introduce the basic concepts of chemical reactions. After that, we discuss the existence of droplets in living cells, where chemical reactions are prevalent. We also introduce the creation of life as another example where droplets and chemical reactions might have been important. Then we outline the wide range of behaviors that are unlike that of associated equilibrium states that have been found in other nonequilibrium driven systems. We conclude the chapter with a brief overview of previous results of phase separating systems with driven chemical reactions.

## 1.1 Phase separation and droplets

Almost every day we see droplets around us, water droplets in air from rain or condensation in the shower, oil droplets in water from preparing vinaigrette, or the small droplets in an emulsion, such as hand creme or mayonnaise or ouzo. Such droplets often can be described by equilibrium properties of the materials involved: A droplet

is created because the energy of the system is lower as a phase-separated state than in the mixed state, due to the molecular interactions between the components. Minimization of the surface energy creates a round shape of the droplet.

There are different models that are used to describe liquid phase separating systems. Here, three models are briefly introduced. One is a microscopic lattice model based on Ising model which gives a good intuitive picture. We also introduce a free-energy based model with a continuous concentration field, and one where the interface is described explicitly by a discontinuous concentration jump, both of which are used throughout the thesis. Additional information can be found in Safran (1994); Bray (1994); Taylor (1998); Cates (2012).

### 1.1.1 A microscopic picture of phase separation

A simple molecule-based picture for phase separation is provided by the Ising model, see Safran (1994). In this picture, molecules of two species have equal sizes and sit on points of a lattice, where the spin  $\sigma_i \in \{0, 1\}$  encodes whether an A or B particle is on lattice site  $i$ . We consider a dense, incompressible liquid, which corresponds to a lattice where every spot is filled with a particle. The Hamiltonian  $H$  consists of the internal energies of the molecules and interactions between particles  $J_{ij}$ . For short-range interactions, we can assume nearest-neighbor interactions ( $J_{ij} = 0$  if  $i$  and  $j$  are not neighboring lattice sites). The Hamiltonian can thus be written as

$$H = \frac{1}{2} \sum_{\langle i,j \rangle} [J_{AA} + J_{BB} - 2J_{AB}] \sigma_i (1 - \sigma_j) \quad (1.1)$$

where  $\langle i, j \rangle$  counts over nearest neighbors  $i, j$  and  $J_{AA}$  encodes interactions between two neighboring A particles,  $J_{BB}$  encodes interactions between B particles, and  $J_{AB}$  describes interactions between different particles. We omitted linear terms in  $\sigma_i$ , as rearrangements of particles do not change the contribution from the term and it is thus not relevant for phase separation. We can thus see that if attractive interactions between the same particles are stronger than different ones, the energy becomes lower for particle configurations with two regions, one rich in A and one rich in B particles.

### 1.1.2 Mean field description

The Ising model for a liquid phase-separating system can be converted into a mean field theory by defining the local volume fraction of B particles  $\phi = \langle s_i \rangle$ , compare Safran (1994). The amount of droplet-forming material is conserved, so that the mean volume fraction

$$\bar{\phi} = \frac{1}{V_{sys}} \int d^3r \phi(r) \quad (1.2)$$

remains constant over time. We can find the free energy  $F$  of the system

$$F[\phi] = \int d^3r \left[ f(\phi) + \frac{\kappa}{2} (\nabla\phi)^2 \right] \quad (1.3)$$

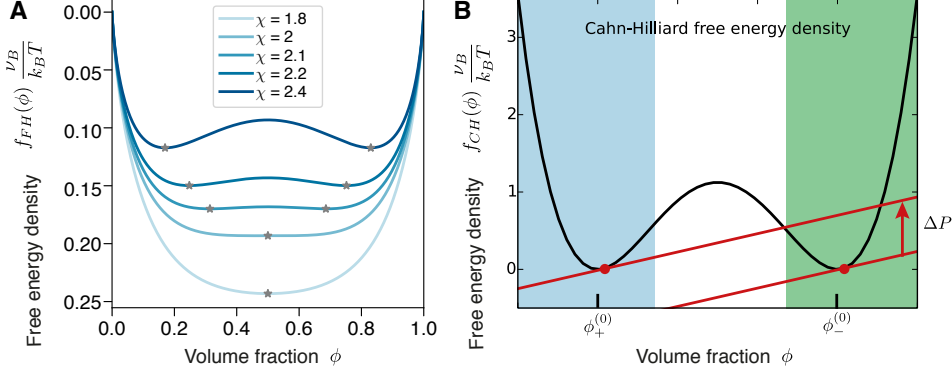


FIGURE 1.1: Phase separating free energy. (A) Flory-Huggins free energy density  $f_0$  for different values of  $\chi a^3/k_B T$ . For  $\chi \leq 2$ , the free energy density is convex, so that the homogeneous system has the smallest energy. For  $\chi > 2$ ,  $f_0$  has regions (between the minima marked by gray stars) where the system has a lower energy in a phase-separated state. (B) Cahn-Hilliard free energy (black) with Maxwell construction of coexisting phases (red). For an average concentration  $\bar{\phi}$  with  $\phi_+^{(0)} < \bar{\phi} < \phi_-^{(0)}$ , the system can phase separate into two phases with concentrations  $\phi_+ \approx \phi_+^{(0)}$  (blue region) and  $\phi_- \approx \phi_-^{(0)}$  (green region). The equilibrium concentrations are given by a Maxwell construction (red lines) given by equal chemical potential of the phases, and the Laplace pressure of the droplet phase (red arrow).

with the Flory-Huggins free energy density  $f = f_{FH}$ , see Huggins (1942); Flory (1942), with

$$\frac{f_{FH}(\phi)}{k_B T} = \frac{\phi}{v_B} \ln \phi + \frac{1-\phi}{v_A} \ln(1-\phi) + \frac{\chi}{v_A} \phi(1-\phi). \quad (1.4)$$

Here the gradient term is created by the neighbor interaction, and the constants  $\kappa$ ,  $\chi$ , and the molecular volumes  $v_A$  and  $v_B$  of both molecules are related to the lattice distance  $v_A = v_B = a^3$  and the interaction strength of the Ising model  $J = J_{AA} + J_{BB} - 2J_{AB}$ . Temperature is denoted with  $T$  and  $k_B$  is the Boltzmann constant. Both the free energy density and the gradient term are direct results from the Ising model. A term linear in  $\phi$  was omitted, because it represents a constant in the case of conserved droplet material in the system.

The free energy contains terms related to mixing entropy density,  $s = \phi/v_B \ln \phi + (1-\phi)/v_A \ln(1-\phi)$  as well as the energetic interaction term  $\chi\phi(1-\phi)$ , which encodes the effective repulsion between different particles. This free energy can also be derived as a simple expansion of the short-range, mean-field interactions to lowest (quadratic) order. The gradient term is necessary to stabilize the concentration field for  $\chi > 2$  with respect to small-wavelength perturbations, where mean field theory would break down. The free energy density is shown for different values of  $\chi$  in

Fig. 1.1A. For small  $\chi$ , the entropic terms dominate, leading to a convex free energy density. In this regime, local concentration differences increase the free energy of the system. Thus the homogeneous state is stable. For  $\chi > \chi_c$ , with  $\chi_c = 2$ , the free energy density has a double-well shape with a concave region for intermediate concentrations. In the concave region, small local deviations from the mean concentration lower the energy of the system, so that the homogeneous state is unstable and the system tends to spontaneously demix into two regions with different concentrations  $\phi_+$  and  $\phi_-$ . This process is called spinodal decomposition. The gradient term for  $\kappa \neq 0$  establishes a smooth transition between the regions. For concentrations with convex free energy density between the two minima of the free energy density, (or, more generally, with a free energy density above the convex envelope of the free energy density), the free energy of the system can be reduced by the formation of two phases, but the homogeneous state is stable. In this region, droplets are typically created by nucleation of a small initial droplet.

### 1.1.3 Equilibrium profile and surface tension

The equilibrium profile of the concentration can be found by minimizing the energy with respect to the concentration profile,

$$\frac{\delta F}{\delta \phi(\mathbf{r})} = 0, \quad (1.5)$$

under the constraint  $\bar{\phi} = const.$  The free energy density can be expanded around the critical point  $\chi_c$  and its extremum at concentration  $\phi_{min} = 0.5$  to yield the Cahn-Hilliard free energy

$$f_{CH}(\phi) = \frac{b}{2\Delta\phi^2}(\phi - \phi_-)^2(\phi - \phi_+)^2. \quad (1.6)$$

with  $\Delta\phi = \phi_- - \phi_+$ . The parameter  $b$  and the concentrations  $\phi_{\pm}$  depend on  $\chi$ . At  $\chi_c$  both concentrations are equal,  $\phi_{\pm} = 0.5$ , for  $\chi > \chi_c$  they diverge to larger and smaller values, respectively. With the Cahn-Hilliard free energy, it is possible to analytically find the equilibrium profile in 1d (corresponding to a flat interface in a higher-dimensional system),

$$\phi(x) = \frac{\phi_- - \phi_+}{2} \tanh(x/w) + \frac{\phi_- + \phi_+}{2} \quad (1.7)$$

with interface width  $w = 2(\kappa/b)^{1/2}$ . The interfacial tension (also called surface tension)

$$\gamma = F[\phi(x)] - \frac{1}{2}(F[\phi_+] + F[\phi_-]) \quad (1.8)$$

is the energy per unit interfacial area that is contained in the interface between the phases. For the Cahn-Hilliard free energy, this can be calculated as  $\gamma = (\phi_- - \phi_+)^2/6 \sqrt{\kappa b}$ .



### 1.1.4 Sharp interface assumption

We have seen in the previous section that we can find the concentration profile and surface tension from the free energy of a system. In many systems, the interfacial width  $w$  has values of 10-100 nm, and thus is often small in comparison to the structures studied, compare Safran (1994). It is therefore useful to use a course-grained theory that treats the interface as infinitely small, with a concentration jump between the phases. For a system with volume  $V_{sys}$  with a spherical droplet of volume  $V$  and area  $A$  with density  $\phi_-$  inside, and a density  $\phi_+$  outside, the energy of the system can be written as

$$F = Vf(\phi_-) + (V_{sys} - V)f(\phi_+) + \gamma A \quad (1.9)$$

with local free energy density  $f_0$  (which, depending on the model chosen, could be the Flory-Huggins free energy or the Cahn-Hilliard free energy, or a different one). Additionally, the total amount of droplet-forming material is conserved,

$$V_{sys}\bar{\phi} = V\phi_- + (V_{sys} - V)\phi_+ . \quad (1.10)$$

Therefore, of the set  $V$ ,  $\phi_-$  and  $\phi_+$ , only two quantities need to be determined by minimizing the free energy. The third is determined by the conservation equation. For a spherical shape of the volume with radius  $R$ , the equilibrium conditions  $dF/d\phi_- = 0$  and  $dF/dV = 0$  with  $\phi_+(\phi_-, V)$  can be written as

$$\mu_+ = \mu_- \quad (1.11)$$

$$p_- = p_+ - 2\gamma H \quad (1.12)$$

where  $H = 1/R$  is the mean curvature of the surface. We introduced the chemical potentials of the bulk phases  $\mu_{\pm} = f'(\phi_{\pm})$ , and the Laplace pressure  $p_{\pm} = \phi_{\pm}\mu_{\pm} - f(\phi_{\pm})$ . These relations can be interpreted geometrically via a Maxwell construction, see Fig. 1.1. The concentrations  $\phi_{\pm}$  of the phases need to fulfill the above equations. Therefore, the slope of the free energy density has to be the same at both concentrations (shown here as parallel red lines with red dots at the respective concentrations). The equation for the Laplace pressure describes the y-axis offset of both red lines (red arrow).

The concentrations in both phases depend on the droplet size, but often it is assumed that the change of the concentrations is small. After finding the concentrations  $\phi_{\pm}^{(0)}$  for a flat interface, we can expand the free energy to quadratic order around these points to find simpler expressions for the changes in concentration for a smaller droplet with a curved interface. We find

$$\phi_+(R) = \phi_+^{(0)} + \beta_+\gamma H(R) \quad (1.13)$$

$$\phi_-(R) = \phi_-^{(0)} + \beta_-\gamma H(R) \quad (1.14)$$

where  $\beta_{\pm} = 2/f''(\phi_{\pm}^{(0)})$  describes the influence of the difference of Laplace pressures in both phases on the concentrations.

### 1.1.5 Dynamical behavior of phase separating systems

We will introduce the dynamical behavior of phase separating systems here from a purely energetic point of view. A system tends to evolve towards a macro-state with minimal (free) energy. For an initial homogeneous concentration in the region of spinodal decomposition, an initial homogeneous state is unstable, compare subsection 1.1.2, so that perturbations grow, where the initial wavelength is given by the stability properties of the system. The resulting two-phase system then evolves by coalescence of regions of the same phase and material exchange between them, until only two bulk phases remain. This minimizes the free energy by minimizing the surface area, highlighted by Eq. (1.9). In the droplet region where the homogeneous state is locally stable, an initial deviation of sufficient size is needed to nucleate a droplet. If a droplet is created that is larger than the nucleation size, it grows by taking up material. The growth is first characterized by coalescence of droplets, and later, when droplets are further apart, by the diffusive exchange of droplet material between droplets. This Ostwald ripening leads to a competition of droplets where the smaller droplets vanish and the larger droplets grow, until only one droplet remains, see Ostwald (1897); Lifshitz and Slyozov (1961).

## 1.2 Chemical reactions

The spatial ordering of components is only one way by which the energy of a system can be lowered. Chemical reactions, the conversion of one molecule into another (or several others), is another way, see Atkins and de Paula (2010). Let us consider a chemical reaction between two components A and B,



In this case, the number of A and B molecules are not conserved in the system separately, but only the sum of both molecules is conserved. The free energy  $F$  can therefore be minimized without constraints. The (number) density of component B changes over time due to the production and degradation rates of B in the reaction,  $\partial_t n_B = s^{\rightarrow} - s^{\leftarrow}$ . In equilibrium, no net reaction occurs,  $s^{\rightarrow} = s^{\leftarrow}$ .

For concentrations close to the equilibrium concentrations, chemical reactions are often described by mass action kinetics, for a reaction  $A + B \rightleftharpoons C$  this is

$$s^{\rightarrow} = k^{\rightarrow} c_A c_B \quad (1.16)$$

$$s^{\leftarrow} = k^{\leftarrow} c_C \quad (1.17)$$

with constants  $k^{\rightarrow}$  and  $k^{\leftarrow}$ . Here, the interpretation is that the reaction rate  $s^{\rightarrow}$  is dominated by the time it takes of components A and B to meet, and the backward rate  $s^{\leftarrow}$  can be interpreted that every C molecule has a certain probability to react in a time window, so that the total rate is proportional to the number of C molecules. In equilibrium, both rates are equal,  $s^{\rightarrow} = s^{\leftarrow}$ , so that the free energy determines the ratio  $k^{\rightarrow}/k^{\leftarrow}$ .

## 1.3 Droplets in biological systems

To understand the relevance of the simple models of phase separation and chemical reactions we will discuss in this thesis, it is helpful to have an idea of the structures and mechanisms of a cell. This will help us to discuss common grounds, but also the large amount of differences between such simple models and life-like structures. Here we will give a brief overview of biological cells, concentrating on the metabolism and liquid phase separation.

### 1.3.1 Cellular structure of life

Life as we know it today is diverse and complex, Alberts et al. (2013). It consists of three principal kingdoms, bacteria, archaea, and eukaryotes. Bacteria and archaea are unicellular lifeforms that adapt and evolve by imperfect division (either due to mutations or asymmetric divisions), and by the exchange of genetic material via horizontal gene transfer. Eukaryotes exist as unicellular and multi-cellular life forms, and they evolve by mutations during divisions and by the recombination of genetic material in sexual reproduction. Compared to bacteria and archaea, eukaryotic cells are typically larger with a more complex structure. All life-forms on Earth today have a number of things in common: They all are composed of cells, enclosed by a cellular membrane that controls the import and export of molecules. They have a number of structural elements and classes of molecules in common, as well as certain metabolic pathways. Their proteins all consist of the same 22 amino acids, and they all have RNA and DNA, which are each built out of the same four nucleic acids. Another unifying feature is their complexity: All cells today have thousands of different components, with a huge metabolic network, which creates an interplay of different regulatory control systems.

Cells are often considered to be the smallest independent unit of life, Alberts et al. (2013). The structure of a cell consists of a membrane-enclosed space, the cytosol, in which various membrane-bound organelles are. The cytosol itself is a complex mixture of many components. The creation of new molecules is controlled by the DNA. The DNA which transcribed into RNA, some of which is translated into proteins. This process is regulated by feedback processes. In eukaryotic cells, the DNA is contained inside the nucleus. Outside the nucleus are RNA, proteins and various smaller substances such as ions. There are a large number of elements that help structuring the cells and fulfill various functions. One class of them are polymer fibers that harden the cell, where molecular motors move along the fibers, transporting cargo or displacing the fibers, which can be used for cell movements. Vesicles – small membrane spheres – transport material to different places. And generally, all these functions are regulated by complex reaction networks, which can be modified by other parts of the cell.

Chemical reactions are the main driving force and organizing principle of a cell. The reaction network of a cell is called the metabolism. This metabolism of the cell is often grouped into two different functions: Catabolic reactions break down

compounds to release energy, while anabolic reactions consume energy to create new molecules. Both parts are heavily interlinked and immensely complex and also different for different species (and at different times in the same organism), although some reaction cycles such as the Krebs cycle are conserved across species. The metabolism is an intrinsically out-of-equilibrium reaction network and even in a stationary state of the cell (between divisions etc), there are constantly chemical reactions.

### 1.3.2 Droplets in cells

Recently, droplets have been found to occur inside living cells, which are enriched in a number of specific proteins and RNA, Brangwynne et al. (2009); Weber and Brangwynne (2012); Elbaum-Garfinkle et al. (2015); Lin et al. (2015); Patel et al. (2015); Feric et al. (2016). While many proteins have a precise folded structure with a globular shape, phase separation tends to be driven by unfolded disordered regions along the protein sequence. These droplets can be considered as membrane-less organelles and are associated with a variety of functions in the cell, Banani et al. (2017). Examples are spatial ordering of molecules, Zwicker (2013); Zwicker et al. (2014); Saha et al. (2016), signaling, Li et al. (2012), stress response, Molliex et al. (2015), and epigenetic regulation, Wan et al. (2018).

Protein droplets are also observed to form in vitro by phase separation in physiological buffer, Sokolova et al. (2013); Aumiller and Keating (2016); Frankel et al. (2016); Saha et al. (2016); Nakashima et al. (2018). It has been found that reaction rates in both phases can be quite different from a well-mixed system, Sokolova et al. (2013), and that chemical reactions can be used to control phase separation and dissolution Aumiller and Keating (2016); Nakashima et al. (2018).

## 1.4 Origin and evolution of life

Droplets do not only exist in cells today, they are also one of the oldest models for protocells. Oparin argued in 1924 that while today life is complicated and not created de novo, life must have started somewhere. He highlighted that many nonliving physical systems show properties considered central to life: Living organisms grow, but so do crystals; cells and organisms have a well-defined structure that forms spontaneously, but so do snowflakes; all life needs energy input, similar to engines, Oparin (1924). He proposed droplets (termed complex coacervates then) as a model for the origin of life, and their equilibrium properties and some active ones were well studied during the next decades, Oparin (1952); Fox (1976). We will now briefly highlight some aspects of research to understand the origin of life on Earth.

Today, the relationship and evolution of different organisms can be studied by comparing their DNA. It is hypothesized that all cells today have one last unified common ancestor (LUCA), which already had the cellular properties discussed above, Weiss et al. (2016). For the evolution of life before LUCA, no traces remain in today's genetic setup, compare Woese et al. (1990); Lanier and Williams (2017). Three principal avenues to study the origin of life remain.

The first such avenue is the extrapolation back from modern organisms. This can be done by making and studying simplified organisms, such as finding the shortest self-replicating DNA by cutting out pieces of modern DNA, or by asking how specific features of life today could have formed, such as the set of amino acids or nucleic acids Brooks et al. (2002); Doi et al. (2005), or by analyzing patterns and functions in modern systems, such as finding the minimal functional core of important organelles, such as the ribosome (which translates DNA into RNA), Lanier and Williams (2017).

Another avenue to study the origin of life is to study the geological history of Earth and other planets, to find evidence for the existence of life at different stages, Knoll and Nowak (2017). This gives evidence on the existence of multicellular life forms 2.1 billion years ago, the evolution of eukaryotic unicellular life-forms 2.7 billion years ago and the origin and spreading of photosynthesis 3.4 and 2.4 billion years ago, respectively. Good evidence of unicellular life forms forming biofilms have been found 3.7 billion years ago, Nutman et al. (2016), and probable finds go as far back as 4.25 billion years ago. This puts the origin of life very close (on geological timescales) to the formation and cooling down of Earth 4.5-4.4 billion years ago, and even coincides with the Late Heavy Bombardment 4.1-3.8 billion years ago. The evidence for the first life on Earth can be expected to be a lower limit, because not much unperturbed rock older than 3.8 billion years remains, so that the sign of life rather coincide with findings of old stone formations, Marchi et al. (2014).

The third avenue is the study of the formation of life *de novo*, by studying scenarios by which life-like structures and the relevant molecules could have been created in a physical/chemical system, Oparin (1924); Haldane (1929). This avenue is strengthened by the geological findings, which place the first life forms very closely after the existence of liquid water on Earth, so that a 'random stroke of luck' seems unreasonable, and the formation of life as a physically driven mechanism seems more likely, Oparin (1924). It has been found that the chemical creation of amino acids and nucleic acids might have been possible on an early Earth, and possible pathways have been recreated experimentally, Fedor and Williamson (2005); Powner et al. (2009); Xu et al. (2019). For the formation of these building blocks into polymers, a nonequilibrium scenario with the cycling of components in a temperature gradient has been proposed, in a system similar to hydrothermal vents that today exist on the bottom of oceans Haldane (1929); Baross and Hoffman (1985); Martin (2012); Mast et al. (2013); Martin et al. (2014); Kreysing et al. (2015). Furthermore, many hypothetical scenarios have been worked out, by which molecules could have formed metabolic reaction networks, or by which membranes could have organized, Gilbert (1986); Unrau and Bartel (1998); Fedor and Williamson (2005); Higgs and Lehman (2015); Morasch et al. (2016); Pearce et al. (2017). However, currently no complete pathway from a physical/chemical world towards cellular life is known, Hanczyc and Szostak (2004); Macía and Solé (2007); Murtas (2013); Lanier and Williams (2017).

For the evolution of cells, two main theories have been proposed. The first model considers the origin of cells to be similar to vesicles, membrane bound organelles, Bachmann et al. (1992); Szostak et al. (2001); Hanczyc and Szostak (2004); Browne et al. (2010). These have been shown to divide, either by rupturing and forming

smaller vesicles if more membrane molecules are inserted into the system over time, Döbereiner et al. (1993), or by using a mixture of lipids that demix into two membrane phases, which can drive a separation of a vesicle into two with different lipids, Döbereiner et al. (1993); Chen et al. (1997); Baumgart et al. (2003); Andes-Koback and Keating (2011). It has been shown for vesicles that chemical reactions can occur confined inside them, Song et al. (2006).

The second model states that cells evolved from simple coacervate droplets, Oparin (1924, 1952); Fox (1976); Koga et al. (2011); Sokolova et al. (2013); Hyman et al. (2014); Morasch et al. (2016); Zwicker et al. (2017). Coacervates are water-rich phases of charged polymers, which form due to entropy-driven phase separation. By bringing the charged regions of the polymers together, they neutralize each other and free the ions that originally bind to them, thus increasing the entropy. Both the versatility of function of liquid droplets in cells, as well as the simple protein structure hint towards an early origin of the use of phase separation in cells, Shin and Brangwynne (2017). Additionally, only simple physical interactions are needed for phase separation, and random polymers have a tendency to phase separate, so that liquid droplets of biological (or prebiotic) material might well have existed at the origin of life Frankel et al. (2016). It has been shown for coacervate droplets that chemical reactions can occur confined inside them. One principal problem of coacervate droplets as the origin of cells is the lack of an intrinsic mechanism for division. The possibility that droplets may spontaneously divide has been discussed in the context of either negative surface tension Browne et al. (2010); Patashinski et al. (2012) or in active nematic droplets Giomi and DeSimone (2014). The transition from coacervate droplets to the acquisition of a membrane around these droplets seems like a natural step towards more complex life-like systems, and combinations of both systems, coacervate droplets composed of organic molecules and enclosed by a membrane, have been studied Hanczyc and Szostak (2004); Browne et al. (2010); Murtas (2013); Li et al. (2014); Tang et al. (2014); Frankel et al. (2016); Lach et al. (2016).

## 1.5 Dynamical behavior of active systems

We have seen in the previous two sections that phase separation and chemical reactions occur simultaneously in biological systems and that they might be relevant for the origin of life as well. In both cases, nonequilibrium conditions play an important role, since life itself is out of equilibrium. We now consider the effect of sustained nonequilibrium conditions on the dynamical behavior of systems, that is, we now consider active systems.

### 1.5.1 Behavior of nonequilibrium systems

Nonequilibrium aspects of different systems are a current active field of research in physics. Turing introduced in 1952 a simple mechanism of chemical reaction and diffusion with constant energy input that can lead to pattern formation, Turing (1952). Turing systems and other models have been used extensively in recent decades to



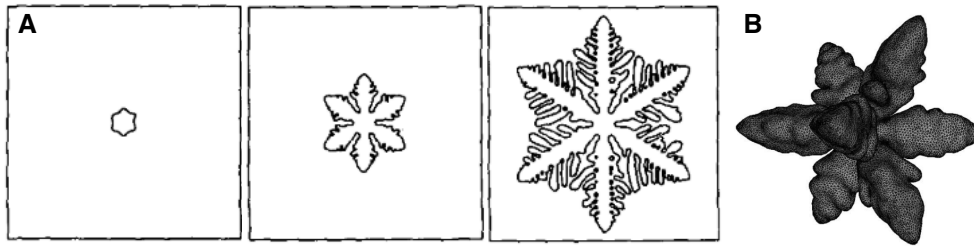


FIGURE 1.2: Examples of the nonlinear shape changes for the dendritic growth of solid structures in a supersaturated liquid. A) Solid shapes during growth at different time points in a 2d simulation. Small initial deformations result in self-similar outgrowths of the solid, called dendrites. Adapted with permission from Kobayashi (1993). B) Three-dimensional shapes in a simulation of a growing solid. Adapted with permission from Cristini and Lowengrub (2004).

explain pattern formation in biological systems, Meinhardt (1992); Karsenti (2008); Green and Sharpe (2015). The influence of nonequilibrium on a variety of physical systems was intensely studied, Cross and Greenside (2009). The Mullins-Sekerka instability that describes the shape instability of a solid precipitate growing in an supersaturated environment is a classical example for a flux-driven shape instability, see Mullins and Sekerka (1963); Langer (1980). This instability is well-studied theoretically and experimentally, and typically leads to dendritic growth of solids, forming tongue-like fractal(ish) shapes, see Fig. 1.2. The consideration of active systems in biological context lead to the study of active matter inspired by moving flocks and Janus particles, Toner et al. (2005). Additionally, it was found that activity can lead to novel behavior of matter, by considering hydrodynamic models for biological tissues, where cells can die and divide, networks of polymers with active driving, and active surfaces, such as membranes in cells, Kruse et al. (2004); Jülicher et al. (2018).

### 1.5.2 Combining phase separation and chemical reactions

The interplay of nonequilibrium chemical reactions on phase separation dynamics was studied in a number of works. It was found that chemical reactions lead to a characteristic size of phases in the case of spinodal decomposition Glotzer et al. (1994); Puri and Frisch (1994); Christensen et al. (1996); Carati and Lefever (1997); Patashinski et al. (2012); Giomi and DeSimone (2014), and that reactions can create and stabilize a characteristic size of droplets, so that Ostwald ripening is suppressed and multiple droplets may stably coexist, Zwicker (2013); Zwicker et al. (2014, 2015). Interactions of chemical gradients with phase separation dynamics has been studied, Weber et al. (2017). Experimentally, the influence of phase separation on chemical reaction rates has been quantified in a number of systems, Song et al. (2006); Crosby et al. (2012); Sokolova et al. (2013); Tang et al. (2015); Frankel et al. (2016); Saha et al. (2016); Drobot et al. (2018). Additionally, systems where chemical reactions can switch be-

tween a phase separating and a homogeneous state has been developed Aumiller and Keating (2016); Nakashima et al. (2018); Rieß et al. (2018). Tread-milling of material can lead to the spontaneous motion of droplets, Tjhung et al. (2012), as can surfactants due to the Marangoni effect, Herminghaus et al. (2014); Maass et al. (2016); Lach et al. (2016). Lastly, it has been found that nematic ordering and membranes or surfactants can have a strong influence on the droplet shape and stability, Yang et al. (2018), allowing for a control of the droplet size, and can lead to a deformation of the droplet (nematic) into an elongated shape or a faceted shape, Guttman et al. (2016), or lead to a split of the droplet into smaller droplets, Derényi and Lagzi (2014).

## 1.6 Overview of the thesis

In this thesis, we will study the dynamics of chemically active droplets. As we have seen in this introductory chapter, driven chemical reactions and phase separation both are found in biological cells. Because both are simple physical/chemical behaviors, they might have played a role at the onset of life. In this thesis, we will explore some aspects of the combination of both effects. In chapter 2, we will extend the theoretical descriptions introduced here for phase separation and chemical reactions into a combined hydrodynamic theory for a multi-component system. In chapter 3, we will introduce a minimal model of chemically active droplets with two components which phase separate into two phases and have active (nonequilibrium) chemical reactions converting them into each other. In the remainder of this thesis, we will discuss the behavior of the minimal model. We start in chapter 4 by considering spherically symmetric droplets. We perform a linear stability analysis to find whether they are stable with respect to shape deformations. We show that chemically active droplets can be unstable with respect to shape deformations, especially elongations of the droplet. Additionally, we discuss the mechanism of this instability and compare it to the droplet instability with the Mullins-Sekerka instability that governs the dendritic growth of solids. In chapter 5 we investigate the dynamical behavior of chemically active droplets numerically. We find that the shape instability of chemically active droplets can lead to growth of a droplet and its elongation and division into two daughter droplets which may grow and divide again. The influence of chemical reactions on other stationary shapes, such as cylindrical droplets, is discussed in chapter 6. In chapter 7, we discuss the effect of hydrodynamic flows on the droplet division. Such flows are important for the rounding up of deformed droplets, and might counteract the instability and division. We will discuss chemically active droplets as a model for protocells at the origin of life in chapter 8. We also discuss the possibility of experimental realizations of chemically active droplets by estimating parameter values for representative systems. Finally, we conclude the thesis by discussing open questions of chemically active droplets in the final chapter 9.

In biological systems, chemical reactions occur frequently in connection with spatial organization of material, such as membranes or phase-separated droplets, see Saha et al. (2016); Banani et al. (2017); Shin and Brangwynne (2017). Similarly, spatial organization of chemical reactions might have played an important role for prebiotic systems at the origin of life, Hanczyc (2011); Crosby et al. (2012); Mast et al. (2013). While membranes have been the subject of experimental and theoretical studies for a long time, the importance of liquid-liquid phase separation in biological systems has become the subject of active research only recently. Therefore, the influence of liquid-liquid phase-separation on chemical reactions, and vice versa, the influence of chemical reactions on the phase separation dynamics, has not been studied in detail. Biological systems are generally out of equilibrium, so that a theoretical description of the dynamic behavior that includes nonequilibrium conditions such as a chemical energy input (such as ATP/ADP) might be worthwhile.

Here we present a theory that describes both phase-separation dynamics and chemical reactions by the same free energy, and employs nonequilibrium thermodynamic theory to derive dynamic equations<sup>1</sup>.

The description is based on irreversible thermodynamics, which is discussed in De Groot and Mazur (2011). The concepts in this chapter can be found also in Jülicher et al. (2018), where irreversible thermodynamics is discussed in a more general framework. Detailed balance of chemical reactions in diffusive environments are also discussed in Kondepudi and Prigogine (2014); Rao and Esposito (2016).

---

<sup>1</sup>The content of this chapter was done in interaction with Christoph Weber.

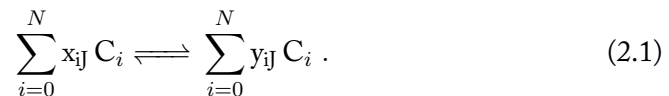
## 2.1 Dynamic description with linear response

Linear response theory is one of the most successful approaches from thermodynamics to describe the dynamical behavior of nonequilibrium systems. It describes fluxes of thermodynamic variables by a linear expansion in the thermodynamic forces of the system around equilibrium. The resulting relations are not a linear theory in the original thermodynamic variables, and can therefore describe complex dynamical situations. We will consider a multi-component system where the number densities of the components can vary in space, with fluxes of particles between volume elements, and chemical reactions between the different components. We concentrate on liquid-like systems, where the liquid can be considered incompressible and space-filling, and where temperature gradients are equalized on faster timescales than the number densities, so that we can consider the temperature as constant.

### 2.1.1 Description of reaction and fluxes by conservation/balance equations

Here we introduce a thermodynamic description of a multi-component system with interactions and reactions between the components, based on a free energy. We study an  $N + 1$  component system with local number densities  $n_i(\mathbf{r}, t) = N_i^{(k)}/V^{(k)}$  for a local subvolume  $V^{(k)}$  at position  $\mathbf{r}$  with  $N_i$  molecules of species  $i$  in the subvolume, with  $i = 0, \dots, N$ . The number densities are space and time dependent fields where  $\mathbf{r}$  is the spatial position and  $t$  the time. We denote molecular volumes  $v_i$ , molecular masses  $m_i$  for component  $i$ .

We study the case of  $N_s$  chemical reactions ( $J = 0 \dots N_s - 1$ ) between components  $C_i$



with the forward and backward reactions rates  $s_J^{\rightarrow}$  and  $s_J^{\leftarrow}$ . For this we introduce the stoichiometric matrix  $s_{iJ} = y_{iJ} - x_{iJ}$ . This matrix describes how many particles of species  $C_i$  are created by reaction  $J$ , which is positive if  $C_i$  is a product of the reaction, negative if it is a reactant and zero if  $C_i$  is a catalyst or not participating in the reaction at all. We study mass-conserving reactions,  $\sum_{i=0}^N s_{iJ} m_i = 0$ .

Due to mass conservation in the system, we can describe the time evolution of the mass density  $\rho = \sum m_i n_i$  by exchange of material between different volume elements,

$$\partial_t \rho + \nabla \cdot (\rho \mathbf{v}) = 0 . \quad (2.2)$$

The hydrodynamic center-of-mass velocity field  $\mathbf{v}$  needs to obey momentum conservation,

$$\partial_t \mathbf{g} + \nabla \cdot \underline{\sigma} = 0 , \quad (2.3)$$

with (local center-of-mass) momentum  $\mathbf{g} = \rho \mathbf{v}$  and stress tensor  $\underline{\sigma}$ . For systems with a small Reynolds number, momentum relaxation is fast,  $D_t \mathbf{g} = 0$  with advected

derivative  $D_t = \partial_t + v_\beta \partial_\beta$ , and we find an equation for stress balance which generalizes the Stokes equation,  $\nabla \cdot \underline{\sigma}^{ad} = 0$ , with  $\sigma_{\alpha\beta}^{ad} = \sigma_{\alpha\beta} + g_\alpha v_\beta$ . Here  $\alpha$  and  $\beta$  number Cartesian coordinates  $x, y, z$  and Einstein summation is used.

The dynamic equations for the number densities are

$$\partial_t n_i + \nabla \cdot \mathbf{J}_i = s_i . \quad (2.4)$$

Here  $s_i = \sum_{J=0}^{N_s} s_{iJ} (s_J^\rightarrow - s_J^\leftarrow)$  describes the net effect of the chemical reactions on component  $C_i$ . The flux  $\mathbf{J}_i$  can be split into advected and diffusive parts,

$$\mathbf{J}_i = n_i \mathbf{v} + \mathbf{j}_i \quad (2.5)$$

where  $\sum_i m_i \mathbf{j}_i = 0$ , thus, adding all equations together to calculate the mass density, we recover Eq. (2.2).

### 2.1.2 Thermodynamic relations

Equations (2.2)-(2.4) describe the dynamical behavior of our system, with as yet unknown fluxes  $s_J, \mathbf{j}_i$  and  $\underline{\sigma}$ . We will use energy conservation and entropy production to find a linear response description for these fluxes. Here we present the thermodynamic relations we will use for this.

Energy conservation can be written as

$$\partial_t u + \nabla \cdot \mathbf{J}_u = 0 . \quad (2.6)$$

for energy density  $u$  and energy flux  $\mathbf{J}_u$ . Entropy is not conserved,

$$\partial_t s + \nabla \cdot \mathbf{J}_s = \theta , \quad (2.7)$$

with entropy density  $s$ , entropy flux  $\mathbf{J}_s$  and local entropy production  $\theta$ . The free energy density can be written as  $f = u - Ts$ , so that we find for the free energy density of an isothermal system

$$\partial_t f + \nabla \cdot (\mathbf{J}_u - T \mathbf{J}_s) = \theta . \quad (2.8)$$

Thus integrating over the whole system, we find the total entropy change over time,  $\dot{S} = \int dV \theta$ , and  $\dot{F} = -T \dot{S}$ , with free energy  $F = \int dV f$ .

For a free energy  $F(\{n_i\}, T, V)$  we can split the free energy density into different terms, with free energy density

$$f = \frac{1}{2} \rho v^2 + f_0(\{n_i\}, T) + \sum_{i,j} \frac{\kappa_{ij}}{2} (\nabla n_i)(\nabla n_j) \quad (2.9)$$

with kinetic contribution  $\rho v^2/2$  and local part of the free energy density  $f_0$ . Energetic interactions between different volume elements are to lowest order represented by gradient terms of second order, with coefficients  $\kappa_{ij}$ . This form can be seen as a generalization of Flory-Huggins free energy to multiple components, or as a lowest

order expansion in the gradient terms. For local stability and validity of the mean field description, the matrix  $\kappa_{ij}$  needs to be positive definite. The free energy is a functional with respect to the number densities  $n_i$ .

We define chemical potentials and pressure as

$$\mu_i = \frac{\delta F}{\delta n_i} = \frac{1}{2}m_i v^2 + \mu_i^{loc} - \kappa_{ii}\Delta n_i - \sum_{j,j \neq i} \frac{\kappa_{ij}}{2} \Delta n_j \quad (2.10)$$

$$P = -\frac{\partial F}{\partial V} = \sum_i n_i \mu_i - f \quad (2.11)$$

with  $\mu_i^{loc} = \frac{\partial f_0(\{n_i\}, T)}{\partial n_i}$ . We can split the chemical potential in the kinetic and the advected part,  $\mu_i^{kin} = \frac{1}{2}m_i v^2$  and  $\mu_i^{ad} = \mu_i - \mu_i^{kin}$ . Pressure and advected chemical potential are related by a Gibbs-Duhem relationship,  $\sum_i n_i d\mu_i^{ad} = V dP$ .

We are interested in the dynamics of the mass density  $\rho$  and the number densities of all components except the solvent, which we denote as component  $C_N$ . Transforming to a description  $F[T, \{n_i\}_{i=0}^{N-1}, \rho]$ , we can define  $N$  independent relative chemical potentials

$$\bar{\mu}_i = \frac{\delta F[T, \{n_i\}_{i=0}^{N-1}, \rho]}{\delta n_i}, \quad (2.12)$$

which are related to the (absolute) chemical potentials via  $\bar{\mu}_i = \mu_i - \frac{m_i}{m_N} \mu_N$ . For these relative chemical potentials, the kinetic contributions from the center of mass movement cancel. Additionally,  $\frac{\delta F}{\delta \rho} = \mu_N / m_N$ . While  $\mu_i$  is associated to the energy change when more particles of component  $i$  are added to the system,  $\bar{\mu}_i$  describes the case where a number of solvent molecules are replaced by a number of molecules of component  $i$  with the same mass.

### 2.1.3 Linear response theory

Let us quickly sketch the idea of linear response theory in nonequilibrium thermodynamics: We will try to find a description of the free energy change  $\dot{F} = \sum_i X_i Y_i$  in terms of the unknown quantities (fluxes)  $Y_i$  paired with other thermodynamic quantities (forces)  $X_i$ , which should be zero at equilibrium. In equilibrium, entropy production is zero, and out of equilibrium, it is positive, thus the entropy production has a minimum at equilibrium, and thus, the free energy production has a maximum. Thus a Taylor expansion of the free energy production in terms of the thermodynamic forces cannot contain constant or linear terms. Therefore we can to lowest order write the fluxes as  $Y_i = \sum_j M_{ij} X_j$ , with a mobility matrix  $M_{ij}$ . Thereby, some couplings might not exist, because the quantities cannot couple if they have different dimensions (scalar vs vector vs matrix). Considering time reversal symmetries leads to additional relationships between the coefficients (Onsager relations).



Calculating the time derivative of our free energy, we find

$$\dot{F} = \int dV \left[ \partial_t \frac{1}{2} \rho v^2 + \partial_t f_0(\{n_i\}, T) + \partial_t \sum_{i,j} \frac{\kappa_{ij}}{2} (\nabla n_i)^2 \right] \quad (2.13)$$

$$= \int dV \left[ v_\alpha \partial_t g_\alpha - \frac{1}{2} v^2 \partial_t \rho + \sum_i \mu_i^{loc} \partial_t n_i - \sum_i \left( \kappa_{ii} (\Delta n_i) + \sum_{j,j \neq i} \frac{\kappa_{ij}}{2} (\Delta n_j) \right) \partial_t n_i \right], \quad (2.14)$$

with index notation  $v_\alpha$ ,  $\sigma_{\alpha\beta}$  for the Cartesian coordinates of vectors and matrices with Einstein summation. For the last term we used integration by parts, and we neglected surface terms from the boundary of our integration volume. Now we insert the conservation equations (2.2), (2.3) and (2.4),

$$\dot{F} = \int dV \left[ v_\alpha \partial_\beta \sigma_{\alpha\beta} + \frac{1}{2} v^2 \partial_\beta g_\beta + \sum_i \mu_i^{ad} (s_i - \partial_\alpha J_{i,\alpha}) \right] \quad (2.15)$$

$$= \int dV \left[ (\partial_\beta v_\alpha) \sigma_{\alpha\beta} - g_\beta \partial_\beta v_\alpha + v_\alpha \sum_i n_i \partial_\alpha \mu_i^{ad} + \sum_i \partial_\alpha \mu_i^{ad} j_{i,\alpha} + \sum_i \mu_i^{ad} s_i \right]. \quad (2.16)$$

Using Gibbs-Duhem relationship,  $\sum_i n_i d\mu_i^{ad} = V dP$ , we can transform the third term to  $-\delta_{\alpha\beta} \partial_\beta v_\alpha P$  (this can also be verified using the explicit expressions in Eq. (2.11)), and collect the first three terms together, to define the dissipative stress tensor

$$\sigma_{\alpha\beta}^d = \sigma_{\alpha\beta} - \rho v_\alpha v_\beta - \delta_{\alpha\beta} P. \quad (2.17)$$

Further, we define reactive forces, called activities,

$$\mathcal{A}_J = \sum_i s_{iJ} \mu_i^{ad} \quad (2.18)$$

for every reaction  $J = 0, \dots, N_s$ , which, using mass conservation of the chemical reactions, can also be written as  $\mathcal{A}_J = \sum_i s_{iJ} \bar{\mu}_i$ ,

$$\sum_{i=0}^{N-1} s_{iJ} \bar{\mu}_i = \sum_{i=0}^{N-1} s_{iJ} \left( \mu_i - \frac{m_i}{m_N} \mu_N \right) = \sum_{i=0}^{N-1} s_{iJ} \mu_i - \frac{\mu_N}{m_N} \sum_{i=0}^{N-1} s_{iJ} v_i = \sum_{i=0}^N s_{iJ} \mu_i. \quad (2.19)$$

We thus find

$$\dot{F} = \int dV \left[ -(\partial_\beta v_\alpha) \sigma_{\alpha\beta}^d + \sum_{i=0}^{N-1} (\partial_\alpha \bar{\mu}_i) j_{i,\alpha} + \sum_{J=0}^{N_s-1} \mathcal{A}_J (s_J^\rightarrow - s_J^\leftarrow) \right]. \quad (2.20)$$

This splits the free energy production in force-flux pairs, where the first term contains matrices, the second vectors and the third scalars.

We can thus write linear response equations,

$$\sigma_{\alpha\beta}^d = 2\eta \left( v_{\alpha\beta} - \frac{1}{3} v_{\gamma\gamma} \delta_{\alpha\beta} \right) + \eta' v_{\gamma\gamma} \delta_{\alpha\beta} + \sum_J b_J \mathcal{A}_J \delta_{\alpha\beta} \quad (2.21)$$

$$j_{i,\alpha} = - \sum_{j=0}^{N-1} m_{ij} \partial_\alpha \bar{\mu}_j \quad (2.22)$$

$$s_J^{\rightarrow} - s_J^{\leftarrow} = \sum_{K=0}^{N_s-1} a_{JK} \mathcal{A}_K + b_J v_{\gamma\gamma} \quad (2.23)$$

with symmetric strain tensor  $v_{\alpha\beta} = (\partial_\beta v_\alpha + \partial_\alpha v_\beta)/2$ , shear viscosity  $\eta$  and compression coefficient  $\eta'$  and mobility coefficients  $m_{ij}$  and  $a_{JK}$ , with  $m_{ij} = m_{ji}$  and  $a_{JK} = a_{KJ}$ . The compression is coupled to the chemical reactions with coupling coefficients  $b_J$ . In the dissipative stress tensor only the symmetric strain tensor (instead of  $\partial_\beta v_\alpha$  enters, due to rotational invariance, also see Jülicher et al. (2018)). The coefficients can depend on the equilibrium concentrations, and can thus be concentration dependent.

Equations (2.21)-(2.23), together with Eq. (2.17), give the relations for the fluxes we need to solve the dynamic equations (2.2)-(2.4) starting from a free energy. In the next section we present a suitable free energy for an incompressible system.

#### 2.1.4 Incompressible system

We are interested in the description of liquid systems, which can usually be considered as incompressible, so that the volume density  $\phi = \sum_i v_i n_i$  is constant everywhere,  $\phi = \phi_0$ . In an incompressible system the pressure takes the form of a Lagrange multiplier to ensure the constant density.

One way to describe the dynamical behavior of an incompressible system is to consider starting conditions with  $\phi = \phi_0$ , and then consider the conservation equation for the volume density,

$$\partial_t \phi + \nabla \cdot \mathbf{u} = 0, \quad (2.24)$$

with volume flow  $\mathbf{u} = \sum_i v_i \mathbf{J}_i$ . Since the volume density is conserved,  $\mathbf{u}$  has to be divergence free,

$$\nabla \cdot \mathbf{u} = 0. \quad (2.25)$$

This then determines the pressure field  $P$ , instead of Eq. (2.11).

We can relate the volume flow  $\mathbf{u}$  to the mass flow  $\mathbf{v}$ ,  $\mathbf{u} = \phi \mathbf{v} + \sum_i v_i \mathbf{j}_i$ , where  $v_i \mathbf{j}_i$  are relative volume fluxes. If the molecular mass/volume ratio is equal for all components,  $m_i/v_i = m_j/v_j$ , the expression simplifies due to mass conservation  $\sum_i m_i \mathbf{j}_i = 0$ . In this case, the volume density and flow is proportional to the mass density and flow,  $\mathbf{u} = \phi \mathbf{v}$ .

### 2.1.5 Multi-component Flory Huggins free energy

An explicit choice for the local free energy density of an incompressible system could be a generalization of Flory-Huggins free energy for a multi-component system,

$$\frac{f_0}{k_B T} = \sum_{i=0}^N n_i \ln(v_i n_i) + \sum_{i=0}^N A_i n_i + \sum_{i,j=0}^N \epsilon_{ij} n_i n_j. \quad (2.26)$$

We can identify the first term in Eq. (2.26) as a mixing entropy. The second term describes the energy of each component separately, while the last term encodes interactions between components. The internal energy includes internal entropic terms  $A_i^S$  and enthalpic terms  $A_i^U$ , with  $A_i = A_i^S + A_i^U / (k_B T)$ , and  $\epsilon_{ij} = \epsilon_{ij}^S + \epsilon_{ij}^U / (k_B T)$ . The entropic terms are created by the internal entropy of molecules, for example due to deformations of the molecule.

For the generalized Flory-Huggins free energy, we find the local part of the chemical potentials

$$\frac{\mu_i^{loc}}{k_B T} = \ln(v_i n_i) + 1 + A_i + \sum_{j=0}^N (\epsilon_{ij} + \epsilon_{ji}) n_j. \quad (2.27)$$

The local part of the  $N$  independent relative potentials  $\bar{\mu}_i = \mu_i - \frac{m_i}{m_N} \mu_N$  is

$$\frac{\bar{\mu}_i^{loc}}{k_B T} = \ln \frac{v_i n_i}{(v_N n_N)^{\hat{m}_i}} + \hat{A}_i + \sum_{j=0}^N \hat{\epsilon}_{ij} n_j \quad (2.28)$$

with constants  $\hat{m}_i = m_i / m_N$ ,  $\hat{A}_i = 1 - \hat{m}_i + A_i - \hat{m}_i A_N$ ,  $\hat{\epsilon}_{ij} = \epsilon_{ij} + \epsilon_{ji} - \hat{m}_i (\epsilon_{Nj} + \epsilon_{jN})$ .

### 2.1.6 Discussion of the linear response equations

In this section, we have discussed a complete set of equations within the framework of linear response theory that describes an incompressible, spatially inhomogeneous system with many components and with chemical reactions between the components. It can describe passive systems relaxing to equilibrium with multiple different (liquid) phases, as well as the dynamical behavior of systems that are kept out of equilibrium via boundary conditions.

Let us briefly discuss the limits of the equations derived here. We only consider isotropic fluids (not nematic or polar ones), and we did not consider temperature as a field variable. Extensions to include polar/nematic and temperature fields would require additional balance equations, with additional couplings to the other variables Jülicher et al. (2018). Electric charges are another aspect that can be relevant in phase-separation of biological systems. They enter through charges of the biological molecules, via the partial charges of water, via additional salts in the system, and via

the splitting of water in hydrogen and hydroxide. Unbalanced charges exhibit long-ranged interactions, and therefore difficult to treat analytically. Due to strong interactions, charges are often balanced locally. They can then be included in the present equations by considering not individual molecules, but combinations of molecules that together are neutral. In this case, the concentration fields of the neutral combinations of molecules should be considered, and an exchange of charged partners corresponds to a reaction between these effective components. Flory-Huggins free energy might still be used for the effective components, albeit with effective interaction parameters, see Johansson et al. (1998).

In biological systems, membrane-bound organelles are an important part of structural organization. Liquid phase separation is often discussed in the form of non-membrane bound organelles, Banani et al. (2017), and we will follow that idea, and study the case without surfactants. Generally, though, membranes, and generally, surfactants may influence phase separation dynamics of systems. Membranes are characterized typically by mono- or bilayer formation, which has a nematic ordering, and a thickness of only one or two molecular layers. The underlying physics is therefore not included in the present presentation. Molecules that act as weak surfactant, however, can be described by the equations presented here if they are soluble in both phases and form an interfacial layer of sufficient width. The aggregation of weakly interacting components at interfaces is rather typical. Consider a three-component system where two components have repulsive interactions ( $\epsilon_{01} > 0$ ), while all other interactions are zero,  $\epsilon_{ij} = 0$  ( $i \neq 0, j \neq 1$ ). If the repulsive interactions are strong enough, two phases may exist, each with a high concentration of one of the two components. The third components will mix in both phases due to mixing entropy, but it will also be enriched in the region between the two phases, thus separating the two repulsive components.

An underlying question of this chapter is: How many different components are needed to describe a multi-component system? Especially in biological systems, thousands of components coexist in the cytosol, and often a number of (related) components form a droplet together, Sear and Cuesta (2003); Jacobs and Frenkel (2017); Banani et al. (2017). It might therefore be often possible to group similar components together, so that effects of the system can be understood with a two-component description, with effective interactions and reactions between these effective components, Sear and Cuesta (2003); Jacobs and Frenkel (2017).

A problem of the approach introduced in this section is that chemical reactions rarely can be described well by linear response. An intuitive argument for this was given by Kondepudi and Prigogine (2014). Linear response in our formulation for fields is a description for system that are close to (local) equilibrium, so that equilibrium conditions can be assumed within each sub-volume, but long-range gradients exist, leading to fluxes between volume elements. All effects discussed here, except chemical reactions, have a spatial driving – the thermodynamic forces all have spatial derivatives in their definition. If the spatial derivatives are zero, no force exists, because all these processes are related to spatial imbalances, such as different stresses and velocities or chemical potentials and fluxes in different regions. If we make the

volume elements that we compare smaller and smaller, the differences between volume elements will become small, so that there is a length-scale  $l$  where linear response holds. If this length-scale is still larger than the size of molecules so that our mean field assumption holds, linear response is a well-justified approach. This is different for chemical reactions. They are a purely local imbalance, which is often visualized as an imbalance along the reaction coordinate. Therefore, the length-scale associated with reactions is zero,  $l = 0$ . Thus, linear response cannot be justified – and also is often found not to describe systems well.

In the next section, we will therefore use a different approach to describe chemical reactions.

## 2.2 Detailed balance of chemical reactions

In equilibrium, concentrations fluctuate over time, with Boltzmann-distributed fluctuations where the mean is given by the minimum of the free energy. The probability of a transition from one state to another is the same as for the backward transition, so that the distribution of states is time-independent and so that no circular fluxes in phase space exist - this is called detailed balance. The multi-component description via coarse grained concentration fields introduced in the previous section corresponds to the mean concentration within each volume element. In equilibrium, every chemical reaction is balanced separately, with  $s_J^{\rightarrow} = s_J^{\leftarrow}$ . The corresponding concentration is the minimum of the free energy with respect to changes due to the reactions,  $\mathcal{A}_J = 0$ . Here, the activity  $\mathcal{A}_J$  is defined in Eq. (2.18).

We can write a generalized detailed balance condition for the forward and backward reactions rates  $s_J^{\rightarrow}$  and  $s_J^{\leftarrow}$  in nonequilibrium conditions,

$$\frac{s_J^{\rightarrow}}{s_J^{\leftarrow}} = \exp\left(-\frac{\mathcal{A}_J}{k_B T}\right). \quad (2.29)$$

This generalized detailed balance condition allows us to determine the sign of the net reaction  $s_J^{\rightarrow} - s_J^{\leftarrow}$ , while it does not allow to determine the reaction speed. In equilibrium (with  $\Delta\mu_J = 0$ ), all reactions are balanced separately, the original definition of detailed balance,  $s_J^{\rightarrow} = s_J^{\leftarrow}$ .

### 2.2.1 Motivation of generalized detailed balance via equilibrium fluctuations

Generalized detailed balance Eq. (2.29) can be derived by considering fluctuations in an equilibrium system. Let us concentrate on two components  $A$  and  $B$  in a small homogeneous volume element. Since all processes need to be balanced independently, we can ignore fluxes between neighboring volume elements and consider the case where the total number of molecules  $N = N_A + N_B$  in the system is conserved. Molecules can be converted by a chemical reaction between type  $A$  and  $B$ .

The probability of the number of  $B$  molecules is Boltzmann distributed,

$$P(N_B) = \frac{1}{Z} e^{-\beta F(N_B)}, \quad (2.30)$$

where  $F(N_B)$  is the free energy of the state of  $N_B$  molecules of type  $B$ , and the partition function  $Z$  normalizes the distribution,  $\int_0^N P(N_B) = 1$ . Additionally,  $\beta = 1/k_B T$ . The probability to go from state  $N_B$  to  $N_B + 1$  and the reverse transition can be given as

$$s_+(N_B) = r_+(N_B) P(N_B) \quad (2.31)$$

$$s_-(N_B + 1) = r_-(N_B + 1) P(N_B + 1), \quad (2.32)$$

where  $r_{\pm}$  is the transition rate to a higher (+) or lower (-) state due to the chemical reaction. In equilibrium,  $s_+(N_B) = s_-(N_B + 1)$ . Inserting the Boltzmann-distribution we can thus write

$$\frac{r_+(N_B + 1)}{r_-(N_B)} = e^{-\beta[F(N_B+1)-F(N_B)]}. \quad (2.33)$$

In the thermodynamic limit of large  $N$ ,  $N_B/V = c_B$  and  $(N - N_B)/V = c_A$ , and  $F(N_B + 1) - F(N_B) \cong \mu_B - \mu_A = \mathcal{A}$ . Furthermore,  $r_+(N_B + 1) \approx r_+(N_B)$ . Therefore we find

$$\frac{r_+(c_B)}{r_-(c_B)} = e^{-\beta \mathcal{A}}. \quad (2.34)$$

We can now interpret a nonequilibrium state with concentration  $c_B$  as a random fluctuation in an equilibrium system, so that Eq. (2.34) holds. Additionally, we start the system in a well-defined state, so that  $P(c_B) = 1$ . Therefore, we find the generalized detailed balance Eq. (2.29) for the reaction rates (where  $s_J^{\rightarrow} \cong s_+(c_B)$ ).

### 2.2.2 The 'equilibrium constant' in phase-separating systems

In discussions of the mass action law of chemical reactions an equilibrium constant is defined, Kondepudi and Prigogine (2014); Atkins (1994). We briefly show in this part that this concept is limited to dilute solutions, and somewhat misleading when phase-separating multi-component systems are considered.

We can formally write the reaction rates introduced in Eq. (2.1) as

$$s_J^{\rightarrow} = k_J^{\rightarrow} \prod_i c_i^{x_{iJ}} \quad (2.35)$$

$$s_J^{\leftarrow} = k_J^{\leftarrow} \prod_i c_i^{y_{iJ}}, \quad (2.36)$$

where all nontrivial kinetics is captured by the terms  $k_J^{\rightarrow}$  and  $k_J^{\leftarrow}$ . For lack of a better name and to follow the generally used nomenclature, we will call  $k_J^{\rightarrow}$  and  $k_J^{\leftarrow}$  reaction constants, even though they are not generally constants, and explicitly not in the case

of interacting molecules. For constant  $k_J^\rightarrow$  and  $k_J^\leftarrow$ , above equation corresponds to the law of mass action. If the law of mass action is to hold for small concentrations of all participating molecules,  $k_J^\rightarrow$  and  $k_J^\leftarrow$  should therefore become constants in this limit.

The generalized detailed balance condition determines the ratio of the two reaction constants  $k_J^\rightarrow$  and  $k_J^\leftarrow$ ,

$$\frac{k_J^\rightarrow}{k_J^\leftarrow} = \exp \left[ -\frac{\mathcal{A}_J}{k_B T} + \sum_i s_{iJ} \ln(v_i c_i) \right]. \quad (2.37)$$

Often this is used to define 'equilibrium constants',

$$K_J = \frac{k_J^\rightarrow}{k_J^\leftarrow}, \quad (2.38)$$

so that the equilibrium concentrations  $\hat{n}_i$  have to fulfill

$$\prod_i \frac{\hat{c}_i^{y_{iJ}}}{\hat{c}_i^{x_{iJ}}} = K_J. \quad (2.39)$$

We can write  $K_J$  explicitly for the multi-component Flory Huggins free energy,

$$K_J = \prod_i \exp[-s_{iJ}(1 + A_i)] \prod_{i,j} \exp[-s_{iJ}(\epsilon_{ij} + \epsilon_{ji})c_j]. \quad (2.40)$$

We find that in non-interacting systems with  $\epsilon_{ij} = 0$  for all indices, the  $K_J$  are indeed constants that depends on the internal energies of the reactants and the change in entropy due to the reaction. Therefore the equilibrium concentrations  $\hat{n}_i$  are well-defined. For  $\epsilon_{ij} \neq 0$  the equilibrium 'constants' becomes dependent on the concentrations of the components in the system. If the  $K_J$  only depend on components that do not participate in the reactions and the system is homogeneous, it can still be considered constant with respect to the reaction dynamics of the specific system. Generally, the situation is more complex: In a phase-separating system, Eq. (2.39) may have more than one solution that is relevant for the dynamical behavior of the system due to different concentrations in the phases. Additionally, during the course of the reaction, components may move between the phases, so that  $K_J$  can change over time even within the phases.

As an example, we consider a phase-separated system in equilibrium with respect to phase-separation. Chemical reactions between components take place, which fulfill the generalized detailed balance condition. We can define a partition coefficient for components  $i$  as

$$p_i = \frac{c_i^-}{c_i^+} \quad (2.41)$$

where we denote the droplet phase with  $-$  (minority phase), and the outer phase with  $+$  (majority phase). The concentrations are given by local equilibrium  $\hat{\mu}_i^- = \hat{\mu}_i^+$ . In

Flory-Huggins model, this can be written as

$$p_i = \exp \left[ \frac{m_i}{m_N} (\mu_N^- - \mu_N^+) - \sum_{j=0}^N (\epsilon_{ij} + \epsilon_{ji})(c_j^- - c_j^+) \right]. \quad (2.42)$$

Using the Flory-Huggins model, we can write the ratio of the equilibrium constant of reaction  $J$  in the phases as

$$\frac{K_J^-}{K_J^+} = \prod_{i,j} \exp \left[ -s_{iJ} (\epsilon_{ij} + \epsilon_{ji})(c_j^- - c_j^+) \right] \quad (2.43)$$

which simplifies to

$$\frac{K_J^-}{K_J^+} = \prod_i p_i^{s_{iJ}} \prod_i \exp \left[ -s_{iJ} \frac{m_i}{m_N} (\mu_N^- - \mu_N^+) \right] \quad (2.44)$$

where the last term is zero because  $\sum_i s_{iJ} m_i = 0$  due to mass conservation in the reaction, so that

$$\frac{K_J^-}{K_J^+} = \prod_i p_i^{s_{iJ}}. \quad (2.45)$$

Therefore, we find that when chemical reactions occur between components A and B that have different partition ratios, the equilibrium constants will be different in both phases, and be given by the ratio of the partition ratios of the products and substrates of the reaction. This results does not depend on the Flory-Huggins free energy, but is general. It is due to the fact that both exchange of material between phases, as well as reaction between components are governed by the same free energy, and that equilibrium cannot have circular fluxes: It is a reformulation of the statement that the partition ratio of a component A can change by two ways: A molecule of A can leave the droplet, or it can be exchanged locally by a reaction  $A \rightarrow B$  by a B molecule, which can leave the droplet, and react back into A outside. In equilibrium, both of these paths should be balanced. Here we show that a similar statement holds in nonequilibrium for reactions that fulfill our generalized detailed balance condition. This simple statement demonstrates that the description of chemical reactions in phase separating systems is inherently connected with the phase separation, and that a simple limit of small concentrations does not generally hold - not even for the equilibrium constants of reactions between components that partition into the phases, but do not form them themselves.

### 2.3 Summary

In this chapter we have presented a dynamic description of a multi-component system that includes phase separating behavior due to interactions and chemical reactions between the components. We can describe the spatial dynamics of the system by



linear response theory based on a multi-component Flory-Huggins free energy. For the chemical reactions, we discussed generalized detailed balance as an alternative basis for a description.



In the next chapters of this thesis, we will study the dynamical behavior of phase-separating systems with nonequilibrium chemical reactions, that is, of chemically active droplets. To facilitate this, we introduce in this chapter a minimal model with two phase-separating components with chemical reactions between them. By decoupling the chemical reaction from the free energy that drives the phase-separation dynamics, the model becomes active, in the sense that the system is permanently kept in a nonequilibrium state by an implicit energy supply via the chemical reaction. We discuss two formulations of such a two-component model of chemically active droplets. The continuum model follows the description based on a free energy introduced in the previous chapter. The effective droplet model describes the droplet interface as much smaller than the spatial dynamics. Local equilibrium across the interface then yields jump conditions of the fields in the two the phase. The interface moves due to the flow of droplet material to the interface. We motivate the minimal model as a limit of a multi-component system with additional reservoir components. These components are converted in the reaction, and thus produce an (effective) breaking of detailed balance of the two component description. Finally, we will give a small outlook on the behavior of chemically active droplets to motivate the study of the dynamics of active droplets in the following chapters.

## 3.1 Continuum model for chemically active droplets

To study the dynamical behavior of chemically active droplets, we introduce here a minimal model with two components using the irreversible thermodynamics description introduced in the previous chapter.

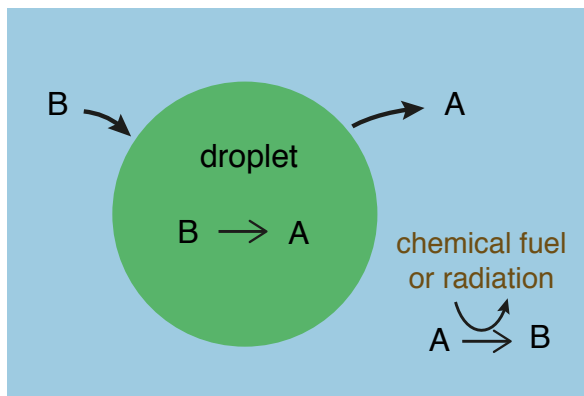


FIGURE 3.1: Simple model, with droplet material  $B$  and soluble component  $A$ . The system is driven by a chemical fuel  $C$  that is transformed to the reaction product  $C'$ .

### 3.1.1 Definition of the continuum model

We now describe the dynamic equations of a chemically active droplet. We consider an incompressible, isothermal fluid composed of two components  $A$  and  $B$ , with number concentration fields  $c_A(\mathbf{r}, t)$  and  $c = c_B(\mathbf{r}, t)$  that depend on position  $\mathbf{r}$  and time  $t$ , and with molecular masses  $m_A$  and  $m_B$  and molecular volumes  $v_A$  and  $v_B$ . We are interested in the case where component  $A$  forms the background fluid and  $B$  is a droplet material that forms droplets by phase separation. Additionally, chemical reactions convert the two components into each other,  $A \rightleftharpoons B$ . We consider these two components to have equal molecular masses to volume ratios  $m_A/v_A = m_B/v_B$ . Mass and volume conserving reactions together with incompressibility imply that the mass density  $\rho = m_A c_A + m_B c_B$  is constant, so that we only need to consider the concentration field of droplet material  $B$ .

Using the irreversible thermodynamic description of the last chapter, the dynamics of the concentration field is described by

$$\partial_t c = -\nabla \cdot \mathbf{j} + s(c) \quad (3.1)$$

$$\mathbf{j} = -m \nabla \bar{\mu} + \mathbf{v} c. \quad (3.2)$$

Here,  $m$  is a mobility coefficient of the droplet material and  $\mathbf{v}$  is the hydrodynamic velocity. The source term  $s(c)$  describes chemical reactions. The chemical potential  $\bar{\mu} = \delta F[c]/\delta c$  governs demixing, with the free energy

$$F[c] = \int d^3 r f(c), \quad (3.3)$$

where the integral is over the system volume. We use the following double-well free energy density, Cahn and Hilliard (1958)

$$f(c) = \frac{b}{2(\Delta c)^2} (c - c_-^{(0)})^2 (c - c_+^{(0)})^2 + \frac{\kappa}{2} (\nabla c)^2, \quad (3.4)$$

with  $\Delta c = |c_-^{(0)} - c_+^{(0)}|$ . The coefficient  $\kappa$  is related to surface tension and the interface width, the positive parameter  $b$  characterizes molecular interactions and entropic contributions, Cahn and Hilliard (1958). This free energy describes the segregation of the fluid in two coexisting phases: one phase rich in droplet material with  $c \approx c_-^{(0)}$  and a dilute phase with  $c \approx c_+^{(0)}$ , compare Desai and Kapral (2009).

The chemical potential  $\bar{\mu}$  is evaluated as

$$\bar{\mu} = \bar{\mu}_0 - \kappa \nabla^2 c \quad (3.5)$$

with

$$\bar{\mu}_0 = \frac{b}{(\Delta c)^2} (c - c_+^{(0)}) (c - c_-^{(0)}) (2c - c_-^{(0)} - c_+^{(0)}) . \quad (3.6)$$

The hydrodynamic velocity  $\mathbf{v}$  can be calculated using momentum conservation,

$$\partial_t(\rho v_\alpha) = \partial_\beta \sigma_{\alpha\beta} , \quad (3.7)$$

with momentum  $\rho v_\alpha$  and stress tensor  $\sigma_{\alpha\beta}$ , where  $\alpha$  and  $\beta$  number Cartesian coordinates  $x, y, z$ , compare chapter 2. We can decompose the stress tensor  $\sigma_{\alpha\beta}$  as

$$\sigma_{\alpha\beta} = -(\rho v_\alpha) v_\beta + \sigma_{\alpha\beta}^{eq} + \sigma_{\alpha\beta}^d , \quad (3.8)$$

where the first term describes advection of the stress tensor,  $\sigma_{\alpha\beta}^{eq}$  and  $\sigma_{\alpha\beta}^d$  denote the equilibrium and dissipative stress tensors. The equilibrium stress tensor is given by

$$\sigma_{\alpha\beta}^{eq} = -(\bar{\mu}c - f)\delta_{\alpha\beta} - \frac{\partial f}{\partial(\partial_\alpha c)} \partial_\beta c - P_0 \delta_{\alpha\beta} . \quad (3.9)$$

Here,  $\bar{\mu}c - f$  is the osmotic pressure of the droplet material, and  $\delta_{\alpha\beta}$  denotes the Kronecker delta. Incompressibility is enforced by an additional partial pressure  $P_0$ . The deviatoric stress tensor is

$$\sigma_{\alpha\beta}^d = 2\eta \tilde{v}_{\alpha\beta} + \eta' v_{\gamma\gamma} \delta_{\alpha\beta} , \quad (3.10)$$

where  $\eta$  and  $\eta'$  denote viscosities,  $v_{\alpha\beta} = (\partial_\alpha v_\beta + \partial_\beta v_\alpha)/2$  is the symmetric strain rate tensor, and  $\tilde{v}_{\alpha\beta} = v_{\alpha\beta} - v_{\gamma\gamma} \delta_{\alpha\beta}/3$  is the traceless symmetric strain tensor.

In the Stokes limit, the inertial terms are neglected,  $D_t(\rho v_\alpha) = 0$ , with advected derivative  $D_t = \partial_t + v_\beta \partial_\beta$ , leaving  $0 = \partial_\beta(\sigma_{\alpha\beta}^{eq} + \sigma_{\alpha\beta}^d)$ . This yields, Cates (2012),

$$\eta \partial_\beta^2 v_\alpha = 3\bar{\mu}_0 \partial_\alpha c - \kappa c \nabla^2(\partial_\alpha c) + \partial_\alpha P_0 . \quad (3.11)$$

The pressure is determined by incompressibility

$$\partial_\alpha v_\alpha = 0 . \quad (3.12)$$

We consider the case where the reaction can be described by a linear form within each phase and has a smooth behavior across the interface,

$$s(c) = \begin{cases} \nu_+ - k_+(c - c_+^{(0)}) & \text{for } c \leq c_c^+ \\ p(c) & \text{for } c_c^+ < c < c_c^- \\ -\nu_- - k_-(c - c_-^{(0)}) & \text{for } c \geq c_c^- \end{cases} , \quad (3.13)$$

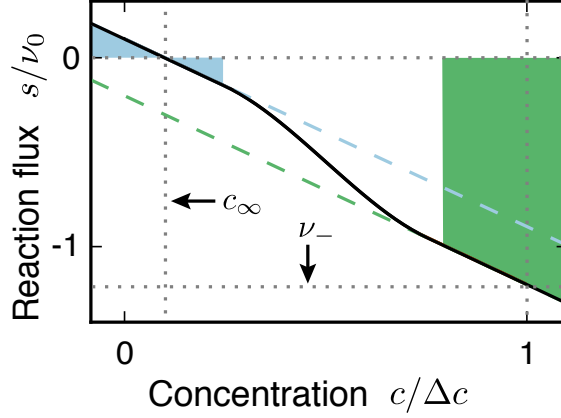


FIGURE 3.2: Chemical reaction flux  $s$  as a function of concentration (black). The linearized fluxes inside (green) and outside the droplet (blue) are indicated as dashed lines. Outside the droplet, the reaction flux is zero for concentration  $c_\infty$ , inside the droplet, the reaction flux is negative with value  $-\nu_-$  for the concentration  $c_-^{(0)}$ . Parameter values:  $k_\pm\tau_0 = 10^{-2}$ ,  $\nu_-/\nu_0 = 1.2$ ,  $\nu_+/\nu_0 = 0.1$ ,  $c_+^{(0)} = 0$  with  $\nu_0 = 10^{-2}\Delta c/\tau_0$ .

shown in Fig. 3.2. Here,  $c_c^+$  and  $c_c^-$  are two characteristic concentrations and  $p(c) = a_0 + a_1c + a_2c^2 + a_3c^3$  is a cubic polynomial that interpolates between the linear regimes. The coefficients  $a_i$  are determined uniquely by the conditions that  $s(c)$  and its derivative are continuous functions:

$$\begin{aligned} p(c_c^+) &= s(c_c^+) & p'(c_c^+) &= -k_+ \\ p(c_c^-) &= s(c_c^-) & p'(c_c^-) &= -k_- . \end{aligned} \quad (3.14)$$

We concentrate on the case of  $\nu_\pm > 0$ , which describes the case of reaction  $B \rightarrow A$  inside and  $A \rightarrow B$  outside the droplet. In the other cases, the dynamics of a single droplet can be qualitatively described: For  $\nu_\pm < 0$ , droplet material is created in the droplet, and outer material outside. This tends to create a competition between the growth of both phases where the phases with stronger reaction and larger initial volume wins and the system becomes homogeneous with a concentration  $c_0$  set by the chemical reaction with  $s(c_0) = 0$ , with  $c_0 < c_+^{(0)}$  or  $c_0 > c_-^{(0)}$ . For different sign of  $\nu_\pm$ , the reaction either creates or destroys droplet material in both phases, so that the system again becomes homogeneous with concentration  $c_0$  set by  $s(c_0) = 0$ . Therefore in all cases except the first, the stable stationary state of the system (if one exists) tends to be a homogeneous system with concentration set by the reaction. Therefore the case  $\nu_\pm > 0$  is the most intriguing. Additionally, we concentrate on the case with  $k_\pm > 0$ , which leads to smooth concentration profiles in both phases, instead of additional Turing-like pattern formation.

The equations for the concentration field (3.1) with fluxes (3.2), the chemical potential (3.5) with (3.6), stress balance (3.11) with incompressibility (3.12) and the

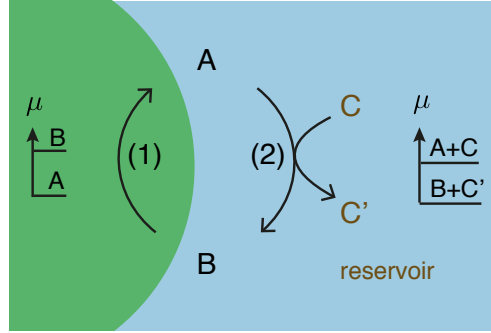


FIGURE 3.3: Reaction rates and energy supply. Schematic representation of the reaction cycle involving the two pathways  $A \rightleftharpoons B$  (1) and  $A + C' \rightleftharpoons B + C$  (2). The differences of the chemical potentials  $\mu$  determine the directions of the spontaneous reactions: Coupling to the chemical fuel  $C$  with reaction product  $C'$  drives reaction pathway (2) in the direction  $A \rightarrow B$  outside the droplet. Inside the droplet, where the concentration of  $C$  is smaller, reaction pathway (1) in the direction  $B \rightarrow A$  dominates. See Appendix A for details.

chemical reaction (3.13) with (3.14) define the continuum model of chemically active droplets. Note that the model may also be used to describe a three component system with reactions  $A \rightleftharpoons B$  and phase-separation between droplet material  $B$  and a mixture of solvent  $S$  and reactant  $A$  occurs, as long as the components  $A$  and  $S$  can be considered well-mixed due to similar interactions and fast mobility of  $A$  compared to droplet material  $B$ .

### 3.1.2 Effective breaking of detailed balance

To highlight the non-equilibrium nature of the reaction scheme in Eq. (3.13), we keep the system out of equilibrium explicitly by introducing reservoir components  $C$  and  $C'$ , which are held at a constant chemical potentials with difference  $\Delta\mu = \mu_{C'} - \mu_C$ . Due to interactions of  $C$  and  $C'$  with the droplet material, the concentrations of both components may be different in both phases. We consider a system where the mobility of  $C$  and  $C'$  is much larger than that of the droplet material, so that we do not need to consider dynamical equations for the two components. We have two chemical reactions,



without energy input, and



where the reservoir components participate. The total reaction rate is then given by

$$s(c) = s_{\rightarrow}^{(1)} - s_{\leftarrow}^{(1)} + s_{\rightarrow}^{(2)} - s_{\leftarrow}^{(2)}, \quad (3.17)$$

where  $s_{\rightarrow}^{(1)}$  denotes the production of B due to the forward direction of reaction (3.15), and  $s_{\leftarrow}^{(1)}$  denotes the degradation of B due to the reverse direction, and equivalently for reaction (3.16). We use generalized detailed balance equations for the chemical reactions. For a reaction  $A \rightarrow B$  we find

$$\frac{s_{\rightarrow}^{(1)}}{s_{\leftarrow}^{(1)}} = e^{-\frac{\bar{\mu}}{k_B T}} \quad (3.18)$$

This equation does not determine the reaction speed, but the direction of the reaction given by  $s_{\rightarrow}^{(1)}/s_{\leftarrow}^{(1)} > 1$  or  $s_{\rightarrow}^{(1)}/s_{\leftarrow}^{(1)} < 1$ , and thus ensures that the reaction always proceeds downhill. The second reaction is described by

$$\frac{s_{\rightarrow}^{(2)}}{s_{\leftarrow}^{(2)}} = e^{-\frac{\bar{\mu} + \Delta\mu}{k_B T}} \quad (3.19)$$

Note that we can add a linear term  $uc$  with constant  $u$  to the free energy density without influencing the phase-separation dynamics. This term corresponds to a free energy difference between components  $B$  and  $A$  and may influence the direction of the reactions according to Eq. (3.18) and (3.19).

We can consider the reaction in a phase-separated system with reaction rates so small that the concentrations are not changed. In a phase-separated system in equilibrium, the chemical potential  $\bar{\mu}$  is the same in both phases,  $\bar{\mu}_- = \bar{\mu}_+$  where '-' denotes the minority phase, the droplet, while '+' denotes the outer majority phase. Therefore, the direction of reaction 1 is the same in both phases, as is the direction of reaction 2. To create different directions of the combined reaction rate in the different phases, we therefore require that both reactions proceed in opposite directions, and that one of the reactions is faster in one phase, while the other is faster in the other. This is shown diagrammatically in Fig. 3.3.

A discussion that explicitly relates the free energy of all four components with the reaction rates can be found in Appendix A.

## 3.2 Effective droplet model for chemically active droplets

In the previous chapter and in section 3.1 we considered a model with a continuous description of the droplet interface. This approach can describe nucleation of new droplets and topological shape changes of droplets, such as division. However, the nonlinear description is unsuitable for analytical treatment.

In most experimental systems, interfacial widths are on the order of few molecular lengths, and thus much smaller than typical reaction-diffusion lengthscales found in experimental systems, Safran (1994). Here we introduce a description that treats the droplet interface as infinitely thin, where the properties on both sides of the interface are in local equilibrium across the interface. Within both phases, we consider diffusive dynamics for the concentration. The interface can move due to fluxes of droplet material towards the droplet interface. This results in the so-called Stefan problem



of partial differential equations for fields with a moving boundary condition (at the droplet interface), Stefan (1891); Crank (1987). Such approaches are commonly used in literature to study growth and deformation of phases, Lifshitz and Slyozov (1961); Mullins and Sekerka (1963), and to study hydrodynamic flows in phase-separated systems, Batchelor (2000). It has been used previously to study the effect of chemical reactions on droplet dynamics, Zwicker (2013); Zwicker et al. (2015). The effective droplet model we introduce in the section includes all physical aspects that were present in the continuum model, namely phase-separation, hydrodynamic flows and nonequilibrium chemical reactions.

### 3.2.1 Definition of the effective droplet model

As in the previous section, we consider an incompressible, phase-separating liquid consisting of droplet material B and solvent component A with a volume preserving chemical reaction  $A \rightleftharpoons B$  with constant mass density. The local composition is characterized by the concentration field  $c(\mathbf{x})$  of component B. We consider a single droplet characterized by high concentration  $c \approx c_-^{(0)}$  of component B coexisting with the surrounding fluid that mainly consists of A and contains B at low concentration  $c \approx c_+^{(0)}$ , see Fig. 3.1. We denote the droplet phase with index  $-$  (for minority phase) and the outer phase with  $+$  (majority phase). Both phases are separated by a sharp interface. Within both phases, the concentration of B satisfies a balance equation, where the chemical reaction provide a source or sink term  $s_{\pm}(c)$ ,

$$\partial_t c + \nabla \cdot \mathbf{j} = s_{\pm}(c) \quad (3.20)$$

$$\mathbf{j} = -D_{\pm} \nabla c + \mathbf{v} c. \quad (3.21)$$

The flux  $\mathbf{j}$  consists of advection by the fluid velocity  $\mathbf{v}$  and a diffusion flux, where  $D_{\pm}$  denotes the diffusion constant of the droplet material in the two phases.

We linearize the chemical reaction rates  $s_{\pm}(c)$  in the vicinity of reference concentrations  $c_{\pm}^{(0)}$  in each phase:

$$s_{\pm}(c) \simeq -k_{\pm}(c - c_{\pm}^{(0)}) \pm \nu_{\pm}, \quad (3.22)$$

with reaction rate  $\nu_{\pm} = s(c_{\pm}^{(0)})$  and reaction constants  $k_{\pm} = ds(c_{\pm}^{(0)})/dc$ . The concentration field varies over the characteristic length scales  $l_{\pm} = (D_{\pm}/k_{\pm})^{1/2}$  inside and outside the droplet, respectively.

The hydrodynamic flow velocity  $\mathbf{v}$  obeys Stokes equation of an incompressible fluid in both phases,

$$\eta_{\pm} \nabla^2 \mathbf{v} = \nabla P \quad (3.23)$$

$$\nabla \cdot \mathbf{v} = 0. \quad (3.24)$$

Here, Eq. (3.23) accounts for stress balance  $\partial_{\alpha} \sigma_{\alpha\beta} = 0$ , where the stress tensor is given by  $\sigma_{\alpha\beta} = \eta_{\pm}(\partial_{\alpha} v_{\beta} + \partial_{\beta} v_{\alpha}) - P \delta_{\alpha\beta}$ . Here  $\eta_{\pm}$  denotes the fluid shear viscosities inside and outside of the droplet. The pressure  $P$  plays the role of a Lagrange multiplier to ensure incompressibility, Eq. (3.24).

The bulk equations (3.20-3.24) are connected by boundary conditions at the droplet interface  $R(s_1, s_2)$  where  $s_1$  and  $s_2$  are coordinates of a parametrization of the droplet interface. The stress boundary condition reads

$$\sigma_{nn}^+(R) - \sigma_{nn}^-(R) = 2\gamma H(R) \quad (3.25)$$

$$\sigma_{nt}^+(R) - \sigma_{nt}^-(R) = 0, \quad (3.26)$$

where  $H(R)$  is the local mean curvature of the interface and  $\gamma$  is the droplet surface tension. The stresses at the interface on the inner and outer side of the droplet are denoted by  $\sigma_{\alpha\beta}^\pm(R)$ . The tensor indices  $n$  and  $t$  refer to tensor components normal and tangential to the interface, respectively. Eq. (3.26) is valid for all tangent vectors. Using no-slip boundary conditions, the velocity field is continuous at the interface,

$$\mathbf{v}^+(R) = \mathbf{v}^-(R). \quad (3.27)$$

The concentration field  $c$  is discontinuous across the interface,

$$c_-(R) = c_-^{(0)} + \beta_- \gamma H(R) \quad (3.28)$$

$$c_+(R) = c_+^{(0)} + \beta_+ \gamma H(R) \quad (3.29)$$

where the concentrations are set by the physics of phase coexistence and a local equilibrium assumption, compare section 1.1 and Appendix B. The coefficients  $\beta_\pm$  describe the effects of the Laplace pressure on the equilibrium concentrations at phase coexistence.

The droplet grows by the addition of droplet material to the interface. The normal velocity of the droplet interface is

$$v_n(R) = \mathbf{n} \cdot \frac{\mathbf{j}^-(R) - \mathbf{j}^+(R)}{c_-(R) - c_+(R)}, \quad (3.30)$$

where  $\mathbf{n}$  denotes the surface normal, Bray (1994). Eq. (3.30) captures both convection of the interface by flows, and droplet growth and shrinkage by addition or removal of material.

For a system that consists of one almost spherical droplet, we can use spherical coordinates  $r, \theta, \phi$  centered on the droplet. The interface defining the droplet surface is positioned at radial distance  $r = R(\theta, \phi)$ , so that the droplet inside is at  $r < R(\theta, \phi)$ , and the outside at  $r > R(\theta, \phi)$ . In a radial description of the droplet interface,  $\mathbf{R}(\theta, \phi) = R(\theta, \phi)\mathbf{e}_r$ , the radial velocity is

$$\frac{\partial R}{\partial t} = \frac{v_n}{\mathbf{e}_r \cdot \mathbf{n}}. \quad (3.31)$$

Eq. (3.20) to (3.31) define the effective droplet model. Due to the explicit description of the interface, topological transitions of the droplet are not described in the model. This includes a large number of typical dynamical behaviors of phase-separating systems, such as nucleation of new droplets, dissolution of droplets, coalescence of two droplets, or the split-up of a cylindrical jet into droplets. However,

the effective droplet model is very useful for an intuitive understanding of the system and for analytical calculations due to its (mostly) linear equations and the explicit description of the droplet size and shape, as we will see in the next chapter.

### 3.2.2 Effective droplet model as a limit of the continuum model

Description	Continuum model	Effective droplet model
Chemical reaction in droplet	$\nu_- t_0 / \Delta c$ $k_- t_0$	$\nu_- t_0 / \Delta c$ $k_- t_0$
Chemical reaction outside droplet	$\nu_+ t_0 / \Delta c$ $k_+ t_0$	$\nu_+ t_0 / \Delta c$ $k_+ t_0$
Chemical reaction across interface	$c_c^+ / \Delta c$ $c_c^- / \Delta c$	- -
Viscosity	$\eta_- w^3 / (e_0 t_0)$ 1	$\eta_- w^3 / (e_0 t_0)$ $\eta_+ / \eta_-$
Diffusion in droplet	1	$D_- / D_+$
Interfacial parameter	1	$\beta_- / \beta_+$
Concentration outside droplet	$c_+^{(0)} / \Delta c$	$c_+^{(0)} / \Delta c$
Concentration difference of phases	$\Delta c = c_-^{(0)} - c_+^{(0)}$	$\Delta c = c_-^{(0)} - c_+^{(0)}$
Interfacial width	$w = 2(\kappa/b)^{1/2}$	$w = 6\beta_+ \gamma / \Delta c$
Diffusion-time across interface	$t_0 = w^2 / (mb)$	$t_0 = w^2 / D_+$
Interfacial energy	$e_0 = \kappa w (\Delta c)^2 / 3$	$e_0 = \gamma w^2$

Table 3.1: Dimensionless parameters of the continuum model and the corresponding parameters in the effective droplet model, together with the characteristic concentration, length, time and energy used for normalization (bottom 4 rows).

It is possible to recover all dynamical equations of the effective droplet model from the continuum model based on irreversible thermodynamics, see Appendix B. For this, we consider the case where the interface width  $w$  is small compared to the droplet size,  $R/w \gg 1$ , and the chemical diffusion length,  $l_{\pm}/w \gg 1$ . Additionally, we focus on the case where the concentrations in the phases are similar to the concentrations in equilibrium and have small concentration gradients. This allows us to relate the parameters  $b$ ,  $\kappa$ , and  $m$  of the continuum model to the parameters  $\gamma$ ,  $\beta_{\pm}$ , and  $D_{\pm}$  of the effective droplet model, compare Appendix B. We use this to define equivalent parameters for both models.

In Table 3.1 we list these parameters of both models. We use the properties of the interface to normalize concentration, length, time and energy (bottom four rows in the table). These correspond to the difference of the reference concentrations  $\Delta c$ , the interfacial width  $w$  or  $\hat{w}$ , the timescale related to diffusion across the interface  $t_0$  or  $\tau_0$  and an energy related to surface tension  $e_0$  or  $\hat{e}_0$ . The specific choice of the free energy in the continuum model leads to specific relations between parameters of the

effective model,  $\beta_+ = \beta_-$  with  $\beta_+ = 2/(b\Delta c)$ , and  $D_+ = D_-$  with  $D_+ = mb$ . Additionally, we have chosen the viscosity as constant,  $\eta_+ = \eta_-$ . The surface tension of the effective model is given by  $\gamma = (\Delta c)^2/6\sqrt{\kappa b}$ . The parameters  $c_c^\pm/\Delta c$  of the continuum model capture properties of chemical reactions inside the interface and therefore do not exist in the effective droplet model. The dimensionless parameter  $c_+^{(0)}/\Delta c$  is unimportant for the dynamical behavior of the system and only leads to a constant shift of the concentration profiles. We therefore set  $c_+^{(0)}/\Delta c = 0$  throughout this thesis.

The conditions for which the models describe similar physical effects are not fulfilled in all systems. Most importantly, the chemical reactions can drive concentrations far away from the equilibrium phase concentrations  $c_\pm^{(0)}$ . The concentration in the outer phase can be considered homogeneous if the concentration far from the droplet  $c_\infty$  set by  $s(c_\infty) = 0$  is close to the reference concentration  $c_+^{(0)}$ . The inside of the droplet is homogeneous if the droplet is much smaller than  $l_-$ , or if the concentration  $c_0^-$  set by the reaction inside the droplet  $s(c_0^-) = 0$  is close to  $c_-^{(0)}$ . In regimes where the concentration in a phases instead permits the formation of new interfaces associated with instabilities of the spinodal decomposition regime, the effective model discussed here cannot capture these behaviors, and thus may yield unphysical results.

### 3.3 Outlook

In this chapter we have introduced a minimal model of chemically active droplets, with two formulations: The continuum droplet model is based on a free energy and can describe a wide range of dynamical behaviors including droplet division and nucleation. The effective droplet model explicitly describes the droplet interface, and is easily accessible for analytic calculations. We showed that the chemical reaction does not satisfy equilibrium properties and is thus active, and can be constructed via additional reservoir components that keep the system permanently out of equilibrium.

In the remainder of this thesis, we will discuss the behavior of the minimal model introduced here. We start in chapter 4 by considering spherically symmetric droplets using the effective droplet model. For this we concentrate on the influence of the chemical reaction on the dynamics, in the absence of hydrodynamic flows. We analyze stationary states with a stationary radius  $\bar{R}$ . We perform a linear stability analysis around such stationary states to find whether they are stable with respect to changes in volume and with respect to shape deformations. We will find that chemically active droplets can be unstable with respect to shape deformations, especially elongations of the droplet. Additionally, we discuss the mechanism of this instability and compare it to the droplet instability with the Mullins-Sekerka instability that governs the dendritic growth of solids. In chapter 5 we investigate the dynamics of the continuum model in the absence of hydrodynamic flows. We will find that the shape instability of chemically active droplets can lead to growth of a droplet and its elongation and division into two daughter droplets which may grow and divide again. The influence

of chemical reactions on other stationary shapes, such as cylindrical droplets, is discussed in chapter 6. In chapter 7, we include hydrodynamic flows. Such flows are important for the rounding up of deformed droplets, and might counteract the instability and division. In chapter 8, we briefly consider chemically active droplets as a model for protocells at the origin of life, where the division might have been a simple mechanism for replication that could have enabled droplets to multiply and evolve into more complex structures. We also discuss the possibility of experimental realizations of chemically active droplets by estimating parameter values for representative systems. We conclude the thesis by discussing open questions of chemically active droplets in the final chapter 9.



In the previous chapter we introduced a model of chemically active droplets. We will now consider the dynamic behavior of such a system, starting with considering stationary states and their linear dynamics. In this chapter we use the effective droplet model to consider the case of large viscosity, where hydrodynamic flows vanish. We first discuss stationary states of spherically symmetric droplets. Then we perform a stability analysis of such states with respect to shape perturbations. We find a stability diagram with regimes of vanishing droplets, stable stationary droplets and stationary droplets that are unstable with respect to elongational deformations. We then discuss the physical mechanism of the observed shape instability. We compare the dynamic behavior with the Mullins-Sekerka instability that leads to dendritic growth of solids in a supersaturated fluid. Finally, we discuss the shape instability of chemically active droplets in the limit of small reaction fluxes, where a scaling approach leads to simple equations for the onset of the instability.

A large part of the content of this chapter has been published in Zwicker et al. (2017).

## 4.1 Stability of spherical droplets with chemical reactions

We will now analyze the dynamical behavior of spherical droplets using the effective droplet model introduced in section 3.2. We consider the case without hydrodynamic flows,  $\mathbf{v} = 0$ , which corresponds to the limit of infinite viscosity, which can be expressed as  $F \rightarrow \infty$ , where  $F = \eta_- w^3 / (e_0 t_0)$  is the dimensionless viscosity inside the droplet, together with  $\eta_+ / \eta_- > 0$ .

The concentration field is given by Eq. (3.20) with fluxes (3.21) with  $\mathbf{v} = 0$  and active chemical reaction (3.22). Boundary conditions at the droplet interface are given

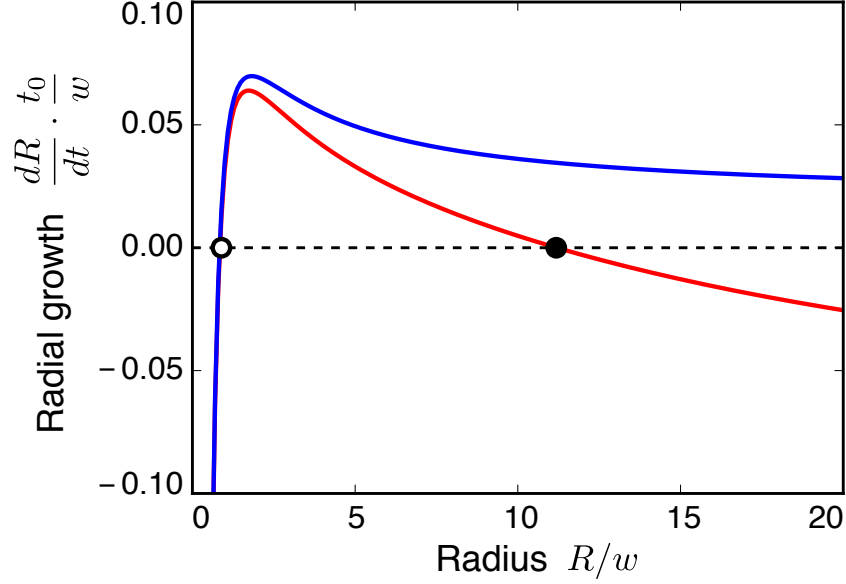


FIGURE 4.1: Size dependence of droplet growth rates. Rate of droplet growth  $dR/dt$  as a function of droplet radius  $R$  in a quasistatic limit without reaction inside the droplet,  $\nu_- = 0$  (blue line), and with reaction  $\nu_- > 0$  inside the droplet (red line), corresponding to a sink of droplet material. The zeros of  $dR/dt$  correspond to stationary radii. An unstable critical radius (white circle) and a stable droplet radius (black circle) are indicated. Parameter values:  $\nu_-/\nu_0 = 1$  (red line) or  $\nu_-/\nu_0 = 0$  (blue line),  $\nu_+/\nu_0 = 0.2$ , with  $\nu_0 = 10^{-2}\Delta c/t_0$ ,  $k_{\pm}t_0 = 10^{-2}$ ,  $c_+^{(0)} = 0$ ,  $\beta_- = \beta_+$ ,  $D_- = D_+$ .

by Eq. (3.28) and (3.29), and the interface moves due to fluxes, Eq. (3.30), with the radial movement in spherical coordinates given by Eq. (3.31).

First we consider the volume changes of spherical droplets to find stationary radii. Then we perform a linear stability analysis of such stationary states to find the stability with respect to shape perturbations.

#### 4.1.1 Stationary states of spherical droplets

We now consider stationary spherical droplets with radius  $\bar{R}$  and spherically symmetric stationary concentration fields  $\bar{c}_{\pm}(r)$  inside and outside the droplet.

First we calculate the stationary concentration fields  $\bar{c}_{\pm}(r)$  for a droplet of radius  $R$ , which fulfill Eq. (3.20) with  $\partial_t \bar{c}_{\pm}(r) = 0$  with boundary conditions (3.28) and (3.29). For the solution outside the droplet we consider the case where the concentration far from the droplet reaches a constant value  $c_{\infty} = \nu_+/k_+ + c_+^{(0)}$  set by the chemical reaction,  $s(c_{\infty}) = 0$ . Inside the droplet, the solution has to be regular at



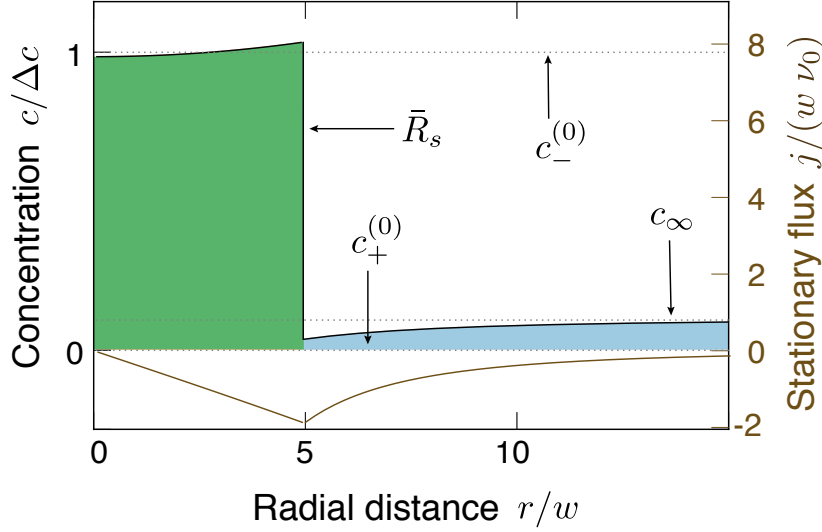


FIGURE 4.2: Stationary concentration profile of the droplet material  $B$  (black) and stationary flux  $j = -D_{\pm}\partial_r c$  (brown, axis on the right). Shaded regions correspond to concentration ranges inside (green) and outside the droplet (blue). The droplet radius  $\bar{R}_s$ , the equilibrium concentrations  $c_{\pm}^{(0)}$ , and the concentration far from the droplet  $c_{\infty}$  are indicated. Parameter values are:  $\nu_-/\nu_0 = 1.2$ ,  $\nu_+/\nu_0 = 0.1$  with  $\nu_0 = 10^{-2}\Delta c/t_0$ ,  $k_{\pm}t_0 = 10^{-2}$ ,  $c_+^{(0)} = 0$ ,  $\beta_- = \beta_+$ ,  $D_- = D_+$ .

$r = 0$ . This yields

$$\bar{c}_+(r) = \frac{\nu_+}{k_+} + c_+^{(0)} + \left( \frac{\gamma\beta_+}{R} - \frac{\nu_+}{k_+} \right) \frac{R}{\exp(-R/l_+)} \frac{\exp(-r/l_+)}{r} \quad (4.1)$$

$$\bar{c}_-(r) = -\frac{\nu_-}{k_-} + c_-^{(0)} + \left( \frac{\gamma\beta_-}{R} + \frac{\nu_-}{k_-} \right) \frac{R}{\sinh(R/l_-)} \frac{\sinh(r/l_-)}{r}, \quad (4.2)$$

with characteristic length scales  $l_{\pm} = (D_{\pm}/k_{\pm})^{1/2}$ . See Appendix C.1 for additional details.

We can use the stationary concentration fields to calculate the interface dynamics, Eq. (3.30) and (3.31). Due to spherical symmetry,  $dR/dt = v_n$ . Inserting the radial fluxes of the stationary concentration fields into Eq. (3.30) we find

$$\frac{dR}{dt} = \frac{j_-(R) - j_+(R)}{\bar{c}_-(R) - \bar{c}_+(R)}, \quad (4.3)$$

with stationary fluxes  $j_{\pm}(r) = -D_{\pm}\bar{c}'_{\pm}(r)$ , where  $'$  denotes the derivative with respect to  $r$ . Using Eq. (4.3) for the dynamics for arbitrary radii  $R$  with the stationary concentration field given by Eq. (4.1) describes the droplet dynamics in the limit

where the interfacial dynamics of the droplet is much slower than the relaxation of the concentration field to a stationary value. We call this the quasistatic approximation. Steady state droplets exist for radii  $R = \bar{R}$  for which  $dR/dt$  vanishes. These stationary radii thus obey

$$j_+(\bar{R}) = j_-(\bar{R}) . \quad (4.4)$$

Fig. 4.1 shows an example of  $dR/dt$  as a function of  $R$  in the presence (red line) and absence (blue line) of chemical reactions inside the droplet for the quasistatic approximation. In both cases, the chemical reaction outside the droplet creates a supersaturation  $c_\infty > c_+^{(0)}$  far from the droplet. Without chemical reactions inside the droplet, droplets have one stationary radius. Droplets with a radius smaller than this critical nucleation radius shrink and vanish, while droplets with a larger radius grow. If chemical reactions inside are present, two steady state radii exist, denoted  $\bar{R}_c$  (white circle) and  $\bar{R}_s$  (black circle). The smaller radius  $\bar{R}_c$  is unstable with respect to changes in droplet volume while the larger radius  $\bar{R}_s$  is stable. This means droplets smaller than  $\bar{R}_c$  will shrink and vanish, while larger ones will grow towards the larger radius  $\bar{R}_s$ . Droplets larger than  $\bar{R}_s$  will shrink towards the stationary size.

The concentration field and fluxes corresponding to the larger stationary radius  $\bar{R}_s$  are shown in Fig. 4.2. Inside the droplet, the concentration is much larger than outside. In the middle of the droplet, the concentration is lower than at the interface, indicating the sink of droplet material inside due to the chemical reaction. Far from the droplet, the concentration outside reaches the stationary value  $c_\infty$  set by  $s(c_\infty) = 0$ , and decreases towards the droplet interface. The flux profile shows stationary fluxes of droplet material towards the droplet center – and, due to incompressibility, fluxes of the outer material  $A$  in the reverse direction. At the interface, the flux inside and outside is equal, showing that the radius is indeed stationary.

The critical radius  $\bar{R}_c$  is closely related to the classical expression for the critical nucleation radius of passive droplets. The critical nucleation radius depends on the supersaturation  $\epsilon = (c_\infty - c_+^{(0)})/\Delta c$ , which, in the case of active droplets, is determined by chemical reactions instead of the amount of material provided, compare Lifshitz and Slyozov (1961). The stationary droplet radius  $\bar{R}_s$  describes an inherently non-equilibrium stationary state that is maintained by opposing fluxes – due to the chemically generated supersaturation outside, the droplet takes up material to grow, while the chemical reaction inside the droplet converts droplet material  $B$  to outer material  $A$  which leaves the droplet, leading to an effective loss of droplet material. The balance of both fluxes creates the stationary radius, Zwicker (2013); Zwicker et al. (2015).

#### 4.1.2 Stability of chemically active droplets

We will now consider whether these stationary droplets are stable with respect to shape perturbations.

We linearize the dynamic equations (3.20)–(3.31) of the effective droplet model without hydrodynamic flows around a stationary solution  $\bar{c}(r)$ , given by Eqs. (4.1)–

(4.4). Additional details of the derivation can be found in Appendix C.2. We consider small perturbations  $\delta c$  and  $\delta R$  of the concentration field and the droplet shape,

$$c(r, \theta, \varphi, t) = \bar{c}(r) + \delta c(r, \theta, \varphi, t) , \quad (4.5)$$

$$R(\theta, \varphi, t) = \bar{R} + \delta R(\theta, \varphi, t) , \quad (4.6)$$

where the stationary concentration profile  $\bar{c}$  is given by  $\bar{c}_-$  inside, and  $\bar{c}_+$  outside the droplet. We denote the derivative of  $\bar{c}(r)$  evaluated at the interface position  $r = \bar{R}$  inside and outside the droplet, respectively, by  $\bar{c}'(\bar{R}_\pm)$ .

The linear droplet dynamics can be decomposed in eigenmodes with amplitude  $\epsilon_{nlm}$ , where the spherically symmetric reference state leads to a decomposition with radial and angular indices  $i = (n, m, l)$  as

$$\begin{pmatrix} \delta c \\ \delta R \end{pmatrix} = \sum_{nlm} \epsilon_{nlm} \begin{pmatrix} c_{nl}(r) \\ \bar{R} \end{pmatrix} Y_{lm}(\theta, \phi) e^{\mu_{nl} t} , \quad (4.7)$$

where  $Y_{lm}$  are spherical harmonics and the corresponding eigenvalues will be denoted  $\mu_{nl}$ . Here we already indicate that the eigenvalue is independent of mode  $m$ , with  $-l \leq m \leq l$ . For  $\mu_{nl} < 0$ , the values  $-\mu_{nl}$  are relaxation rates. The steady state is stable if all  $\mu_{nl} < 0$ . To determine the stability of the droplet, we thus want to find out if any mode can be marginal, corresponding to  $\mu_{nl} = 0$ , or unstable,  $\mu_{nl} > 0$ .

The radial part of the eigenfunctions obeys

$$\left( \frac{1}{r^2} \frac{\partial}{\partial r} r^2 \frac{\partial}{\partial r} - (\lambda_{nl}^\pm)^2 - \frac{l(l+1)}{r^2} \right) c_{nl}(r) = 0 , \quad (4.8)$$

where

$$(\lambda_{nl}^\pm)^2 = \frac{k_\pm + \mu_{nl}}{D_\pm} . \quad (4.9)$$

Eq. (4.8) is solved by the modified spherical Bessel functions  $k_l(\lambda_\pm r)$  and  $i_l(\lambda_\pm r)$ , defined in Abramowitz et al. (1965). For real variables, the functions  $k_l(x)$  are monotonously decaying towards zero, while  $i_l(x)$  are monotonously growing for increasing  $x$ . For imaginary variables corresponding to  $(\lambda_{nl}^\pm)^2 < 0$ , they are related to the spherical Bessel functions  $j_l(x)$  and  $y_l(x)$  with a real variable  $x$ , which oscillate with decreasing amplitude for increasing  $x$ . See Appendix C.2 for additional details, where Fig. C.1 shows the respective Bessel functions.

The boundary conditions (3.28)-(3.29) at  $r = \bar{R}$  can be written to linear order as

$$c_{nl}(\bar{R}_+) = \gamma \beta_+ \frac{h_l}{\bar{R}} - \bar{c}'(\bar{R}_+) \bar{R} \quad (4.10)$$

$$c_{nl}(\bar{R}_-) = \gamma \beta_- \frac{h_l}{\bar{R}} - \bar{c}'(\bar{R}_-) \bar{R} \quad (4.11)$$

where  $h_l = (l^2 + l - 2)/2$  encodes the effect of the interfacial curvature of the respective mode, see Zhong-can and Helfrich (1987). The derivatives  $'$  are explicitly written as  $\bar{c}'(\bar{R}_+) = d\bar{c}_+(r)/dr|_{r=\bar{R}}$ . This boundary condition determines the coefficients of

the solutions to Eq. (4.8) inside and outside the droplet, together with convergence for  $r \rightarrow 0$  and  $r \rightarrow \infty$ . Using the description of the interfacial dynamics, Eq. (3.31), we obtain an equation for the eigenvalue  $\mu_{nl}$ ,

$$\mu_{nl} = \frac{D_+}{\Delta c} \bar{c}''(\bar{R}_+) - \frac{D_-}{\Delta c} \bar{c}''(\bar{R}_-) + \frac{D_+}{\Delta c} \frac{c'_{nl}(\bar{R}_+)}{\bar{R}} - \frac{D_-}{\Delta c} \frac{c'_{nl}(\bar{R}_-)}{\bar{R}}. \quad (4.12)$$

Note that this is an implicit equation for  $\mu_{nl}$ , because the right-hand side of Eq. (4.12) depends on the eigenvalue via the length-scales  $\lambda_{nl}^\pm$  in the functions  $c_{nl}$ .

Let us now discuss the shape of the solutions to Eqs. (4.9)-(4.12). We can differentiate between two main cases by the sign of  $(\lambda_{nl}^+)^2$ .

The case  $(\lambda_{nl}^+)^2 < 0$  corresponds to small eigenvalues  $\mu_{nl} < -k_+$ . We find a continuous spectrum of eigenvalues in this region. In Appendix C.2 the detailed solution is presented, but we briefly sketch the main points here: We consider a solution in terms of spherical Bessel functions  $j_l(x)$  and  $y_l(x)$ . For large  $x$ , both functions vanish, so that both can be used for the concentration field outside the droplet. This leads to an undetermined constant in the description of the concentration field, and thus in Eq. (4.12). We find that with this constant, we can fulfill Eq. (4.12) for any eigenvalue with  $\mu_{nl} < -k_+$ , yielding a continuous spectrum of eigenvalues in this regime.

For  $(\lambda_{nl}^+)^2 > 0$ , the concentration mode is completely determined by the boundary conditions and the inverse length-scales  $\lambda_{nl}^\pm$ . The equation for the eigenvalue (4.12) then only gives a discrete number of solutions for eigenvalues  $\mu_{nl} > -k_+$ . For  $k_\pm > 0$ , marginal and unstable modes are found for  $\lambda_{nl}^\pm > 0$ , corresponding to  $\mu_{nl} > -k_\pm$ . We can write the equation explicitly as

$$\begin{aligned} \mu_{nl} = & D_+ \bar{c}''(\bar{R}_+) - D_- \bar{c}''(\bar{R}_-) \\ & + \frac{D_+ c_{nl}(\bar{R}_+)}{\bar{R}^2} f_k(\lambda_{nl}^+ \bar{R}) - \frac{D_- c_{nl}(\bar{R}_-)}{\bar{R}^2} f_i(\lambda_{nl}^- \bar{R}), \end{aligned} \quad (4.13)$$

with  $f_k(x) = x k'_l(x)/k_l(x)$  and  $f_i(x) = x i'_l(x)/i_l(x)$ , where  $'$  denotes the derivative  $f'(x) = df/dx$ , shown in the Appendix in Fig. C.1. The terms  $c_{nl}(\bar{R}_\pm)$  are given by Eq. (4.10) and (4.11). We find that this equation has a finite number of solutions for a mode  $l$ , typically we find either no or one solution. We distinguish the solutions by index  $n$ , whereby  $n = 1$  denotes the solution with the largest eigenvalues for a given  $l$ . These solutions correspond to different radial concentration profiles, with inverse length-scales  $\lambda_{nl}^\pm$ .

The dependency of solutions to Eq. (4.13) on the parameters and the mode  $l$  generally is nontrivial. However, we can find analytically that the  $l = 1$  mode always has a solution  $\mu_{n1} = 0$  where all terms on the right-hand side of Eq. (4.13) cancel, using the properties of Bessel functions and of the stationary concentration field. This corresponds to a mode where the whole droplet including the concentration field is displaced by a small distance. Due to translational symmetry in an infinite system, the droplet will simply stay at its new position.

Using the quasistatic assumption introduced in the previous section, where the concentration profile for a growing droplet is described by the stationary field  $\bar{c}_\pm(r)$ ,

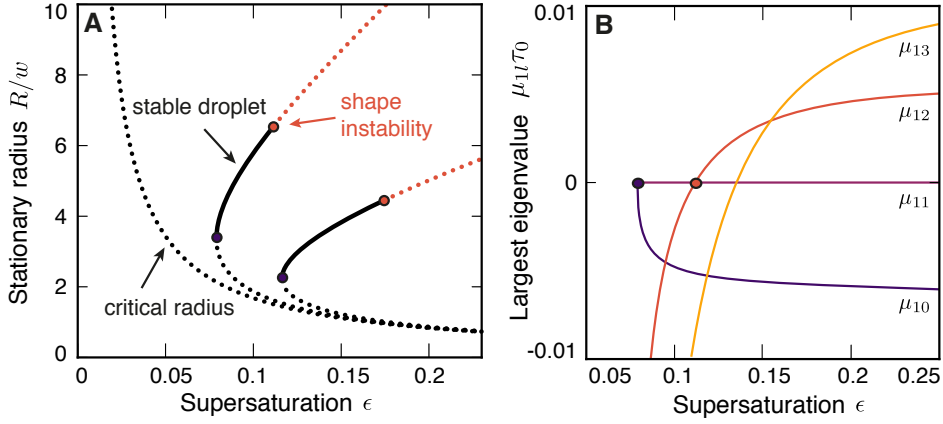


FIGURE 4.3: A) Stationary radii of active droplets. The droplet radius  $\bar{R}$  of spherical droplets is shown as a function of supersaturation  $\epsilon$  for different reaction rates inside the droplet  $\nu_-/\nu_0 = 0, 1, 3$  (from left to right). Radii of stable droplets are shown as solid black lines. Dotted lines indicate states where droplets are unstable with respect to size (black) or shape (red). B) Largest eigenvalues  $\mu_{1l}$  of modes  $l = 0, 1, 2, 3$  as a function of supersaturation  $\epsilon$  along the larger stationary radius  $\bar{R}_s$  for  $\nu_-/\nu_0 = 1$ . At the onset of the instability (red dot) the second mode becomes unstable, leading to droplet deformation. For larger values of  $\epsilon$ , higher modes become unstable as well. Parameter values:  $\nu_0 = 10^{-2} \Delta c/t_0$ ,  $k_+ t_0 = 10^{-2}$ ,  $c_+^{(0)} = 0$ ,  $\beta_- = \beta_+$ ,  $D_- = D_+$ .

Eq. (4.12) for  $l \neq 0$  describes the shape instability of a growing droplet, with  $\bar{R}$  denoting the radius of the growing droplet.

### 4.1.3 Stability diagram of chemically active droplets

We now discuss results of the shape instability of stationary droplet of radius  $\bar{R}_s$  for different modes and parameters. We concentrate on two parameters that drive the fluxes in the two phases and capture the effects we discussed for the stationary radii in subsection 4.1.1: The chemically generated supersaturation  $\epsilon = (c_\infty - c_+^{(0)})/\Delta c$  characterizes the reaction outside the droplet, where the concentration  $c_\infty$  far from the droplet is created by the chemical reactions  $c_\infty = c_+^{(0)} + \nu_+/k_+$ . This supersaturation drives the diffusion flux  $j_+$  toward the droplet interface – if the supersaturated concentration  $c_\infty$  is larger than the concentration at the droplet interface  $c_+(R)$ , droplet material flows towards the droplet. Inside the droplet, droplet material is degraded with dimensionless turnover  $\nu_- t_0/\Delta c$ . This reaction leads to a concentration profile inside the droplet with a minimum in the droplet center for  $\nu_- > 0$ , causing a diffusion flux  $j_-$  towards the center, see Fig. 4.2.

Fig. 4.3A shows the behavior of the stationary droplet radius as a function of the supersaturation  $\epsilon$  for different turnovers  $\nu_-$ , while keeping all other parameters

constant. Without chemical reactions inside the droplet,  $\nu_- = 0$ , the only stationary radius is the critical nucleation radius  $\bar{R}_c$ . The intuitive explanation for the stationary radius is that at this radius the concentration far from the droplet and at the interface are equal,  $c_\infty = c_+(R)$ , so that the flux  $j_+(R)$  vanishes. With chemical reactions,  $\nu_- = \nu_0$  and  $\nu_0 t_0 / \Delta c = 10^{-2}$ , the reaction inside the droplet acts against the growth of the droplet due to the flux outside. For supersaturations below a threshold value  $\epsilon_0$ , droplets of all initial sizes shrink and vanish. Above this threshold value a second stationary radius  $\bar{R}_s$  exists, so that droplets smaller than  $\bar{R}_c$  vanish, and droplets larger than  $\bar{R}_c$  grow or shrink towards  $\bar{R}_s$ . For a larger turnover  $\nu_- / \nu_0 = 2$ , the threshold value  $\epsilon_0$  is larger, and the stationary radius  $\bar{R}_s$  smaller as compared to  $\nu_- / \nu_0 = 1$ .

In Fig. 4.3B the largest eigenvalue  $\mu_{1l}$  of shape instabilities of different modes  $l$  are shown for the larger stationary radius  $\bar{R}_s$  with  $\nu_- / \nu_0 = 1$  shown in Fig. 4.3A. The mode  $l = 0$  corresponding to changes in volume is zero at the threshold  $\epsilon_0$ , where both stationary solutions  $\bar{R}_c$  and  $\bar{R}_s$  are the same. For supersaturations above  $\epsilon_0$ , the mode is stable,  $\mu_{10} < 0$ , as we already found from analyzing the growth rate  $\dot{R}$  in the quasistatic limit. For the translational mode  $l = 1$  we find that the largest solution is the meta-stable solution  $\mu_{11} = 0$  that can also be derived analytically, corresponding to a translation of the droplet and concentration field. The mode  $l = 2$  corresponds to an elliptical deformation, either prolate for positive initial deformation amplitude  $\epsilon_{nlm} > 0$ , or oblate ('smartie-shaped') with a negative initial deformation. It becomes unstable above a supersaturation  $\epsilon_2$  and corresponding radius  $R_2$ . Additional modes may become unstable for larger supersaturations. The third mode  $l = 3$  becomes unstable above a supersaturation  $\epsilon_3 > \epsilon_2$ , and may have a larger growth rate than the second mode. Higher modes may become unstable for even larger supersaturation. We thus find that the elongational mode  $l = 2$  marks the onset of instability, marked by a red dot in Fig. 4.3A and B.

For a larger turnover, the onset of instability is at a larger supersaturation, compare the red dots in Fig. 4.3A for  $\nu_- / \nu_0 = 1$  and  $\nu_- / \nu_0 = 2$ .

In Fig. 4.4A, the influence of the turnover inside the droplet on the existence of a stationary radius and on the instability of the  $l = 2$  mode is shown as a stability diagram. We show the existence of the stationary radius  $\epsilon_0$  (blue line) and the onset of instability  $\epsilon_2$  (red line). These supersaturations separate three regions – a region where all droplets vanish (white), one where stable stationary droplet radii exist (blue), and a region where the stationary droplet is unstable with respect to deformations of the elongational mode (red). In the unstable region, a small initial deformation of the  $l = 2$  mode grows, which may lead to a deformation of the droplet into a dumbbell shape. We may hypothesize that such droplets with a dumbbell shape may divide into two daughter droplets, due to the surface tension of the droplet phase.

In a passive system without chemical reactions, surface tension would typically lead to a round stable droplet shape. Therefore, the shape instability we find here is an interesting new feature of chemically active droplets. We will now discuss the physical mechanism that creates the instability. Subsequently, we will analyze the equations in the limit of vanishing reactions to derive simple analytic expressions.

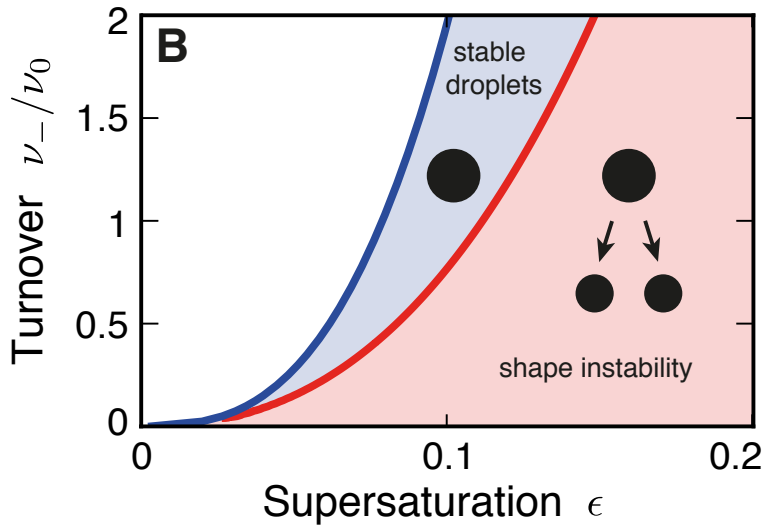


FIGURE 4.4: Stability diagram of active droplets as a function of supersaturation  $\epsilon = \nu_+/(k_+\Delta c)$  and turnover  $\nu_-/\nu_0$  of droplet material. Droplets either dissolve and disappear (white region), are spherical and stable (blue region), or undergo a shape instability into a dumbbell shape, which may lead to division (red region). Parameter values:  $\nu_0 = 10^{-2}\Delta c/t_0$ ,  $k_{\pm}t_0 = 10^{-2}$ ,  $c_+^{(0)} = 0$ ,  $\beta_- = \beta_+$ ,  $D_- = D_+$ .

## 4.2 Physical mechanism driving the shape instability

In this section we will briefly discuss the physical interpretation of the shape instability of chemically active droplets. This shape instability is a new example for a larger class of flux-driven instabilities where a stationary shape in a sustained nonequilibrium situation may become unstable due to stationary fluxes. For this we consider shape deformations and the resulting dynamics for a passive droplet without chemical reactions and a droplet with chemical reactions. We will concentrate on a qualitative description that highlights the physical effects – the quantitative description is already captured by the stability analysis. As in the whole chapter, we ignore hydrodynamics flows,  $\mathbf{v} = 0$ , which will be considered in chapter 7, and only consider diffusive fluxes.

### 4.2.1 Shape relaxation of passive droplets

We first consider the fluxes that lead to the shape relaxation of a passive droplet towards its round shape. In a finite system with a spherical droplet in equilibrium, the droplet radius  $R_0$  is set by the amount of droplet material in the system, and the shape of the droplet is round, stabilized by surface tension. In both phases, concentrations are constant,  $c_{\pm} = c_{\pm}^{(0)} + \beta_{\pm}\gamma H_0$  with mean curvature  $H_0 = 1/R_0$ .

We now consider a small elongational deformation  $R = R_0 + \delta R(\theta, \phi)$  of such a droplet. The concentration at the interface  $c_{\pm}(\theta, \phi) = c_{\pm}^{(0)} + \beta_{\pm}\gamma H(\theta, \phi)$  is in

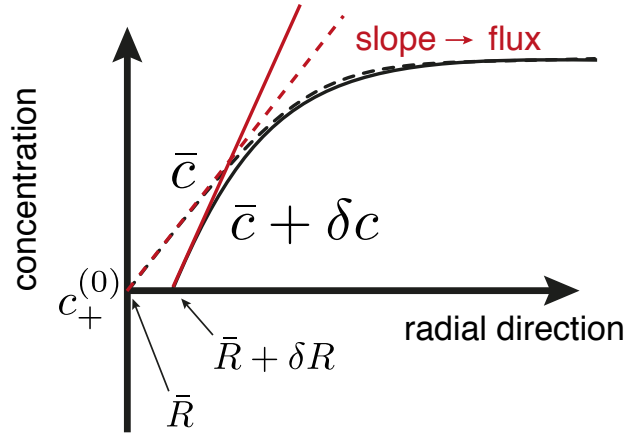


FIGURE 4.5: Sketch of the concentration profile for a flux-driven shape instability. Shown is the concentration outside the droplet in radial direction at the tip of the deformation of a spherical droplet without surface tension,  $\gamma = 0$ . In the unperturbed state, the concentration at the droplet interface at position  $\bar{R}$  is  $c_+^{(0)}$ , and far from the droplet, the concentration is supersaturated with concentration  $c_\infty$ . The concentration profile  $\bar{c}$  has a gradient (dotted red line), which implies a nonzero flux  $j = -D_+ \nabla c$ . After deformation of the droplet interface to  $\bar{R} + \delta R$ , the concentration profile is given by  $\bar{c} + \delta c$ . The slope at the droplet interface is significantly larger than in the unperturbed case, so that the droplet tip might move further outwards.

both phases larger at the tip of the deformed droplet, where the mean curvature  $H$  is larger than for the unperturbed droplet, while at the inward-deformed sides of the droplet, the concentration is smaller due to a smaller mean curvature. For a local perturbation of the concentration field, the concentration is unperturbed far from the droplet. Fluxes are driven by gradients in concentration,  $j = -D_\pm \nabla c$ , so that material flows from the regions with high concentrations towards the regions with lower concentration. Therefore, for a passive droplet with smooth concentration gradients, droplet material flows away from the tip of the droplet in all directions, and from all directions towards the sides. According to Eq. (3.30), the interface then also moves so that the droplet will relax towards its spherical shape.

#### 4.2.2 Shape deformation of chemically active droplets

We next consider a stationary droplet with chemical reactions. Inside the droplet, reactions degrade the droplet material, while outside they create a supersaturation with  $c_\infty > c_+(\bar{R})$ . Material is constantly transported from the supersaturated region outside the droplet towards the center of the droplet due to gradients in the concentration field  $j = -D_+ \nabla c$ , compare Fig. 4.2.

We now consider the fluxes in a droplet with a small elongational shape perturba-



tion. The boundary conditions at the droplet interface behave as for a passive droplet, with larger concentrations at the tip of the deformed droplet, and smaller at the sides. Thus material flows along the droplet interface from the tip to the sides due to the different boundary conditions. The shape instability is created by the interaction of the perturbation gradient with the stationary gradient in radial direction.

To demonstrate this, we ignore the concentration change at the boundary,  $\beta_{\pm}\gamma = 0$ . If the length-scale of the perturbation of the concentration field is smaller than the length-scale of the stationary field, the concentration field is perturbed only locally due to the droplet deformation. In this case, the droplet tip with concentration  $c_+(R) < c_{\infty}$  is pushed into the stationary gradient outside the droplet, and the perturbation field mediates between the boundary value and the stationary concentration field far from the droplet. Since the perturbation is short ranged, the gradient at the interface thus has to be stronger than for the stationary field. This is sketched in Fig. 4.5. This stronger gradient means that more droplet material is transported towards the interface. At the sides, the opposite happens: the interface is moved away from the gradient, so that the local perturbation makes the gradient more shallow, leading to less influx of droplet material. Inside the droplet, the same effects take place, but with reversed sign, so that the instability is enhanced there as well.

With surface tension, different effects compete. The concentration at the tip of the perturbed droplet  $c_{\pm}(\bar{R} + \delta R)$  may be larger than the stationary profile at this position was,  $\bar{c}_{\pm}(\bar{R} + \delta R)$ , compare Fig. 4.5. In this case, the flux towards the interface outside the tip would be decreased, stabilizing the spherical droplet - the corresponding holds for the inside and the sides of the droplet. Additionally, there is a competition between the radial fluxes and the stabilizing fluxes tangential to the interface, and the different geometry inside and outside the droplet may additionally influence the resulting dynamical behavior. The combination of these different effects is captured by the linear stability analysis.

The instability is created by the existence of stationary fluxes in the spherical unperturbed droplet, and thus requires a nonequilibrium stationary state.

### 4.3 Relationship to Mullins-Sekerka instability

A classical example for such a flux-driven shape instability is the Mullins-Sekerka instability that describes the shape instability of a solid precipitate growing in an supersaturated environment, see Mullins and Sekerka (1963). This instability is well-studied theoretically and experimentally, and typically leads to dendritic growth of solids, forming tongue-like fractal(ish) shapes, see Fig. 1.2. In this section we will compare the instability and dynamic behavior of active droplets with the Mullins-Sekerka instability.

Consider a spherical particle or droplet perturbed by a small shape deformation. Using a decomposition of infinitesimal shape changes by spherical harmonics, the mode with  $l = 0$  corresponds to a changing radius  $R_0(t)$ , the modes with  $l = 1$  generate pure translations, and the modes with  $l = 2$  are the shape deformation

modes that become unstable first. We can thus ignore the modes with  $l = 1$  and focus here on the radius change and the dynamics of the modes with  $l = 2$ , which are most relevant for the droplet division problem. Without loss of generality, we consider the case  $m = 0$ . Following the arguments of Mullins and Sekerka (1963), we express the shape of a droplet as a function of the azimuthal and polar angles for a small deformation by a mode with  $l = 2$ :

$$R(\theta, \phi; t) \simeq R_0(t) + \epsilon_2(t) \hat{Y}_{20}(\theta, \phi), \quad (4.14)$$

where  $\epsilon_2 \ll R_0$ ,  $\hat{Y}_{20}(\theta, \phi) = Y_{20}(\theta, \phi)/Y_{20}(0, 0)$  and we have neglected modes with  $l > 2$ . For such a perturbation, the interface moves locally with a radial velocity  $v = \partial R/\partial t$ , which reads

$$v(\theta, \phi) \simeq \frac{dR_0}{dt} + \frac{d\epsilon_2}{dt} \hat{Y}_{20}(\theta, \phi). \quad (4.15)$$

#### 4.3.0.1 Droplet with chemical reaction

In our model of chemically active droplets, we consider a droplet in the vicinity of the stationary radius  $\bar{R}_s$ . We can express the droplet radius as  $R_0(t) = \bar{R}_s + \epsilon_0(t)$ . For small perturbations of the stationary state,  $\epsilon_0, \epsilon_2 \ll \bar{R}_s$ , the growth rates are given by  $dR_0/dt = \mu_{10}\epsilon_0(t)$  and  $d\epsilon_2/dt = \mu_{12}\epsilon_2(t)$ , see Eq. (4.7). At the stationary radius  $R_0 = \bar{R}_s$ , the volume growth is zero,  $dR_0/dt = 0$ , so that the  $l = 2$  mode determines the radial velocity,

$$v(\theta, \phi) \simeq \mu_{12}\epsilon_2(t) \hat{Y}_{20}(\theta, \phi). \quad (4.16)$$

If the mode  $l = 2$  is unstable,  $\mu_{12} > 0$ , we find for  $\epsilon_2 > 0$  that  $v(0, \phi) > 0$  and  $v(\pi/2, \phi) < 0$ . The droplet thus elongates along the long axis, and constricts along the waistline, see Fig. 4.6A. If we start sufficiently close to the stationary radius,  $R_0 \approx \bar{R}_s$ , contributions from the dynamics of  $R_0(t)$  can be neglected as  $\mu_{10} < 0$  and  $R_0(t)$  thus approaches the stationary value.

#### 4.3.0.2 Mullins-Sekerka model

In the case of the Mullins-Sekerka model, droplets grow with  $dR_0/dt > 0$  if  $R_0 > R_c$ , where  $R_c$  denotes the critical nucleation radius, see Mullins and Sekerka (1963). These growing droplets may undergo a shape instability corresponding to mode  $l$  when the radius reaches the value

$$R_l^{\text{ms}} = \gamma \frac{(4 + 3l + l^2)D_+\beta_+ + l(l + 2)D_-\beta_-}{2D_+(c_\infty - c_+^{(0)})}. \quad (4.17)$$

When modes with  $l > 2$  become unstable they lead to shape deformations that grow into dendritic structures, compare Davis (2001), while the modes with  $l = 2$  are insufficient to generate complex shape changes. To show this, we follow the arguments

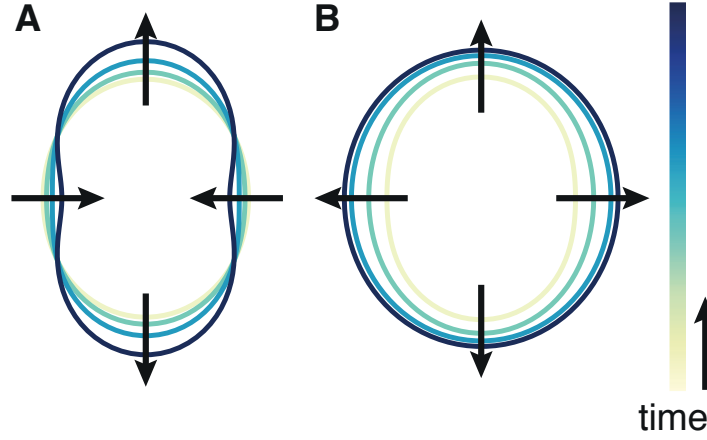


FIGURE 4.6: Shape deformations resulting from an instability of the deformation mode with  $l = 2$  for a chemically active droplet (A) and a growing droplet in the Mullins-Sekerka model (B). The  $l = 2$  mode corresponds to an ellipsoidal deformation. The black arrows indicate the direction of interfacial motion. (A) In the model of chemically active droplets, a stationary droplet constricts around the waistline as the amplitude of the perturbation increases. (B) In the Mullins-Sekerka model, an unstable  $l = 2$  mode gives rise to an ellipsoidal shape with an aspect ratio that approaches 1 as the droplet grows. This implies that the shape is not unstable with respect to the  $l = 2$  mode even if this mode is linearly unstable, Mullins and Sekerka (1963). The shape deformations shown in A and B correspond to the linear regime valid if amplitudes are small. They are shown with finite amplitude for clarity.

outlined in Mullins and Sekerka (1963) and consider an instability of a mode with  $l = 2$ , which grows with the rate

$$\mu_{12} = \frac{1}{R_0} \frac{R_0 - R_2^{\text{ms}}}{R_0 - R_c} \frac{dR_0}{dt}. \quad (4.18)$$

Here,  $R_2^{\text{ms}}$  with  $R_2^{\text{ms}} > R_c$  is the radius for which the  $l = 2$  mode becomes unstable in the Mullins-Sekerka model, see Eq. (4.17). The interfacial velocity behaves in the Mullins-Sekerka model as

$$v(\theta, \phi) \simeq \left( 1 + \frac{R_0 - R_2^{\text{ms}}}{R_0 - R_c} \frac{\epsilon_2}{R_0} \hat{Y}_{20}(\theta, \phi) \right) \frac{dR_0}{dt}. \quad (4.19)$$

Thus, for sufficiently small amplitudes  $\epsilon_2$  of the  $l = 2$  mode, the droplet radius  $R$  increases in all spatial directions,  $v(\theta, \phi) > 0$  for all angles  $\theta, \phi$ . This corresponds to a weak ellipsoidal deformation of the growing spherical droplet. As the droplet grows, the aspect ratio of this ellipsoid stays constant or approaches 1, see also Fig. 4.6B. Therefore, an unstable  $l = 2$  mode does not trigger a shape instability of an initially spherical object in the Mullins-Sekerka model. Thus, instabilities of modes with  $l > 2$  are required for the Mullins-Sekerka instability to take effect.

### 4.3.0.3 Comparison of both instabilities

These arguments show that there are interesting differences between the instability in our model and in the Mullins-Sekerka model. In the Mullins-Sekerka model an instability of a mode with  $l = 2$  does not directly trigger a shape instability because the droplet grows at the same time as the instability develops. Conversely, for the chemically active droplets discussed in this thesis, the instability of the modes with  $l = 2$  generates to linear order a shape change that leads to a dumbbell shape.

In the present description where only diffusive fluxes are considered, the dynamic equations of both models are similar – the surface tension of the liquid droplet corresponds to the capillarity of solid precipitates, and the supersaturation created by chemical reactions is similar to an externally generated supersaturation. Small differences exist: Often, the concentration field inside the solid precipitates is considered constant, while this is not justified for liquid droplets. Additionally, in our system the chemical reaction rates together with the diffusion coefficients introduce the length scales  $l_{\pm}$ , which do not exist in the Mullins-Sekerka case. Therefore, the instability condition of droplet shape, obtained by solving Eq. (4.13), is generally different from the Mullins-Sekerka case. However, extensions of both models may differ due to the different physics described. For the Mullins-Sekerka instability, temperature profiles and asymmetries due to the crystalline order may be included. In our case, we will consider the effect of hydrodynamic flows in chapter 7. The main difference in the present description, though, is the existence of the stationary radius of chemically active droplets. In the next chapter, we will study the effect the stationary radius has on the dynamical behavior of chemically active droplets.

The different waistline dynamics between our model and in the Mullins-Sekerka model might also lead to different behaviors in the nonlinear regime. In the case of the Mullins-Sekerka model, modes with smaller wavelengths become unstable as the volume increases. In the nonlinear regime, this leads to large dendritic structures. In our model of chemically active droplets, the droplet does not grow and modes with shorter wavelength thus remain stable. The chemically active droplet instead constricts at the waistline, which may subsequently lead to droplet division.

## 4.4 Droplet shape stability in the limit of a small reaction amplitude

Both the stationary radius  $\bar{R}$  and its eigenmodes  $\mu_{nlm}$  are described by implicit equations, see Eq. (4.4) and (4.13), that cannot be readily written in an explicit form that shows the dependency of the radius and the eigenvalues on the parameters. In this section we consider the limit of small chemical reaction fluxes  $s_{\pm}$  to find scaling behavior for both quantities, which lead to simple explicit expressions.

#### 4.4. Droplet shape stability in the limit of a small reaction amplitude

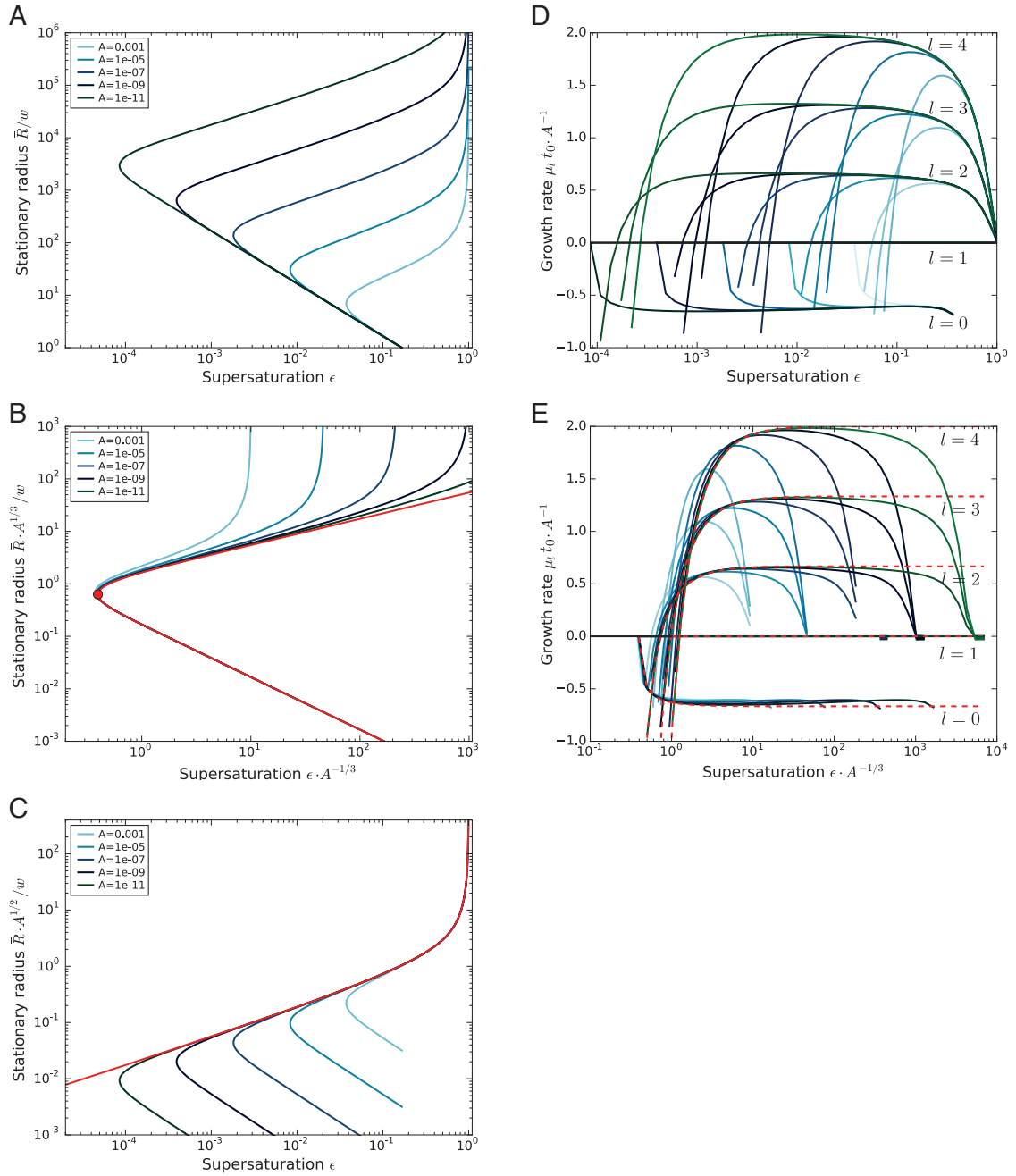


FIGURE 4.7: (A) Stationary radius as function of supersaturation for several reaction amplitudes. For larger reaction amplitudes, the stationary radius for fixed supersaturation diverges. (B) Scaling of the stationary radius for  $R \ll l_{\pm}$ , in red the analytical prediction Eq. (4.21) (line) and Eq. (4.22)-(4.23) (dot). (C) Scaling of the stationary radius for  $R \gg \bar{R}_0$ , in red the analytical prediction Eq. (4.26). (D) Growth rates of perturbations of spherical harmonics according to Eq. (4.13) with modes  $l = 0$  to  $l = 4$  along the upper branch of the stationary radius. For  $\epsilon \approx \epsilon_0$  and  $\epsilon \approx \epsilon_{\infty}$ , occasionally no numerical solution of the eigenvalue equation was found, leading to sudden cutoffs of the lines. (E) Scaling of the growth modes for small radii: Onset of instability and maximal value. (Parameter:  $\nu_{-}/(k_{-}\Delta c) = 1$ ,  $k_{+} = k_{-}$ ,  $D_{+} = D_{-}$ )

#### 4.4.1 Stationary radius

Here we discuss the stationary radius in the limit of small chemical reaction amplitude  $A = \nu_- \tau / \Delta c$  while keeping the ratios  $\nu_- / (k_- \Delta c)$  and  $k_+ / k_-$  of reaction parameters fixed. This corresponds to the introduction of a prefactor in the reaction,  $s(c) = A \cdot s(c; A = 1)$  so that the reaction rate varies with  $A$  in both phases but the supersaturation  $\epsilon$  remains constant. For  $A = 0$ , this yields the Mullins-Sekerka case without chemical reactions and externally generated supersaturation, so that the limit is well-defined.

In Fig. 4.7A, the stationary radius  $\bar{R}(\epsilon)$  is shown as function of the supersaturation for different values of  $A$  on a log-log scale. The lower stationary radii  $\bar{R}_c$  collapse for the different reaction rates onto a straight line, the larger solutions  $\bar{R}_s$  show scaling behavior, but with different values for different reaction rates. Close to supersaturation  $\epsilon_0$ , a continuous 'bend' connects both solutions  $\bar{R}_c$  and  $\bar{R}_s$ . For a critical supersaturation  $\epsilon_\infty$ , which is independent of the reaction amplitude, the stationary radius  $\bar{R}_s$  diverges.

We can identify two crossover regimes between the different scaling behaviors in the figure. The first is the region of small  $\epsilon$ ,  $\epsilon \sim \epsilon_0$ , which corresponds to the minimum of  $\epsilon(\bar{R})$ . The second is the region of  $\epsilon_\infty$  where the stationary radius diverges. For  $A \rightarrow 0$ , we see that  $\epsilon_0$  goes to zero while  $\epsilon_\infty$  stays constant, and both are connected by a straight line that indicates scaling behavior of  $\bar{R} = \bar{R}_s$ . This increasing separation between  $\epsilon_0$  and  $\epsilon_\infty$  (and the corresponding stationary radii) in the limit of small  $A$  means that we can analyze the behavior of the stationary radius in these two regimes separately. For this we consider Eq. (4.1) for the concentration field and (4.4) for the stationary radius. We can rewrite Eq. (4.4) to obtain an expression relating the supersaturation to the stationary radius,

$$\epsilon = \frac{\beta_+ \gamma}{\Delta c \bar{R}} + \left( \frac{\beta_- \gamma}{\Delta c \bar{R}} + \frac{\nu_-}{k_- \Delta c} \right) \frac{D_- \frac{\bar{R}}{l_-} \coth \frac{\bar{R}}{l_-} - 1}{D_+ \frac{\bar{R}}{l_+} + 1}. \quad (4.20)$$

In this limit of small  $A$ , the characteristic length-scales of the concentration field become large with  $l_\pm \propto A^{-1/2}$ . To find scaling regimes in Eq. (4.20), we change variables in Eq. (4.20) from  $(A, \bar{R})$  to  $(A, \hat{R})$  with scaling ansatz  $\hat{R} = \bar{R} A^a / w$ , where  $a$  is an exponent. Additional information can be found in Appendix C.3.

For  $a = 1/3$  we find the behavior of  $\epsilon(\hat{R})$  close to  $\epsilon_0$  and  $\hat{R}_0$ ,

$$\hat{\epsilon} = \frac{1}{6} \hat{R}^{-1} + \frac{1}{3} \hat{R}^2 + O(A^{1/6}) \quad (4.21)$$

where  $\hat{\epsilon} = \epsilon A^{-1/3}$  becomes independent of  $A$  for small  $A$ . This function describes the supersaturation as a function of radius around the threshold value  $\epsilon_0$ . Due to the inverted presentation  $\epsilon(\bar{R})$  instead of  $\bar{R}(\epsilon)$  the function captures both the nucleation radius  $\bar{R}_c$  and the larger radius  $\bar{R}_s$ . The threshold value  $\epsilon_0$  can be obtained from Eq. (4.21) by minimizing  $\hat{\epsilon}$  for fixed  $A$  as  $\partial \hat{\epsilon} / \partial \hat{R} = 0$ . It behaves as

$$\epsilon_0 = 4^{-2/3} A^{1/3} + O(A^{1/2}), \quad (4.22)$$

with radius

$$\bar{R}_0 = w(4A)^{-1/3} + O(A^{-1/2}) . \quad (4.23)$$

For large and small  $\hat{R}$ , Eq. (4.21) describes the steady radii  $\bar{R}_s$  and  $\bar{R}_c$ , respectively, for which  $\epsilon \geq \epsilon_0$ . For large  $\epsilon$ , the critical radius obeys

$$\bar{R}_c \simeq \frac{w}{6\epsilon} , \quad (4.24)$$

while the larger stationary radius is

$$\bar{R}_s \simeq w(3\epsilon/A)^{1/2} . \quad (4.25)$$

In Fig. 4.7B, the stationary solutions of Fig. 4.7A are shown rescaled, together with the scaling function Eq. (4.21). The scaling behaviors given by Eq. (4.25) and Eq. (4.24) are the two straight lines of the red curve for large supersaturation. The threshold value  $\epsilon_0$  and  $R_0$  is indicated as red dot. We see that the threshold values and  $\bar{R}_c$  are described accurately already for  $A = 0.001$ . The approximation for  $\bar{R}_s$  deviates from the full solution as  $\bar{R}$  increases, but becomes more accurate for decreasing  $A$ .

The scaling exponent  $a = 1/2$  captures the behavior of Eq. (4.20) for larger radii with  $\bar{R} \approx l_{\pm}$  and  $\bar{R} > l_{\pm}$ . In this regime,  $\bar{R}/l_{\pm}$  becomes independent of  $A$  and the supersaturation is related to the radius by

$$\epsilon = \frac{D_- \nu_-}{D_+ k_- \Delta c} \frac{\frac{\bar{R}}{l_-} \coth\left(\frac{\bar{R}}{l_-}\right) - 1}{1 + \frac{\bar{R}}{l_+}} + O(A^{1/2}) \quad (4.26)$$

For  $\bar{R}/l_{\pm} \ll 1$ , we recover Eq. (4.25) which describes the larger stationary radius  $\bar{R}_s$ . For  $\bar{R}/l_{\pm} \gg 1$ , we obtain the divergence of  $\bar{R}_s$  as  $\epsilon$  approaches  $\epsilon_{\infty}$  with

$$\epsilon_{\infty} = \sqrt{\frac{D_- k_- \nu_-}{D_+ k_+ k_- \Delta c}} . \quad (4.27)$$

In Fig. 4.7C, the stationary solutions are shown rescaled for this scaling regime, together with the scaling function Eq. (4.26). We find that it describes the stationary radius well for radii sufficiently larger than  $R_0$ , and captures the divergence for  $\epsilon \rightarrow \epsilon_{\infty}$  well ( $\epsilon_{\infty} = 1$  for the parameters shown).

Note that for  $R \approx l_{\pm}$ , spontaneous nucleation inside the droplet may play a role in real systems, such as the bubbles we discussed in chapter 5 in the continuum model. Such behavior is not described in the effective droplet model, which can limit the predictive power of Eq. (4.26). Since the stationary radius is not a model parameter, Eq. (4.27) can be useful to estimate the supersaturation where  $R \geq l_{\pm}$ . Therefore, equations (4.21)-(4.25) describing the scaling for  $\bar{R} < l_{\pm}$  are more relevant for the description of real systems.

#### 4.4.2 Shape instability

We now discuss scaling relations for the shape instability of chemically active droplets, Eq. (4.13), in the limit of small  $A$ . Additional information can be found in Appendix C.3. Fig. 4.7D shows the largest eigenvalues  $\mu_l = \mu_{1lm}$  of modes  $l = 0, 1, \dots, 4$  along the upper solution of the stationary radius in Fig. 4.7A. We see that for a fixed reaction amplitude  $A$  (lines of one color), the deformation eigenvalues become unstable ( $\mu_l = 0$ ) at supersaturation  $\epsilon_l$  that increases with increasing mode  $l$ . For supersaturations  $\epsilon > \epsilon_l$  the eigenvalue shows a mode-dependent plateau, and decays towards zero for  $\epsilon \rightarrow \epsilon_\infty$ , where the stationary radius diverges. For decreasing reaction amplitudes, the supersaturation  $\epsilon_l$  at which modes become unstable first decreases, so that the plateau is stretched, while the plateau value decreases (note that the y-axis shows  $\mu_l t_0 A^{-1}$ ). To find the onset of instability and the plateau value, we concentrate on the scaling regime  $\bar{R} \ll l_\pm$  of the stationary radius with rescaled parameters  $\hat{R} = \bar{R}A^{1/3}/w$ ,  $\hat{\epsilon} = \epsilon A^{-1/3}$  and  $\hat{l}_\pm = l_\pm A^{1/2}$ . We find the rescaled eigenvalue  $\hat{\mu}_l = \mu_l \tau A^{-1}$  given by

$$\hat{\mu}_l \approx (l-1) \left( -\frac{1+g_l}{6\hat{R}^3} + \frac{\hat{\epsilon}}{\hat{R}^2} + \frac{1}{3} \right). \quad (4.28)$$

with

$$g_l = \frac{h_l(l+1) + \frac{D_- \beta_-}{D_+ \beta_+} h_l l}{l-1} \quad (4.29)$$

and  $h_l = (l^2 + l - 2)/2$ .

The stationary radius  $\hat{R}$  is related to  $\hat{\epsilon}$  by Eq. (4.21). Inserting this relation in Eq. (4.29) yields a simple equation for the eigenvalue as a function of the stationary radius,

$$\hat{\mu}_l = (l-1) \left( \frac{2}{3} - \frac{g_l}{6\hat{R}^3} \right) + O(A^{1/6}). \quad (4.30)$$

which depends only on the mode  $l$ , the (rescaled) stationary radius and the ratio  $D_+ \beta_+ / (D_- \beta_-)$ . For mode  $l = 0$  corresponding to changes in volume, the eigenvalue changes sign at  $R_0$ , so that the larger stationary radial solution  $\bar{R}_s$  is stable, while the smaller one  $\bar{R}_c$  is unstable. For the translational mode  $l = 1$ , we find  $\hat{\mu}_1 = 0$  for all stationary radii. For deformational modes  $l \geq 2$ , the eigenvalue changes sign for

$$\hat{R}_l \simeq \left( \frac{g_l}{4} \right)^{1/3} \quad (4.31)$$

with corresponding supersaturation

$$\hat{\epsilon}_l \simeq \frac{1}{6} \left( 1 + \frac{1}{2} g_l \right) \hat{R}_l^{-1}. \quad (4.32)$$

Stationary radii smaller than  $\hat{R}_l$  are stable, while larger radii are unstable. For large radii  $\hat{R} \ll \hat{R}_l$ , the eigenvalue approaches a constant plateau value

$$\mu_l^p = 2(l-1)/3. \quad (4.33)$$



#### 4.4. Droplet shape stability in the limit of a small reaction amplitude

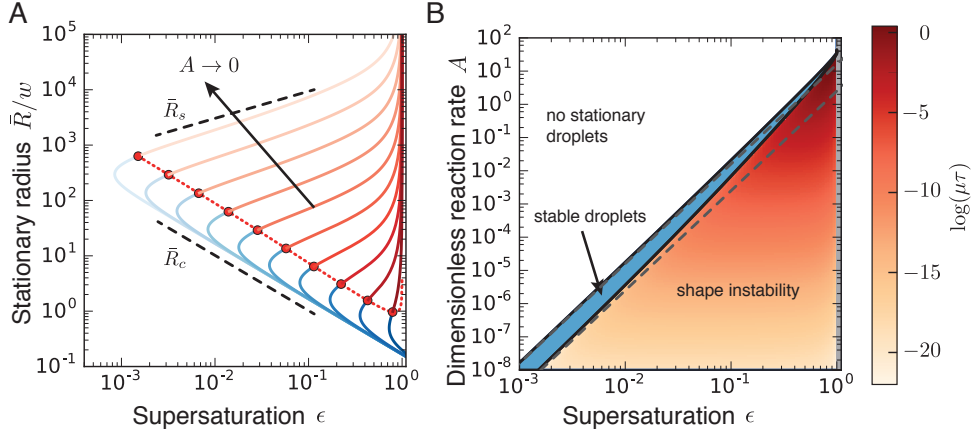


FIGURE 4.8: Stationary radii and onset of shape instability. A: Stationary radius as a function of supersaturation for different reaction amplitudes  $A = 10^{-8}, 10^{-7}, \dots, 10^1$ . The blue line colors mark stable, the red ones unstable stationary radii with respect to the elongational  $l = 2$  mode. In panel B the scaling behavior of the nucleation radius  $\bar{R}_c$  and the stationary radius  $\bar{R}_s$  are indicated. B: Stability diagram of stationary droplets of size  $\bar{R}_s$ , as a function of reaction amplitude  $A$  and supersaturation  $\epsilon$ . For small supersaturation and large reaction amplitudes, no stationary radius exists (white). For large supersaturation, the stationary radius diverges (gray). In the region between these regimes, the stationary solution can be stable (blue) or unstable (red) with respect to shape perturbations of the  $l = 2$  mode. The scaling relations (dashed lines) for the regime of stable droplets and the onset of instability are indicated. (Parameters:  $k_+/k_- = 1$ ,  $\nu_/(k_- \Delta c) = 1$ ,  $D_+/D_- = 1$ ,  $\beta_- = \beta_+$ ,  $c_+^{(0)} = 0$ )

Fig. 4.7E shows  $\hat{\mu}_l$  as a function of the rescaled supersaturation  $\hat{\epsilon}$  together with the scaling function Eq. (4.30) for different modes  $l$ . The scaling function describes the onset of the instability and the plateau well for small reaction amplitudes. Eq. (4.32) captures the scaling behavior of the onset of instability for different parameters in the  $\bar{R} - \epsilon$  plane, corresponding to the red dotted line in Fig. 4.8A for  $l = 2$ .

Using Eq. (4.32), we find for  $\mu_l = 0$  as relation between  $A$  and  $\epsilon$

$$A \simeq 54 \frac{gl}{(1 + \frac{1}{2}gl)^3} \epsilon^3. \quad (4.34)$$

In Fig. 4.8, the dashed line indicates this scaling solution in the limit  $A \rightarrow 0$  for  $l = 2$ , which we find to be the first mode to become unstable. For small reaction rates, the scaling relations for the stationary state and the instability capture the behavior of the stability diagram very well. For larger reaction rates, the supersaturation  $\epsilon_0$  characterizing the existence of the stationary droplet state is a bit overestimated. For the onset of the instability, the deviations between the full solution and the scaling

equation becomes larger, overestimating the supersaturation where droplets become unstable by a factor of 2.

Eq. (4.28) is valid also for growing droplets in the appropriate scaling regime if the stationary concentration profiles for a radius  $R$  describe the concentration profiles of the growing droplet (quasistatic assumption). This can be written in an unscaled version as

$$\mu_l \tau \approx (l-1) \left[ -\frac{1}{6}(1+g_l) \left(\frac{R}{w}\right)^{-3} + \left(\frac{R}{w}\right)^{-2} \epsilon + \frac{1}{4}A \right]. \quad (4.35)$$

Using this equation, we see that for finite radii and vanishing reaction amplitude  $A$  the onset of instability  $\mu_l = 0$  leads to a simple expression

$$R_l \approx w \frac{1+g_l}{6\epsilon}. \quad (4.36)$$

This expression was reported previously by Mullins and Sekerka for the shape instabilities of growing solids, compare Eq. (4.17) with  $w = 6\beta_+\gamma/\Delta c$ . For nonzero reaction amplitudes, we find that chemical reactions modify the equation, increasing the instability. For vanishing supersaturation, the radius  $R_l$  where droplets become unstable would diverge in the classical case of Mullins and Sekerka. In the present case of active droplets, we find for  $\epsilon \rightarrow 0$  instead a finite value

$$R_l^* \approx \left( \frac{1+g_l}{2A} \right)^{1/3}. \quad (4.37)$$

We can use Eq. (4.36) to consider in which order different deformation modes become unstable for a droplet that grows towards its stationary size  $\bar{R}_s$ . We see that the eigenvalue depends on the mode  $l$  only via two terms. The factor  $(l-1)$  indicates that if several modes are unstable, larger modes tend to have a larger eigenvalue. Inside the bracket that determines the sign of the eigenvalue, the stabilizing term monotonously grows with the mode, while all other terms are independent of the mode. Therefore, we find that the deformation modes become unstable consecutively as the droplet grows, starting with the elongational mode  $l = 2$ . This indicates that the dynamic behavior of chemically active droplets might be dominated by this mode, as it can grow and thus have a large amplitude before the other modes become unstable, even though they may have larger eigenvalues at the stationary size.

## 4.5 Summary

In this chapter we discussed the behavior of chemical active droplets in the effective droplet model in the limit of large viscosity where hydrodynamic flows can be neglected. We showed that chemical reactions create a stationary droplet size, which is stable with respect to changes in volume, which was reported before in Zwicker (2013); Zwicker et al. (2014, 2015). We then analyzed the stability of stationary

spherical droplets with respect to shape deformations in a basis of spherical harmonics and corresponding radial functions for the concentration field. We found that spherical droplets may become unstable with respect to different shape deformations. The mode that becomes unstable first is the elongational mode  $l = 2$ . This shape instability is contrary to expectations based on the typical behavior of droplets we observe in daily life. Droplets in equilibrium systems are stable due to their surface tension, which minimizes the surface area. In our daily life, we see mostly spherical droplets as a result. Many results indicate that nonequilibrium driving can destabilize the preferred state of equilibrium systems, such as the Mullins-Sekerka instability for growing solid phases in supersaturated liquid or gas, which creates dendritic shapes. However, a shape instability of simple liquid droplets due to chemical reactions has, to our knowledge not been discussed theoretically or experimentally.

To gain a better understanding of this new effect, we then discussed the physical origin of the instability and its relationship to other instabilities. We discussed the physical origin of the shape instability as a flux-driven instability. Small perturbations of the droplet shape and the concentration field can be increased because the interface moves into the gradient of the stationary concentration profile, thus increasing the gradient and creating stronger fluxes. These fluxes then 'feed' the deformation, leading to the instability. The surface tension of the droplet counteracts this instability, so that regimes exist where spherical droplets are stable, and regimes where they are unstable.

We compared the instability with Mullins-Sekerka instability, which describes a flux-driven instability of growing solids in a supersaturated liquid, which leads to dendritic shapes. We find that a major difference of our model is the existence of the stationary droplet size, created by the reaction inside the droplet. This leads to qualitatively different behavior - to linear order, volume conservation of our droplets lead to a thinning in of the droplet around the waistline of the deformation, while in the Mullins-Sekerka model, the solid grows in all directions (though with different speed). We find that due to this, the unstable elongational  $l = 2$  mode can lead to deformation of the droplet into a dumbbell shape, while the mode does not lead to a deformation in the Mullins-Sekerka model.

In the last section of this chapter, we discussed the properties of the stationary droplet radius and the instability in the limit of vanishing chemical reactions,  $A \rightarrow 0$ . This leads to simple equations for the existence and size of stationary droplets and for the shape instability. We find that these relations are a good estimation of the full solution. More importantly, the scaling equations allow for the prediction of the stationary size and the instability for parameters not discussed explicitly. Our model has 6 parameters ( $A$ ,  $\epsilon$ ,  $k_+/k_-$ ,  $\nu_/(k_- \Delta c)$ ,  $D_+/D_-$  and  $\beta_-/\beta_+$ ). Here we discussed the dependence of system on two of them,  $A$  and  $\epsilon$ , while keeping the other parameters constant and equal to one, corresponding to equal conditions in both phases. The scaling analysis predicts that different properties of both phases will not qualitatively change the stability diagram, and in which way quantitative differences will appear.

We therefore now have a good understanding of the origin of the shape instability, and a simple description that shows the dependency on the parameters of the system.



We will now consider the nonlinear shape dynamics of chemically active droplets using the continuum model introduced in chapter 3. We want to study how the out-of-equilibrium chemical reactions influence the droplet dynamics. For this, we consider the case of large viscosity where hydrodynamic flows can be neglected. The influence of hydrodynamic flows is discussed in chapter 7.

We have shown in chapter 4 using the effective droplet model that chemically active droplets have two stationary sizes, a critical nucleation radius  $\bar{R}_c$  and a larger stationary radius  $\bar{R}_s$ . Droplets smaller than  $\bar{R}_c$  tend to shrink and vanish, while larger droplets grow towards the stationary radius  $\bar{R}_s$  if they are smaller than  $\bar{R}_s$ , and shrink towards it if they are larger. We found that the shape of stationary spherical droplets can become unstable due to the continuous fluxes of the stationary state which counteract surface tension. The first mode to become unstable is the elongational mode  $l = 2$ .

In this chapter, we investigate the nonlinear dynamical behavior of chemically active droplets using numerical solutions of the continuum droplet model. A special focus lies on the droplet dynamics in the unstable regime, to determine the dynamic shape changes of the instability.

A large part of the content of this chapter has been published in Zwicker et al. (2017).

## 5.1 Numerical solution of droplet dynamics in the continuum model

We consider an incompressible system that consists of droplet material B and outer material A, so that the system is described by the concentration field  $c$  of B, compare the introduction of the continuum model in section 3.1. We use the properties of the interface to normalize concentration, length, time and energy, see table 3.1. The

Cahn-Hilliard free energy with minima at  $c_+^{(0)}$  and  $c_-^{(0)}$  favors a phase separated state for systems with intermediate mean concentrations  $\bar{c}$  with  $c_+^{(0)} < \bar{c} < c_-^{(0)}$  with a smooth interface separating the phases. Nonequilibrium chemical reactions convert A to B and vice versa, with a net reaction  $B \rightarrow A$  for large concentrations, so that the concentration field has a sink inside a droplet with turnover  $\nu_- t_0/\Delta c$  at reference concentration  $c_-^{(0)}$ . For small concentrations corresponding to the outer phase, the reaction leads to a net reactions  $A \rightarrow B$ , which creates a concentration  $c_\infty = c_+^{(0)} + \epsilon\Delta c$  outside the droplet, with a (dimensionless) supersaturation  $\epsilon = \nu_+/(k_+\Delta c)$  of droplet material. Therefore, the droplet material is not conserved in the system, and can change dynamically due to the chemical reaction. We will now consider the effect that this chemical reaction has on the dynamics of the system, and explicitly on the dynamics of a droplet.

We here consider the case without hydrodynamic flows, corresponding to the limit of infinite viscosity,  $F \rightarrow \infty$  with dimensionless viscosity  $F = \eta w^3/(e_0 t_0)$  – we will discuss the case of finite viscosity in chapter 7. We solve the time evolution of the concentration field, Eq. (3.1) with  $\mathbf{v} = 0$ , using a semi-implicit Runge-Kutta method for the time step, with a spectral method for the spatial operators, whereby the gradient terms are evaluated in Fourier space, with no-flux boundary conditions. This yields the concentration field at discrete time steps on a three-dimensional rectangular lattice. The numerical details are given in Appendix D.2. This method is specifically chosen to deal with the difficulties of solving the Cahn-Hilliard equation, which contain fourth order spatial derivatives  $\kappa m \nabla^4 c$  that arise from the gradient term of the free energy. This enables us to consider long-time dynamics of a droplet, in a three-dimensional box that is large enough to have a dynamics that is (reasonably) independent of the boundaries of the box. See Appendix D.2 for details.

To study the dynamics of a chemically active droplet, we start with an initial droplet of radius  $R$  with a small initial perturbation of the droplet shape in the center of the simulation box, with a concentration  $c_-^{(0)}$  inside the droplet, and concentration  $c_\infty$  outside, set by the chemical reaction parameters. A small shape deformation can be incorporated via  $R(\theta, \phi) = R_0(1 + \epsilon_2 \hat{Y}_{20}(\theta, \phi))$ , where the droplet interface at position  $R$  is given in spherical coordinates. Here,  $\epsilon_2$  is the deformation amplitude,  $\hat{Y}_{20}(\theta, \phi) = Y_{20}(\theta, \phi)/Y_{20}(0, 0)$  denotes the normalized spherical harmonic with mode  $l = 2$  and  $m = 0$ , corresponding to an elongation of the droplet, and  $\theta$  and  $\phi$  denote the polar and azimuthal angles, where  $\theta = 0$  coincides with the axis of the deformation. We can study the droplet dynamics visually by plotting the concentration field. To analyze the size and shape changes of a droplet, we fit a droplet shape with large concentration inside and small concentration outside to the concentration field, see Appendix D.3.

## 5.2 Dynamics of the homogeneous state

Let us now quickly review the basic dynamics of the system. First, let us start with the dynamics of a homogeneous system with concentration  $c_0$ . If no fluctuations exist, the system remains homogeneous, with a concentration that changes over time due to the chemical reactions,  $\partial_t c_0 = s(c_0)$ , and reaches a steady state with concentration  $c_\infty$ . Along the way, small spatial fluctuations (for example due to noise in the initialization) can lead to spinodal decomposition into two phases. Without chemical reactions, the concentration regime where such phase separation is found is given by the region of negative curvature of the free energy density with  $f_0''(c_0) < 0$ , where  $f_0$  is defined by Eq. (3.4) with  $\kappa = 0$  (or equivalently  $\bar{\mu}'_0(c_0) < 0$ , with the definition of the local chemical potential in Eq. (3.6)). With chemical reactions, a linear stability analysis yields as eigenvalue for a perturbation with wavevector  $q$

$$\eta(q) = - [k(c_0) + f_0''(c_0)q^2 + m\kappa q^4] . \quad (5.1)$$

where  $k(c_0)$  is given by  $k(c) = ds/dc$ . Details can be found in Appendix D.1. Within the regime of a linear reaction rate around  $c_+^{(0)}$ , we find  $k = k_+$ . For  $k(c_0) > 0$ , the chemical reaction thus stabilizes the homogeneous state. For large wavelengths, the homogeneous state is thus stable ( $q \rightarrow 0$ ) due to the chemical reaction, and for small wavelengths, the surface tension term  $m\kappa q^4$  stabilizes the homogeneous state. For an intermediate regime,  $\eta(q)$  has a local maximum for  $f_0''(c_0) < 0$ , given by

$$q_* = \sqrt{-f_0''(c_0)/(2m\kappa)} \quad (5.2)$$

$$\eta(q_*) = \frac{f_0''(c_0)^2}{4m\kappa} - k(c_0) . \quad (5.3)$$

For  $\eta(q_*) > 0$ , the homogeneous state with concentration  $c_0$  is thus unstable. For the parameters used in this chapter with  $k_\pm t_0 = 10^{-2}$ , we find that concentrations  $c_0 = c_+^{(0)} + \delta\Delta c$  are unstable for  $\epsilon_c < \delta < 1 - \epsilon_c$  with  $\epsilon_c \approx 0.24$ . Numerical solutions of the homogeneous state with some initial noise agree with this result.

The behavior of the homogeneous system is relevant for the study of droplet dynamics for two reasons. First, the concentration far from the droplet may be unstable for  $\epsilon \geq \epsilon_c$ , so that droplets may nucleate around the initial droplet and influence the dynamics of the initial droplet. This may occur also for supersaturations slightly smaller than  $\epsilon_c$ , due to nonlinear effects, and because the initial dynamics of the system may show a concentration increase around the droplet before the stationary profile is reached. Second, the concentration inside the droplet becomes inhomogeneous due to the chemical reaction inside the droplet, which leads to a lowering of the concentration in the droplet center, compare Fig. 4.2 in the effective droplet model. Our calculation of the stability of the homogeneous state indicates that the center of the droplet may become unstable for a concentration  $c_0$  with  $\delta < 1 - \epsilon_c$ , which might lead to a nucleation of a droplet of the outer phase inside the droplet, creating a droplet bubble. The results from the effective model further indicate that this would happen

for  $R \gtrsim l_-$ , where the concentration field inside the droplet deviates sufficiently from the boundary value.

This section highlights that the effective droplet model and the continuum model are related, but may feature quite different scenarios, since the nucleation of new phases is not included in the effective droplet model, but may be quite prominent in the continuum model we study in this chapter.

### 5.3 Volume growth of chemically active droplets

We now consider the dynamic growth of an active droplet in the continuum model.

Let us briefly discuss the volume growth and droplet dynamics for different supersaturations and initial droplet sizes. Starting with an initial droplet, we find small initial changes in droplet size when a quasi-stationary concentration field is established. The quasi-stationary concentration field in both phases resembles the fields that we found for the effective droplet model, compare Fig. 4.2. After this initial dynamics, the droplet shows the types of dynamics predicted by the effective droplet model: For small supersaturations, the droplet vanishes, independent of its initial size. For larger supersaturations, the droplet vanishes for small initial sizes ( $R < \bar{R}_c$ ), and grows towards a larger stationary size. Droplets that are slightly larger than the stationary size shrink towards this size. We find the numerically observed stationary radius to be close to the radius  $\bar{R}_s$  from the effective droplet model (with differences of  $\leq 20\%$ ), large deviations were observed only in regimes where the stationary droplet diameter together with the size of the depletion region, estimated to be approximately  $l_+ = \sqrt{(mb)/k_+}$ , exceeded the size of the simulation box. For droplets with a radius similar to or larger than the reaction-diffusion length scale  $l_- = \sqrt{(mb)/k_-}$  inside the droplet, the nucleation of a droplet of the outer phase is possible inside the droplet phase, so that the droplet becomes a bubble. Such a bubble consists of a spherical shell of constant width with high concentration, while the concentration inside this shell is similar to the outer phase, see Fig. 5.3A. Beyond a critical supersaturation and initial radius, a spherical droplet may become unstable with respect to shape deformations and deform. This will be discussed in the next section. For large supersaturations  $\epsilon \gtrsim \epsilon_c$ , additional droplets nucleate in the outer phase. Both the formation of bubbles and the nucleation of new droplets can be understood by considering the stability of the homogeneous state, as discussed in the previous section. For droplets with a radius that is similar or larger than the reaction-diffusion length scale, the droplet becomes inhomogeneous, with a concentration minimum in the droplet center. If the concentration in the center drops enough, the concentration allows the nucleation of a droplet of the outer phase. Similar, nucleation is possible if the concentrations outside the droplet is larger than the critical concentration for nucleation.

Fig. 5.2 shows a stability diagram of droplets as a function of the supersaturation  $\epsilon$  and the reaction rate  $\nu_-$ . Droplets were initiated with a size of  $0.8\bar{R}_s$ , where  $\bar{R}_s$  is the larger stationary radius of the effective droplet model with equivalent parameters. We



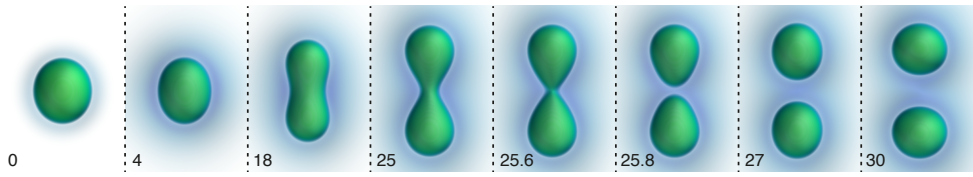


FIGURE 5.1: Division of chemically active droplets. A droplet with small initial deformation elongates and splits into two symmetrical daughter droplets. The droplet shapes are shown as equal concentration contours (green). The concentration field outside the droplet (blue) has small values  $c \approx c_+^{(0)}$  (violet blue) close to the droplet and concentrations close to  $c_\infty$  (transparent) far from the droplet, set by the chemical reaction  $s(c_\infty) = 0$ . The dynamic equations of the continuum model were solved numerically in 3d, see Appendix D.2. Parameters:  $\nu_- t_0 / \Delta c = 1.3 \cdot 10^{-3}$ ,  $\nu_+ t_0 / \Delta c = 1.9 \cdot 10^{-3}$ ,  $k_\pm t_0 = 10^{-2}$ , and  $F \rightarrow \infty$ . Indicated times are given in units of  $10^2 t_0$ .

find regimes where droplets vanish (dots), where stable spherical droplets exist (blue spheres), and where a small initial shape perturbation grows (red shapes). For the regime of vanishing droplets, larger initial sizes were tested as well. A comparison with the corresponding diagram of the effective droplet model Fig. 4.4 shows that the regimes in both models show the same trends. For small turnover  $\nu_- / \nu_0$ , the stationary droplet radius diverges in the effective droplet model, while it is limited by the size of the simulation box for the continuum model. The numerical results were tested in a larger box, but may still contain finite size effects.

## 5.4 Division of chemically active droplets

We now concentrate on the shape dynamics of chemically active droplets. We initialize the system with a droplet with a small prolate deformation of the spherical harmonic mode  $l = 2$ ,  $m = 0$ . Fitting deformed droplet shapes to the concentration field, we find that the amplitude of the deformation mode shrinks over time for some parameters, indicating a stable spherical droplet with respect to this mode, while the deformation grows for others, indicating an unstable mode. In the stability diagram Fig. 5.2, the stability of spherical droplets with initial radii close to the predicted stationary size, growing towards the stationary size, is indicated for the elongational mode. Stable droplets are marked in blue, unstable ones in red. We find that for fixed turnover  $\nu_-$ , droplets become unstable for supersaturations beyond a critical supersaturation. For increasing turnover  $\nu_-$ , this critical supersaturation increases. This agrees well with the stability analysis of the effective droplet model, compare Fig. 4.4. For vanishing turnover rates, the results of both models differ to some extent. This is likely due to the divergence of the chemically set stationary droplet radius which is limited in the continuum model by the box size.

We find that typically, an unstable initial deformation leads to a division of the

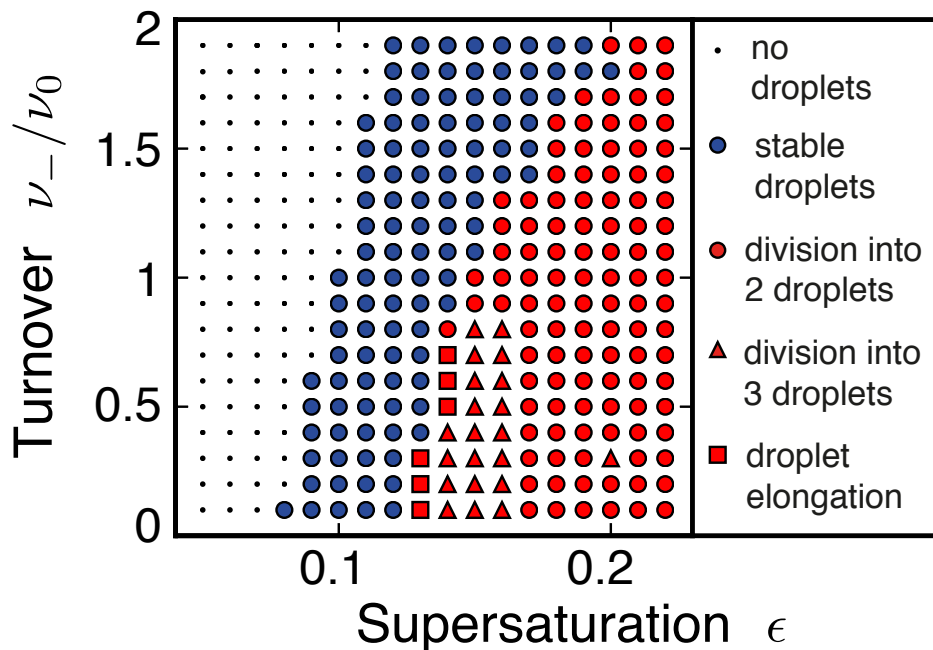


FIGURE 5.2: Stability diagram of active droplets as a function of supersaturation  $\epsilon = \nu_+/(k_+\Delta c)$  and turnover  $\nu_-/\nu_0$  of droplet material using the continuum model. Droplets either dissolve and disappear (white region), are spherical and stable (blue region), or undergo a shape instability and typically divide (red region). The behavior of droplets is indicated by symbols for different values of  $\nu_-$  and  $\epsilon$ . Parameter values are:  $k_{\pm}t_0 = 10^{-2}$ ,  $F \rightarrow \infty$ , and  $\nu_0 = 10^{-2}\Delta c/\tau_0$ .

droplet into two symmetric daughter droplets. Fig. 5.1 shows 3d graphical representations, where the droplet interface is shown as equal concentration contours (green) and the concentration field around it as semi-transparent volume elements (shades of blue). We start with an initial droplet with a size close to the stationary size of the droplet, with a small initial deformation (panel 1). The concentration outside is initially set to  $c_\infty$ , the fix-point of the chemical reaction  $s(c_\infty) = 0$ . In a fast initial dynamics, a minimum of the concentration field (blue) develops around the droplet, with  $c \approx c_+^{(0)}$  (violet blue) close to the droplet and  $c \approx c_\infty$  (transparent/white) far from the droplet (panel 2). Within the same time-window, the droplet volume changes towards its stationary size – for the parameter value shown, the volume dynamics is much faster than the shape deformations. Over time, the droplet elongates (panel 2) and forms a dumbbell shape (panel 3), which then thins in around the waistline of the droplet (panel 4). This waistline pinches off (panel 5 to 6), and the two daughter droplets round up into approximately spherical shapes (panel 6-8). During this division, the total droplet volume increases, so that the daughter droplets have volumes similar to the initial droplet, so that they again might be able to deform and divide.

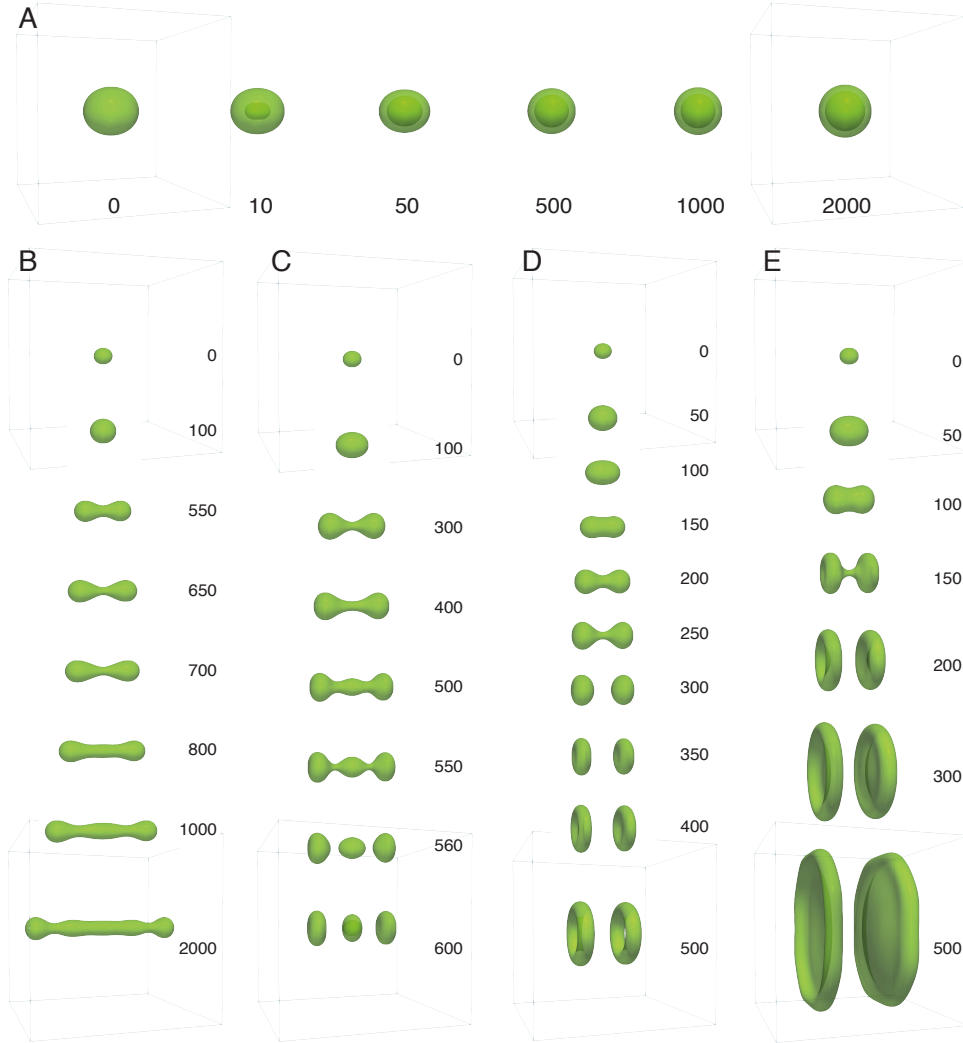


FIGURE 5.3: Dynamical behavior of droplets with different supersaturations. To demonstrate the diversity of the dynamics of chemically active droplets, we show here results for small turnover  $\nu_-/\nu_0 = 0.7$ . A) For a large initial droplet,  $R_0 = 15w$ , a droplet of the outer phase can nucleate in its center, leading to a bubble. (Parameter:  $\epsilon = 0.15$ ) B) For supersaturations close to the onset of instability,  $\epsilon = 0.13$ , the droplet elongates into a long cylindrical structure. C) For  $\epsilon = 0.15$ , the droplet divides into a chain of three droplets. D) For  $\epsilon = 0.16$ , the droplet divides into two daughters, which then deform into oblate shapes and finally become tori E) For  $\epsilon = 0.21$ , the droplet divides into two daughters, which deform into two parallel plates. Shown are droplet contours (green) for concentration  $(c - c_+^{(0)})/\Delta c = 0.5$  for time steps  $t = n \cdot 10t_0$  with index  $n$  indicated on the panels. Parameters:  $\nu_- t_0/\Delta c = 7 \cdot 10^{-3}$ ,  $k_{\pm} t_0 = 10^{-2}$ , and  $F \rightarrow \infty$ . The initial shape deformation is  $\epsilon_2 = 0.1$ . For panels B-E, the initial radius is  $R_0 = 5w$ .

For increasing supersaturation, the division is accompanied by deformations due to the deformations of modes with higher order. These higher modes typically don't influence the division, only in one set of parameters ( $\epsilon = 0.2$ ,  $\nu_-/\nu_0 = 0.3$ ) did the deformations lead to a division into three droplets instead.

We can find additional dynamic behavior in the unstable regime, shown as red squares and triangles in Fig. 5.2. For a small turnover and small supersaturations close to the onset of instability, the shape elongates, but does not become thin at the waistline but instead grows into a cylinder-like form, connecting two spheres that move with seemingly constant speed apart, elongating the cylinder during the simulation time, see Fig. 5.3B. For intermediate supersaturations, droplets elongate and divide into a chain of 3 droplets, Fig. 5.3C. However, the droplet division shown in Fig. 5.1 is the typical shape dynamics of unstable chemically active droplets for the parameters investigated, shown as red circles in Fig. 5.2.

The droplet division discussed here shows that active reactions can not only suppress Ostwald ripening against surface tension, but can lead to a deformation of a spherical droplet that increases the surface area, eventually leading to a division of the droplet into two. This new effect is completely different from our everyday experiences, where droplets do not spontaneously split, but instead coalesce and ripen over time.

## 5.5 Cycles of growth and division

We now discuss the dynamics of the two daughter droplets after the first division. We find that occasionally, the droplets do not divide again after the first division, but deform into oblate ('smarty-like') shapes, which then grow outward into two plates with a fixed width, or open in the center of the flattened shape to form tori, Fig. 5.3D and E. Both of these shapes typically grow outward until they reach the limits of the box.

However, our numerical calculations reveal that droplets typically undergo multiple rounds of divisions, see Fig. 5.4A. After a first division, the smaller daughters grow until they divide again when they reach the radius  $R_{div}$ . Interestingly, the division axes are not independent of each other, see Fig. 5.4A. In the absence of system boundaries, the division axes of both daughters are perpendicular to the first division axis, see Fig. 5.4B. Similarly, when the four granddaughters divide, their division axes are perpendicular to both the division axes of the first and the second division. The division axes in subsequent droplet divisions are determined by droplet interactions via the concentration fields surrounding the droplets. The two growing daughter droplets effectively compete for droplet material, leading to the depletion of droplet material in the space between them. Therefore, diffusion fluxes and growth rates are larger along axes perpendicular to the previous division axis, see Fig. 5.4C. This bias due to droplet interactions determines the division axes. In our numerical calculations, boundary conditions also influence the droplet divisions and slightly modify the division axes, see Fig. 5.4A.

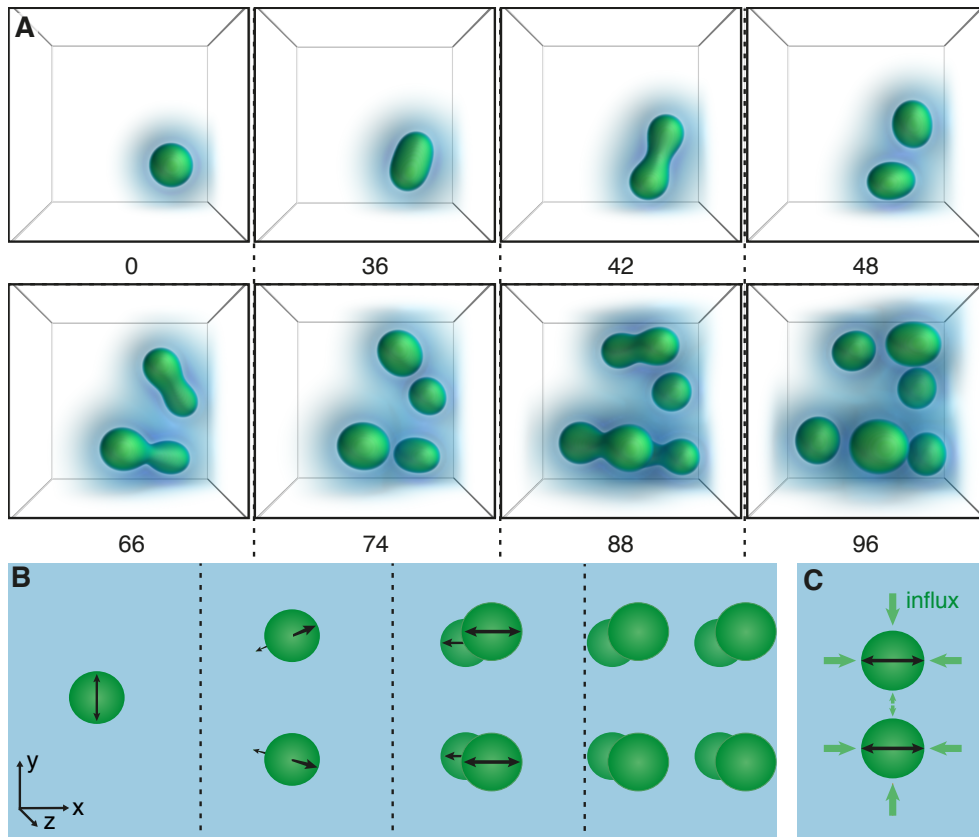


FIGURE 5.4: Cycles of growth and divisions. A) Sequence of droplet divisions at different times as indicated in units of  $10^2 t_0$ . Droplet configurations obtained from numerical solutions to the continuum model are represented as three dimensional shapes (green), the outside concentration field is shown in blue (low concentration,  $c \approx c_+^{(0)}$ ) to transparent white (supersaturated outside concentration  $c \approx c_\infty$ ). Parameters:  $\nu_- t_0 / \Delta c = 1.3 \cdot 10^{-2}$ ,  $\nu_+ t_0 / \Delta c = 2 \cdot 10^{-3}$ ,  $k_\pm t_0 = 10^{-2}$ , and  $F \rightarrow \infty$ . B) Schematic representation of the orientation of subsequent division axes. C) Droplet division is oriented along the axis for which diffusion fluxes (green arrows) are maximal.

## 5.6 Summary

We have shown in this chapter that the shape instability of chemically active droplets that we found in the effective droplet model indeed leads to a deformation of droplets in the continuum model. In the majority of cases, this leads to cycles of growth and division of droplets. For a small number of parameter values, for small supersaturations and small turnover  $\nu_-$ , droplets show a tendency to form cylindrical shapes. Occasionally, other shapes such as droplet tori and plates are observed as well. We will consider the existence of stationary cylindrical droplets and their stability in the

next chapter.

It has been reported previously that chemically active systems show new behaviors. Nonequilibrium chemical reactions can lead to a suppression of Ostwald ripening, whereby the size of phases does not increase over time, but a fixed length-scale is created. This has been shown for spinodal decomposition, see Puri and Frisch (1994); Glotzer et al. (1994), and for droplets, whereby a number of droplets with a stationary size set by the chemical reactions can stably coexist in a system, Zwicker et al. (2015). The instability and division of chemically active droplets has not been reported before. Droplet division is especially interesting because it demonstrates a simple physical mechanism of self-replication. Both daughter droplets have the same properties and behavior as the original droplet, and they can divide again. In the finite simulation box, droplets divide until they reach a critical density. In an infinite system, no such limit exists. Therefore, we expect that droplets would keep dividing, leading to an increase in the droplet population, as long as enough droplet material exists in the outside environment - implemented here via the constant supersaturation. This self-replication can be interpreted as life-like behavior. We will return to this point in chapter 8 to discuss chemically active droplets as a model for protocells at the origin of life.

## Shape instability of droplets with various geometries

6

---

Passive cylindrical droplets (usually called jets) appear often in daily life, usually in the context of liquid-air phase separation, for example water flowing out of a tap or a fountain. The water jet usually quickly splits up into separate droplets due to the surface tension. The formation of width-oscillations along the cylinder is described by the Plateau-Rayleigh instability. The effect is driven by minimizing the surface area, and the most unstable deformation with wavelength  $q^*$  is set by purely geometric arguments,  $q^*R \approx 0.7$ , and all unstable modes satisfy  $qR < 1$ .

Here we study the shape dynamics of chemically active droplets. We consider a two components system with components A and B with active chemical reactions  $A \rightarrow B$  between the components. The species phase separate into a phase with a low concentration of B, where the reaction produces new droplet material B,  $A \rightarrow B$ , and a phase with a high concentration of B, where B is degraded into the outer component,  $B \rightarrow A$ . See chapter 3 for details. We have seen in chapter 5 that a deformed spherical droplet in such an active system has a stationary size, which can be unstable so that the droplet can divide into two daughter droplets, which may grow and divide again. We also found that such droplets can form other shapes, such as dumbbell shapes with growing length and tori with a growing major radius, see Fig. 5.3. In both of these cases, the dynamic behavior seems to lead towards an infinitely long cylinder with a finite radius. We also saw examples of flat disk/plate like structures and bubbles, see Fig. 5.3, both of which resemble a flat plate with finite width in one direction and that is extended in the other two directions.

In this chapter, we discuss stationary shapes with different geometries and in different spatial dimensions, and analyze their stability with the effective droplet model in the limit of large viscosity, see 3. As in chapter 4, the droplet material B is converted into the outer material A with reaction amplitude  $A$ , and outside droplet material is created from the bulk material which creates a supersaturation  $\epsilon$ . We again ignore hy-

drodynamic flows by considering the limit of large viscosity. The interface movement for small deformations of the stationary state is generally described by Eq. (3.31) with normal vector  $\mathbf{n}$  of the deformed interface and normalization factor  $a_n = 1/(\mathbf{e}_r \cdot \mathbf{n})$ , where  $\mathbf{e}_r$  now is the normal unit vector of the undeformed stationary interface. Additionally, we compare our analytical predictions with numerical solutions of the dynamical behavior using the continuum model. We consider droplet shapes with a flat interface in different dimensions, as well as droplet disks in 2d systems and cylindrical droplet shapes in 3d. In our case, the droplet volume is not constrained as in the passive case, but set by the chemical reactions. Additionally, our system is out of equilibrium, so that the minimization of energy is not necessarily the driving dynamic force. Therefore it will be interesting to study the effect of active chemical reactions on the stability of cylindrical and other shapes.

## 6.1 Droplet shapes with a flat interface in 1d, 2d and 3d: Line-segments, bands and plates

In this section we consider droplet shapes with flat interfaces. A stationary system with a flat interface has a concentration profile with gradients perpendicular to the interface, and is constant in the other directions. The stationary state itself can therefore be understood by considering the 1d system perpendicular to the interface. We consider this to be the  $x$  direction. The deformation of such a flat system deforms the interface and concentration field in the  $x$  directions but also in the directions along the interface, so that the deformation modes and their stability depend on the dimension of the system. We will consider the stability of flat interfaces in 1, 2 and 3 dimensions. The most simple example is a line segment in 1d with stationary concentration field and fluxes. Systems in higher dimensions are created by extending the interface into the other dimension, creating a droplet band in 2d and a droplet plate in 3d. See Fig. 6.1 for a sketch of the systems.

We find that the stationary state in 1d is a line segment with width  $2L$ , where the half-width  $L$  is given by

$$\tanh(L/l_-) = \frac{l_+\nu_+}{l_-\nu_-} \quad (6.1)$$

which has one solution for  $-1 < \frac{l_+\nu_+}{l_-\nu_-} < 1$ , and none otherwise. See Appendix E for the calculation and the stationary concentration field. In Fig. 6.2A, the length  $L$  of stationary line segments are shown in comparison to the stationary droplet radius in 3d. The stationary size has a different dependence on the supersaturation, there is only one solution, with slope  $L \propto \epsilon$  for  $L/l_- \ll 1$ . Similar to the larger solution in 3d, it has a divergence at  $\nu_+ = \nu_-l_-/l_+$ , above which no finite stationary solution exists. In a passive system, we typically find solutions with two bulk phases with concentrations  $c_{\pm}^{(0)}$ , separated by a flat interface. In the case of chemically active droplets, the chemical reactions create concentrations  $c_{\infty}^{\pm}$  in the bulk phases with  $s_{\pm}(c_{\infty}^{\pm}) = 0$ . Such bulk phases are found for  $\nu_+ \geq \nu_-l_-/l_+$ . In Fig. 6.2A, we



6.1. Droplet shapes with a flat interface in 1d, 2d and 3d: Line-segments, bands and plates

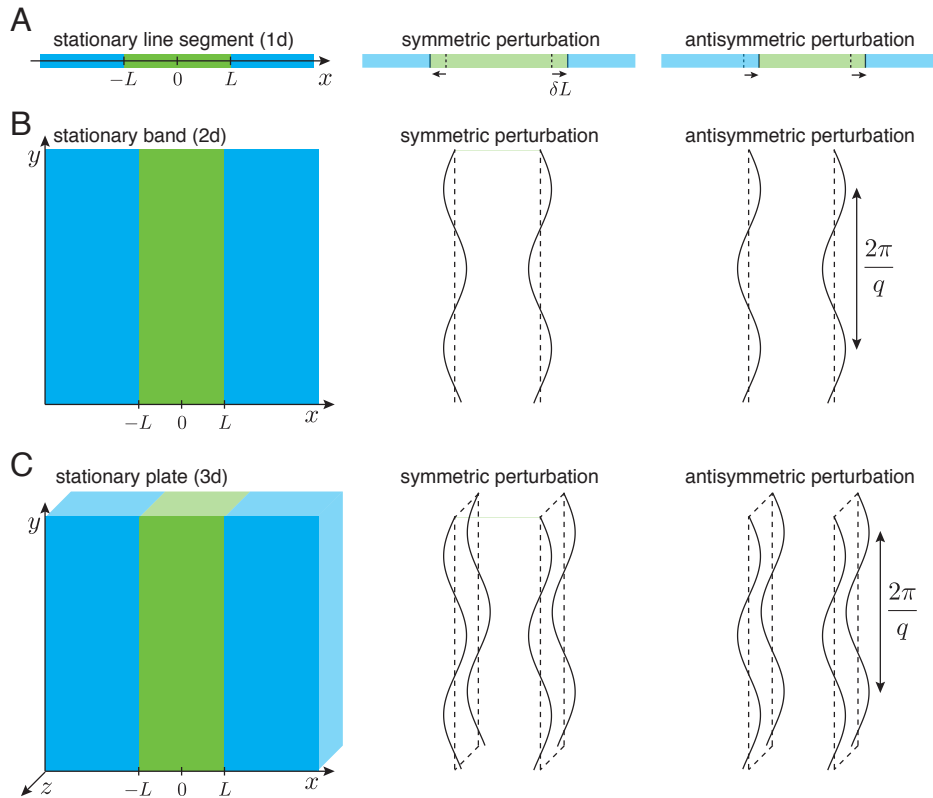


FIGURE 6.1: Stationary droplet states with a flat interface and their deformation modes. The stationary states are: (A) line segment in 1d, (B) band in 2d, and (C) plate in 3d. The stationary droplet phase (green) has a width  $2L$  in one direction and is extended in the other directions for 2d and 3d (left panels). Symmetric perturbations are mirror symmetric around  $x = 0$  and change the width of the droplet (center panels), while antisymmetric perturbations displace the droplet center around  $x = 0$  while keeping the width constant (right panels). Perturbations are periodic in one extended direction with wave-vector  $q$ .

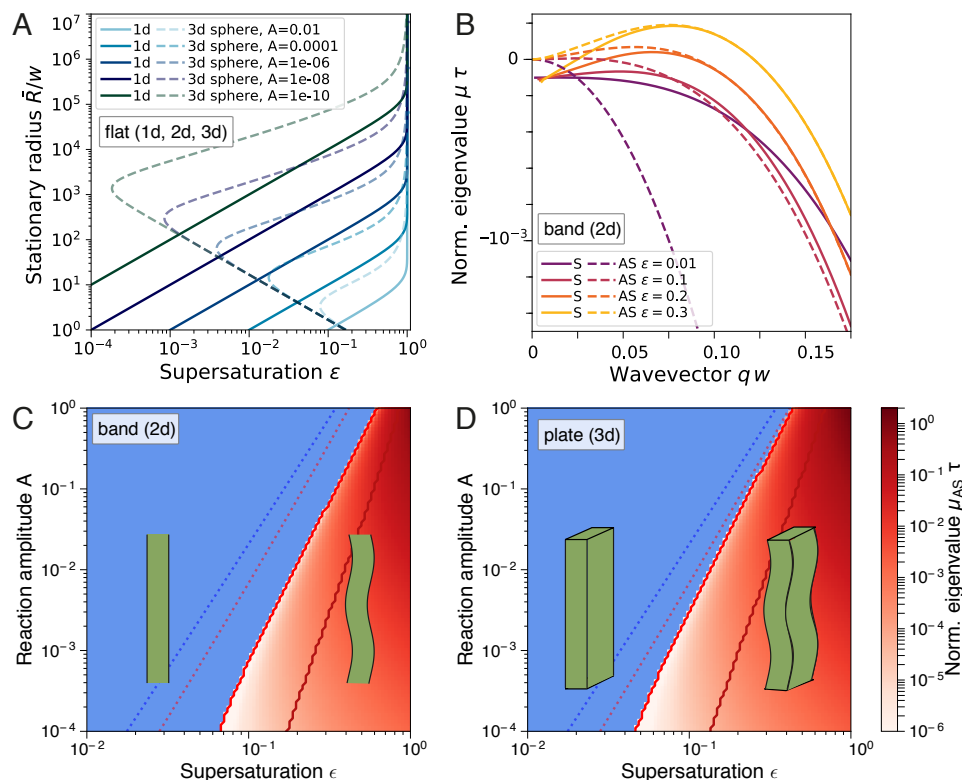


FIGURE 6.2: Characteristics of stationary droplet states with a flat interface. (A) Half-width  $L$  of flat stationary droplets as a function of supersaturation  $\epsilon$  for different reaction rates inside the droplet (lines). Valid for 1d line segments, 2d bands and 3d plates. As a comparison, the stationary droplet radius in 3d is shown (dashed lines). (B) Eigenvalues of symmetric (lines) and antisymmetric deformations (dashed lines) of 2d bands as function of the deformation wavelength  $q$  for  $A = 10^{-4}$  for different supersaturations (line color). Depending on parameter values, stationary bands can be stable ( $\epsilon = 0.01$ ) or unstable ( $\epsilon = 0.2$ ) with respect to shape deformations. (C) Stability diagram of droplet bands in 2d as function of the supersaturation and reaction amplitude. Blue color denotes stable stationary bands, the largest eigenvalues of unstable bands, corresponding to antisymmetric deformations are shown in red (see color bar). A red line marks the onset of instability with respect to antisymmetric perturbations, a darker red line the onset with respect to symmetric perturbations. For comparison, the existence of stationary droplets (blue dotted line) and their instability (red dotted line) for spherical droplets in 3d is shown. (D) Stability diagram of droplet plates in 3d as function of the supersaturation and reaction amplitude. See (C) for description. (Parameters:  $k_+/k_- = 1$ ,  $\nu_-/(k_- \Delta c) = 1$ ,  $D_+/D_- = 1$ ,  $\beta_- = \beta_+$ ,  $c_+^{(0)} = 0$ )

## 6.1. Droplet shapes with a flat interface in 1d, 2d and 3d: Line-segments, bands and plates

consider strong chemical reactions inside the droplet, with a value of  $c_\infty^- = c_+^{(0)}$ , so that we only find realistic solutions with a finite droplet phase, and no solutions with a bulk droplet phase. The critical nucleation radius that we find in 3d is due to the Laplace pressure  $2\gamma H(R)$  of the droplet, where the mean curvature depends on the radius,  $H(R) = 1/R$ . In 1d, the mean curvature is always zero, and thus no critical nucleation radius exists. In both cases, we find a stationary radius where the influx of droplet material into the droplet is balanced by the conversion and outflow of A-material that is created inside the droplet by chemical reactions. For droplets smaller than the reaction-diffusion length scale inside the droplet  $l_-$ , the droplet is roughly homogeneous, so that the outflux scales with the droplet volume (line-segment length in 1d), leading to the observed scaling behaviors. For  $L \approx l_-$ , the droplet becomes inhomogeneous, and the reaction only occurs at the boundary of the droplet up to a depth of length  $l_-$ . Thus an increase in droplet size does not lead to an increase in outflow of A-material, leading to the observed divergence of the stationary size for a critical inflow value (set here by  $\epsilon$ ).

In 1d, we can perturb the stationary line segment in two ways: A symmetric perturbation where the interface is moved outwards on both sides so that the width of the line segment changes and by an antisymmetric perturbation, which moves the interface on both sides in the same direction, so that the position of the line segment changes, see Fig. 6.1A. We find that the symmetric mode is stable for  $\nu_- \neq 0$ , while the antisymmetric mode is marginal. See Appendix E for the calculation.

We now consider the stability of stationary droplet bands in 2d. We can describe perturbations in the 2d system as

$$(\delta c, \delta L_1, \delta L_2) = \sum_n \epsilon_{s,n} \cos(qy) (\rho_{s,n}(x), L, L) e^{\mu_{s,n} t} \quad (6.2)$$

$$+ \sum_n \epsilon_{a,n} \cos(qy) (\rho_{a,n}(x), L, -L) e^{\mu_{a,n} t} \quad (6.3)$$

where we again can find a split into symmetric and antisymmetric modes with wave-vector  $q$ , amplitudes  $\epsilon_{s/a,n}$  and eigenvalues  $\mu_{s/a,n}$ . Symmetric modes describe a variation in the droplet width along the  $y$  axis, while antisymmetric modes describe a displacement of the droplet center in  $x$  direction which oscillates when moving along the  $y$  axis, while the droplet width stays constant. See Appendix E for details. Stationary band and deformations can be seen in Fig. 6.1B. Some typical results are shown in Fig. 6.2B. In the limit  $q \rightarrow 0$ , we find the same results as in the 1d case, with a stable symmetric and a marginal antisymmetric mode. For small  $\epsilon$ , both curves decrease for  $q > 0$ , so that all deformation modes are stable. For larger  $\epsilon$ , both the antisymmetric mode and the symmetric one reach a maximum at a very similar wavelength  $q$ , where the deformation modes are unstable. In Fig. 6.2C, the stability diagram of stationary bands is shown. It shows a region of stable bands for large reaction amplitude and small supersaturation, and a region of instability. For a fixed reaction amplitude, symmetric modes become unstable for larger supersaturation with  $\epsilon_{sym} \approx 2\epsilon_{asym}$ .

The stability of stationary droplet plates in 3d is described by the same modes as the 2d system, which are constant in the third dimension, compare Fig. 6.1C and Appendix E. In Fig. 6.2D, the stability diagram of stationary plates is shown. It is

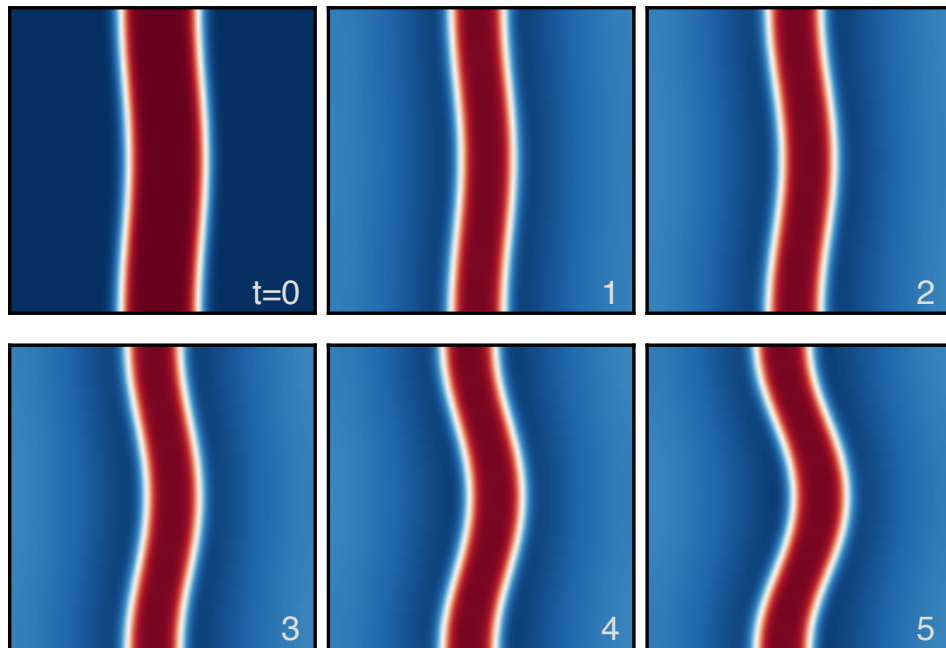


FIGURE 6.3: Numerical solution of the continuum droplet model of a droplet band with initial half-width  $L = 20w$  and shape perturbation of the antisymmetric mode with  $q = 2\pi/L_0$  with  $L_0 = 160w$ . Time between snapshots  $\Delta t = 8 \cdot 10^3 t_0$ . (Parameters:  $A = 2.5 \cdot 10^{-4}$ ,  $\epsilon = 0.3$ ,  $k_+/k_- = 1$ ,  $\nu_-(k_- \Delta c) = 1$ ,  $c_+^{(0)} = 0$ )

similar to the stability diagram of stationary bands, but with a larger unstable region, compare Fig. 6.2C.

We now compare the analytical results of the effective droplet model with numerical solutions of the continuum model. We consider the behavior of droplet bands in 2d for a reaction amplitude  $A = 2.5 \cdot 10^{-4}$  in a box of length  $L_0 = 160w$  with no-flux boundary conditions. We considered initial conditions with a band of (half-) width  $L = 20w$  with small initial deformations of symmetric and antisymmetric modes with different wave-vectors  $q$  with  $q = n\pi/L_0$  with integer  $n$ . We find no stationary bands for  $\epsilon \leq 0.1$ . For most initial conditions and values of  $\epsilon$ , initial bands vanish. For  $\epsilon = 0.1$  for initial perturbations with a long wave-length, bands shrink and divide into stable stationary droplet disks. The stationary width predicted by the effective droplet model for  $\epsilon = 0.1$  is  $L < 10w$ , and therefore close to the interfacial width of the continuum model - therefore, it is not surprising that the models deviate there. A comparison with stationary disks, see section E.6, shows that stationary disks are predicted to exist for  $\epsilon > 0.07$ , which corresponds well with the stationary droplets found. For  $\epsilon \leq 0.2$ , we all modes we investigated are stable. For  $\epsilon = 0.25$ , the antisymmetric mode with wavelength  $\lambda = L_0$ , with  $\lambda = 2\pi/q$ , is unstable. All other modes are stable. For  $\epsilon = 0.3$ , the antisymmetric modes with wavelengths  $\lambda = L_0/2$ ,  $L_0$  and

$3L/0/2$  are unstable. In Fig. 6.3, the dynamic behavior of mode  $\lambda = L_0$  is shown. We find a stationary (half-)width of approx.  $L \approx 0.7$ , close to the value predicted by the effective droplet model. The initial deformation increases, leading to a bending band with constant width. Comparison with Fig. 6.2C shows that the droplet bands in the continuum model are slightly more stable than predicted by the effective droplet model, but that the qualitative behavior matches well. In a simulation with larger box size  $L_0 = 512w$  and correspondingly also modes with smaller wave-vector  $q$ , we find similar results. In this case, we find stationary bands for  $\epsilon \geq 0.12$  and the mode with  $n = 2$  becomes unstable already for  $\epsilon \approx 0.15$ . Nucleation is found for  $\epsilon \geq 0.23$ . This fits the analytical results, compare Fig. 6.2B, where antisymmetric modes with long wavelengths become unstable for smaller supersaturation.

## 6.2 Stationary droplet disks in 2d

We now consider stationary disks in 2d, the equivalent of a spherical droplet in 3d. A sketch of a stationary disk and its deformations can be seen in Fig. 6.4. The calculation of stationary state and its stability can be found in Appendix E. In Fig. 6.4B, the stationary radii of droplet disks in 2d are shown in comparison to spheres. The lower solution of the nucleation radius  $\bar{R}_c$  is virtually the same as for spheres, since they have the same mean curvature. The larger stationary radius  $\bar{R}_s$  is approximately half the radius compared to the spherical case, with a logarithmic correction. The threshold supersaturation  $\epsilon_0$  below which no stationary solution exists, is larger than for the spherical case. The mode  $m$  describes deformations of the droplet disk, equivalent to mode  $l$  in spherical droplets. The eigenvalues of different deformation modes with  $m = 0$  to 3 are shown in Fig. 6.4C for the larger stationary radius as a function of the supersaturation for  $A = 10^{-4}$ . Their functional behavior is similar to the modes of the spherical droplet, which are shown in comparison. The  $m = 0$  mode describes changes in volume and is stable, the translational  $m = 1$  mode is marginal, and deformation modes become unstable consecutively for increasing supersaturation, starting with the elongational mode  $m = 2$ . The stability diagram of droplet disks with respect to supersaturation and reaction amplitude is shown in Fig. 6.4D. It shows regions of vanishing disks, stable stationary disks and unstable disks. Qualitatively, the results are quite similar to spherical droplets, but shifted towards larger supersaturations and smaller reaction amplitudes.

Numerical studies of 2d disks in the continuum model correspond well with the analytical predictions of the effective droplet model. For  $A = 2.5 \cdot 10^{-4}$ , droplet disks vanish for  $\epsilon \leq 0.05$ , stationary disks are seen for  $\epsilon \geq 0.1$ . The disks shape is unstable for  $\epsilon \geq 0.2$  with respect to the  $m = 2$  mode, corresponding to an elliptical deformation, while other modes remain stable. For  $\epsilon \geq 0.25$ , nucleation occurs. In Fig. 6.5, snapshots are shown for  $\epsilon = 0.22$ . We find that the droplet elongates into a long band-like structure with two disk-like structures at both ends which move apart, extending the band. For larger reaction amplitude  $A = 2.510^{-3}$ , stable stationary droplet with size of only a few times the interfacial width exist for  $\epsilon \geq 0.22$ , a larger

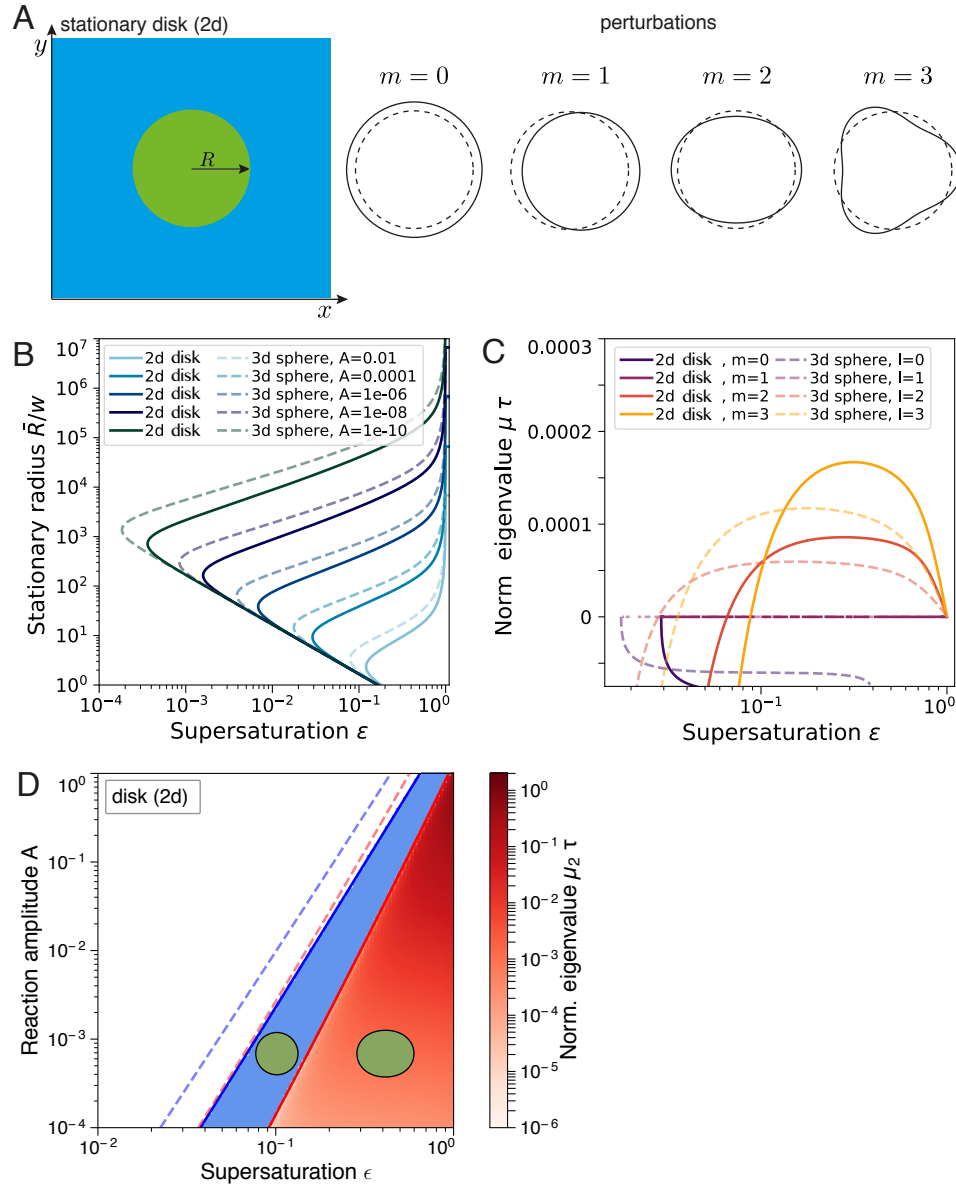


FIGURE 6.4: Stability of droplet disks in 2d. (A) Stationary droplet disk and its deformation modes in 2 dimensions. A stationary disk in 2d (left) can be perturbed with modes  $m$ , corresponding to a change in area ( $m = 0$ ), a translation ( $m = 1$ ), an elliptical deformation  $m = 2$  or higher order deformations. (B) Stationary disk radius as function of the supersaturation for different reaction amplitudes. Dashed lines show the equivalent results for spherical droplets in 3d. (C) Eigenvalues of modes  $m = 0, 1, 2, 3$  as function of the supersaturation for  $A = 10^{-4}$ . Dashed lines show the equivalent results of modes  $l = 0, 1, 2, 3$  for spherical droplets in 3d. (D) Stability diagram of droplet disks in 2d as function of the supersaturation and reaction amplitude for elongational mode  $l = 2$ . Blue color denotes stable stationary disks, the largest eigenvalue of unstable elongational deformations are shown in red (see color bar). For comparison, the existence of stationary droplets (blue dotted line) and their instability (red dotted line) for spherical droplets in 3d is shown. (Parameters:  $k_+/k_- = 1$ ,  $\nu_/(k_- \Delta c) = 1$ ,  $D_+/D_- = 1$ ,  $c_+^{(0)} = 0$ )

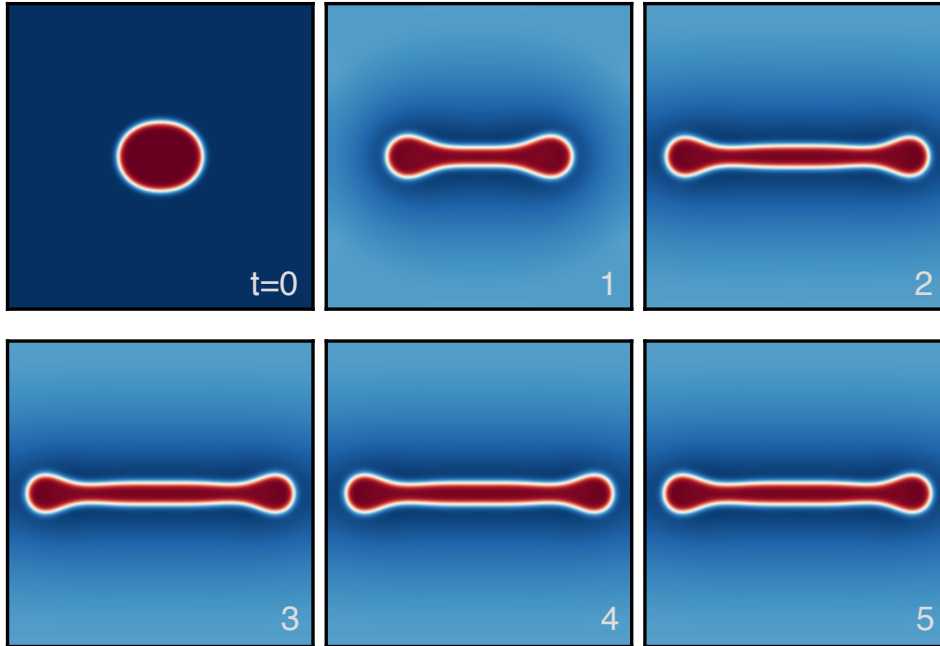


FIGURE 6.5: Numerical solution of the continuum droplet model of a droplet disk with initial shape perturbation. Time between snapshots  $\Delta t = 4 \cdot 10^4 t_0$ . (Parameters:  $A = 2.5 \cdot 10^{-4}$ ,  $\epsilon = 0.22$ ,  $k_+/k_- = 1$ ,  $\nu_-(k_- \Delta c) = 1$ ,  $c_+^{(0)} = 0$ . Simulation parameters: box length  $L_0 = 320w$ , initial radius  $R = 40w$ )

supersaturation compared to the case of a smaller reaction amplitude. For  $\epsilon \geq 0.3$ , nucleation of new droplets occurs. The dependency of the existence and stability of stationary disks on the supersaturation and the reaction amplitude thus agrees well with the prediction of the effective droplet model. For the parameters of Fig. 6.5, our simulations of stationary bands show that the band would be unstable with respect to antisymmetric deformations, so that it eventually might deform, leading to shapes similar to the ones shown in Fig. 6.3. For  $A = 2.5 \cdot 10^{-4}$ , no divisions seem to occur, but for smaller reaction amplitudes disks might divide. The simulation time increases strongly with lower reaction amplitudes – the dynamics becomes slower, and the stationary size increases, so that a larger simulation box is necessary (compare scaling analysis in chapter 3). Therefore, we did not test whether disks can divide for smaller reaction amplitudes.

### 6.3 Stationary droplet cylinders in 3d

In chapter 5, we have seen that spherical droplets may elongate and then form cylindrical shapes instead of dividing. Here we will investigate the stability of cylindrical droplets. In Fig. 6.6 the stationary state and different deformation modes are shown.

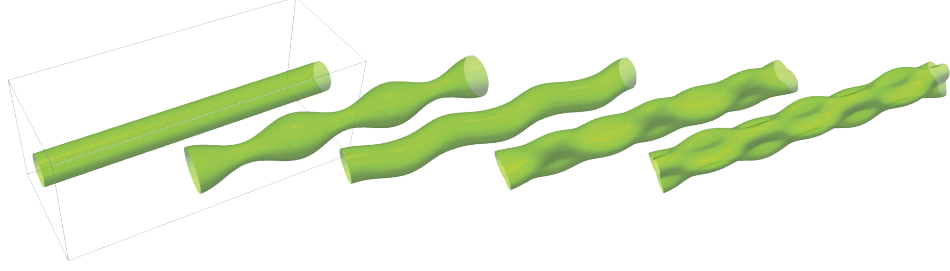


FIGURE 6.6: Cylinder with deformations of different modes. From left to right: undeformed cylinder, modes  $m = 0, 1, 2, 3$  (with constant wave-vector  $q$ ).

The stationary solution of the cylindrical droplet and its concentration field share features with the droplet disk in 2d. The functional form of the concentration field resembles that of a disk, but with a different mean curvature of the cylinder,  $H(\bar{R}) = 1/(2\bar{R})$ . In Fig. 6.7A, stationary droplet radii for the spherical and the cylindrical case are shown. The stationary solutions and their dependence on the parameters are very similar to the spherical case, except that the stationary cylindrical solutions are smaller by a factor of two. We can approximate the nucleation radius in the limit  $R \ll l_{\pm}$  as

$$R = \frac{\beta_+ \gamma}{2\nu_+ / k_+} \quad (6.4)$$

which is half the size of a spherical droplet. For the larger solution we find approximately

$$\left(\frac{R}{l_+}\right)^2 \ln \frac{R}{l_+} = -2 \frac{\nu_+}{\nu_-} \quad (6.5)$$

which, if the slowly varying logarithm is set to a constant,  $\ln(R/l_+) = -C$ , gives a square-root behavior, with

$$R = l_+ \sqrt{2C \frac{\nu_+}{\nu_-}}. \quad (6.6)$$

This is similar to the stationary radius found for spherical droplets,  $\bar{R} \approx l_+ \sqrt{3 \frac{\nu_+}{\nu_-}}$ , compare section 4.4.

We now consider the stability of stationary cylindrical droplets. The eigenfunctions can be chosen as

$$\begin{pmatrix} \delta c \\ \delta R \end{pmatrix} = \sum_{nlm} \epsilon_{nlm} \begin{pmatrix} P_{nmq}(r) \Phi_m(\varphi) Z_q(z) \\ \bar{R} \cdot \Phi_m(\varphi) Z_q(z) \end{pmatrix} e^{\mu_{nlm} t}. \quad (6.7)$$

Here, the functions  $\Phi$  and  $Z$  can be expressed as

$$\Phi_m(\varphi) = \begin{cases} \sin(m\varphi) \\ \cos(m\varphi) \end{cases}, \quad Z_q(z) = \begin{cases} \sin(qz) \\ \cos(qz) \end{cases} \quad (6.8)$$



with  $m \in \mathbb{Z}$  and  $q \in \mathbb{R}$ , as the angle  $\varphi$  lies between 0 and  $2\pi$  and cylinder in our discussion is infinite in the  $z$ -direction. This describes all possible deformations in one plane. Additional modes can be constructed by rotation  $\varphi' = \varphi - \varphi_0$  and translation  $z' = z - z_0$ . Due to the symmetry of the stationary shape, these do not give rise to different dynamical behavior. In Fig. 6.6, some deformation modes are shown. For  $q = 0$ , the modes change the cylinder cross-section with the perturbation modes  $m$  of a droplet disk, compare Fig. 6.4A. For  $q = 0$ , the mode  $m = 0$  corresponds to a constant change in the cylinder radius. A perturbation of the  $m = 0$  mode with  $q > 0$  is shown in the first panel of Fig. 6.6, showing variations of the cylinder radius with a spherical cylinder cross-section. The  $m = 1$  mode for  $q = 0$  corresponds to a translation of the cylinder, and for  $q > 0$  it has a constant cross-section, but the cylinder shape oscillates in one spatial direction, similar to a winding snake. For  $l = 2$  and  $q = 0$ , the cylinder is deformed in one direction, so that the cross-section has an elliptic shape. For  $q > 0$ , this deformation varies along the cylinder, so that the cross-section is deformed in one spatial direction, then the cross-section is spherical, then the cross-section is deformed in the orthogonal direction. For higher modes, the pattern of the  $l = 2$  mode continues, but instead of elliptic shapes, the shape of the cross-section shows more variations.

We can calculate the stability of these modes, see Appendix E. In Fig. 6.7B-D the stability diagrams of a stationary cylinder as a function of supersaturation and reaction amplitude are shown for different modes  $m$ . The maximal eigenvalue  $\mu(q_{max})$  of a mode  $m$  is shown (red color). The existence of stationary cylinders (blue line) is almost equal to the existence of spherical droplets (dotted blue line). For mode  $m = 0$  (panel B), we find that stationary cylinders with small supersaturations are unstable (red color). For increasing supersaturation, cylinders become stable with respect to deformations of mode  $m = 0$  (blue color), and then become unstable again. We find that the intermittent region of stability includes the parameter region where spherical droplets become unstable (dotted red line). The mode  $m = 1$  (panel C) is stable for small supersaturations, and becomes unstable at a supersaturation that is slightly smaller than the instability of spherical droplets. Larger modes become unstable consecutively for larger supersaturation, as demonstrated for mode  $m = 2$  (panel D). Additional detail is found in Appendix E. Considering all modes together, explicitly the  $m = 0$  and  $m = 1$  modes, we find that almost everywhere, cylindrical droplets are unstable, except for a small region for supersaturations smaller than  $\epsilon_2$ , the value where spherical droplets become unstable (dotted red line), where the  $m = 0$  and the  $m = 1$  modes both are stable.

In Fig. 6.8, the dynamic behavior of cylindrical droplets in the continuum model are shown. We consider a set of parameters where several modes are unstable, with initial conditions of a droplet cylinder with a small shape perturbation of mode  $m$  and wave-vector  $q = n\pi/L_0$ , where  $L_0$  is the length of the simulation box in the direction along the cylinder. A selection of unstable modes are shown in the figure. We find different dynamic behavior of the cylindrical droplets depending on the initial conditions. For changes of the droplet radius along the cylinder length, mode  $m = 0$ , the cylinder deforms and divides into separate droplets, which flatten and

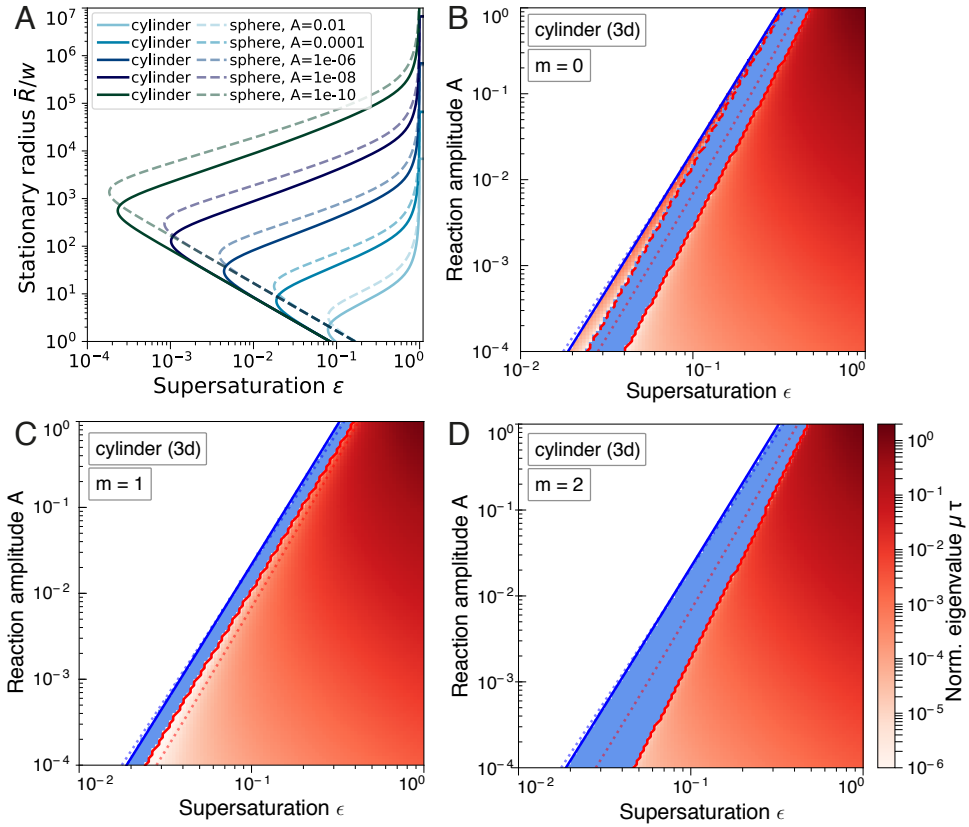


FIGURE 6.7: (A) Stationary radius  $\bar{R}$  of stationary spherical droplets (dashed) and stationary cylinders (lines) as function of the supersaturation  $\epsilon$  for different reaction amplitudes  $A$ . (B-D) Stability diagrams for different modes  $m = 0, 1, 2$  as function of the supersaturation  $\epsilon$  and reaction amplitude  $A$ . The blue line shows the threshold value above which stationary cylinders exist. The red line shows the onset of instability for the given mode  $m$  with any wavelength  $q$ . The dotted lines show the existence (blue) and stability (red) for spherical droplets. (Parameters:  $k_+/k_- = 1$ ,  $\nu_-(k_- \Delta c) = 1$ ,  $D_+/D_- = 1$ ,  $c_+^{(0)} = 0$ )

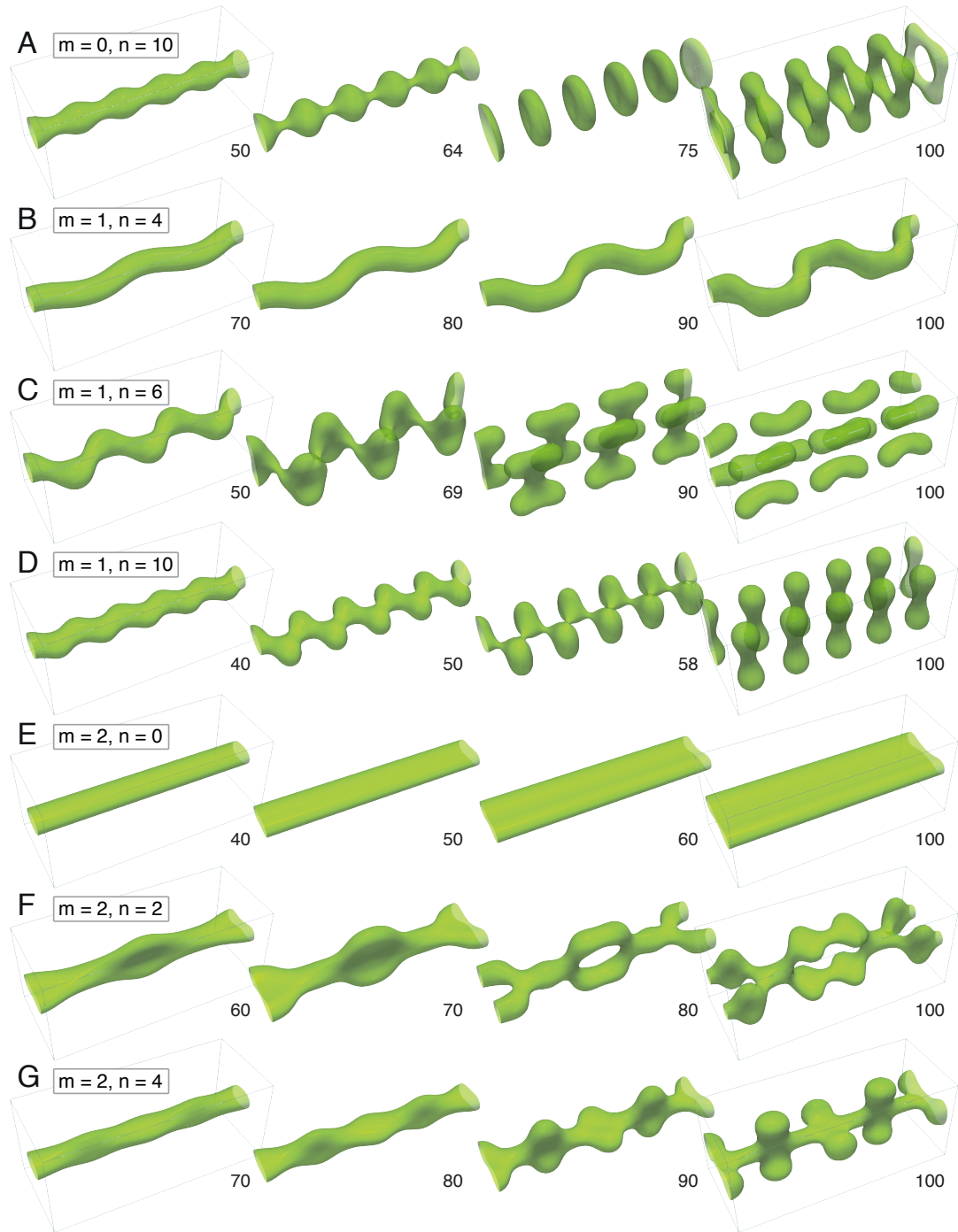


FIGURE 6.8: Snapshots of the dynamics of a droplet cylinder in the continuum model. The panels A-G show the time evolution of a droplet cylinder with initial shape perturbation of mode  $m$  and wave-vector  $q = n\pi/L_0$ . Time is given in units of  $\Delta t = 50t_0$ . Different initial conditions lead to different dynamical behavior. We find that cylinders can divide into smaller substructures (panel A, C and D), they can form connected elongated structures (panel A, B, F and G) and plates (panel E). (Parameters:  $A = 8 \cdot 10^{-3}$ ,  $\epsilon = 0.2$ ,  $k_+/k_- = 1$ ,  $\nu_/(k_- \Delta c) = 0.8$ ,  $c_+^{(0)} = 0$ . Simulation parameters: box length  $L_0 = 100w$ , box width  $W = 40w$ , initial radius  $R = 5$ .)

become tori (panel A). The size of tori is set by the box, and we find that the radius along the tori is unequal. The snake-like deformation modes with  $m = 1$  have different dynamical behavior for different wave-vectors. We find connected bent shapes, with a variation of the cylinder radius along the shape (panel B), , or a division of the deformed cylinder into separate droplet-like shapes (panel C and D), which may deform and divide again (panel C). A larger wave-vector with corresponding smaller deformation wavelength leads to denser droplets after the first division, so that no second division occurs (panel D). The mode  $m = 2$  with no variation along the cylinder,  $q = 0$ , develops into a plate-like structure, where the finite box-size sets the width of the plate. For finite wave-vector  $q$ , we find that the cylinder deforms into round flat shapes which are connected by thinner segments, which may either open in the center, forming a connected structure with rings (panel F), or a straight cylindrical structure with round structures branching off (panel G).

We therefore find a rich dynamical behavior of unstable stationary cylinders. The dynamics shows two typical features: Formation of connected structures with variations of the radius of the cross-section along the structure, and a division of such structures into droplet-like shapes. Occasionally, also the formation of flat plate-like regions is observed.

## 6.4 Summary

We found in this chapter that stationary states of chemically active droplets with different geometries exist in 1, 2 and 3 dimensions. These stationary shapes in 2 and 3 dimensions may, depending on parameter values, be stable or unstable with respect to shape deformations. We find that active chemical reactions tend to stabilize a finite size of droplets in the direction perpendicular to the interface not just for spherical droplets, but for all shapes considered here.

Let us now try to sum up the qualitative similarities and differences between the different geometries we considered in this chapter.

First, we find that stationary shapes without mean curvature do not have a critical nucleation radius in the effective droplet model. This holds of stationary line segments in 1d, bands in 2d and plates in 3d. In this model, flat stationary droplet shapes with decreasing width exist for vanishing supersaturation, while an upper cutoff  $\epsilon_\infty$  is set for larger supersaturations by  $R \approx l_-$ . In the continuum model where droplets have a finite interfacial width  $w$ , we find that droplet with predicted stationary sizes of a few  $w$  vanish instead.

Second, we find that a lower dimension tends to lead to more stable stationary structures, which become unstable only for larger supersaturation or smaller reaction amplitude. Comparing flat stationary droplet shapes, we find that line segments in 1d are always stable (meta-stable for the translational mode), and bands in 2d are more stable compared to plates in 3d, becoming unstable only for larger supersaturation. Equally, we find that disks in 2d become unstable only for larger values of supersaturation than spherical droplets.

Finally, let us comment on the qualitative behavior of unstable systems. We found that the antisymmetric modes become unstable first, and often dominate the observed dynamics for many of the stationary structures we discussed here. For these antisymmetric modes, the width of the structure remains constant, and the structure is only deformed, such as antisymmetric modes in bands and plates, and  $m = 1$  modes in cylinders. Such modes do not exist for disks and spheres, where instead elongational modes dominate the dynamical behavior. We have seen for stationary cylinders that the resulting dynamics is characterized by a competition between droplet division and the creation of elongated connected structures.

We have demonstrated in this chapter that the dynamic behavior of the stationary states of chemically active droplets is quite different from the behavior of passive droplet shapes. Passive droplet shapes, such as droplet cylinders (also called jets) are always unstable with respect to certain deformations variations of the cylinder radius along its length, corresponding to the  $m = 0$  mode we discussed for cylinders, see Rayleigh (1878); Eggers (1997). We found for chemically active cylinder droplets that the  $m = 0$  mode is not generally the most unstable one. For intermediate supersaturations only the  $m = 1$  mode corresponding to snake-like deformations is unstable, and other modes become unstable for large supersaturations. We even find regimes where the cylindrical shape is stable with respect to all shape deformations, where the Plateau-Rayleigh instability is suppressed by the active chemical reactions in our system. This is due to the fact that the instability of chemically active droplet shapes is a flux-driven instability as for spherical active droplets, and not driven by the surface tension as in the passive case. We therefore again see in this chapter that chemically active droplets may behave in novel ways that demonstrate their out-of-equilibrium nature.



In the previous chapters, we considered the dynamics of chemically active droplets with a minimal model of two components which phase separate, and are converted into each other by nonequilibrium chemical reactions so that inside the droplet the outer material is created, and a supersaturation of droplet material is maintained outside. We found that in the limit of large viscosity such droplets have a stationary size that can be unstable with respect to shape changes so that droplet can divide. Generally, such droplet dynamics is a hydrodynamic problem because surface tension in non-spherical droplets drives hydrodynamic flows that redistribute material and deform the droplet shape, see Rayleigh (1892); Chandrasekhar (1981); Constantin et al. (1993); Paulsen et al. (2014). In this chapter, we study the influence of hydrodynamic flows on the shape changes of chemically active droplets. We show that chemical reactions in active droplets can perform work against surface tension and flows, giving rise to a shape instability that can result in droplet division even in the presence of hydrodynamic flows.

The content of this chapter has been published in Seyboldt and Jülicher (2018).

## 7.1 Stability of droplets with hydrodynamic flows

Until now, we ignored the contribution of hydrodynamic flows in the shape dynamics of deformed droplets by considering the limit of infinite viscosity,  $F \rightarrow \infty$  with normalized viscosity  $F = w\eta_-/(\gamma\tau)$  inside the droplet, and a finite ratio  $\eta_+/\eta_-$  of the viscosities in both phases.

Here we consider stationary droplets and their stability with the inclusion of hydrodynamic flows, for the full set of equation, Equations (3.20)-(3.31), of the effective droplet model. For this, we solve the Stokes equation of an incompressible

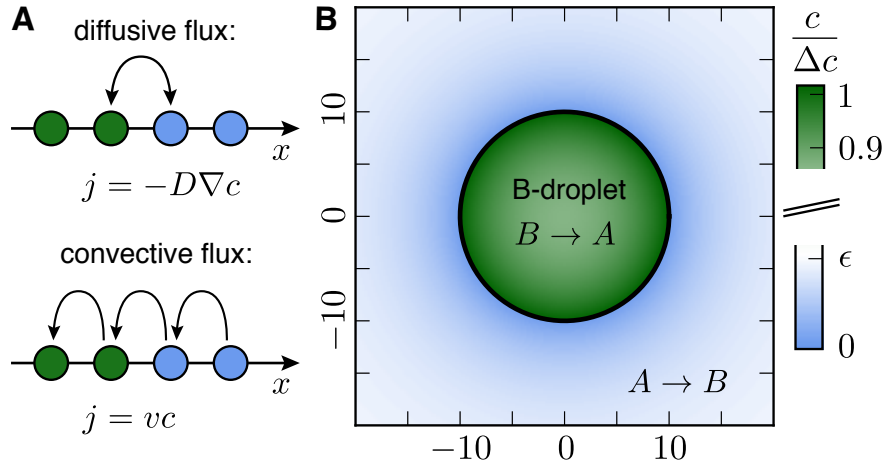


FIGURE 7.1: Chemically active droplet described by an effective droplet model. (A) Sketch to illustrate diffusive and convective fluxes (in 1d). In a diffusive flux, particles (colored spheres) exchange positions, leading to a transport of material without net momentum which decreases concentration differences between volume elements, described by diffusive flux  $j = -D\nabla c$ . In a convective flux, all particles move in one direction (in 1d) so that a net momentum exists, and the particle movement is independent of the concentration within the phases, with a convective flux  $j = vc$ . (B) Concentration field  $c$  of the droplet material B (blue and green color) of a stationary droplet (interface in black). Chemical reactions  $B \rightarrow A$  create a sink of droplet material B in the droplet, and reactions  $A \rightarrow B$  create a supersaturation  $\epsilon$  of droplet material in the A-rich phase outside. This creates concentration gradients of B, which drive diffusion fluxes of droplet material, while A flows in the opposite direction. The stationary droplet size results from the balance of the fluxes across the interface. (Parameters:  $\epsilon = 0.176$ ,  $A = 10^{-2}$ ,  $\eta_+/\eta_- = 1$ ,  $k_+/k_- = 1$ ,  $\nu_-(k_- \Delta c) = 1$ ,  $D_+/D_- = 1$ ,  $\beta_- = \beta_+$ ,  $c_+^{(0)} = 0$ )

fluid for both phases separately, with jump conditions across the interface. The fluid flow is driven by stress differences at different positions at the droplet interface. The flux of the concentration field in both phases then has two contributions, a diffusive and a convective one. These are sketched in Fig. 7.1B. The diffusive flux is driven by gradients in concentration, and is created by an exchange of molecules between neighboring volume elements, without any net momentum. The convective flux is created by the fluid moving with hydrodynamic velocity  $v$ , so that the concentration field gets advected and thus moves along the flow, so that the concentration within a volume element changes. The hydrodynamic velocity in the effective droplet model is independent of the concentration field and only depends on the shape of the droplet.

First, we find that hydrodynamic flows do not influence the stationary state of a spherical droplet. We find nonequilibrium steady state solutions to Equations (3.20)-(3.31) with a spherical droplet of stationary radius  $\bar{R}$  and stationary concentration



field  $\bar{c}(r)$ , where  $r$  is the radial coordinate, see Appendix F.1. The stationary pressure  $\bar{p}$  exhibits a jump  $2\gamma/\bar{R}$  across the interface and no hydrodynamic flows exist,  $\bar{\mathbf{v}} = 0$ . An example for a stable non-equilibrium steady state with steady state concentration profile inside and outside the droplet of radius  $\bar{R}$  is shown in Fig. 7.1.

As in the previous chapters, we discuss the properties of the system as a function of external supersaturation  $\epsilon = \nu_+/(k_+\Delta c)$  and the dimensionless reaction rate  $A = \nu_-\tau/\Delta c$  inside the droplet. The supersaturation is in our system generated by reactions outside the droplet and in steady state corresponds to the concentration for which  $s_+ = 0$ . Here,  $\Delta c = c_-^{(0)} - c_+^{(0)}$  and we have introduced the time scale  $\tau = w^2/D_+$ , where  $w = 6\beta_+\gamma/\Delta c$  is a characteristic length scale. Let us briefly recap the properties of the stationary solutions. The stationary radii as a function of supersaturation  $\epsilon$  are shown in Fig. 7.2A-C as solid lines for different values of  $A$ . For values of  $\epsilon$  smaller than a threshold value  $\epsilon_0$ , no stationary radius exists. For values  $\epsilon > \epsilon_0$  two steady state radii  $\bar{R}_c$  and  $\bar{R}_s$  exist, which become equal at  $\epsilon_0$  where they approach a value  $\bar{R}_0$ . The smaller steady state radius  $\bar{R}_c$  is a critical nucleation radius similar to the critical droplet radii found in passive systems. The larger radius denoted  $\bar{R}_s$  stems from the interplay of phase separation and chemical reactions, Zwicker (2013); Zwicker et al. (2015, 2017). As the supersaturation reaches a value  $\epsilon_\infty = \sqrt{(D_-k_-)/(D_+k_+)}\nu_-/(k_-\Delta c)$ , the stationary radius  $\bar{R}_s$  diverges.

We discussed in 4 simple expressions for the stationary radii in the limit of small  $A$  while keeping the ratios  $\nu_-/(k_-\Delta c)$  and  $k_+/k_-$  of reaction parameters fixed. In this limit, the chemical reactions fluxes vanish as  $s_\pm \propto A$  and the threshold value  $\epsilon_0$  vanishes as  $\epsilon_0 \propto A^{1/3}$ . The critical nucleation radius then behaves as  $\bar{R}_c \simeq w/(6\epsilon)$  and the larger steady state radius  $\bar{R}_s \simeq w(3\epsilon A)^{1/2}$  where  $\epsilon_0 \ll \epsilon \ll \epsilon_\infty$ , see Fig. 7.2B and Appendix F.2.

The steady state solutions are independent on the fluid viscosity, however the droplet dynamics is affected by hydrodynamic effects. We now investigate the role of hydrodynamic flows on chemically driven shape instabilities that can give rise to droplet division. We perform a linear stability analysis at the stationary state given by  $\bar{X} = (\bar{c}, \bar{R}, \bar{p}, \bar{\mathbf{v}})$  for small perturbations  $\delta X = (\delta c, \delta R, \delta p, \delta \mathbf{v})$ . The dynamics of these perturbations can be represented using eigenmodes

$$\delta X = \sum_{n,l,m} \epsilon_{nlm} X_{nlm} e^{\mu_{nlm} t}, \quad (7.1)$$

with  $X_{nlm} = (c_{nl} Y_{lm}, \bar{R} Y_{lm}, p_l Y_{lm}, \mathbf{v}_{lm})$ , where  $Y_{lm}(\theta, \phi)$  are spherical harmonics with angular mode indices with  $l = 0, 1, \dots$  and  $m = -l, \dots, l$ . The index  $n = 0, 1, \dots$  denotes radial modes. The eigenmodes exhibit an exponential time dependence with a relaxation rate given by the eigenvalue  $\mu_{nlm}$ . The mode amplitudes are denoted  $\epsilon_{nlm}$ . The concentration modes are characterized by the radial functions  $c_{nl}(r)$ . The pressure modes are described by  $p_l(r)$  and the velocity modes  $\mathbf{v}_{lm}(r, \theta, \varphi)$  can be expressed as

$$\mathbf{v}_{lm} = v_{lm}^r \mathbf{Y}_{lm} + v_{lm}^{(1)} \boldsymbol{\Psi}_{lm} + v_{lm}^{(2)} \boldsymbol{\Phi}_{lm}. \quad (7.2)$$

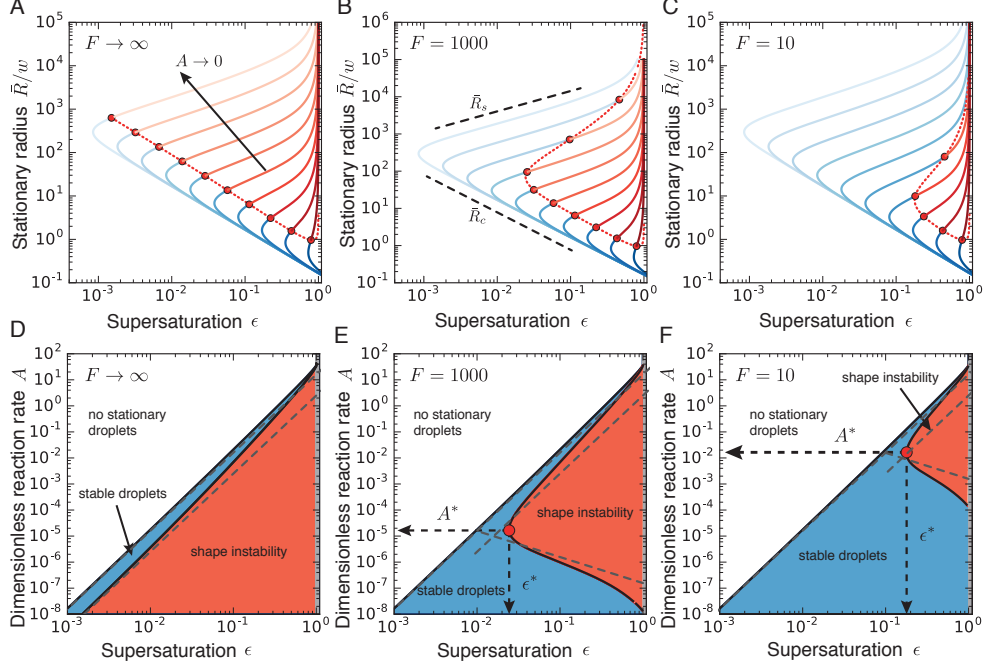


FIGURE 7.2: Stationary radii and onset of shape instability. A–C: Stationary radius as a function of supersaturation for different reaction amplitudes  $A = 10^{-8}, 10^{-7}, \dots, 10^1$ . The stationary radii (lines) are independent of the dimensionless viscosity  $F = w\eta_-/(\gamma\tau)$ , while the onset of instability (red dots, connected by dotted red line) for the different curves varies in the three figures, which show dimensionless viscosities  $F = \infty, 1000, 10$  (left to right). The blue line colors mark stable, the red ones unstable stationary radii with respect to the elongational  $l = 2$  mode. In panel B the scaling behavior of the nucleation radius  $\bar{R}_c$  and the stationary radius  $\bar{R}_s$  are indicated. D–F: Stability diagram of stationary droplets of size  $\bar{R}_s$ , as a function of reaction amplitude  $A$  and supersaturation  $\epsilon$  for different dimensionless viscosities  $F = \infty, 1000, 10$  (left to right). For small supersaturation and large reaction amplitudes, no stationary radius exists (white). For large supersaturation, the stationary radius diverges (gray). In the region between these regimes, the stationary solution can be stable (blue) or unstable (red) with respect to shape perturbations of the  $l = 2$  mode. For decreasing  $F$ , the stable regime grows, and the minimal supersaturation  $\epsilon^*$  at which an instability can be found increases, as well as the corresponding reaction amplitude  $A^*$ . The scaling relations (dashed lines) for the regime of stable droplets and the onset of instability are indicated, with prefactors according to F.2. (Parameters:  $\eta_+/\eta_- = 1$ ,  $k_+/k_- = 1$ ,  $\nu_-/(k_- \Delta c) = 1$ ,  $D_+/D_- = 1$ ,  $\beta_- = \beta_+$ ,  $c_+^{(0)} = 0$ )

where  $\mathbf{Y}_{lm}(\theta, \varphi) = \mathbf{e}_r Y_{lm}$ ,  $\mathbf{\Psi}_{lm}(\theta, \varphi) = r \nabla Y_{lm}$  and  $\mathbf{\Phi}_{lm}(\theta, \varphi) = \mathbf{e}_r \times \mathbf{\Psi}_{lm}$  are vector spherical harmonics Barrera et al. (1985) and the radial functions  $v_{lm}^r(r)$ ,  $v_{lm}^{(1)}(r)$  and  $v_{lm}^{(2)}(r)$  characterize the velocity field. The radial functions can be obtained by solving the linearized dynamic equations using the corresponding boundary conditions, see Appendix F.1. The Stokes equation can be solved for a given shape perturbation independent of the concentration field so that the velocity field and pressure field is independent of the radial mode  $n$ . The radial part of the concentration field obeys a Helmholtz equation with an inhomogeneity that stems from hydrodynamic flows. The homogeneous part is solved by modified spherical Bessel functions and the inhomogeneous solution can be found using Greens functions. Using the dynamic equation for the shape changes of the droplet Eq. (3.31), we obtain an equation for the eigenvalue  $\mu_{nlm}$ ,

$$\mu_{nlm} = \frac{v_l^r(\bar{R})}{\bar{R}} + \frac{D_+}{\Delta c} \left( \bar{c}''(\bar{R}_+) + \frac{c'_{nl}(\bar{R}_+)}{\bar{R}} \right) - \frac{D_-}{\Delta c} \left( \bar{c}''(\bar{R}_-) + \frac{c'_{nl}(\bar{R}_-)}{\bar{R}} \right). \quad (7.3)$$

Here, the primes denote radial derivatives. Note that Eq. (7.3) is an implicit equation for the eigenvalues  $\mu_{nlm}$  because the radial concentration modes  $c_{nl}(r)$  depend on  $\mu_{nlm}$ , see Appendix F.1. Eq. (7.3) is independent of the index  $m$ , therefore the degeneracy of an eigenvalue  $\mu_{nl}$  is at least  $2l + 1$ . The description of the shape is the same as in the previous chapters: When all  $\mu_{nl}$  are negative, the spherical shape is stable. The modes with  $l = 0$  correspond to changes in droplet size without flows. They are always stable for  $\bar{R} = \bar{R}_s$  and unstable for  $\bar{R} = \bar{R}_c$ . Thus droplet smaller than  $\bar{R}_c$  will vanish and droplets larger will grow towards the size  $\bar{R}_s$ . Thus we consider the stability of  $\bar{R} = \bar{R}_s$  in the following. The modes with  $l = 1$  do not involve shape deformations of the droplet and are thus not associated with flows. There always exists a marginal mode with  $\mu_{l=1} = 0$  corresponding to overall translations where the droplet and all concentration fields are displaced and then stay in the new position. Here we consider shape instabilities for which a mode with  $l > 1$  becomes unstable. Because shape deformations induce flows, this instability depends on the dimensionless viscosity  $F = w\eta_-/(\gamma\tau)$ , as well as the ratio of viscosities in the two phases,  $\eta_+/\eta_-$ .

The hydrodynamic flows influence the solution in two ways. First, they contribute a term to the concentration field, which has a different spatial form due to the convection. Numerically, we find that this term tends to be rather small in the cases discussed here. Second, the hydrodynamic flows advect the droplet interface, so that the flows directly influence the shape dynamics. This is reflected by the first term in Eq. (7.3). For the passive flows we consider, the hydrodynamic flows always oppose the droplet deformation. The modes of the flow field depends on only a few quantities in our linear description: The normalized viscosities, represented by  $F = w\eta_-/(\gamma\tau)$  and  $\eta_+/\eta_-$ , the deformation mode  $l$  and the relative distance from the droplet interface, via  $r/\bar{R}$ . The inverse of the normalized viscosity  $F$  can also be interpreted as a

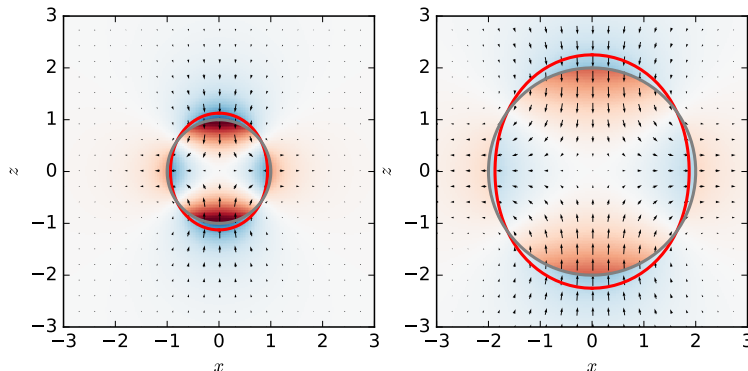


FIGURE 7.3: Pressure and velocity profiles for droplets with different size but equal deformation of mode  $l = 2$  within the linear analysis of the effective droplet model. Different pressure profiles (red: increase in pressure, blue: decrease) lead to equal velocities (arrows) at the interfaces in both examples. The undeformed droplets are shown in gray, the deformed in red. (Parameters: Deformation  $\epsilon_{020} = 0.1$ )

characteristic velocity, with  $v \propto 1/F$ . The perturbation modes of the pressure and hydrodynamic flow for the  $l = 2$  mode are shown in Fig. 7.3 for two droplets of different sizes, but the same relative deformation (red shapes) in an infinite system. Due to the linear analysis, the fields are evaluated in the regions of the undeformed droplet (gray). We see that the pressure modes of the deformation are stronger in the smaller droplet. The Laplace pressure at the tips of the deformed droplet is larger inside, and smaller outside, while the reverse is true at the sides of the droplet. The flow field has the same amplitude in both examples (compare the lengths of the arrows), and points against the deformation, flowing inward at the tips and outward at the sides.

We now discuss the influence of hydrodynamic flows on the stability diagram with respect to  $\epsilon$  and  $A$ . If we increase the supersaturation  $\epsilon$  while keeping the other parameters fixed, the steady state can become unstable with respect to the mode  $l = 2$  for a critical value  $\epsilon = \epsilon_c$ . In Fig. 7.2A-C, the onset of instability  $\mu = 0$  for the largest eigenvalue  $\mu$  of the stationary radius is shown as a red dot, and unstable radii are indicated by red lines. Different lines correspond to different supersaturations, and the panels show different values of  $F$ . In Fig. 7.2D-E, the corresponding stability diagrams of stationary droplets are shown as a function of the supersaturation and the reaction amplitude for different values of  $F$ . For large  $A$  and small  $\epsilon$ , no stationary radius exists (white regions), so that any droplet would shrink and disappear. For large  $\epsilon$ , the stationary state diverges (gray regions). Spherical droplets are stable in the blue regions. Stationary spherical droplets are unstable inside the red region, the surrounding black line marks the shape instability with respect to the  $l=2$  mode. The region where spherical droplets undergo a shape instability exists for  $\epsilon \geq \epsilon^*$ , which depends on  $F$ . The value of  $A$  for which the shape instability occurs at  $\epsilon = \epsilon^*$  is

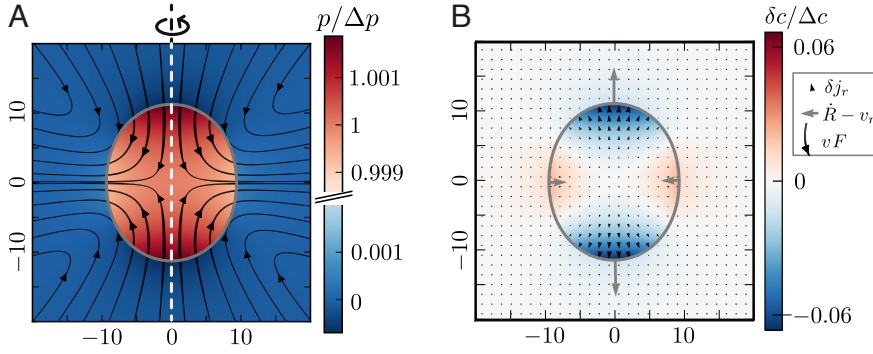


FIGURE 7.4: Droplet deformation due to hydrodynamic flows (A) and diffusive fluxes (B). (A) Flow and pressure profile of a droplet of stationary radius  $R/w = 10$  with deformation of the  $l = 2, m = 0$  mode within the linear analysis of the effective droplet model. The profiles are symmetric around the deformation axis. The pressure inside and outside is shown in red/blue (see legend), while streamlines show the normalized flow  $vF$ , where the thickness of the streamlines indicates regions of stronger/weaker flow. (B) Perturbation of the concentration field (color) and associated radial diffusive flow (black arrows) without hydrodynamic flows,  $F \rightarrow \infty$ . The interface movement due to the diffusive flows (gray) shows that the droplet is unstable. For small reaction amplitude  $A$ , the hydrodynamic and diffusive flows can simply be added to yield the interface movement (compare scaling analysis). (Parameters:  $\epsilon = 0.176$ ,  $A = 10^{-2}$ ,  $\eta_+/\eta_- = 1$ ,  $k_+/k_- = 1$ ,  $\nu_/(k_- \Delta c) = 1$ ,  $D_+/D_- = 1$ ,  $\beta_- = \beta_+$ ,  $c_+^{(0)} = 0$ )

denoted  $A^*$ , see Fig. 7.2. Comparing Fig. 7.2E-F with D, we see that hydrodynamic flows introduce a lower cutoff for the instability with respect to the reaction rate  $A$  which increases for an increasing influence of hydrodynamic flows, corresponding to decreasing value of  $F$  and also depends on supersaturation  $\epsilon$ . For larger reaction rates,  $A > A^*$ , the stability diagram is mostly independent of the hydrodynamic flows. Both the reaction rate  $A$  and the supersaturation  $\epsilon$  are quantities that are intrinsically nonequilibrium and are driven by an energy input. We can thus interpret the results as a competition between nonequilibrium driving which creates the shape instability, and hydrodynamic flows which tend to bring the system towards equilibrium. For strong nonequilibrium driving, with  $A$  and/or  $\epsilon$  large enough, and small hydrodynamic flows, we therefore find the instability even in the presence of hydrodynamic flows.

## 7.2 Scaling of the hydrodynamic stability diagram

For small  $A$ , the onset of instability can be described by simple scaling behaviors that capture the competition between flows and nonequilibrium reactions. We find that in this limit the contribution of the advection to the concentration field vanishes, so that only the advection of the interface enters. Therefore, the dynamics of the droplet interface is a simple sum of its advection with the hydrodynamic flows and

the contribution of the flux-driven instability of the concentration field, see Fig. 7.4. For the scaling of the stationary radius  $\bar{R}$  with  $\hat{R} = \bar{R}A^{1/3}/w$ ,  $\hat{\epsilon} = \epsilon A^{-1/3}$  and  $\hat{l}_{\pm} = l_{\pm}A^{1/2}$ , we find for the eigenvalue

$$\hat{\mu}_{nlm} = -\frac{d_l A^{-2/3}}{\hat{R}} \frac{2}{F} + \frac{2}{3}(l-1) - \frac{D_+ (l-1)g_l}{D_- \hat{R}^3} + O(A^{1/6}). \quad (7.4)$$

The first term describes the influence of hydrodynamic flows on the instability. The remaining two terms describe the instability without hydrodynamic flows. The supersaturation is hidden in parameter  $\hat{R}$ , via Eq. (4.21). For the larger solution  $\bar{R}_s$ , a larger supersaturation corresponds to a larger stationary radius, with approximately  $\hat{R} \simeq \sqrt{3\hat{\epsilon}}$ . The last two terms capture the competition of surface tension and the flux-driven instability for the concentration field, where larger supersaturation increases the instability. The first term that describes the hydrodynamic flows is negative (for  $d_l > 0$ ), implying a stabilizing influence. The term decreases in amplitude for increasing supersaturation, increasing reaction amplitude, or increasing normalized viscosity.

We can analyze Eq. (7.4) in detail, see Appendix F.2. We find  $\epsilon^* \propto F^{-1/2}$  and  $A = A^*$  with  $A^* \sim F^{-3/2}$  (compare Fig. 2E-F). For  $A < A^*$ , hydrodynamic flows govern the onset of instability which occurs at a value of  $A$  which behaves as  $A \propto \epsilon^{-1}F^{-2}$ . For  $A > A^*$ , hydrodynamic flows can be neglected as compared to diffusion fluxes and the onset of instability occurs for  $A \propto \epsilon^3$ . These two scaling regimes are indicated in in Fig. 7.2D-F by dashed lines. A derivation of these results including prefactors is given in F.2.

### 7.3 Droplet division with hydrodynamic flows

We next address the question whether the shape instability found in the linear stability analysis can indeed give rise to droplet divisions in the presence of hydrodynamic flows in the nonlinear regime of the dynamics. We use the continuum model introduced in Chapter 3, which is based on the Cahn-Hilliard model, see Cahn and Hilliard (1958), for phase separation dynamics, extended to include chemical reactions and hydrodynamic flows, that can capture topological changes of the interface. We include chemical reactions via a source term linear in the concentration as well as advection by the hydrodynamic flow which is described by the incompressible Stokes equation. Using a semi-spectral method, Chen and Shen (1998), we obtain numerical solutions in a cubic box with no-flux boundary conditions, see Appendix D.2.2.

Starting from a weakly deformed spherical droplet, we find regimes where the droplet disappears, where it relaxes to a stable spherical shape and where it undergoes a shape instability, consistent with the linear stability analysis of the effective droplet model. The transitions between these regimes occur for parameter values close to those predicted by the linear stability analysis, compare Appendix D.3. In the unstable regime, droplets typically divide. This shows that the droplet division reported previously can also occur in the presence of hydrodynamic flows. Fig. 7.5 shows snapshots of the droplet shape together with corresponding hydrodynamic flow fields on

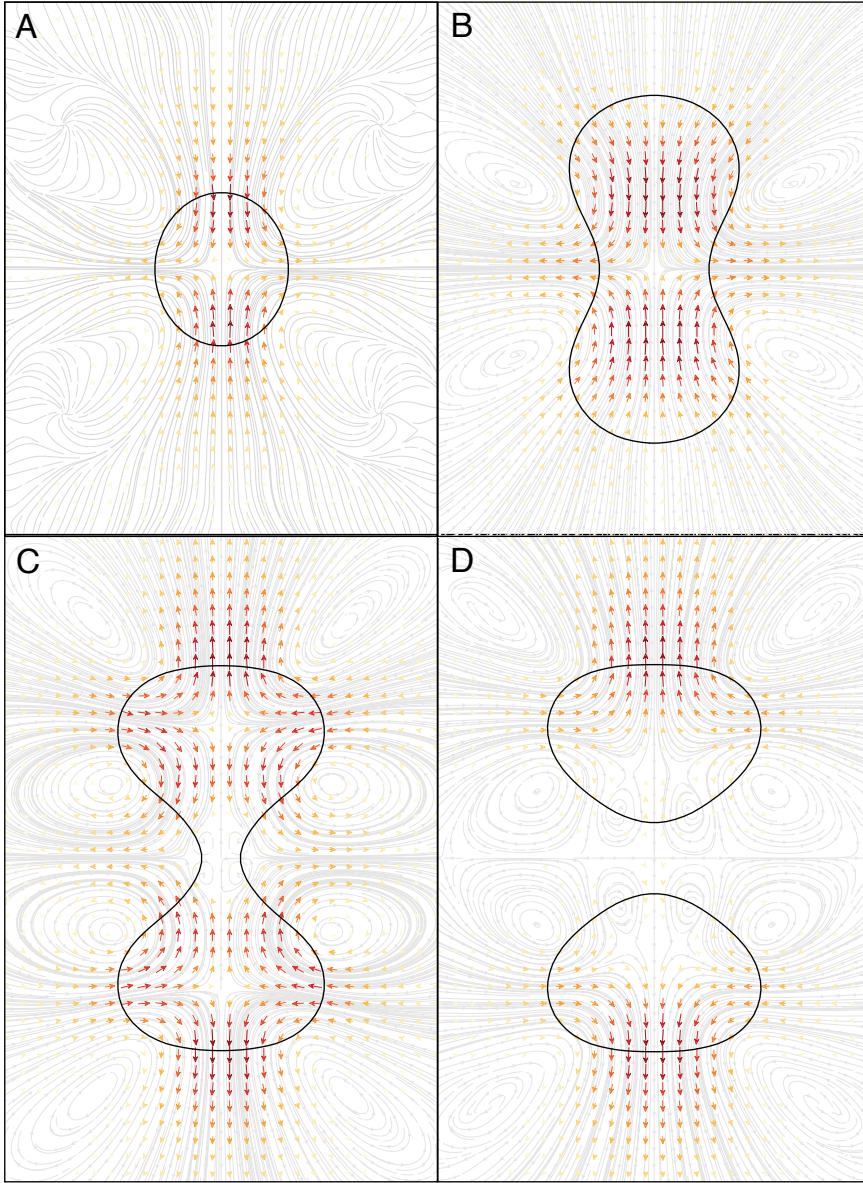


FIGURE 7.5: Numerical solution in 3d of an extended Cahn-Hilliard model with chemical reactions and hydrodynamic flows reveals that droplets can divide despite the presence of hydrodynamic flows. Panels A-D correspond to time points  $t/\tau = 100, 2100, 2700, 2800$ , respectively, where  $\tau = w^2/D$  is a diffusion time, with diffusion constant  $D$  and interfacial width  $w$ . The dynamic equations were solved numerically in a three-dimensional box. Shown are two-dimensional cross-sections of the droplet shape (black) together with streamlines (gray). Arrows (colored) indicate the direction and magnitude of the flow (normalized by respective maximal velocities  $v_{max} \cdot w/D = 0.0016$ (in A),  $0.0048$ (B),  $0.0034$ (C) and  $0.0047$ (D) ). (Parameters:  $F = 24$ ,  $A = 8 \cdot 10^{-3}$ ,  $\epsilon = 0.2$ ,  $\eta_-/\eta_+ = 1$ ,  $c_+^{(0)}/\Delta c = 0$ ,  $k_+/k_- = 1$ ,  $\nu_-/(k_- \Delta c) = 0.8$ )



the symmetry plane of a dividing droplet at different times. At early times when the droplet deformation is weak, the flow field is similar to the  $l = 2$  mode obtained from the linear theory, Fig. 7.5 A. As the droplet elongates and its waistline shrinks, the flow field becomes more complex, see Fig. 7.5 B,C. The flow field shown in Fig. 7.5 C exhibits two additional vortex lines that form rings around the axis of rotational symmetry. Similarly, after division, two further vortex rings occur, see Fig. 7.5 D. Interestingly, for small deformations the hydrodynamic flow opposes the directions of interface motion at the main droplet axes, see Fig. 7.5 A,B. For larger deformations at later times the flow switches its direction along the long droplet axis where it assists interface motion. At the waistline, the flow velocity becomes small, see Fig. 7.5 C. After division, the flow field between the daughter droplets has very small magnitude, while strong flows at the outer sides move the droplets apart Fig. 7.5 D.

This example shows that division of active droplets can occur even if hydrodynamic flows that oppose division are taken into account. Because flows act in opposition to the initial deformation of the sphere, the linear stability analysis already provides the key information of whether droplet division can occur for a given value of dimensionless viscosity  $F$ , see Fig. 7.2.

## 7.4 Summary

We have shown that the spontaneous division of chemically active droplets involves mechanical work against surface tension as droplets deform. Active droplets thus can transduce chemical energy to mechanical work and droplet division is therefore a mechano-chemical process. The surface tension of the droplet creates pressure gradients as the droplet becomes non-spherical that lead to hydrodynamic flows. Because the flows generated act against the shape deformation, droplets divide only for sufficiently large viscosity or sufficiently small surface tension and sufficiently large reaction rates. We show that the dependence of the onset of stability on parameters is captured for small reaction fluxes by simple scaling relations.



We will now discuss the minimal model presented in this thesis and its dynamic behavior in the context of the origin of life. For this we present a list of properties that might constitute a protocell. Then we discuss chemically active droplets as a model for such a protocell. Finally, we estimate parameter values of the model for realistic systems to assess in which regimes the droplet division might be observable. We close with a short discussion of possible realizations.

Parts of this chapter has been published in Zwicker et al. (2017) and Seyboldt and Jülicher (2018).

## 8.1 Protocells – simple precursors of biological cells

Living systems today consist of cells that can grow and divide. Cells take up matter from the outside world to grow, they release waste products, and they are able to divide, creating more cells. All of these processes are organized, performed and regulated by a large network of chemical reactions with the participation of a great number of different biological molecules such as proteins, RNA and DNA.

We might imagine that during the evolution of life, precursors of cells (called protocells) formed, which had already some of the properties of cells, but with a simpler structure and reaction network, and with less precise control over the processes occurring inside. Since we do not know which property of a cell evolved at which point in time, we propose instead the following list of minimal properties that make cells alive:

- The protocell should be a distinct chemical environment. Inside the protocell should be different molecules than outside – these could be thought of as organic molecules or precursors thereof – and different chemical reactions than

outside (the 'metabolism' of the protocell). Cells today are homeostatic, that is, they can regulate themselves to have constant conditions for the reactions inside. Therefore a controlled or regulated environment would be a useful property for a protocell to have as well.

- The protocell should consume food and produce waste. All cells today need food in the form of energy and certain materials, and the reactions inside them (their metabolism) convert food into energy carriers such as ATP and into building blocks for the cell, and produce a low-energetic waste that leaves the cell. If cells don't metabolize food, they are dead or in stasis. Therefore the steady supply of food and the metabolic reactions in the cell can be considered as one of the most important properties of living systems.
- The system of protocell and environment should be a non-equilibrium system. As the protocell consumes the food, new food should be created outside it, and the waste should dissipate. Living systems in a closed system, such as bacteria in a Petri dish, die after using up all food.
- The protocell should be able to divide. If a protocell could not divide, local fluctuations might destroy it. A dividing cell however, can multiply, change on the way (thus providing a simple mechanism for evolution) and conquer new territories. Therefore, to have a transition from a protocell to cells today, division is a necessary property.

This short list neglects many properties of cells that are important today, such as a membrane or DNA, but concentrates instead on the most abstract properties of life. The list of properties also does not specify what or how complex the participating molecules should be, and therefore the order of the formation of life is left open, so that protocells could have formed from simple inorganic material, or after a long time of chemical evolution of complex molecules in an RNA world or out of proteins, RNA and DNA.

## 8.2 Discussion of chemically active droplets as protocells

We will now consider droplets with chemical reactions as a simple model system for such protocells.

### 8.2.1 Model of chemically active droplets as protocells

We propose a simple model for a protocell that consists of a droplet of organic material. We describe the material of the droplet by an effective component  $D$  that phase separates from the surrounding solvent  $S$  (typically water) and forms a droplet. Chemical reactions create droplet material from nutrient  $N$ ,  $N \rightarrow D$ , predominantly inside the droplet. Over time, the droplet material decays into low energy waste  $W$ ,

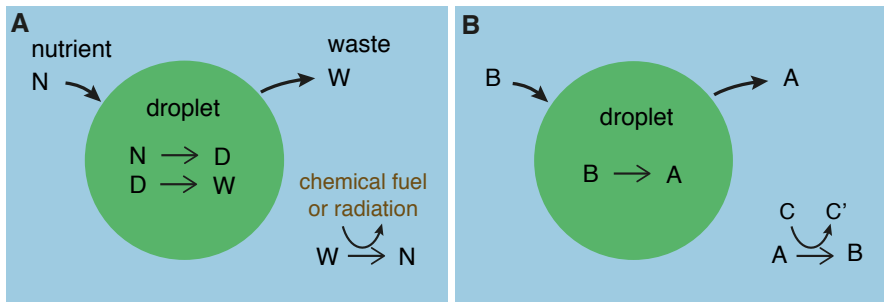


FIGURE 8.1: Chemically active droplet as model for a protocell. A) Schematic representation of an active droplet as a simple model of a protocell. The droplet (green) consists of a droplet material  $D$ . Nutrients  $N$  of high chemical energy can diffuse into the droplet. Inside the droplet,  $N$  is transformed to  $D$  by chemical reactions. Droplet material  $D$  is degraded chemically into low energy waste  $W$  that leaves the droplet. B) Simple model, with droplet material  $B$  and soluble component  $A$ . The system is driven by a chemical fuel  $C$  that is transformed to the reaction product  $C'$ .

$D \rightarrow W$ . Thus the protocell droplet consumes food and produces waste. Both reactions should occur spontaneously, so that the energy of the nutrient is higher than the droplet material, which has a higher energy than the waste. Both reactions together form a minimal description of the metabolism of the droplet while leaving the concrete realization open. Such a system would over time decay into an equilibrium system containing large amounts of waste. The same thing would happen with cells in a closed environment - they would eat all food and then die. This can be remedied by considering an open system with a reservoir of nutrients, and one of waste, so that the concentrations of both remain constant over time. We can also consider a system where the waste is recycled into the nutrient using an external energy input,  $W \rightarrow N$ .

To animate the possible existence of such a system, let us consider a droplet formed of polymers. Typically polymers  $D$  decay over time into monomers  $W$ , due to the entropic difference, which disperse in water, modeling reaction  $D \rightarrow W$ . The addition of activated monomers  $N$  extend the polymers, or form new ones, yielding reaction  $N \rightarrow D$ . Both processes might be controlled by catalysts that predominantly partition into the droplet.

The simple model for a protocell consisting of a droplet with chemical reaction is shown in Fig. 8.1A. The model thus fulfills the first three conditions for a protocell presented in the previous section - the protocell droplet forms a distinct chemical environment, it consumes nutrient and produces waste, and the system is out of equilibrium due to the external energy input in the backward reaction. Combining water and waste into an effective component  $A$  and to combine nutrient and droplet material into an effective component  $B$  yields the minimal model studied throughout this thesis. This reduced system is shown in Fig. 8.1B. Mathematically, this reduced model corresponds to a system where water and waste are always well mixed (for example due to a large mobility of waste in water), and where the same applies to nutrient

and droplet material.

### 8.2.2 Droplet division in the context of protocells

We showed in this thesis that chemically active droplets such as described here have stationary spherical states, which can become unstable with respect to shape deformations, and divide. We therefore find a simple division mechanism of droplets that is driven by nonequilibrium chemical reactions, which model the protocell metabolism and nutrients.

The stability diagram of chemically active droplets, compare Fig. 7.2E, can be interpreted in the context of droplets as protocells: the supersaturation  $\epsilon$  corresponds to the amount of nutrients available for the protocell droplet, while the reaction rate  $A$  characterizes the metabolism of the protocell. If a protocell operates at a metabolic rate  $A$  near or below  $A^*$ , which is set by the droplet viscosity and surface tension, it can control the division via the metabolic rate – a faster metabolism (larger  $A$ ) may lead to a division of the droplet due to the shape instability, while a slower metabolism would lead to a stable, stationary size of the protocell. For larger amounts of nutrients, the metabolic rate necessary for division would decrease. Additionally, the amount of nutrients available control the stationary size of the protocell, and below a critical amount of nutrients, protocells would 'starve to death', in the region without stationary droplets. In a noisy system where the nutrients vary over time, a metabolic rate below  $A^*$  would ensure a wide regime of possible supersaturations where stationary protocells may exist, while divisions might be triggered in times with ample amounts of nutrients. Comparing the phase diagrams for different parameters (for example the dimensionless viscosity  $F$  as in Fig. 7.2D-F), we see that the physical parameters of the droplet influence the operation of the system. This poses a route for protocells to adapt and evolve by varying their physical properties due to the use of enzymes for the reactions or due to changes in the droplet composition, which might change viscosity or surface tension.

It also poses a possibility to test the usefulness of chemically active droplets as a model for protocells. We will estimate realistic parameters in the next section.

### 8.2.3 Are chemically active droplets alive?

We will now briefly discuss a rather philosophical question: Are chemically active droplets alive?

We introduced chemically active droplets as a physical nonequilibrium system, and our minimal model is much simpler than a biological cell. Therefore, intuitively, the answer should be a clear no. On the other hand, life has occasionally been defined as 'an open system which makes use of gradients in its surroundings to create imperfect copies of itself', see Prigogine et al. (1972). We have not shown that the droplets are 'imperfect copies', but considering division in the context of a noisy system, this seems a reasonable extension. Therefore, according to this simple physicist's

definition, dividing droplets might be considered alive. Similar definitions, such as via self-organization and reproduction, could similarly be considered.

However, these are rather abstract definitions. Let us now consider a more biological definition, according to which life needs to have the following characteristics: Homeostasis, Organization, Metabolism, Growth, Adaptation, Response to stimuli and Reproduction, Alberts et al. (2013).

- Homeostasis, the regulation of the internal environment to maintain a constant state, is, at least in part, provided by the phase separation. The phase separation can be perturbed by some changes in the environment, but the same is true for cells.
- Life needs to be composed of one or more cells (Organization). Naturally, chemically active droplets do not fulfill this point. However, this point seems rather restrictive, especially without a proper definition of 'cell', and will likely not work for early life on Earth, but also not for life on other planets. We might therefore replace it by the requirement of certain molecules, such as polymers composed of amino acids (proteins) and of nucleic acids (RNA, DNA), chemical reactions such as translation and transcription, and possibly a membrane. Because we did not assume particular molecules in our model, droplets might be composed of proteins and RNA, which have been shown to phase separate together. However, a membrane would constitute a major barrier to the division discussed in this thesis. Additionally, our minimal model is quite different from the complex structure and chemical network of a cell. Therefore, we might judge that chemically active droplets do not fulfill this point.
- Life needs a metabolism, which converts energy and chemicals into cellular components and decomposing them. Our chemical reactions provide a simple model for this.
- Life needs to be able to grow. We have shown that our droplets grow towards a stationary size.
- Adaptation is another necessity of life - by changing over time in response to the environment, evolution may take place. This point is not fulfilled by our current model of chemically active droplets.
- Response to stimuli, such as plants turning towards the sun, is a difficult point to discuss, because it conflicts with homeostasis. However, droplets inside a gradient of food (locally varied supersaturation) may move into the gradient due to a net growth in that direction. Since a droplet is an open system, other responses can be considered possible as well. Finally, the reproduction of life sexually or asexually into two organisms has been described via droplet division, and therefore is possible for chemically active droplets.

To conclude, chemically active droplets fulfill a number of the characteristics of life, all except the organization in cells and adaptation. Considering adaptation and

evolution as one of the main traits of life, we would be led to conclude that chemically active droplets are not alive, at least not using the minimal model discussed in this thesis.

#### 8.2.4 Open questions

We have shown that chemically active droplets have properties that can be associated with protocells at the origin of life. Also, we have argued that they do not fulfill all points of the definition of being live. If we assume that life might have started as protocell droplets as explained in this section, a number of questions arise. Open questions are: What kind of molecules could have formed protocell droplets? A number of experiments on the basis of protein/RNA-droplets and/or complex coacervates exist, Aumiller and Keating (2016); Nakashima et al. (2018); Rieß et al. (2018). These might be suitable starting points to consider. We will estimate parameters for droplet division of such systems in the next section. This leads us to the next question: How would the droplet behavior change if a large number of different components are present? The current theory uses a binary system, so a study of phase separation and droplet division in multi-component systems would be helpful to understand how the behavior differs in complex systems. We might assume that the dynamic behavior can be similar to the binary system if the components can be split into groups with similar behavior. However, we generally expect additional effects, such as the formation of different droplet phases, the possibility of surface changes due to surfactants and additional spatial dynamics, Lach et al. (2016). Such a multi-component mixture could provide solutions for additional questions. The most intriguing one is that they could open a path from chemically active droplets towards living cells, by providing ways of adaptation and growing complexity. One major obstacle of droplets evolving into cells is the acquisition of a membrane: The attraction of a membrane (or generally, surfactants) to droplet interfaces is a natural occurrence. However, the division mechanism of droplet protocells would likely need to change with the acquisition of a membrane.

Finally, we might ask if droplets were precursors to life on Earth. Sadly, it will likely not be possible to answer this question. The origin of life is a historical event, which would need to be studied with geological measures where it seems highly unlikely to find remnants of chemically active droplets and following their historical evolution. The only way to understand the origin of life today therefore seems to be understanding the different avenues that this process could have followed, and providing scenarios in which they would have been more or less likely. It will be interesting to see which further contributions nonequilibrium physics and chemistry may hold.

### 8.3 Examples of parameter values for dividing droplets

Could the shape instability and division discussed in this thesis occur in experiments and what conditions are needed? In order to address this question, we provide in

### 8.3. Examples of parameter values for dividing droplets

	$D_{\pm}[\mu\text{m}^2/\text{s}]$	$w[\text{nm}]$	$\gamma[\text{mN}/\text{m}]$	$c_-^{(0)}[\text{mM}]$	$c_+^{(0)}[\text{mM}]$	$\nu_-[\text{mM}/\text{s}]$	$l_{\pm}[\text{mm}]$	$\epsilon$	$t_R[\text{s}]$	$R_{div}[\mu\text{m}]$
Case I	10	10	$10^{-3}$	100	1	1	0.1	$2 \cdot 10^{-3}$	100	3
Case II	10	1	10	$10^3$	$10^{-3}$	10	5	$8 \cdot 10^{-4}$	100	1

Table 8.1: Examples of parameter values for dividing droplets. Parameters are defined in the Methods. For these parameters, the resulting supersaturation  $\epsilon$ , the turnover time  $t_R = c_-^{(0)}/\nu_-$ , and the radius  $R_{div}$  where the stationary droplet shape becomes unstable in the absence of hydrodynamic flows are given. Case I is motivated by colloidal droplets or liquid protein phases with low surface tension. For Case II we chose properties of typical water/oil droplets.

Table 8.1 two examples of parameter sets for which droplets would have a shape instability according to the model, in the limit of infinite viscosity  $F \rightarrow \infty$ . Case I is based on the properties of colloidal droplets or liquid protein phases with low interfacial tension, Brangwynne et al. (2009); Li et al. (2012); Safran (1994). We find that the shape instability could be realized experimentally for droplets with sizes of several micrometers. In case I the radius where droplets become unstable is  $R_{div} \approx 3 \mu\text{m}$ . Case II is based on the properties of water/oil interfaces, Safran (1994); Peters and Arabali (2013); Page et al. (2000); Atkins and de Paula (2010). This example shows that even for these larger interfacial tensions as compared to case I, droplets can still have a stationary radius of the order of micrometers at the instability. These examples show that small droplets that could be observable under the microscope could indeed have a shape instability for plausible rates of chemical reactions and realistic interfacial tensions. However, as shown in Appendix G, droplet division for macroscopic droplets of millimeter or centimeter size will be difficult to achieve.

To address the influence of hydrodynamic flows, we have to estimate the dimensionless viscosity  $F = w\eta_-/(\gamma\tau) \simeq k_B T/(6\pi\gamma wa)$ , where we have used  $\tau = w^2/D$  and  $D \simeq k_B T/(6\pi\eta a)$  with molecular radius  $a$ . Thus,  $F$  is an equilibrium property of the phase separating fluid. For an oil-water system, we estimate  $F \approx 0.1$ , see Appendix G. For soft colloidal liquids or p-granules, we estimate values between  $F \approx 10 - 10^4$ . We can discuss these values using the stability diagrams in Fig. 7.2. Oil-water like droplets with  $F \approx 0.1$  are unlikely to divide, as the unstable region in the stability diagram is very narrow. For soft colloidal systems with  $F \approx 10 - 10^4$ , droplet division might be experimentally observable. We can estimate typical reaction rates required for division to occur based on the reaction rate  $A^*$  for which the range of supersaturation is maximal. The value of  $A^*$  corresponds to a reaction rate in the droplet of the order of  $\nu_- = 10^{-4} \text{mM}/\text{s}$ . A comparison with reported enzymatic reaction rates suggests that such values can be achieved in real systems, Stenesh (2013).

## 8.4 Summary

We have proposed in this chapter that the chemically active droplets discussed in this thesis can be seen as a model for protocells at the origin of life. We have argued that they have a number of properties that can be associated with life-like behavior: The droplet itself constitutes an environment that is separate and different from the surrounding, the chemical reaction inside the droplet models a metabolism, the reaction outside the droplet represents a non-equilibrium environment with replenishment of nutrients out of waste. The dynamical behavior of the droplet shows a stationary droplet size, which can be unstable, and the resulting division into two droplets might then constitute a mechanism for replication of protocells.

We have argued that using the model studied throughout this thesis, chemically active droplets would not be considered alive. This is partially due to the simplicity of the current (minimal) model, which does not contain the complexity of modern cells with the different biological molecules and intricate reaction network. The main difference, however, is that the chemically active droplets discussed here are missing a mechanism to adapt and evolve. We have argued that a multi-component treatment might provide pathways to adaptation. This might then provide a route from simple chemically active droplets towards more complex evolving (proto-) life-forms.

To estimate whether dividing chemically active droplets can be relevant for protocell models and whether they can be implemented experimentally, we estimated parameter sets for the case of droplets of organic material inside cells today, which are characterized by a large viscosity and small surface tension, and for oil droplets in water, with a large surface tension. We find that division would be strongly suppressed by hydrodynamic flows in oil droplets. For organic droplets, we find that chemically active droplets might divide for stationary sizes of a few micrometers for realistic reaction rates. This indicates that the dynamic behavior of chemically active droplets discussed in this thesis can be relevant for biologic and prebiotic system.



---

In this thesis we have introduced a simple model to show that chemically active droplet can undergo cycles of growth and division reminiscent of cells. Our model combines the set of features that are minimally required for droplet division: (i) two different chemical components undergoing reactions; (ii) phase separation; (iii) external energy input which maintains the system away from thermodynamic equilibrium. Our work shows that such droplet division would be expected to occur in phase-separating systems with small surface tension for small droplets of a few micrometers or less. The fact that active droplets tend to become unstable and divide is an unusual behavior of droplets because surface tension usually opposes such shape changes. An instability of the droplet shape requires non-equilibrium conditions. In our model, these non-equilibrium conditions are provided by the energy input of a chemical fuel. The resulting chemical reactions drive diffusive fluxes across characteristic length-scales as known for reaction diffusion systems, Turing (1952); Gierer and Meinhardt (1972). In the presence of droplet interfaces, these fluxes can induce a shape instability of stationary droplets. In the absence of chemical reactions and the resulting fluxes, the shape instability does not occur. The shape instability leading to droplet division introduced here can be compared to the Mullins-Sekerka instability often discussed in the context of crystal growth, Mullins and Sekerka (1963). Both instabilities require a diffusion flux toward the interface. In the case of the Mullins-Sekerka instability the shape of a growing aggregate becomes unstable. For example, an interface can become unstable with respect to growing spikes called dendrites beyond a critical interface velocity. In contrast, the chemical reaction induced shape instability discussed here can occur for a stationary, non-growing droplet. This difference is important because in the case of a Mullins-Sekerka instability, the instability of a droplet does not lead to a shrinking waistline and fission but rather to the formation of a growing dendritic structure, Langer (1980). Only for the instability of a steady state droplet found here does the instability generate a narrowing of the waist-

line of the initial droplet shape leading to fission in two droplets. The droplet division is a simple mechanism of self-replication that is reminiscent of the division of living cells. It is therefore an interesting question whether protocells at the origin of life could have resembled droplets, and replicated via chemically controlled divisions.

This thesis only touches on or completely ignores many aspects of chemically active droplets that would merit future work. It would be intriguing to consider the effect of noisy dynamics on the division, especially in the limit of small systems with a finite number of participating molecules. This is of particular relevance for biological systems, where often only a small number of specific molecules exist, and noise plays an important role, Rao et al. (2002). A further extension for which we have laid some of the groundwork in this thesis in chapter 2 is the study of multi-component systems. Many possible extensions towards more components are both needed to capture experimental systems in more detail, and to find and describe additional effects. One possible extension is the inclusion of Waste and Nutrient, as discussed in chapter 8 as motivation of chemically active droplets as protocells. An even simpler extension is the study of a nonequilibrium reaction  $A \rightarrow B$  in a three component system with an additional solvent S. Beyond these simple extensions, the study of polymerization reactions in such an active phase-separating system might be relevant for many applications. Another idea could be to consider interactions and reactions between multiple phase-separating components, which form different droplets, so that a network of interacting droplets is created. Then, the question of network stability can be considered. In an origin of life scenario, such a system might correspond to an ecosystem of different protocells. Finally, in an origin of life context, it is interesting to ask whether chemically active droplets can support the chemical evolution of participating molecules into molecules more suited to tasks relevant for a protocell. Last, most multi-component systems include surfactants. It could be interesting to study whether droplet division is still possible for droplets with strong or weak surfactant molecules, and whether the division can be combined with additional effects such as the Marangoni effect, which leads to a spontaneous movement of a droplet with surfactant, see Maass et al. (2016).

As we have pointed out here, many interesting theoretical avenues exist, by which novel behavior of chemically active droplets can be studied. Additionally, it will be an important challenge to observe this droplet division in future experiments. We have provided in chapter 8 examples of parameter values for which micrometer sized droplets would divide. These parameter values could in principle be achieved in artificial droplets or in *in vitro* studies of protein droplets.

Let us now briefly consider possible applications of such a droplet division. The creation of emulsions has been intensely studied, because of the many uses in material design, for building materials, cosmetic products and food, Taylor (1998); Zarzar et al. (2015). If multiple divisions of chemically active droplets are possible, this would create an emulsion with a well-controlled droplet size. It would be interesting to consider whether an injection of the reservoir components instead of a continuous supply could create cycles of division, so that an emulsion of the material can be created when needed. Phase-separation and chemical reactions typically occur within

---

cells. This poses the question whether the combination of both is employed by cells to control droplet size and dynamics. In such a biological example, the reservoir components could represent ATP and ADP, which are much smaller than many other biological molecules, with faster diffusion, and extensively participate in chemical reactions within the cell. It will be interesting to see whether dividing droplets exist in biological systems, and whether they can be created in experimental systems of synthetic biology.



# Appendices



# Appendix A

## Reaction rates with broken detailed balance

---

In our models, chemical reaction rates and diffusion fluxes are maintained in a non-equilibrium steady state. They are driven by the free energy supplied by the chemical potential difference of a higher energy chemical fuel  $C$  and a lower energy waste product  $C'$ , which are maintained by external reservoirs. We illustrate these non-equilibrium conditions in a simple model based on four components  $A, B, C, C'$  in a system that exhibits phase separation of the two components  $A$  and  $B$ .

The chemical potentials of components  $n = A, B, C, C'$  can be expressed as

$$\mu_n = k_B T \ln(v_n c_n) + w_n \quad , \quad (\text{A.1})$$

where  $v_n$  denote molecular volumes. The first term describes the entropy of molecular rearrangements. The contribution  $w_n$  captures internal free energies of molecules as well as effects of interactions between molecules Cahn and Hilliard (1958). Therefore,  $w_n$  depends on composition. For simplicity, we only consider here the dependence on the concentrations of  $A$  and  $B$ ,  $w_n(c_A, c_B)$ . For a phase-separated system at thermodynamic equilibrium, the chemical potentials of all components  $n$  are equal in both phases,

$$\mu_n^+ = \mu_n^- \quad , \quad (\text{A.2})$$

where "+" and "-" refer to the phases outside and inside the droplet, respectively. Because of the dependence of  $w_n$  on  $c_A$  and  $c_B$ , the concentrations of all molecular species differ in both phases,  $c_n^+ \neq c_n^-$ , with

$$\frac{c_n^+}{c_n^-} = \exp\left(\frac{w_n^- - w_n^+}{k_B T}\right) \quad . \quad (\text{A.3})$$

This difference implies that molecules of a given species typically have a higher affinity to one phase as compared to the other as a result of interactions with other molecules.

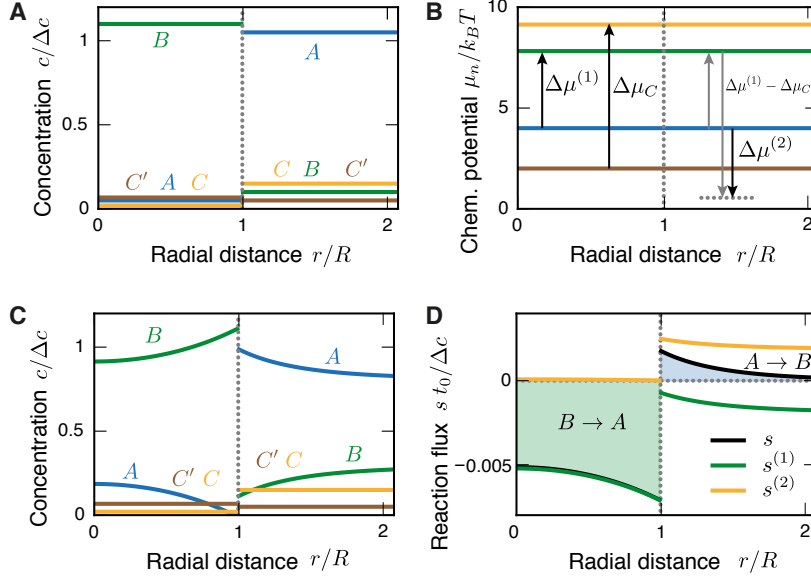


FIGURE A.1: Concentration profiles and reaction rates in a four-component model including fuel and waste. Radial profiles of concentrations (A) and chemical potentials (B) of molecular species  $A$ ,  $B$ ,  $C$  and  $C'$  for an equilibrium droplet without chemical reactions. The differences in chemical potentials  $\Delta\mu^{(1)}$  and  $\Delta\mu^{(2)}$  can drive chemical reactions. In the presence of chemical reactions, radial concentration profiles change slightly (C). The corresponding reaction fluxes are shown in (D). The active droplet shown in (C) correspond to the stationary unstable spherical droplet shown in Fig. 5.1 which undergoes a division. Parameter values for (A) and (B) are  $c_-^{(0)}/\Delta c = 1.1$ ,  $c_+^{(0)}/\Delta c = 0.1$ ,  $v_A \Delta c = 0.87$ ,  $c_C^+/\Delta c = 0.15$ ,  $c_{C'}^+/\Delta c = 0.05$ ,  $(w_C^- - w_C^+)/k_B T = 2$ ,  $(w_{C'}^- - w_{C'}^+)/k_B T = -0.3$ ,  $\Delta w_+^{(1)}/k_B T = -6.17$ , and  $\Delta w_+^{(2)}/k_B T = 0.135$ . In (C) and (D) the same parameters are used together with the reaction parameters  $k^{(1)}t_0 = 0.0065$ ,  $k^{(2)}t_0\Delta c = 0.017$ ,  $\epsilon_{\pm}^{(1)} = 0$ , and  $\epsilon_{\pm}^{(2)} = 0$ .

The case of a  $B$ -rich droplet at equilibrium (without chemical reactions) is illustrated in Fig. A.1. Here we consider the case where the concentrations  $c_C$  and  $c_{C'}$  are higher outside the droplet than inside, corresponding to a smaller affinity to the droplet phase.

We choose a system where the chemical potential  $\mu_B$  is larger than  $\mu_A$ , such that  $\Delta\mu^{(1)} = \mu_B - \mu_A > 0$ , and where the chemical potential  $\mu_C$  is large enough that  $\Delta\mu^{(2)} = \mu_B - \mu_A - \mu_C + \mu_{C'} < 0$ , see Fig. A.1B. Note that the value of  $\mu_C$  can be set by varying the concentration in the external reservoir.

The system can be driven away from equilibrium by the chemical reactions (1) and (2), which are driven by the chemical potential differences  $\Delta\mu^{(1)}$  and  $\Delta\mu^{(2)}$ . The flux



of the reaction (1),  $B \rightleftharpoons A$ , can be written as (see Methods section in the main text)

$$s^{(1)} = s_{\leftarrow}^{(1)} \left[ \exp \left( -\frac{\Delta\mu^{(1)}}{k_B T} \right) - 1 \right] , \quad (\text{A.4})$$

which obeys a local detailed balance condition. Here, the reaction amplitude  $s_{\leftarrow}^{(1)}$  is in general concentration dependent. Similarly, for the reaction (2),  $A + C \rightleftharpoons B + C'$ , the reaction flux is

$$s^{(2)} = s_{\rightarrow}^{(2)} \left[ 1 - \exp \left( \frac{\Delta\mu^{(2)}}{k_B T} \right) \right] . \quad (\text{A.5})$$

Considering these expressions, we find for the situation illustrated in Fig. A.1B that  $s^{(1)} < 0$  and  $s^{(2)} > 0$  in both phases, so that reaction (1) produces  $A$  molecules, while reaction (2) produces  $B$  molecules, both inside and outside the droplet. However, the reaction amplitudes  $s_{\leftarrow}^{(1)}$  and  $s_{\rightarrow}^{(2)}$  can vary strongly with concentration and therefore the magnitudes of the fluxes  $s^{(1)}$  and  $s^{(2)}$  differ inside and outside the droplet, see Fig. A.1C. The total reaction flux

$$s = s^{(1)} + s^{(2)} \quad (\text{A.6})$$

does not obey a local detailed balance condition. The sign of  $s$  depends not only on the chemical potential differences, but also on the reaction amplitudes  $s_{\leftarrow}^{(1)}$  and  $s_{\rightarrow}^{(2)}$ , which depend on local concentrations. For example, the reaction amplitude  $s_{\leftarrow}^{(1)}$  is in general a function of concentrations. For vanishing concentration of  $B$ , reaction (1) cannot proceed in backward direction and  $s_{\leftarrow}^{(1)} = 0$ . we therefore write  $s_{\leftarrow}^{(1)} = c_B f(c_A, c_B, c_C, c_{C'})$ . In the simplest case  $f$  is constant. We thus consider

$$s_{\leftarrow}^{(1)} \approx c_B k^{(1)} , \quad (\text{A.7})$$

where  $k^{(1)}$  is a concentration-independent reaction constant. Using a similar argument for reaction (2), we consider

$$s_{\rightarrow}^{(2)} \approx c_C c_A \cdot k^{(2)} , \quad (\text{A.8})$$

with reaction constant  $k^{(2)}$ .

We can now discuss a typical scenario that corresponds to production of  $A$  molecules inside the droplet and production of  $B$  molecules outside (see Fig. A.1). The amplitude  $s_{\rightarrow}^{(2)}$  is smaller inside the droplet where the concentrations  $c_C$  and  $c_A$  are small, as compared to outside. Furthermore  $s_{\leftarrow}^{(1)}$  is smaller outside the droplet, where the concentration  $c_B$  is small compared to inside. The total reaction flux  $s$  then is typically negative inside the droplet and positive outside (see Fig. A.1).

We can relate this detailed description of the chemical reactions to the simplified representation of the chemical reactions given in Eq. (3.13). First, using (A.4) and (A.5), we have

$$s^{(1)} \simeq k^{(1)} \left( c_A \exp \left[ \frac{w_A - w_B}{k_B T} \right] - c_B \right) \quad (\text{A.9})$$

and

$$s^{(2)} \simeq k^{(2)} \left( c_C c_A - c_{C'} c_B \exp \left[ \frac{w_B - w_A - w_C + w_{C'}}{k_B T} \right] \right), \quad (\text{A.10})$$

where we have considered the simple case where molecular volumes do not change during chemical reactions,  $v_A = v_B$  and  $v_C = v_{C'}$ .

We neglect for simplicity the contributions of the molecules  $C$  and  $C'$  to the total volume,

$$c_A \simeq \frac{1}{v_A} - c_B. \quad (\text{A.11})$$

The concentration  $c$  in Eq. (3.13) is  $c = c_B$ , and the variables  $c_{\pm}^{(0)}$  in Eq. (3.4) correspond to the equilibrium concentrations  $c_B^{\pm}$  of  $B$  molecules inside and outside the interface. We can now identify

$$\begin{aligned} \nu_{\pm} = & \pm k^{(1)} \left[ \left( \frac{1}{v_A} - c_{\pm}^{(0)} \right) \exp \left[ \frac{w_A^{\pm} - w_B^{\pm}}{k_B T} \right] - c_{\pm}^{(0)} \right] \\ & \pm k^{(2)} \left[ c_C^{\pm} \left( \frac{1}{v_A} - c_{\pm}^{(0)} \right) - c_{C'}^{\pm} c_{\pm}^{(0)} \exp \left[ \frac{w_B^{\pm} - w_A^{\pm} - w_C^{\pm} + w_{C'}^{\pm}}{k_B T} \right] \right] \end{aligned} \quad (\text{A.12})$$

and

$$\begin{aligned} k_{\pm} = & k^{(1)} \left[ \exp \left[ \frac{w_A^{\pm} - w_B^{\pm}}{k_B T} \right] + 1 \right] + k^{(2)} \left[ c_C^{\pm} + c_{C'}^{\pm} \exp \left[ \frac{w_B^{\pm} - w_A^{\pm} - w_C^{\pm} + w_{C'}^{\pm}}{k_B T} \right] \right] \\ & - k^{(1)} \left( \frac{1}{v_A} - c_{\pm}^{(0)} \right) \exp \left[ \frac{w_A^{\pm} - w_B^{\pm}}{k_B T} \right] \frac{1}{k_B T} \left. \frac{d(w_A - w_B)}{dc} \right|_{c_{\pm}^{(0)}} \\ & + k^{(2)} c_C^{\pm} c_{\pm}^{(0)} \exp \left[ \frac{w_B^{\pm} - w_A^{\pm} - w_C^{\pm} + w_{C'}^{\pm}}{k_B T} \right] \frac{1}{k_B T} \left. \frac{d(w_B - w_A - w_C + w_{C'})}{dc} \right|_{c_{\pm}^{(0)}} \end{aligned} \quad (\text{A.13})$$

These expressions show that the parameters  $\nu_{\pm}$  and  $k_{\pm}$  depend explicitly on the fuel concentration  $c_C$  and the concentration  $c_{C'}$  of the waste product. Furthermore, they depend on molecular interactions described by the energies  $w_n^{\pm}$ .

Thus, the active droplet system defined in the Methods section in the main text results from the more detailed model of chemical reactions described here. The dimensionless parameters that need to be specified are:  $c_-^{(0)}/\Delta c$ ,  $c_+^{(0)}/\Delta c$ ,  $v_A \Delta c$ ,  $c_C^{\pm}/\Delta c$ ,  $c_{C'}^{\pm}/\Delta c$ ,  $\exp[(w_C^- - w_C^+)/k_B T]$ ,  $\exp[(w_{C'}^- - w_{C'}^+)/k_B T]$ ,  $\exp[\Delta w_+^{(1)}/k_B T]$ ,  $\exp[\Delta w_+^{(2)}/k_B T]$ ,  $k^{(1)} t_0$ ,  $k^{(2)} t_0 \Delta c$ , and  $\epsilon_{\pm}^{(1)}$ ,  $\epsilon_{\pm}^{(2)}$ , and we consider for simplicity the limit of large diffusion coefficients of  $C$  and  $C'$ , for which  $c_C$  and  $c_{C'}$  are constant inside and outside of the droplet. Here, we denoted internal energy differences of reactions (1) and (2) as  $\Delta w_{\pm}^{(1)} = w_A^{\pm} - w_B^{\pm}$ ,  $\Delta w_{\pm}^{(2)} = w_B^{\pm} - w_A^{\pm} - w_C^{\pm} + w_{C'}^{\pm}$ , and derivatives of the internal energy with respect to the concentration of  $B$  as  $\epsilon_{\pm}^{(1)} = \frac{\Delta c}{k_B T} \left. \frac{d(w_A - w_B)}{dc} \right|_{c_{\pm}^{(0)}}$  and  $\epsilon_{\pm}^{(2)} = \frac{\Delta c}{k_B T} \left. \frac{d(w_B - w_A - w_C + w_{C'})}{dc} \right|_{c_{\pm}^{(0)}}$ . We can calculate the

---

concentrations  $c_{C'}^-$ ,  $c_{C''}^-$  and  $c_A$  using Eq. (A.3) and Eq. (A.11). Thus the simplified models of chemical reactions discussed in the main text can be related to a more detailed description of the reactions including explicit concentrations of fuel and waste. An example of a stationary droplet is shown in Fig. A.1.



## Appendix B

### Relation between the continuum model and the effective droplet model

---

We now discuss the relationship between the effective droplet model and the continuum model. To relate the two models, we first use the continuum model to derive jump conditions for the concentration in the effective droplet model in equilibrium. We then consider stress balance across this interface and derive stress boundary conditions in the effective droplet model. Finally we discuss the dynamical equations in the bulk and at the interface in non-equilibrium situations.

#### B.1 Derivation of jump conditions for equilibrium phase separation

First we consider the phase separation in equilibrium without chemical reactions in the continuum model.

In a one-dimensional system with a mean concentration  $\bar{c}$  with  $c_+^{(0)} < \bar{c} < c_-^{(0)}$ , the free energy of the system in Eq. (3.3) is minimized by the concentration profile

$$c^*(x) = \frac{c_-^{(0)} + c_+^{(0)}}{2} + \frac{c_-^{(0)} - c_+^{(0)}}{2} \tanh \frac{x}{w}, \quad (\text{B.1})$$

where  $w = 2(\kappa/b)^{1/2}$  denotes the interfacial width and  $x$  is the normal distance to the interface. The concentration profile describes two phases of concentration  $c_-^{(0)}$  and  $c_+^{(0)}$  separated by a flat interface of width  $w$ . The surface tension can be defined as

$$\gamma = \int_{-\infty}^{\infty} F[c^*(x)] - \frac{1}{2}(F[c_-^{(0)}] + F[c_+^{(0)}])dx. \quad (\text{B.2})$$

For the free energy Eq. (3.3) with the concentration profile Eq. (B.1), this can be written as  $\gamma = \int_{-\infty}^{\infty} \kappa (\nabla c^*)^2 dx$  which yields  $\gamma = (\Delta c)^2 / 6 \sqrt{\kappa b}$ , Safran (1994).

This interfacial tension governs the concentration jump condition in the effective droplet model, which can be derived as follows. To describe a curved interface, we consider two homogeneous phases with concentrations  $c_{\pm}$ . For a finite volume  $V_s$  with a droplet of size  $V$  and area  $A$  the concentrations  $c_{\pm}$  can be found by minimizing the free energy  $F = f(c_-)V + f(c_+)(V_s - V) + \gamma A$  with  $\partial F / \partial c_-|_V = 0$  and  $\partial F / \partial V|_{c_-} = 0$ , where the concentration of both phases are related by  $V_s \bar{c} = V c_- + (V_s - V) c_+$  where  $\bar{c}$  denotes the average concentration in the system. Thus for two phases to be in equilibrium, their chemical potential  $\bar{\mu}$  and osmotic pressure  $\Pi = c\bar{\mu} - f$  need to obey

$$0 = \bar{\mu}(c_-) - \bar{\mu}(c_+) \quad (\text{B.3})$$

$$0 = \Pi(c_+) - \Pi(c_-) - 2\gamma H, \quad (\text{B.4})$$

where  $H$  the mean curvature of the droplet and  $2\gamma H$  is the Laplace pressure. These equations determine the concentrations in the phases  $c_{\pm}$  of coexisting phases, Safran (1994).

For small Laplace pressures, we can express the equilibrium concentrations  $c_{\pm}$  of a curved interface by the concentrations of a flat interface  $c_{\pm}^{(0)}$  plus a small perturbation,

$$c_- = c_-^{(0)} + \beta_- \gamma H \quad (\text{B.5})$$

$$c_+ = c_+^{(0)} + \beta_+ \gamma H \quad (\text{B.6})$$

where  $\beta_{\pm} = 2 / (f''(c_{\pm}^{(0)}) \Delta c)$ . For the free energy Eq. (3.3), we find  $\beta_{\pm} = 2 / (b \Delta c)$ , which is related to the interfacial width as  $w = 6\gamma \beta_+ / \Delta c$ .

## B.2 Stress balance across the interface

We now consider stress balance of the continuum model across the droplet interface to derive stress jump conditions at the interface in the effective droplet model. We discuss the mechanical equilibrium in a small volume across a curved interface with a local mean curvature  $H$  corresponding to a (local) effective radius  $\tilde{R} = 1/H$ . We focus on the case where the interface is rotationally symmetric around the considered point  $\mathbf{R}$ , and where the curvature does not change along the interface. We use spherical coordinates, where the radial vector  $\mathbf{e}_r$  is aligned with the (outward pointing) normal vector  $\mathbf{n}$  and the tangential vectors  $\mathbf{t}$  and  $\mathbf{s}$  are aligned with  $\mathbf{e}_{\theta}$  and  $\mathbf{e}_{\phi}$ , respectively (with the vector directions for  $\phi = 0$  in the limit  $\theta = 0$ ). We consider a small box enclosing  $\mathbf{R}$  where the outer and inner surfaces  $A_{out}$  and  $A_{in}$  have a constant distance of  $\delta$  to the interface, and the lateral surface  $A_{lat}$  is at a constant angle  $\theta_0$  with respect to the symmetry axis. The geometry is shown in Fig. B.1.

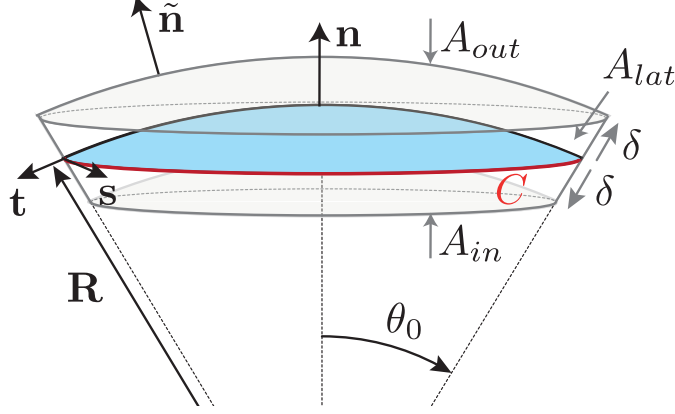


FIGURE B.1: Geometry for the force balance. We consider a spherical cap of the droplet interface, with a box with constant distance  $\delta$  to the interface inside and outside. The normal and tangential vectors  $\mathbf{n}$ ,  $\mathbf{t}$  and  $\mathbf{s}$  of the interface are shown, as well as the normal vector  $\tilde{\mathbf{n}}$  of the box. The origin of the spherical coordinate system is the center of the sphere that describes the interfacial curvature, with radius  $\tilde{R}$ , while  $\theta_0$  gives the polar angle of the cap.

Now let us consider the balance of the stress tensor Eq. (3.7) across the box, taking into account the curved geometry. The stress balance  $\partial_\beta \sigma_{\alpha\beta}$  can be written as

$$0 = \oint dA \tilde{\mathbf{n}}_\beta \sigma_{\alpha\beta} \quad (\text{B.7})$$

where  $\alpha$  and  $\beta$  are Cartesian coordinates and  $\tilde{\mathbf{n}}$  the (local, outward pointing) normal vector of the box-surface. We can split this in three terms,

$$0 = \int dA_{out} \sigma_{\alpha n} - \int dA_{in} \sigma_{\alpha n} + \int dA_{lat} \sigma_{\alpha t}, \quad (\text{B.8})$$

where we used that the orientation of the normal vectors of the box coincides with the normal/tangential vector of the interface.

On the inner and outer areas  $A_{in}$  and  $A_{out}$ , the stress tensor presented in Eq. (3.8) with equilibrium stress tensor in Eq. (3.9) reduces to the form of the effective droplet model given after Eq. (3.24) in the main text, as the gradient terms are negligible for  $\delta \gg w$ . We now consider the limit of a sharp interface  $w \rightarrow 0$  with finite surface tension  $\gamma$ , and consider the case of a small box of thickness  $\delta$ , which remains larger than the interfacial width. The components  $\alpha = x, y$  of Eq. (B.8) vanish by symmetry. For  $\alpha = z$  we find

$$0 = \pi \tilde{R}^2 \sin^2 \theta_0 \sigma_{nn}^+ - \pi \tilde{R}^2 \sin^2 \theta_0 \sigma_{nn}^- - 2\pi \tilde{R} \sin^2 \theta_0 \gamma, \quad (\text{B.9})$$

where  $\sigma_{nn}^\pm$  are the stress tensor components of the effective model, Eq. (3.23), inside and outside the interface at  $\mathbf{R}$ . Integration over the lateral box surface  $A_{lat}$  yields the

last term,  $\int dA_{lat} \sigma_{\alpha t} \cong 2\pi \tilde{R} \sin^2 \theta_0 \gamma$ . We thus find that the mechanical equilibrium of a curved interface introduces a Laplace pressure  $2\gamma H$ ,

$$0 = \sigma_{nn}^+ - \sigma_{nn}^- - 2\gamma H. \quad (\text{B.10})$$

We therefore recover the stress jump condition of the effective droplet model, Eq. (3.25). Additionally, (B.10) together with (B.4) implies that the partial pressure needed to satisfy incompressibility is continuous across the interface,  $P_0^+ = P_0^-$ .

### B.3 Dynamics of the effective droplet model

We now consider the dynamics of a non-equilibrium system with a droplet. We show how the continuum model is related to the bulk equations and jump conditions of the effective droplet model. For this we consider a droplet with a interface that is thin compared to the dynamical length scales  $l_{\pm}$ , so that we can describe the interface by local equilibrium. In the bulk phases we focus on the case where deviations from the equilibrium concentrations are small.

In the bulk phases, we expand the chemical potential Eq. (3.5) around the reference concentrations  $c_{\pm}^{(0)}$ . The gradient term  $-\kappa \nabla^2 c$  in the chemical potential is important within the interface, but can be ignored in the bulk phases, where the length-scales on which the concentration field varies are much larger than the interfacial width. Thus we can describe the chemical potential by

$$\bar{\mu}_{\pm}(c) \approx \left. \frac{d\bar{\mu}_0}{dc} \right|_{c_{\pm}^{(0)}} (c - c_{\pm}^{(0)}), \quad (\text{B.11})$$

which is  $\bar{\mu}_{\pm}(c) \approx b(c - c_{\pm}^{(0)})$  for our specific free energy. With this simplification, Eqns. (3.1) and (3.2) become the reaction-diffusion-convection equations (3.20) and (3.21) with diffusion constants  $D_{\pm} = M (d\bar{\mu}_0/dc)|_{c_{\pm}^{(0)}}$  or  $D_{\pm} = Mb$ . Similarly we linearize the chemical reaction rate Eq. (3.13) in both phases. As we already chose a linear rate for the continuum model, we only need to relate the parameters  $k$  and  $\nu$  with the constants  $k_{\pm}$  and  $\nu_{\pm}$  of the effective model, with  $k_{\pm} = k$ ,  $\nu_+ = \nu$  and  $\nu_- = k\Delta c - \nu$ . Inserting the linearized chemical potential Eq. (B.11) into the equilibrium stress tensor (3.9) we find that momentum conservation in the bulk phases is given by the Stokes equation (3.23) with viscosities  $\eta_{\pm} = \eta$ , where the pressure  $p$  is determined by the incompressibility condition  $\partial_{\alpha} v_{\alpha} = 0$ .

We consider the droplet interface to be in local equilibrium. We therefore obtain Eq. (3.28) for the jump of the concentration field in the effective model. The incompressibility condition  $\partial_{\alpha} v_{\alpha} = 0$  implies  $v_n^-(R) = v_n^+(R)$  at a sharp interface, and we consider an interface without slip length, so that  $\mathbf{v}^-(R) = \mathbf{v}^+(R)$ . We thus find Eq. (3.30) of the effective model. The normal stress balance in Eq. (3.25) is derived in B.2.

As a last point we need to find Eq. (3.31) for the interface movement. We consider the concentration change in a box of width  $\delta$  around the interface, see Fig. B.1.



We consider a box enclosing a point  $\mathbf{R}$  on the interface at the time  $t$  aligned with the normal and tangential directions of the interface at  $\mathbf{R}$ . The interface may move with normal movement  $\partial_t \hat{R}(t)$ , with  $\hat{R}(t) = \mathbf{R}(t) \cdot \mathbf{n}$  and normal vector  $\mathbf{n}$ , while the box stays at a fixed position. The total change of material in the volume is given by

$$\partial_t \int_V dV c = - \int_A dA \tilde{\mathbf{n}} \cdot \mathbf{j} + \int_V dV s(c) \quad (\text{B.12})$$

where  $V$  denotes the volume and  $A$  the area of the box. For small  $w$  and finite  $\delta$  the concentration field  $c$  makes a jump from the surface  $A_{in}$  to  $A_{out}$  given by conditions (3.28) and (3.29) at  $\hat{R}$ . Within each phase, we can express the field by the boundary values at the interface Eq. (B.6) and a linear expansion,

$$c(\mathbf{r}, t) \simeq \begin{cases} c_-(\mathbf{R}(t)) + \nabla c_-(\mathbf{r}, t) \cdot (\mathbf{r} - \mathbf{R}(t)) & \text{inside droplet} \\ c_+(\mathbf{R}(t)) + \nabla c_+(\mathbf{r}, t) \cdot (\mathbf{r} - \mathbf{R}(t)) & \text{outside droplet} \end{cases} \quad (\text{B.13})$$

The chemical reaction is given in both phases by Eq. (3.13). For small  $\delta$  and  $\theta_0$ , we find for the left-hand side of Eq. (B.12) that  $\delta c$  vanishes to lowest order and

$$\partial_t \int_V dV c = A_R (c_-(\mathbf{R}(t)) - c_+(\mathbf{R}(t))) \partial_t \hat{R} + O(\epsilon) + O(\theta_0) \quad (\text{B.14})$$

where  $A_R$  is the area of the droplet interface enclosed by the box. For a spherical cap,  $A_R = 2\pi(1 - \cos \theta_0) \hat{R}^2$ . We further find that the source term due to the chemical reaction scales with the volume of the box, and thus vanishes for a small box,  $\int_V dV s(c) = 0 + O(\epsilon) + O(\theta_0)$ . The flux across the box can be expressed as

$$- \int_A dA \tilde{\mathbf{n}} \cdot \mathbf{j} = A_R \mathbf{n} \cdot (\mathbf{j}_-(\mathbf{R}(t)) - \mathbf{j}_+(\mathbf{R}(t))) + O(\epsilon) + O(\theta_0) \quad (\text{B.15})$$

where  $\mathbf{j}_\pm(\mathbf{R}(t))$  denotes the flux at  $\mathbf{R}$  inside/outside the droplet. We thus find the normal movement of the interface,

$$\partial_t \hat{R} = \mathbf{n} \cdot \frac{\mathbf{j}_-(\mathbf{R}(t)) - \mathbf{j}_+(\mathbf{R}(t))}{c_-(\mathbf{R}(t)) - c_+(\mathbf{R}(t))}. \quad (\text{B.16})$$

In the main text we use spherical coordinates centered at the droplet center. For a spherical droplet, the normal and radial movement would thus be the same. For a deformed droplet, we need to consider the relation between the normal interface movement,  $\hat{R}(t) = \mathbf{R}(t) \cdot \mathbf{n}$  and the radial movement  $R(t) = \mathbf{R}(t) \cdot \mathbf{e}_r$ . At fixed angles  $\theta$  and  $\phi$ , the interface movement is given by  $\partial_t \mathbf{R} = \partial_t R \mathbf{e}_r$ . Using  $\partial_t \hat{R} = \partial_t \mathbf{R}(t) \cdot \mathbf{n}$ , we find a relation between the radial and normal movement,  $\partial_t R = \partial_t \hat{R} / (\mathbf{n} \cdot \mathbf{e}_r)$ . This relation, together with Eq. (B.16), yields the interfacial movement Eq. (3.31) presented in the main text.

We thus recover all dynamical equations of the effective droplet model from the continuum model based on irreversible thermodynamics. Note that the specific choice

of the free energy leads to specific relations between parameters of the effective model such as  $D_+ = D_-$ . Our derivation shows the relation between both models in the case where the interface width  $w$  is small compared to the droplet size,  $R/w \gg 1$ , and the chemical diffusion length,  $l_{\pm}/w \gg 1$ . Additionally, we focused on the case where the concentrations in the phases are similar to the concentrations in equilibrium and have small concentration gradients. These conditions are not valid in all systems. Most importantly, the chemical reactions can drive concentrations far away from the equilibrium phase concentrations  $c_{\pm}^{(0)}$ . The resulting behaviors, such as the formation of new interfaces associated with instabilities of the spinodal decomposition regime, are not captured in the effective droplet model.

## Appendix C

### Details on the effective droplet model

---

#### C.1 Stationary states of spherical droplets

Stationary solutions to Eq. (3.20) with spherically symmetric concentration field can be expressed as

$$\bar{c}(r) = A_{\pm} + B_{\pm} \frac{e^{r/l_{\pm}}}{r} + C_{\pm} \frac{e^{-r/l_{\pm}}}{r}, \quad (\text{C.1})$$

where  $l_{\pm} = (D_{\pm}/k_{\pm})^{1/2}$  are characteristic length scales. Here, the coefficients  $A_{\pm}$  are set by the chemical reactions,

$$A_{\pm} = \pm \frac{\nu_{\pm}}{k_{\pm}} + c_{\pm}^{(0)}. \quad (\text{C.2})$$

Regular behavior at  $r = 0$  implies  $C_- = -B_-$ . For an infinite system, the concentration far from the droplet reaches a constant value. This implies  $B_+ = 0$ . Using the boundary conditions (3.28) and (3.29) at the interface of a spherical droplet of radius  $R$  we obtain the remaining coefficients

$$C_+ = \left( \frac{\gamma\beta_+}{R} - \frac{\nu_+}{k_+} \right) R \exp(R/l_+) \quad (\text{C.3a})$$

$$B_- = \left( \frac{\gamma\beta_-}{R} + \frac{\nu_-}{k_-} \right) \frac{R}{2 \sinh(R/l_-)}. \quad (\text{C.3b})$$

The normal fluxes at the droplet interface are

$$j_+(R) = \frac{D_+}{R} \left( \frac{\gamma\beta_+}{R} - \frac{\nu_+}{k_+} \right) \left( 1 + \frac{R}{l_+} \right) \quad (\text{C.4a})$$

$$j_-(R) = \frac{D_-}{R} \left( \frac{\gamma\beta_-}{R} + \frac{\nu_-}{k_-} \right) \left( 1 - \frac{R}{l_-} \coth \frac{R}{l_-} \right). \quad (\text{C.4b})$$

Using these steady state fluxes in Eq. (3.31) with Eq. (3.30) provides a relation between  $dR/dt = v_n$  and the droplet radius  $R$  in a quasi-static limit. Steady state droplets exist for radii  $R = \bar{R}$  for which  $dR/dt$  vanishes. These stationary radii thus obey

$$j_+(\bar{R}) = j_-(\bar{R}) . \quad (\text{C.5})$$

## C.2 Stability analysis of a spherical droplet without hydrodynamic flows

In the previous subsection, we discussed spherically symmetric stationary droplet states in the presence of chemical reactions. We saw that reactions can introduce a stationary droplet that is stable with respect to perturbations of the droplet volume. Next we will consider whether such stationary droplets are stable with respect to shape perturbations.

### C.2.0.1 Linearization at the stationary solution

We linearize the dynamic equations (3.20)–(3.31) of the effective droplet model without hydrodynamic flows around a stationary solution  $\bar{c}(r)$ , given by Eqs. (4.1)–(4.4). We consider small perturbations  $\delta c$  and  $\delta R$  of the concentration field and the droplet shape,

$$c(r, \theta, \varphi, t) = \bar{c}(r) + \delta c(r, \theta, \varphi, t) , \quad (\text{C.6})$$

$$R(\theta, \varphi, t) = \bar{R} + \delta R(\theta, \varphi, t) , \quad (\text{C.7})$$

where the stationary concentration profile  $\bar{c}$  is given by  $\bar{c}_-$  inside, and  $\bar{c}_+$  outside the droplet. The concentration perturbation then obeys

$$\partial_t \delta c = D_{\pm} \nabla^2 \delta c - k_{\pm} \delta c . \quad (\text{C.8})$$

The boundary conditions (3.28) and (3.29) become

$$\delta c(\bar{R}_{\pm}) = \beta_{\pm} \gamma \delta H - \bar{c}'(\bar{R}_{\pm}) \delta R , \quad (\text{C.9})$$

where  $\delta H = H(\bar{R} + \delta R) - H(\bar{R})$ . We denote the derivative of  $\bar{c}(r)$  evaluated at the interface position  $r = \bar{R}$  inside and outside the droplet, respectively, by  $\bar{c}'(\bar{R}_{\pm})$ . Using Eq. (3.31), the time dependence of the droplet shape perturbation is described to linear order by

$$(c_-^{(0)} - c_+^{(0)}) \partial_t \delta R = D_+ \partial_r \delta c(\bar{R}_+) - D_- \partial_r \delta c(\bar{R}_-) + [D_+ \bar{c}''(\bar{R}_+) - D_- \bar{c}''(\bar{R}_-)] \delta R . \quad (\text{C.10})$$

### C.2.0.2 Dynamic modes and relaxation spectrum

The linearized dynamics of droplet perturbations near the steady state defines a linear operator  $\mathcal{L}$  by

$$\partial_t \begin{pmatrix} \delta c \\ \delta R \end{pmatrix} = \mathcal{L} \begin{pmatrix} \delta c \\ \delta R \end{pmatrix}. \quad (\text{C.11})$$

An eigenfunctions  $(c_i, R_i)^\top$  of the operator  $\mathcal{L}$  obeys

$$\mathcal{L} \begin{pmatrix} c_i \\ R_i \end{pmatrix} = \mu_i \begin{pmatrix} c_i \\ R_i \end{pmatrix}, \quad (\text{C.12})$$

where  $\mu_i$  is the corresponding eigenvalues, and  $i$  is the mode index. The linear droplet dynamics can be decomposed in eigenmodes with amplitude  $A_i$  as

$$\begin{pmatrix} \delta c \\ \delta R \end{pmatrix} = \sum_i A_i \begin{pmatrix} c_i \\ R_i \end{pmatrix} e^{\mu_i t}, \quad (\text{C.13})$$

where the sum is over all eigenmodes. Thus, the eigenfunctions of  $\mathcal{L}$  correspond to dynamic modes of the system. For  $\mu_i < 0$ , the values  $-\mu_i$  are relaxation rates. The steady state is stable if all  $\mu_i < 0$ . To determine the stability of the droplet, we thus want to find out if any mode can be marginal, corresponding to  $\mu_i = 0$ , or unstable,  $\mu_i > 0$ .

### C.2.0.3 Determination of eigenmodes

We determine the eigenmodes and the spectrum of relaxation rates of a stationary droplet with radius  $\bar{R}$ . Because of the spherically symmetric reference state, we introduce radial and angular indices  $i = (n, m, l)$  and use the ansatz

$$\begin{pmatrix} c_{nlm}(r, \theta, \phi) \\ R_{nlm}(\theta, \phi) \end{pmatrix} = \begin{pmatrix} c_{nl}(r) \\ \epsilon_{nl} \bar{R} \end{pmatrix} Y_{lm}(\theta, \phi), \quad (\text{C.14})$$

where  $Y_{lm}$  are spherical harmonics and the corresponding eigenvalues will be denoted  $\mu_{nl}$ . Here we already indicate that the eigenvalue is independent of mode  $m$ , with  $-l \leq m \leq l$ . Using Eq. (C.8) with  $r^2 \nabla^2 Y_{lm} = l(l+1)Y_{lm}$ , the radial part of the eigenfunctions obeys

$$\left( \frac{1}{r^2} \frac{\partial}{\partial r} r^2 \frac{\partial}{\partial r} - (\lambda_{nl}^\pm)^2 - \frac{l(l+1)}{r^2} \right) c_{nl}(r) = 0, \quad (\text{C.15})$$

where

$$(\lambda_{nl}^\pm)^2 = \frac{k_\pm + \mu_{nl}}{D_\pm}. \quad (\text{C.16})$$

Eq. (C.15) is solved by the modified spherical Bessel functions  $k_l(\lambda_\pm r)$  and  $i_l(\lambda_\pm r)$ , which are shown in Fig. C.1. To avoid the imaginary parts arising for  $(\lambda_{nl}^\pm)^2 < 0$ , the spherical Bessel functions  $j_l(\hat{\lambda}_\pm r)$  and  $y_l(\hat{\lambda}_\pm r)$  can be used instead in this regime,

### C. DETAILS ON THE EFFECTIVE DROPLET MODEL

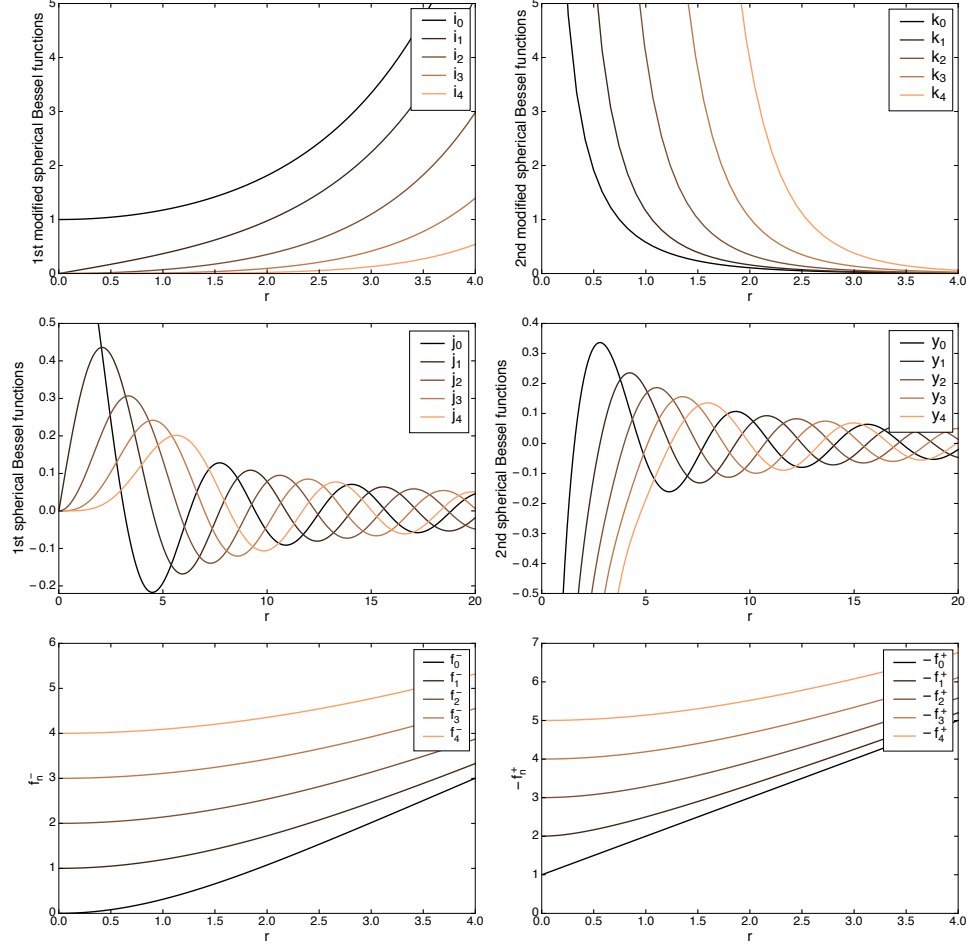


FIGURE C.1: top: modified Bessel functions, middle: spherical modified Bessel functions, bottom: functions  $f_i$  and  $f_k$  that arise in the stability analysis.

with  $(\hat{\lambda}_{nl}^\pm)^2 = -(\lambda_{nl}^\pm)^2$ . Both sets of functions are related by  $i_l(x) = i^{-n} j_l(ix)$  and  $k_l(x) = -i^{-n}(j_l(ix) + iy_l(ix))$ .

The boundary conditions (C.9) at  $r = \bar{R}$  can be written as

$$c_{nl}(\bar{R}_+) = a_l^+ \epsilon_{nl} \quad (\text{C.17a})$$

$$c_{nl}(\bar{R}_-) = a_l^- \epsilon_{nl} \quad (\text{C.17b})$$

with

$$a_l^\pm = \gamma \beta_\pm \frac{h_l}{\bar{R}} - c'(\bar{R}_\pm) \bar{R}, \quad (\text{C.18})$$

where  $h_l = (l^2 + l - 2)/2$ , see Zhong-can and Helfrich (1987). From Eqs. (C.17)

we obtain a boundary condition at  $r = \bar{R}$ :

$$\frac{c_{nl}(\bar{R}_+)}{c_{nl}(\bar{R}_-)} = \frac{a_l^+}{a_l^-}. \quad (\text{C.19})$$

This boundary condition determines the relation between coefficients of the solutions to Eq. (C.15) inside and outside the droplet. The total amplitude of the eigenfunction is undetermined and can be chosen freely. Using Eq. (C.10), we obtain an equation for the eigenvalue  $\mu_{nl}$ ,

$$\left(c_-^{(0)} - c_+^{(0)}\right) \mu_{nl} = D_+ \bar{c}''(\bar{R}_+) - D_- \bar{c}''(\bar{R}_-) + \frac{D_+ a_l^+}{\bar{R}} \frac{c'_{nl}(\bar{R}_+)}{c_{nl}(\bar{R}_+)} - \frac{D_- a_l^-}{\bar{R}} \frac{c'_{nl}(\bar{R}_-)}{c_{nl}(\bar{R}_-)}. \quad (\text{C.20})$$

Note that the right-hand side of Eq. (C.20) depends on the eigenvalue via the length-scales  $\lambda_{nl}^\pm$  in the functions  $c_{nl}$ . We order different solutions for the same  $l$  and  $m$  using the index  $n$  with  $\mu_{nl} > \mu_{n+1,l}$ . Using the quasistatic assumption, that is, that the concentration profile around a growing droplet with radius  $R$  is given by  $\bar{c}_\pm(r)$  with jump conditions at  $r = R$ , Eq. (C.20) for  $l \neq 0$  describes the shape instability of a growing droplet.

#### C.2.0.4 Radial profiles and relaxation rates of dynamic modes

Let us now discuss the shape of the solutions to Eqs. (C.14)-(C.20). We can differentiate between two main cases by the sign of  $(\lambda_{nl}^\pm)^2$ . Thereby, positive values correspond to large eigenvalues  $\mu_{nl} > -k_+$ , while negative values correspond to small eigenvalues  $\mu_{nl} < -k_+$ .

**Large eigenvalues: discrete spectrum** First we discuss  $(\lambda_{nl}^\pm)^2 > 0$  in both phases. For the concentration field we find

$$c_{nl}(r) = \begin{cases} k_l(\lambda_{nl}^+ r) & \text{for } r > \bar{R} \\ C_{nl} i_l(\lambda_{nl}^- r) & \text{for } r < \bar{R} \end{cases}, \quad (\text{C.21})$$

where we only considered solutions that are finite at  $r = 0$  and which do not diverge for large  $r$ . Any coefficient in front of  $k_l(\lambda_{nl}^+ r)$  outside the droplet may be set to one without loss of generality. The coefficient  $C_{nl}$  is determined by boundary conditions (C.19) as

$$C_{nl} = \frac{a_l^- k_l(\lambda_{nl}^+ \bar{R})}{a_l^+ i_l(\lambda_{nl}^- \bar{R})}. \quad (\text{C.22})$$

The equation for the eigenvalue (C.20) becomes

$$\begin{aligned} \left(c_-^{(0)} - c_+^{(0)}\right) \mu_{nl} = & D_+ \bar{c}''(\bar{R}_+) - D_- \bar{c}''(\bar{R}_-) \\ & + \frac{D_+ a_l^+}{\bar{R}^2} f_{k,l}(\lambda_{nl}^+ \bar{R}) - \frac{D_- a_l^-}{\bar{R}^2} f_{i,l}(\lambda_{nl}^- \bar{R}), \end{aligned} \quad (\text{C.23})$$

with  $f_{k,l}(x) = xk'_l(x)/k_l(x)$  and  $f_{i,l}(x) = xi'_l(x)/i_l(x)$ , shown in Fig. C.1. We find that Eq. (C.23) has a finite number of solutions, typically we find either no or one solution. The finite number of solutions can be seen by considering the asymptotic behavior  $\lambda_{nl}^+ \rightarrow \infty$  for the right-hand and left-hand side. The dependency of solutions to Eq. (C.23) on the parameters and the mode  $l$  generally is nontrivial. However, we can find analytically that the  $l = 1$  mode always has a solution  $\mu_{n1} = 0$  where all terms on the right-hand side of Eq. (C.23) cancel, using the properties of Bessel functions and of the stationary concentration field. This corresponds to a mode where the whole droplet including the concentration field is displaced by a small distance. Due to translational symmetry in an infinite system, the droplet will simply stay at its new position.

In the case  $(\lambda_{nl}^+)^2 > 0$  and  $(\lambda_{nl}^-)^2 < 0$ , we find for the concentration Eq. (C.21), but with  $f_{y,l}(\hat{\lambda}_{nl}^- \bar{R})$  instead of  $f_{i,l}(\lambda_{nl}^- \bar{R})$ , with  $f_{y,l}(x) = xy'_l(x)/y_l(x)$ . This case also yields a finite number of solutions with eigenvalues  $-k_- > \mu_{nl} > -k_+$ .

We therefore find a discrete, finite number of eigenvalues for  $\mu_{nl} > -k_+$  for every  $l, m$ . We distinguish the solutions by index  $n$ , whereby  $n = 1$  denotes the solution with the largest eigenvalues for a given  $l$ . These solutions correspond to different radial concentration profiles, with inverse length-scales  $\lambda_{nl}^\pm$ .

**Small eigenvalues: continuous spectrum** We now discuss the regime  $(\lambda_{nl}^+)^2 < 0$ . The spherical Bessel functions  $j_l$  and  $y_l$  vanish for large  $x$  as  $j_l(x) \sim x^{-1} \sin(x - l\pi/2)$  and  $y_l(x) \sim x^{-1} \cos(x - l\pi/2)$ . Therefore, both may be used as ansatz for the concentration field perturbation outside the droplet. This leads to a continuous spectrum of eigenvalues in this regime, for  $\mu_{nl} < -k_+$  for every  $l, m$ . We discuss this for the case  $(\lambda_{nl}^-)^2 < 0$ . The concentration field is given by

$$c_{nl}(r) = \begin{cases} A_{nl} j_l(\hat{\lambda}_{nl}^+ r) + B_{nl} y_l(\hat{\lambda}_{nl}^+ r) & \text{for } r > \bar{R} \\ C_{nl} j_l(\hat{\lambda}_{nl}^- r) & \text{for } r < \bar{R} \end{cases}. \quad (\text{C.24})$$

Without loss of generality, we may normalize the concentration eigenfunction, for example by  $c_{nl}^+(\bar{R}) = 1$ . The coefficient  $C_{nl}$  is determined by the boundary condition at the interface (C.19),

$$C_{nl} = \frac{a_l^-}{a_l^+} \frac{1}{j_l(\hat{\lambda}_{nl}^- \bar{R})}. \quad (\text{C.25})$$

The equation for the eigenvalue (C.20) becomes in this case

$$\begin{aligned} (c_-^{(0)} - c_+^{(0)}) \mu_{nl} = & D_+ \bar{c}''(\bar{R}_+) - D_- \bar{c}''(\bar{R}_-) - \frac{D_- a_l^-}{\bar{R}^2} \hat{\lambda}_{nl}^- \bar{R} \frac{j'_l(\hat{\lambda}_{nl}^- \bar{R})}{j_l(\hat{\lambda}_{nl}^- \bar{R})} \\ & + \frac{D_+ a_l^+}{\bar{R}^2} \hat{\lambda}_{nl}^+ \bar{R} \left( A_{nl} j'_l(\hat{\lambda}_{nl}^+ \bar{R}) + B_{nl} y'_l(\hat{\lambda}_{nl}^+ \bar{R}) \right). \end{aligned} \quad (\text{C.26})$$

for the case  $(\lambda_{nl}^-)^2 < 0$ . For  $j_l(\hat{\lambda}_{nl}^+ \bar{R}) \neq 0$  and  $y_l(\hat{\lambda}_{nl}^+ \bar{R}) \neq 0$  (thus, for almost all  $\hat{\lambda}_{nl}^+$ ), we can determine  $B_{nl}$  from  $A_{nl}$  using the normalization condition  $c_{nl}^+(\bar{R}) = 1$ .



This yields for the last line in Eq. (C.26)  $Aj' + By' = y'/y + A(j' - jy'/y)$  (where we omitted the indices). Using the relations between Bessel functions, Abramowitz et al. (1965) (Equations 10.1.21 and 10.1.31), we can show that  $j' - jy'/y$  is nonzero for all finite values  $\hat{\lambda}_{nl}^+ \bar{R}$ . We can thus solve Eq. (C.26) for any such fixed  $\lambda_{nl}^+$  by choosing an appropriate  $A_{nl}$ . For  $j_l(\hat{\lambda}_{nl}^+ \bar{R}) = 0$ , the coefficient  $B_{nl}$  is fixed by the normalization, while  $A_{nl}$  is free. In this case,  $j'_l(\hat{\lambda}_{nl}^+ \bar{R}) \neq 0$ , and thus we can solve Eq. (C.26) for any such fixed  $\lambda_{nl}^+$  by choosing  $A_{nl}$ . The equivalent argument holds for  $y_l(\hat{\lambda}_{nl}^+ \bar{R}) = 0$ . The argument is independent of the sign of  $(\lambda_{nl}^-)^2$ . We therefore find a continuous spectrum of eigenvalues for  $\mu_{nl} < -k_+$  for every  $l, m$ .

### C.3 Scaling behavior of stationary radius and instability in the effective droplet model

In the main text we discuss the stationary radius and its shape stability in the effective droplet model. We consider the limit of vanishing chemical reactions  $A \rightarrow 0$ , corresponding to  $\nu_- \rightarrow 0$ . We additionally keep the ratios  $\nu_-/k_-$  and  $k_-/k_+$  fixed, so that the reaction-diffusion length-scales  $l_{\pm}$  in both phases diverge. In this case, the supersaturation  $\epsilon$  is an independent variable. For vanishing chemical reactions, the supersaturation is not chemically generated, but rather a boundary value far from the droplet, which may be created by a reservoir or transport, or by considering an initially supersaturated state in which the droplet forms. This is a well-controlled limit that is both mathematically rigorous and physically relevant. Additionally, it provides a continuous path from our current discussion of chemically active droplets towards passive droplets in an Ostwald-ripening scenario, as discussed by Lifshitz and Slyozov (1961). We present details of the calculation in this appendix.

#### C.3.1 Scaling behavior of the stationary radius

When we vary only  $A$ , and keep all other parameters constant, the length-scales diverge as  $l_{\pm} = \hat{l}_{\pm} w A^{-1/2}$  with  $\hat{l}_+ = (\frac{k_-}{k_+} \frac{\nu_-}{k_- \Delta c})^{1/2}$  and  $\hat{l}_- = (\frac{D_-}{D_+} \frac{\nu_-}{k_- \Delta c})^{1/2}$ . The relation between supersaturation and the stationary radius is given by Eq. (4.4), or explicitly

$$\epsilon(R) = \frac{\beta_+ \gamma}{R \Delta c} + \left( \frac{\beta_- \gamma}{R \Delta c} + \frac{\nu_-}{k_- \Delta c} \right) \frac{D_-}{D_+} \frac{\frac{R}{\hat{l}_-} \coth \frac{R}{\hat{l}_-} - 1}{1 + \frac{R}{\hat{l}_+}}. \quad (\text{C.27})$$

We assume that  $R$  scales inversely with  $A$  with some unknown exponent  $a$ , such that  $R = \hat{R} w A^{-a}$ . This gives

$$\epsilon = \frac{1}{6 \hat{R}} A^a + \left( \frac{\beta_-}{\beta_+} \frac{1}{6 \hat{R}} A^a + \frac{\nu_-}{k_- \Delta c} \right) \frac{D_-}{D_+} \frac{\frac{\hat{R}}{\hat{l}_-} A^{\frac{1}{2}-a} \coth \left( \frac{\hat{R}}{\hat{l}_-} A^{\frac{1}{2}-a} \right) - 1}{1 + \frac{\hat{R}}{\hat{l}_+} A^{\frac{1}{2}-a}}, \quad (\text{C.28})$$

where we used the definition of our length-scale  $w = 6\beta_+ \gamma / \Delta c$ . We can now analyze the scaling behavior of  $f(R)$  for different values of  $a$ . To expand the terms, we use  $x \coth x = 1 + x^2/3 + O(x^4)$  and  $1/(1+x) = 1 - x + O(x^2)$  for  $x \rightarrow 0$ , and  $x \coth x \rightarrow x(1 + 2(e^{2x} - 1))$  for  $x \rightarrow \infty$ .

**Scaling with  $a = 1/2$**  For  $a = 1/2$ , the terms with  $A^a$  vanish, and only the constants with  $A^{1/2-a}$  are relevant,

$$\epsilon(R) \rightarrow \frac{D_-}{D_+} \frac{\nu_-}{k_- \Delta c} \frac{\frac{\hat{R}}{\hat{l}_-} \coth \left( \frac{\hat{R}}{\hat{l}_-} \right) - 1}{1 + \frac{\hat{R}}{\hat{l}_+}} + O(A^{1/2}). \quad (\text{C.29})$$

### C.3. Scaling behavior of stationary radius and instability in the effective droplet model

Depending on the parameters of the chemical reaction and diffusion, we can consider the two limits  $\hat{R} \gg \hat{l}_\pm$  and  $\hat{R} \ll \hat{l}_\pm$ . We find  $\epsilon(R) \rightarrow \frac{1}{3} \frac{D_-}{D_+} \frac{\nu_-}{k_- \Delta c} \left( \frac{\hat{R}}{\hat{l}_-} \right)^2$  for  $\hat{R} \ll \hat{l}_\pm$ , and  $\epsilon(R) \rightarrow \epsilon_\infty$  for  $\hat{R} \gg \hat{l}_\pm$  with

$$\epsilon_\infty = \sqrt{\frac{D_- k_-}{D_+ k_+} \frac{\nu_-}{k_- \Delta c}}. \quad (\text{C.30})$$

**Scaling with  $a = 0$**  For  $a = 0$ , we find to lowest order  $\epsilon(R) \rightarrow \frac{1}{6\hat{R}} + O(A)$ .

**Scaling with  $0 < a < 1/2$**  For  $0 < a < 1/2$ , it is not a priori clear which of the terms  $A^a$  or  $A^{1/2-a}$  are dominant. So generally expanding all terms, we find

$$\epsilon(R) \rightarrow \frac{1}{6\hat{R}} A^a + \frac{1}{3} \frac{D_-}{D_+} \frac{\nu_-}{k_- \Delta c} \left( \frac{\hat{R}}{\hat{l}_-} \right)^2 A^{1-2a} + O(A^{1-a}, A^{3(1/2-a)}). \quad (\text{C.31})$$

We observe that of the two dominant terms, the first goes with  $1/\hat{R}$ , and the second with  $\hat{R}^2$ . Thus, for increasing  $\hat{R}$ , the first shrinks and the second one grows. Thus the minimum of  $\epsilon(R)$  we observe numerically, which characterizes the threshold in  $\epsilon$  above which stationary droplet radii exist, can be found when both terms are relevant, so for  $a = 1/3$ .

**Scaling with  $a = 1/3$**  The onset of stationary solutions is described by the minimum of  $\epsilon(R)$ , which obeys scaling with  $a = 1/3$ ,

$$\epsilon(R) \rightarrow \underbrace{\left( \frac{1}{6\hat{R}} + \frac{1}{3} \frac{D_-}{D_+} \frac{\nu_-}{k_- \Delta c} \left( \frac{\hat{R}}{\hat{l}_-} \right)^2 \right)}_{\hat{\epsilon}(\hat{R})} A^{1/3} + O(A^{1/2}), \quad (\text{C.32})$$

where we can define a rescaled function  $\hat{\epsilon}(\hat{R})$ , which can be rewritten as

$$\hat{\epsilon} = \frac{1}{6} \hat{R}^{-1} + \frac{1}{3} \hat{R}^2. \quad (\text{C.33})$$

We can find the minimum via  $\hat{\epsilon}'(\hat{R}_0) = 0$ , which yields  $\hat{R}_0 = 4^{-1/3}$ . Inserting this in Eq. (C.33) gives  $\hat{\epsilon}_0 = 4^{-2/3}$ .

#### C.3.2 Scaling behavior of the instability for $a = 1/3$

We now discuss the scaling of the shape instability, described by Eq. (4.13) in the regime where the stationary radius scales with  $a = 1/3$ . To calculate the scaling

behavior of the instability, we need the following expansions, for  $l_{\pm} = \hat{l}_{\pm} w A^{-1/2}$  and  $R = \hat{R} w A^{-1/3}$ , and  $\epsilon = \hat{\epsilon} A^{1/3}$ . We find

$$\bar{c}'_+(R) \approx \frac{\Delta c}{w} \frac{1}{\hat{R}} \left( \hat{\epsilon} - \frac{1}{6\hat{R}} \right) A^{2/3} + O(A^{5/6}) \quad (\text{C.34})$$

$$\bar{c}'_-(R) \approx \frac{\Delta c}{w} \frac{1}{3} \frac{D_+}{D_-} \hat{R} A^{2/3} + O(A^1) \quad (\text{C.35})$$

$$\bar{c}''_+(R) \approx \frac{\Delta c}{w^2} \frac{2}{\hat{R}^2} \left( \frac{1}{6\hat{R}} - \hat{\epsilon} \right) A^1 + O(A^{7/6}) \quad (\text{C.36})$$

$$\bar{c}''_-(R) \approx \frac{\Delta c}{w^2} \frac{1}{3} \frac{D_+}{D_-} A^1 + O(A^{4/3}) \quad (\text{C.37})$$

For  $\bar{c}'_{\pm}$ , we thus recover the previous results for the stationary radius in scaling regime  $a = 1/3$  via  $j_-(R) = j_+(R)$ .

Inserting this in the equation for the eigenvalue Eq. (4.13) we find

$$\begin{aligned} \mu \approx & \left[ D_+ \frac{\Delta c}{w^2} \frac{2}{\hat{R}^2} \left( \frac{1}{6\hat{R}} - \hat{\epsilon} \right) - D_- \frac{\Delta c}{w^2} \frac{1}{3} \frac{D_+}{D_-} \right. \\ & + \frac{D_+}{\hat{R}^2} \frac{1}{w^2} \frac{1}{6\hat{R}} h_l (-l-1) - \frac{D_+}{\hat{R} w} \frac{\Delta c}{w} \frac{1}{\hat{R}} \left( \hat{\epsilon} - \frac{1}{6\hat{R}} \right) (-l-1) \\ & \left. - \frac{D_-}{\hat{R}^2} \frac{1}{w^2} \frac{1}{6\hat{R}} h_l l + \frac{D_-}{\hat{R} w} \frac{\Delta c}{w} \frac{1}{3} \frac{D_+}{D_-} \hat{R} l \right] A + O(A^{7/6}), \quad (\text{C.38}) \end{aligned}$$

which can be written for the rescaled eigenvalue  $\hat{\mu} = \mu t_0 A^{-1}$  as

$$\hat{\mu} \approx (l-1) \left( \frac{\hat{\epsilon}}{\hat{R}^2} + \frac{1}{3} \right) - \frac{1}{6\hat{R}^3} \left( l-1 + h_l(l+1) + h_l \cdot l \frac{D_- \beta_-}{D_+ \beta_+} \right) \quad (\text{C.39})$$

with curvature term  $h_l = (l^2 + l - 2)/2$ . For this result, we assumed  $\lambda_{\pm} R \ll 1$ , which, in our scaling calculation for small  $A$ , is valid for small (or zero)  $\mu$ . In above description, the first line contains the stabilizing, and the second line the destabilizing terms. We see here that for fixed parameters (and fixed radius), the stabilizing terms increase faster for growing mode  $l$  than the destabilizing terms. Seen as a function of  $\hat{R}$ , the destabilizing terms grow with the radius, while the stabilizing ones vanish. In non-rescaled form, this can be written as

$$\mu t_0 \approx (l-1) \left( \frac{\epsilon w^2}{R^2} + \frac{1}{3} A \right) - \frac{w^3}{6R^3} \left( l-1 + h_l(l+1) + h_l \cdot l \frac{D_- \beta_-}{D_+ \beta_+} \right). \quad (\text{C.40})$$

This form highlights the term  $A/3$  which is created by the chemical reaction inside the droplet, which separates the chemically active system from the growth of a non-reactive droplet in supersaturated background.

The description of the eigenvalues is valid also in a quasistatic limit where the droplet radius is close to a stationary radius and changes only slowly over time. In this case, we can treat the radius and concentration field as constant, but with  $j_-(R) \neq$

$j_+(R)$ . Therefore an interpretation in terms of a slowly growing radius (growing from  $R > R_c$  towards  $R = \bar{R}$ ) is possible. In this case we see that for a small radius ( $R \approx R_c$ ) the stabilizing terms dominate, and then consecutive modes (starting with  $l = 2$ ) can become unstable - how many modes become unstable is limited in a purely linear idea only by the size of the stationary radius. In a nonlinear case, other effects might dominate, for example the droplet division we observed, by which the droplet volume can decrease before it reaches the stationary radius.

### C.3.2.1 Stability of the stationary radius

Looking purely at the stationary radius, we find via  $j_-(R) = j_+(R)$  a relation between  $\bar{c}'_+(R)$  and  $\bar{c}'_-(R)$ :

$$\bar{c}'_-(R) = \frac{D_+}{D_-} \bar{c}'_+(R) \quad (\text{C.41})$$

Inserting this in our equation for  $\mu$ , we find

$$\hat{\mu} \hat{R}^2 \approx 2(l-1)\hat{\epsilon} - \frac{1}{6\hat{R}} \left( 2(l-1) + h_l(l+1) + h_l \cdot l \frac{D_-\beta_-}{D_+\beta_+} \right) \quad (\text{C.42})$$

We can thus express the onset of instability  $R_l^*$  of the stationary radius similar to the nucleation radius as a function of the mode  $l$  and the supersaturation

$$R_l^* \approx \frac{w}{6\epsilon} \frac{2(l-1) + h_l(l+1) + h_l \cdot l \frac{D_-\beta_-}{D_+\beta_+}}{2(l-1)}. \quad (\text{C.43})$$

Using  $w = 6\beta_+\gamma/\Delta c$ , this can be compared to the corresponding equation of the Mullins-Sekerka instability, Eq. (4.17). We find that the reaction inside the droplet, which also creates the stationary size, leads to a difference in both functions. Evaluating the equation gives

$$R_2^* \approx \frac{\beta_+\gamma}{\epsilon\Delta c} \left( 4 + 2 \frac{D_-\beta_-}{D_+\beta_+} \right), \quad (\text{C.44})$$

compared to

$$R_2^{ms} \approx \frac{\beta_+\gamma}{\epsilon\Delta c} \left( 7 + 4 \frac{D_-\beta_-}{D_+\beta_+} \right), \quad (\text{C.45})$$

in the case of the Mullins-Sekerka instability.

Using Eq. (C.41) to replace  $\epsilon$  in Eq. (C.39) instead, we find

$$\hat{\mu} \approx \frac{2}{3}(l-1) - \frac{1}{6\hat{R}^3} \left( h_l(l+1) + h_l \cdot l \frac{D_-\beta_-}{D_+\beta_+} \right) \quad (\text{C.46})$$

This form can be used to estimate the eigenvalue  $\mu$  as a function of the stationary radius: For  $l = 0$  the first term is negative, while the second term is positive, thus,

the mode is unstable for small radii and stable for larger ones. For  $l = 1$ , the right-hand side is zero, so that we find that in this limit, the translational mode is marginal. For  $l > 1$ , small stationary radii are stable, while larger ones become unstable, and the mode reaches a constant value for large  $\hat{R}$ ,

$$\hat{\mu} \approx \frac{2}{3}(l - 1) \quad (\text{C.47})$$

For the onset of the instability we find

$$R_l^* = w \left( \frac{1}{4} \frac{h_l(l+1) + \frac{D_-\beta_-}{D_+\beta_+} h_l l}{l-1} \right)^{1/3} A^{-1/3} \quad (\text{C.48})$$

and evaluated for some modes

$$R_0^* = \left( \frac{1}{4} \right)^{1/3} A^{-1/3} \quad (\text{C.49})$$

$$R_2^* = \left( \frac{3}{2} + \frac{D_-\beta_-}{D_+\beta_+} \right)^{1/3} A^{-1/3} \quad (\text{C.50})$$

For the  $l = 0$  mode, the sign of  $\mu$  around this value is reversed (because  $h_{l=0}$  is negative), so for larger radii, the mode becomes stable, while for all other modes the mode becomes unstable beyond this radius. The  $l = 0$  mode becomes unstable at stationary radius  $R_0$ , as calculated below Eq. (C.33).

### C.3.2.2 Scaling behavior of phase diagram

Equating both forms for  $R_l^*$ , we find the scaling behavior that the onset of the instability of mode  $l$  would have in a phase diagram of  $A$  and  $\epsilon$ . For all modes ( $l \neq 1$ ) we find  $A_l \propto \epsilon^3$ , and explicitly

$$A_l \approx 54 \frac{gl}{(1 + \frac{1}{2}gl)^3} \epsilon^3 \quad (\text{C.51})$$

with

$$gl = \frac{h_l(l+1) + h_l l \frac{D_-\beta_-}{D_+\beta_+}}{l-1}. \quad (\text{C.52})$$

We find the existence of a stationary solution

$$A_0 \approx 16\epsilon^3. \quad (\text{C.53})$$

For the mode  $l = 2$  we find (for  $D_+ = D_-$  and  $\beta_+ = \beta_-$ )

$$A_2 \approx \frac{5}{2}\epsilon^3. \quad (\text{C.54})$$

### C.3.3 Scaling behavior of the instability for $a = 1/2$

To calculate the scaling behavior of the instability Eq. (4.13) in the regime  $a = 1/2$ , where the stationary state is described by Eq. (C.29), we need the following expansions, for  $l_{\pm} = \hat{l}_{\pm} w A^{-1/2}$  and  $R = \hat{R} w A^{-1/2}$ . We find

$$\bar{c}'_+(R) \approx \frac{\Delta c}{w} \frac{1}{\hat{R}} \epsilon \left( -f_{k,0} \left( \frac{\hat{R}}{\hat{l}_+} \right) \right) A^{1/2} + O(A^1) \quad (\text{C.55})$$

$$\bar{c}'_-(R) \approx \frac{\Delta c}{w} \frac{1}{\hat{R}} \frac{\nu_-}{k_- \Delta c} f_{i,0} \left( \frac{\hat{R}}{\hat{l}_-} \right)^2 A^{1/2} + O(A^1) \quad (\text{C.56})$$

$$\bar{c}''_+(R) \approx -\frac{\Delta c}{w^2} \frac{\epsilon}{\hat{R}^2} \left( 2 + 2 \left( \frac{\hat{R}}{\hat{l}_+} \right) + \left( \frac{\hat{R}}{\hat{l}_+} \right)^2 \right) A^1 + O(A^{3/2}) \quad (\text{C.57})$$

$$\bar{c}''_-(R) \approx \frac{\Delta c}{w^2} \frac{1}{\hat{R}^2} \frac{\nu_-}{k_- \Delta c} \left( 2 + \left( \frac{\hat{R}}{\hat{l}_-} \right)^2 - 2 \left( \frac{\hat{R}}{\hat{l}_-} \right) \coth \left( \frac{\hat{R}}{\hat{l}_-} \right) \right) A^1 + O(A^{3/2}) \quad (\text{C.58})$$

For the instability, Eq. (4.13), we find

$$\begin{aligned} \mu t_0 = & -\frac{\epsilon}{\hat{R}^2} \left( 2 + 2 \left( \frac{\hat{R}}{\hat{l}_+} \right) + \left( \frac{\hat{R}}{\hat{l}_+} \right)^2 \right) A^1 - \\ & \frac{D_-}{D_+} \frac{1}{\hat{R}^2} \frac{\nu_-}{k_- \Delta c} \left( 2 + \left( \frac{\hat{R}}{\hat{l}_-} \right)^2 - 2 \left( \frac{\hat{R}}{\hat{l}_-} \right) \coth \left( \frac{\hat{R}}{\hat{l}_-} \right) \right) A^1 \\ & + \frac{\epsilon}{\hat{R}^2} \left( -f_{k=0} \left( \frac{\hat{R}}{\hat{l}_+} \right) \right) (-f_k(\lambda_+ R)) A^1 + \frac{D_-}{D_+} \frac{1}{\hat{R}^2} \frac{\nu_-}{k_- \Delta c} f_i(\lambda_- R) A^1 \quad (\text{C.59}) \end{aligned}$$

For small values of  $\mu R^2/D_+$ , we can expand

$$\lambda_{\pm} R \approx \frac{\hat{R}}{\hat{l}_{\pm}} + \frac{1}{2} \frac{\hat{R}}{\hat{l}_{\pm}} \mu t_0 \hat{R}^2 A^{-1} + O\left(\frac{\mu R^2}{D_{\pm}}\right) \quad (\text{C.60})$$

We can study this in two limits: For  $\hat{R}/\hat{l}_{\pm} \ll 1$ , and for  $\hat{R}/\hat{l}_{\pm} \gg 1$ .

#### C.3.3.1 Limit $\hat{R}/\hat{l}_{\pm} \ll 1$

In this limit we find

$$\mu A^{-1} t_0 \hat{R}^2 \approx \epsilon \left( (l-1) \left( 1 + \frac{\hat{R}}{\hat{l}_+} \right) - \left( \frac{\hat{R}}{\hat{l}_+} \right)^2 \right) + \frac{1}{3} (l-1) \frac{D_-}{D_+} \frac{\nu_-}{k_- \Delta c} \left( \frac{\hat{R}}{\hat{l}_-} \right)^2 \quad (\text{C.61})$$

Replacing the last term for the stationary radius by  $j_-(R) = j_+(R)$ , we find

$$\mu A^{-1} t_0 \hat{R}^2 \approx \epsilon \left( (l-1) \left( 2 + \frac{\hat{R}}{\hat{l}_+} \right) - \left( \frac{\hat{R}}{\hat{l}_+} \right)^2 \right) \quad (\text{C.62})$$

In our limit,  $\hat{R} \ll \hat{l}_+$ , this is always positive for  $l > 1$  and negative for  $l = 0$ . We can use this to estimate the growth mode  $\mu$ ,

$$\mu t_0 A^{-1} \approx \frac{2}{3} (l-1), \quad (\text{C.63})$$

which matches the limit for the scaling regime  $a = 1/3$ , Eq. (C.47).

### C.3.3.2 Limit $\hat{R}/\hat{l}_\pm \gg 1$

In this limit, with  $f_i(x) \approx -1 + x$  and  $f_k(x) \approx -1 - x$  (for  $x$  large), and taking the linear order for  $\mu$  in  $\lambda_\pm R/D_\pm$  into account, we find

$$\mu t_0 A^{-1} \hat{R}^2 \approx \frac{-\epsilon(1 + \frac{\hat{l}_\pm}{\hat{l}_-})}{1 - \frac{\epsilon}{2}(1 + \frac{D_\pm \hat{l}_\pm}{D_- \hat{l}_-})} \quad (\text{C.64})$$

where we used the limit  $\epsilon_\infty$  for  $\epsilon$  given in Eq. (4.27). In this regime,  $\hat{R} \rightarrow \infty$ , so that we find  $\mu t_0 A^{-1} \approx 0$  there.



# Appendix D

## Details on the continuum droplet model

---

### D.1 Linear stability of the homogeneous state in the continuum droplet model

We can use the extended Cahn-Hilliard model to study the dynamic shape changes of droplets in different geometries. For droplets much larger than the interfacial width, and for dynamical behavior without topological changes, we expect similarities between our stability analysis using the sharp droplet model and the dynamics in the extended Cahn-Hilliard model. The dynamic equation is  $\partial_t c = m\Delta\mu_{loc} - m\kappa\Delta^2 c + s(c)$ , with local relative chemical potential  $\mu_{loc}(c)$ .

The extended Cahn-Hilliard model describes nucleation of new droplets, and topological changes. This means that the homogeneous state can become unstable, an effect that was not considered in the linear stability analysis. The difference between the models is here created by the way the effective droplet model is derived - to get the linearized diffusive dynamics, the free energy density is approximated as parabolic in both phases, and thus convex. The full free energy density has an inflection point, however, beyond which local density variations lead to a lowering of the energy, resulting in spinodal decomposition. This instability is changed in the presence of chemical reactions, which can increase or decrease the stability of the homogeneous state.

We can expand the dynamic equation for a small spatial perturbation  $\delta c$  around a homogeneous concentration  $c_0$ ,  $c = c_0 + \delta c$ . We assume that the concentration  $c$  is in the regime where the linearization for the chemical reaction outside the droplet still holds,  $s(c) = \nu_+ - k_+(c - c_+^{(0)})$ . We find  $\partial_t c_0 = s(c_0)$ , and

$$\partial_t \delta c = \mu'(c_0)\Delta\delta c - m\kappa\Delta^2\delta c - k_+\delta c, \quad (\text{D.1})$$

with  $\mu'(c) = d\mu_{loc}(c)/dc$ . For a decomposition in sinusoidal perturbations,

$$\delta c = \sum_q \epsilon_q \sin(qx) e^{\eta(q)t} \quad (\text{D.2})$$

we find the eigenvalue

$$\eta(q) = -(k_+ + \mu'(c_0)q^2 + m\kappa q^4). \quad (\text{D.3})$$

Contrary to the linear stability analysis of different droplet shapes, this is an explicit equation for the eigenvalue. The only way the reactions enters is through the constant  $k_+$ , which shifts the eigenvalue by a constant, independent of the wavevector  $q$ . For large wavevectors, the eigenvalue is negative, leading to a stable perturbation. The long wave-length limit  $q \rightarrow 0$  is determined by  $k_+$ . The intermediate range is determined by the sign of  $\mu'(c_0)$ . For  $\mu'(c_0) < 0$  modes can be unstable, and the dominant mode (most unstable one) is determined as

$$q_* = \sqrt{-\mu'(c_0)/(2m\kappa)} \quad (\text{D.4})$$

with maximal eigenvalue

$$\eta(q_*) = \frac{\mu'(c_0)^2}{4m\kappa} - k_+. \quad (\text{D.5})$$

## D.2 Numerical solution of the continuum model

### D.2.1 A semi-implicit quasi-spectral solver

We numerically solve the dynamic equations of the continuum model of active droplets introduced in section 3.1. This includes the equations for the concentration field (3.1) with fluxes (3.2), the chemical potential (3.5) with (3.6), stress balance (3.11) with incompressibility (3.12) and the chemical reaction (3.13) with (3.14).

For this we use a spectral method in a 3d rectangular box. This has the advantage that in a spectral decomposition, the spatial operators become simple multiplications with the wavenumber Chen and Shen (1998). However, our equations contain a number of nonlinear functions, which are easier to evaluate in real space. We therefore transform forward and back in each time step.

To calculate the next time step  $t_i$  from the fields found in time step  $t_{i-1}$ , we use a semi-implicit Runge-Kutta method Ascher et al. (1997) (method (2,3,3)) for the concentration field. This evaluates the gradient term in  $\bar{\mu}$ , Eq. (3.5), implicitly, while evaluating the rest of  $\bar{\mu}$  as well as the advection term of the fluxes,  $\mathbf{v}c$ , explicitly. This effectively means that the terms related to the interfacial profile are calculated implicitly, which allows for larger time steps as an explicit scheme.

For the concentration field, we choose no-flux boundary conditions ( $\partial_n c = 0$ , where the derivative is in a direction normal to the simulation box), which leads to a decomposition in cosine functions in the spectral description. The Laplacian then

is  $-k^2$  for a mode with wave vector  $\mathbf{k}$ . The Stokes equation can also be solved using spectral methods. Here, no-flux conditions lead to  $v_n = 0$ . Additionally we enforce incompressibility using a reprojection method. For this, the velocity field calculated by neglecting the partial pressure,  $P_p = 0$ , can be split into two parts (Helmholtz decomposition),

$$\mathbf{v} = \mathbf{v}_\psi + \mathbf{v}_\phi = \nabla \times \boldsymbol{\psi} - \nabla \phi \quad (\text{D.6})$$

with vector field  $\boldsymbol{\psi}$  and scalar field  $\phi$ , and velocity parts  $\mathbf{v}_\psi = \nabla \times \boldsymbol{\psi}$  and  $\mathbf{v}_\phi = -\nabla \phi$ . With this, we find

$$\nabla \cdot \mathbf{v} = \Delta \phi \quad (\text{D.7})$$

and thus, using incompressibility,  $\nabla \cdot \mathbf{v} = 0$ , we can calculate  $\phi$ . We thus find the incompressible part of the velocity field

$$\mathbf{v}_\psi = \mathbf{v} - \nabla \phi. \quad (\text{D.8})$$

We can evaluate this in Fourier space using a spectral method. For a rectangular box aligned with the coordinate system, we thus find that each velocity component  $v_\alpha$  is decomposed by sines in one direction and cosines in the other direction. Spatial derivatives convert a sine-description into cosines, and vice versa.

We normalize concentration, length, time and energy by  $\Delta c = c_-^{(0)} - c_+^{(0)}$ ,  $w = 2(\kappa/b)^{1/2}$ ,  $t_0 = w^2/D$  and  $\hat{e}_0 = \kappa w(\Delta c)^2/3$ , respectively.

### D.2.2 Numerical details for simulations with hydrodynamics

For the simulation with hydrodynamic flows, Fig. 7.5, we employed the method detailed in D.2.1. We choose  $c_+^{(0)}/\Delta c = 0$ ,  $kt_0 = 10^{-2}$ ,  $\nu t_0 = 2 \cdot 10^{-3}$  and  $\eta \hat{w}^3/(t_0 \hat{e}_0) = 2$ . Additionally, we use as box-length  $L/\hat{w} = 100$  in all 3 dimensions, number of grid-points in one direction  $N = 128$  and simulation time  $T/t_0 = 4 \cdot 10^3$ . For the time step, we start with a time step of  $\Delta t/t_0 = 10^{-4}$ , and double the time step to a final step size of  $\Delta t/t_0 = 0.01$ .

We start with initial conditions  $R = R_0(1 + \epsilon Y_{2,0})$ . The concentration field at positions  $\mathbf{r}$  is initialized by the function

$$c(\mathbf{r}) = \frac{c_+^{(0)} + c_-^{(0)}}{2} + \frac{c_+^{(0)} - c_-^{(0)}}{2} \tanh \frac{d(\mathbf{r})}{w}. \quad (\text{D.9})$$

where  $d(\mathbf{r})$  is the oriented distance of  $\mathbf{r}$  to the nearest point on the ellipsoid. The value of  $d(\mathbf{r})$  is negative for points inside the droplet and positive for points outside.

### D.2.3 Numerical details for simulations without hydrodynamics

We employed two methods to solve the dynamic equations without hydrodynamic flows. For the results in Fig. 5.2, Fig. 5.1 and Fig. 5.4, we solved the dynamic equations for the case  $\mathbf{v} = 0$  numerically using the xmds2 software package, Dennis et al.

(2013) (version 2.2.2), with an adaptive Runge-Kutta scheme of order 4/5, with tolerance  $10^{-5}$ . For the results in Fig. 5.3, we used the semi-implicit method described in D.2.1, with  $\mathbf{v} = 0$ . We tested that both methods yield similar results and converge for vanishing stepsizes. In both cases, the Laplace operator was evaluated by a spectral method, while the chemical rates were evaluated in real space. Numerical calculations were performed in a finite volume with no flux boundary conditions.

We normalize concentration, length and time by  $\Delta c = c_-^{(0)} - c_+^{(0)}$ ,  $\hat{w}$  and  $t_0 = \hat{w}^2/D$ , respectively, where the characteristic length scale is  $\hat{w} = 2(\kappa/b)^{1/2}$ . The relevant dimensionless model parameters are  $c_+^{(0)}/\Delta c$ ,  $k_{\pm}t_0$ ,  $\nu_{\pm}t_0/\Delta c$  and  $c_c^{\pm}/\Delta c$ . In all numerical calculations, we chose  $c_+^{(0)}/\Delta c = 0$  and  $k_{\pm}t_0 = 10^{-2}$ .

### D.2.3.1 Stability diagram

Using three dimensional calculations in Cartesian coordinates, we observed that droplet configurations during the division of isolated single droplets were approximately axisymmetric. To determine the stability diagram shown in Fig. 5.2 we therefore performed calculations in cylindrical coordinates imposing axisymmetry. We used an axisymmetric cylindrical box with length  $60\hat{w}$  and radius  $30\hat{w}$ , discretized with 120 and 60 points, respectively.

The initial conditions were given by a concentration profile that corresponded to a droplet geometry of a slightly prolate ellipsoid with unequal half axes of length  $R/\hat{w} - 0.1$  and  $R/\hat{w} + 0.1$ , centered at the box center. The initial droplet size was chosen close to the stationary size in the continuum model. As an estimate for the stationary size we typically chose  $R/\hat{w} = 0.9\bar{R}_s/w$ . Here,  $\bar{R}_s$  is the stationary radius calculated in the effective droplet model and  $w = 6\beta_+\gamma/\Delta c$ , see Section 3.2. The concentration field at positions  $\mathbf{r}$  was initialized by the function

$$c(\mathbf{r}) = \frac{c_{\infty} + c_-^{(0)}}{2} + \frac{c_{\infty} - c_-^{(0)}}{2} \tanh \frac{d(\mathbf{r})}{\hat{w}}. \quad (\text{D.10})$$

where  $d(\mathbf{r})$  is the oriented distance of  $\mathbf{r}$  to the nearest point on the ellipsoid. The value of  $d(\mathbf{r})$  is negative for points inside the droplet and positive for points outside. The concentration far from the droplet is  $c_{\infty} = \nu_+/k_+ + c_+^{(0)}$ .

We calculated the dynamics of the concentration field over a time interval  $T/t_0 = 10^4$ , for different values of  $\nu_{\pm}t_0/\Delta c$ . The parameters  $c_c^{\pm}$  related to the chemical reaction were chosen as  $c_c^+/\Delta c = 0.25$  and  $c_c^-/\Delta c = 0.75$ . Because close to the shape instability the dynamics slows down, we may slightly overestimate the region of stability, since we cannot detect the exact instability with the finite time intervals simulated.

### D.2.3.2 Calculations for multiple divisions

Several subsequent divisions break cylindrical symmetry. The calculations shown in Fig. 5.4 were therefore performed in three dimensions using Cartesian coordinates.

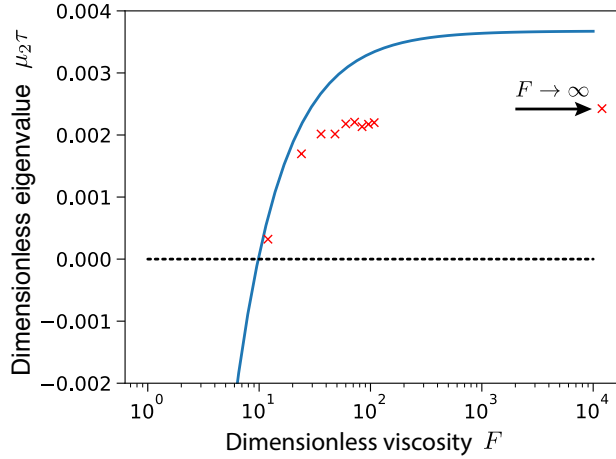


FIGURE D.1: Growth of shape perturbations of the  $l = 2$  mode for different normalized viscosities  $F = \eta w / (\gamma \tau)$  for the continuous model (red crosses) and effective model (blue curve). The last data point (with arrow) corresponds to  $F \rightarrow \infty$ . (Parameters:  $A = 8 \cdot 10^{-3}$ ,  $\epsilon = 0.2$ ,  $\eta_- / \eta_+ = 1$ ,  $c_+^{(0)} / \Delta c = 0$ ,  $k_+ / k_- = 1$ ,  $\nu_- / (k_- \Delta c) = 0.8$ )

We chose a cubic box with side length  $L = 50\hat{w}$  and an equidistant discretization of 100 points along each dimension.

Initial conditions corresponded to a spherical droplet centered at  $\mathbf{r} = (L/4, L/4, L/4)$ . The concentration field was initialized with  $c = c_-^{(0)}$  inside the droplet and  $c = c_\infty$  outside. The parameters for the calculations were  $\nu_- t_0 / \Delta c = 1.3 \cdot 10^{-2}$ ,  $\nu_+ t_0 / \Delta c = 2 \cdot 10^{-3}$  and  $c_c^+ / \Delta c = c_c^- / \Delta c = 0.5$ . Surfaces shown in Fig. 5.4 correspond to  $c / \Delta c = 0.5$ .

### D.3 Comparison of droplet deformation in the continuum model and the effective droplet model

Here we compare the analytical predictions of the effective model for the instability with numerical calculations of the continuous model for different values of the renormalized viscosity  $F$ . For this we numerically solved the dynamic equations of the continuous model starting with a droplet with a small initial deformation of mode  $l = 2$ . We fitted the dynamical behavior of the mode to an exponential function, which yields a numerical estimate for the eigenvalue  $\mu_2$ . In Fig. D.1 the resulting eigenvalues are shown, together with the eigenvalue of corresponding parameters of the effective model. We find that the value of  $F$  for which droplet shapes become unstable is very similar to the value predicted by the effective model. The eigenvalues are qualitatively similar to the ones of the effective model, despite working in a parameter regime

where the interfacial width and the differences of concentration within a phase cannot be considered very small, so that the models are not necessarily comparable.

To generate the data in the figure, we initialized droplets with a small shape perturbation for different values of  $F$ . All parameters and initial conditions were chosen as described in D.2.2. We found that for  $F \geq 100$  droplets divide, while they are stable for  $F \leq 1$ . For  $F = 10$ , the shape deformation was very slow, so that division was not seen in the time interval  $T/\tau = 4000$ . For  $10 < F < 100$ , as well as  $F = \infty$ , we fitted radius and spherical harmonic deformation to the concentration field using Eq. (D.10). For short times, the droplet radius changes as the concentration field and droplet size go towards the stationary values. After that, the shape deformation grows until the droplet deforms so strongly that the fitting fails. By hand we chose intermediate time windows for the simulations where the size was stationary and the shape deformation small. In these windows we fitted the deformation amplitude  $\epsilon$  (compare Eq. (D.10)) with an exponential function,  $Ae^{\mu_2 t} + B$  with parameters  $A$ ,  $B$  and eigenvalue  $\mu_2$  to the  $l = 2$  mode of the shape deformation.

# Appendix E

## Stability analysis of different geometrical droplet shapes

---

In this appendix, stationary states and their stability are discussed in 1, 2 and 3 dimensions for a (binary) phase separating systems with chemical reactions. We consider finite droplet structures, such as line segments in 1d and circles in 2d, and infinite structures, such as bands in 2d and plates and cylinders in 3d. Here the calculations are shown, figures and discussion can be found in chapter 6.

### E.1 Effective droplet model for active droplets

We consider the different shapes and dimensions using the effective droplet model introduced in chapter 3, section 3.2. The system consists of two components A and B with volume-conserving chemical reactions  $A \rightleftharpoons B$  between them. The chemical reaction can be active non-equilibrium reactions fueled by additional effects not described here. We consider an incompressible system where the system is described by the concentration  $c$  of B only, and we ignore the influence of hydrodynamic fluxes, corresponding to the limit of infinite viscosity,  $\eta \rightarrow \infty$ .

We concentrate on the case of a minority phase ('droplet') with high density of B in an environment of mainly A. Fields and parameters inside the droplet are denoted with index  $-$ , outside with  $+$ . For a flat interface, and without chemical reactions, the equilibrium volume densities inside and outside the droplet will be denoted  $c_-^{(0)}$  and  $c_+^{(0)}$ , respectively.

We consider stationary symmetric 'droplets' of different symmetries with vanishing chemical reaction rate  $s_+ \rightarrow 0$  far from the droplet,  $r \rightarrow \infty$ . Additionally, we will consider the linear stability of the stationary shapes. The interface moves due to a difference in ingoing and outgoing fluxes of B-material normal to it, Eq. (3.30). To

linear order, Eq. (3.31) can be used, by replacing the spherical coordinates with the coordinate system fitting the geometry of the respective stationary state, where  $e_r$  is the unit vector normal to the stationary interface.

## E.2 Stationary line segments in 1d

### E.2.1 Stationary states

In one dimension, we can consider stationary line segments, with length  $2L$  and stationary concentration profile  $\bar{c}(x)$ . See Fig. 6.1A in the main text for a sketch of the system. We center the stationary line segment at  $x = 0$ , where, assuming symmetry,  $\bar{c}'(0) = 0$ . The curvature of the interface is zero,  $H(L) = 0$ . We find the stationary concentration field,

$$c_+(x) = Ae^{-x/l_+} + C_+ \quad (\text{E.1})$$

$$c_-(x) = B \cosh(x/l_-) + C_- \quad (\text{E.2})$$

with

$$A = -\frac{\nu_+}{k_+} e^{L/l_+} \quad (\text{E.3})$$

$$B = \frac{\nu_-}{k_-} (\cosh(L/l_-))^{-1} \quad (\text{E.4})$$

$$C_{\pm} = \pm \frac{\nu_{\pm}}{k_{\pm}} + c_{\pm}^{(0)}. \quad (\text{E.5})$$

With this we find an expression for the stationary size,

$$\tanh(L/l_-) = \frac{l_+\nu_+}{l_-\nu_-} \quad (\text{E.6})$$

which has one solution for  $-1 < \frac{l_+\nu_+}{l_-\nu_-} < 1$ , and none otherwise.

### E.2.2 Stability of the stationary states

We now study the stability of the stationary state with respect to a small deformation,  $(c, L_1, L_2) = (\bar{c}, L, -L) + (\delta c, \delta L_1, -\delta L_2)$ . Here,  $L_1$  denotes the interface position at  $x > 0$ , and  $L_2$  denotes the position at  $x < 0$ . We can split the deformations into symmetric and antisymmetric deformations,

$$(\delta c, \delta L_1, \delta L_2) = \sum_n \epsilon_{s,n}(\rho_{s,n}(x), L, L)e^{\mu_{s,n}t} + \sum_n \epsilon_{a,n}(\rho_{a,n}(x), L, -L)e^{\mu_{a,n}t} \quad (\text{E.7})$$

where  $a$  and  $s$  denotes the symmetric/antisymmetric modes, and different modes are numbered with  $n$  and have an amplitude  $\epsilon_{a/s,n}$  and eigenvalue  $\mu_{a/s,n}$ . Symmetric modes have concentration field  $\rho_{s,n}$  with  $\rho_{s,n}(x) = \rho_{s,n}(-x)$  and antisymmetric



modes have a concentration field  $\rho_{a,n}$  with  $\rho_{a,n}(x) = -\rho_{a,n}(-x)$ . Symmetric modes thus correspond to a change in droplet size (a change of the length of the line segment), while antisymmetric modes describe a displacement of the droplet, while the size stays constant, see Fig. 6.1A for a sketch of the deformation modes. Linearizing the dynamic equations inside and outside the droplet, and the interfacial movement, we find for every mode

$$0 = \rho_{\pm}'' - \lambda_{\pm}^2 \rho_{\pm} \quad (\text{E.8})$$

$$\Delta c \mu = -\frac{D_-}{L} \rho'_-(L) - D_- \bar{c}''(L) + \frac{D_+}{L} \rho'_+(L) + D_+ \bar{c}''(L) \quad (\text{E.9})$$

with inverse length-scale

$$\lambda_{\pm} = \sqrt{\frac{k_{\pm} + \mu}{D_{\pm}}} \quad (\text{E.10})$$

and  $\rho = \rho_{s/a,n}$  and  $\mu = \mu_{s/a,n}$ .

For a discussion of the solution, we focus on the case  $\lambda_{\pm}^2 > 0$  without loss of generality, as solutions for  $\lambda_{\pm}^2 < 0$  are contained in the descriptions as oscillating spatial solutions with imaginary  $\lambda_{a/s,n}^{\pm}$ .

### E.2.2.1 Symmetric modes

For the symmetric case, the linearized boundary conditions are  $\rho_{\pm}(L) = -\bar{c}'_{\pm}(L) \cdot L$ , as well as  $\rho'_-(0) = 0$  and  $\rho_+(x \rightarrow \infty) \rightarrow 0$ . Solving the linear equations, we find

$$\rho(x) = \begin{cases} A_s e^{\lambda_+ x} & , x < L_2 \\ B_s \cosh(\lambda_- x) & , L_2 < x < L_1 \\ A_s e^{-\lambda_+ x} & , x > L_1 \end{cases} \quad (\text{E.11})$$

with coefficients  $A_s$  and  $B_s$ ,

$$A_s = -\frac{\nu_+}{k_+} \frac{L}{l_+} e^{\lambda_+ L} \quad (\text{E.12})$$

$$B_s = -\frac{\nu_-}{k_-} \frac{L}{l_-} \frac{\tanh(L/l_-)}{\cosh(\lambda_+ L)}. \quad (\text{E.13})$$

We find an implicit equation for the eigenvalue of the symmetric mode  $\mu = \mu_{s,n}$ ,

$$\Delta c \mu = \nu_+ l_+ \lambda_- \tanh(\lambda_- L) + \nu_+ l_+ \lambda_+ - \nu_- - \nu_+ \quad (\text{E.14})$$

We can see whether this equation has solutions  $\mu = 0$ . Inserting the equation for the stationary size, we find  $0 = -\nu_- (1 - \tanh^2(L/l_-))$ . Therefore, no marginal solutions exist for  $\nu_- \neq 0$ . Numerically, we find that stationary 1d droplets are always stable with respect to changes in size,  $\mu < 0$ , similar to the results of the  $l = 0$  mode for 3d droplets.

### E.2.2.2 Antisymmetric modes

The linearized boundary conditions for antisymmetric modes are  $\rho_{\pm}(L) = -\bar{c}'_{\pm}(L) \cdot L$ , as well as  $\rho_{-}(0) = 0$  and  $\rho_{+}(x \rightarrow \pm\infty) \rightarrow 0$ . The antisymmetric case yields

$$\rho_{a,n}(x) = \begin{cases} -A_a e^{\lambda_n^+ x} & , x < L_2 \\ B_a \sinh(\lambda_n^- x) & , L_2 < x < L_1 \\ A_a e^{-\lambda_n^+ x} & , x > L_1 \end{cases} \quad (\text{E.15})$$

with coefficients  $A_a$  and  $B_a$ ,

$$A_a = -\frac{\nu_+ L}{k_+ l_+} e^{\lambda_n^+ L} \quad (\text{E.16})$$

$$B_a = -\frac{\nu_- L}{k_- l_-} \frac{\tanh(L/l_-)}{\sinh(\lambda_n^+ L)}. \quad (\text{E.17})$$

We find the implicit equation for the eigenvalue for the antisymmetric mode  $\mu = \mu_{a,n}$ ,

$$\Delta c \mu = \frac{\nu_+ l_+ \lambda_-}{\tanh(\lambda_- L)} + \nu_+ l_+ \lambda_+ - \nu_- - \nu_+ \quad (\text{E.18})$$

The antisymmetric modes always have a marginal solution  $\mu = 0$ , corresponding to translational invariance. We did not find any solutions with  $\mu > 0$  numerically, or indications that several solutions might exist for  $\lambda_{\pm} > 0$ .

## E.3 Stationary bands in 2d

In two dimensions, stationary bands exist, which have a fixed width  $L$  in one spatial direction, denoted  $x$ , and are extended into the other direction, denoted  $y$ . The width of the band is given by the length of 1d stationary line segments, see previous section.

The stability analysis, has to take perturbations of different wavevectors  $q$  into account, and thus differs from the 1d case. We can describe perturbations as

$$(\delta c, \delta L_1, \delta L_2) = \sum_n \epsilon_{s,n} \cos(qy) (\rho_{s,n}(x), L, L) e^{\mu_{s,n} t} \quad (\text{E.19})$$

$$+ \sum_n \epsilon_{a,n} \cos(qy) (\rho_{a,n}(x), L, -L) e^{\mu_{a,n} t} \quad (\text{E.20})$$

where we again can find a split into symmetric and anti-symmetric modes. Symmetric modes describe a variation in the droplet width along the  $y$  axis, while antisymmetric modes describe a displacement of the droplet center in  $x$  direction which oscillates when moving along the  $y$  axis, while the droplet width stays constant. Stationary band and deformations can be seen in Fig. 6.1B. The equations describing the interface motion stay the same as in 1d, Eq. (E.9), but with a modified inverse length-scale

$$\lambda_{\pm}^2 = \frac{k_{\pm} + \mu}{D_{\pm}} + q^2. \quad (\text{E.21})$$

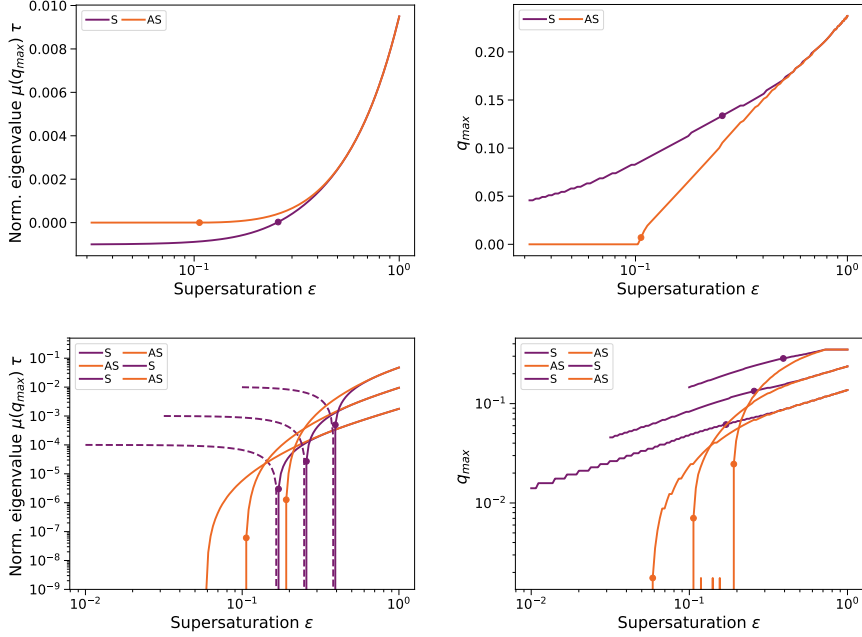


FIGURE E.1: Stability of droplet bands in 2d. (A) Largest eigenvalue of symmetric (purple) and antisymmetric (orange) deformations as function of the supersaturation with (B) corresponding deformation wavelength  $q_{max}$  for  $A = 10^{-3}$ . Dots mark the points where the respective modes become unstable. (C, D) same as (A), (B), but on a double-logarithmic scale for reaction amplitudes  $A = 10^{-4}, 10^{-3}, 10^{-2}$ . Negative values are shown as dashed lines, positive values as regular lines. Wavevectors  $q$  are given in units of  $1/w$ . (Parameters:  $k_+/k_- = 1, \nu_-/k_- = 1, D_+/D_- = 1, c_+^{(0)} = 0$ )

We find as boundary conditions for the concentration modes  $\rho_{s/a,n}(L) = a_q^\pm$ , with  $a_q^\pm = \beta_\pm \gamma h_q - \bar{c}'_\pm(L) \cdot L$ , with curvature term  $h_q = q^2 L$ . For the symmetric modes, we can find the concentration modes using conditions  $\rho'_-(0) = 0$  and  $\rho_+(x \rightarrow \infty) \rightarrow 0$ , as in Eq. (E.11) with  $A_s = a_q^+ e^{\lambda_+ x}$  and  $B_s = a_q^- / \cosh(\lambda_- L)$ . For the antisymmetric modes, we find the form in Eq. (E.15), with  $A_a = a_q^+ e^{\lambda_+ x}$  and  $B_a = a_q^- / \sinh(\lambda_- L)$ . Solving the implicit equation Eq. (E.9) for the eigenvalue  $\mu$ , we find the stability of the stationary bands with respect to deformations of different wavelengths. Some typical results are shown in Fig. 6.2B. In the limit  $q \rightarrow 0$ , we find the same results as in the 1d case, with a stable symmetric and a marginal antisymmetric mode. For small  $\epsilon$ , both curves decrease for  $q > 0$ , so that all modes are stable. For larger  $\epsilon$ , both the antisymmetric mode and the symmetric one reach a maximum at a very similar wavelength  $q$ , where the deformation modes are unstable.

In Fig. E.1, the maximal eigenvalue  $\mu$  of the symmetric and antisymmetric modes, together with the corresponding wavevector  $q_{max}$  are shown.

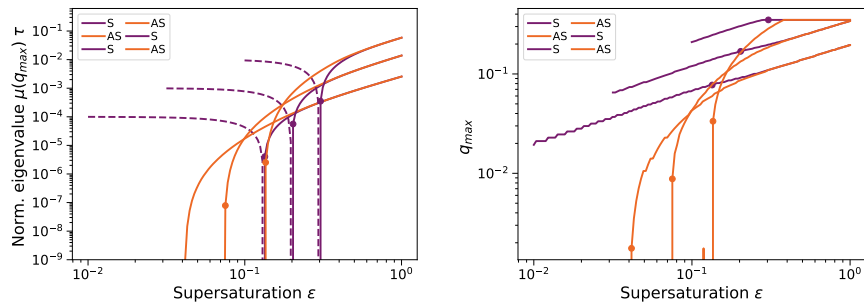


FIGURE E.2: Stability of droplet plates in 3d. (A) Largest eigenvalue of symmetric (purple) and antisymmetric (orange) deformations as function of the supersaturation with (B) corresponding deformation wavelength  $q_{max}$  for  $A = 10^{-4}, 10^{-3}, 10^{-2}$ . Dots mark the points where the respective modes become unstable. Negative values are shown as dashed lines, positive values as regular lines. Wavevectors  $q$  are given in units of  $1/w$ . (Parameters:  $k_+/k_- = 1$ ,  $\nu_-/k_- = 1$ ,  $D_+/D_- = 1$ ,  $c_+^{(0)} = 0$ )

#### E.4 Stationary plates in 3d

We now discuss stationary plates in 3d, which have a finite width  $L$  in  $x$  direction, and extend in  $y$  and  $z$  direction.

As for the 2d bands, the stationary concentration field in  $x$  direction and the width are the same as for line segments in 1d. The stability analysis for 3d plates is analogous to the 2d band system, as any perturbation can be decomposed in waves in  $y$ -direction and waves in  $z$ -direction. The perturbations in the different directions decouple, and thus the equations for the 2d band system are valid for every direction separately. The only change is in the curvature term  $h_q$ . As the plane is only deformed in one direction for every mode, and flat in the other direction, the mean curvature is half the value found for bands in 2d:

$$h_q = \frac{q^2 L}{2}, \quad (\text{E.22})$$

for a wavevector  $\mathbf{q}$  in the  $x$ - $y$  plane with amplitude  $q$ .

In Fig. E.2A and B, the largest eigenvalue and corresponding wavevector of the symmetric and antisymmetric mode are shown for several values of  $A$ . Qualitatively, they behave very similar to 2d bands. The antisymmetric mode becomes unstable for smaller values of supersaturation by about a factor of 4.

#### E.5 Stationary cylinders in 3d

We now consider stationary droplet cylinders in 3d. We use cylindrical coordinates  $r, \varphi, z$ , where the  $z$  axis aligns with the axis of the droplet cylinder.

### E.5.1 Stationary state

We determine stationary solutions of the cylinder radius  $R$  and the concentration field  $c_{\pm}$ , inside ("-") and outside ("+") the cylinder. We want to consider only solutions that are z-independent and cylindrically symmetric. We denote the stationary state with  $\bar{x}$  (for variable/field  $x$ ).

The modified Helmholtz equation that describes the concentration field is solved in cylindrical symmetry by  $I_0(r)$  and  $K_0(r)$ , the modified Bessel functions of order 0 of the first and second kind, and in spherical symmetry by  $i_0(r)$  and  $k_0(r)$ , the corresponding spherical modified Bessel functions. Using boundary conditions at the interface, Eq. (3.28) and (3.29) and convergence at 0 and infinity, we find as solutions for the cylindrical case

$$\bar{c}_+(r) = +\frac{\nu_+}{k_+} + c_+^{(0)} + A_+ K_0(r/l_+) \quad (r > \bar{R}) \quad (\text{E.23})$$

$$\bar{c}_-(r) = -\frac{\nu_-}{k_-} + c_-^{(0)} + A_- I_0(r/l_-) \quad (r < \bar{R}), \quad (\text{E.24})$$

with characteristic length scales  $l_{\pm} = (D_{\pm}/k_{\pm})^{1/2}$  set by reaction and diffusion, and parameters  $A_{\pm}$  determined by the boundary condition at the droplet interface,

$$A_+ = \left( \gamma\beta_+ H(\bar{R}) - \frac{\nu_+}{k_+} \right) \frac{1}{K_0(\bar{R}/l_+)} \quad (\text{E.25})$$

$$A_- = \left( \gamma\beta_- H(\bar{R}) + \frac{\nu_-}{k_-} \right) \frac{1}{I_0(\bar{R}/l_-)}. \quad (\text{E.26})$$

The mean curvature of a cylinder is  $H(\bar{R}) = 1/(2\bar{R})$ .

The stationary fields above have the stationary radius  $\bar{R}$  of the cylinder as variable. It can be determined by Eq. (3.31), which yields the implicit equation

$$0 = D_+ \bar{c}'_+(\bar{R}) - D_- \bar{c}'_-(\bar{R}). \quad (\text{E.27})$$

For the spherical case, the same equations are valid, with  $k_0$  and  $i_0$  instead of  $K_0$  and  $I_0$ , and with mean curvature  $H(\bar{R}) = 1/\bar{R}$ . See Fig. 6.7A for stationary solutions.

### E.5.2 Linear stability analysis of stationary shapes

For small perturbations  $\delta c$ ,  $\delta R$  of the stationary, cylindrically symmetric system, the dynamics are described by the linearized system

$$\partial_t \delta c = -\delta v_r \bar{c}' + D_{\pm} \Delta \delta c - k_{\pm} \delta c \quad (\text{E.28})$$

$$\begin{aligned} (c_-^{(0)} - c_+^{(0)}) \partial_t \delta R &= D_+ \partial_r \delta c_+(\bar{R}) - D_- \partial_r \delta c_-(\bar{R}) \\ &\quad + (D_+ \bar{c}''_+(\bar{R}) - D_- \bar{c}''_-(\bar{R})) \delta R. \end{aligned} \quad (\text{E.29})$$

With  $\delta c_-$  and  $\delta c_+$  we denote perturbations of the concentration field inside and outside the droplet. The same notation holds for the other fields. In this linear analysis,

## E. STABILITY ANALYSIS OF DIFFERENT GEOMETRICAL DROPLET SHAPES

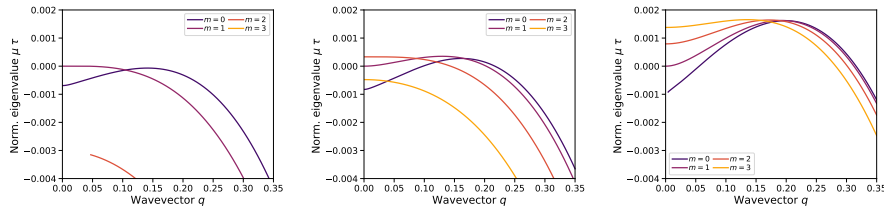


FIGURE E.3: Instability of stationary cylinders for modes  $m = 0, 1, 2, 3$  as function of the wavevector  $q$  for  $\epsilon = 0.05, 0.1, 0.2$ . A) For  $\epsilon = 0.05$ , the  $m = 1$  mode is metastable for  $q = 0$ , which corresponds to a translation of the cylinder, all other modes are stable. B) For  $\epsilon = 0.1$ , the  $m = 0, 1$  and  $2$  are unstable for small/intermediate  $q$ -modes. C) For  $\epsilon = 0.2$ , all modes shown are unstable for small/intermediate  $q$ -modes. The wavevectors  $q_{max}$  where each modes are most unstable are closer to each other than for smaller  $\epsilon$ . Wavevectors  $q$  are given in units of  $1/w$ .

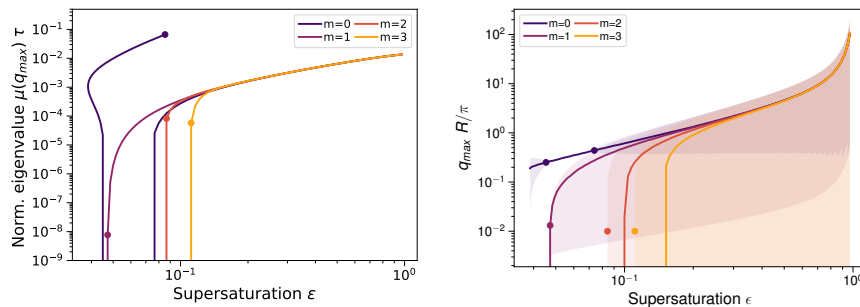


FIGURE E.4: Largest eigenvalue  $\mu_m(q_{max})$  and corresponding wavevector  $q_{max}$  of stationary cylinders for modes  $m = 0, 1, 2, 3$  as function of the supersaturation  $\epsilon$ . A) Maximal eigenvalue of each mode. Dots indicate where each mode becomes unstable. For small supersaturations, the modes have different values, for large supersaturations, the eigenvalues converge towards a common value, which increases for increasing supersaturation with sub-powerlaw behavior. B) Wavevector where the eigenvalue of a mode  $m$  is maximal (lines). The shaded regions indicate unstable  $q$ -modes. Dots indicate the onset of the instability. All modes except  $m = 0$  become unstable first for the  $q = 0$  mode.

the boundary conditions for these perturbations are specified at the stationary radius  $\bar{R}$ ,

$$\delta c_{\pm}(\bar{R}) = \beta_{\pm} \gamma \delta H - \bar{c}'_{\pm}(\bar{R}) \delta R \quad (\text{E.30})$$

with perturbation of the curvature  $\delta H = H(R) - H(\bar{R})$ .

For the stability analysis, we are looking for a description of the unknown functions  $\delta c_+$  (for  $r < \bar{R}$ ),  $\delta c_-$  (for  $r > \bar{R}$ ) and  $\delta R$  in eigenfunctions  $c_i, R_i$ , so that

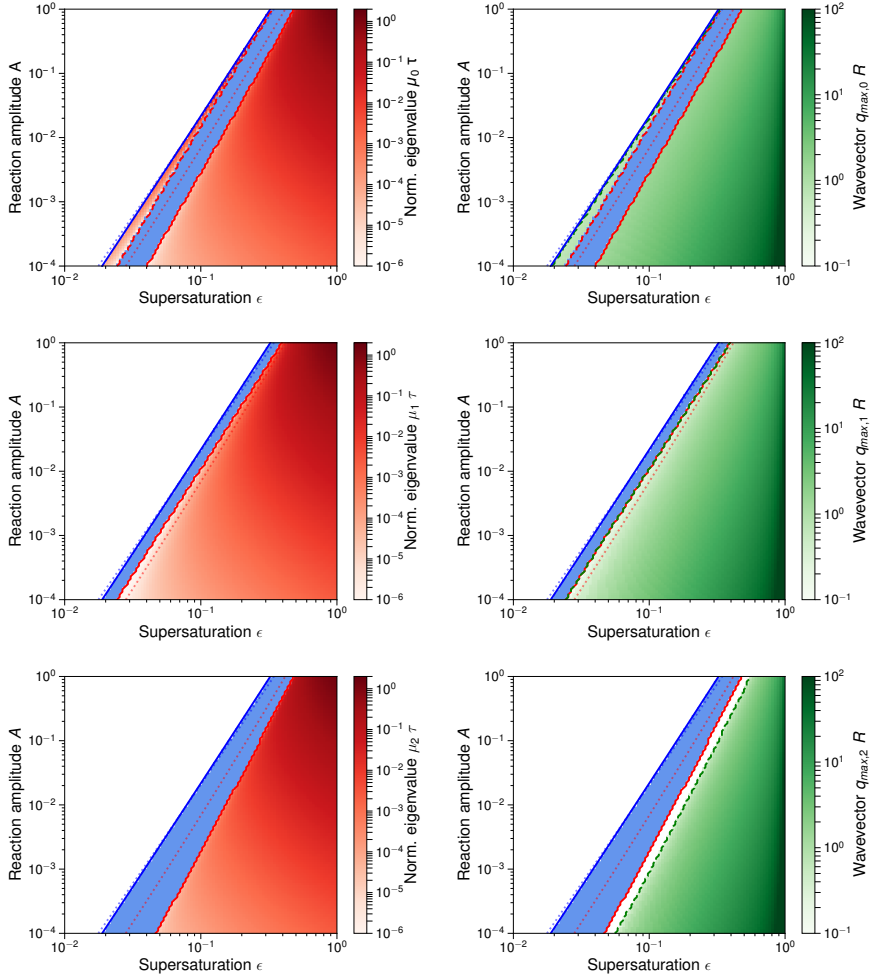


FIGURE E.5: Stability diagrams for different modes  $m$  (top to bottom:  $m = 0, 1, 2$ ) as function of the supersaturation  $\epsilon = \nu_+/k_+$  and reaction amplitude  $A$ . The blue line shows the threshold value above which stationary cylinders exist. The red line shows the onset of instability (for any wavelength  $q$  and the given mode  $m$ ). The dotted lines are the corresponding lines for spherical droplets. For the left plot, the color shows the value of  $\mu\tau$ , on the right side, the wavelength  $q$  with the maximal value of  $\mu$  is shown as  $\hat{q} = qR$ . Parameters:  $\nu_0 = k_- \Delta c$ ,  $k_{\pm} \tau = 0.01$ ,  $D_+ = D_-$ ,  $\beta_+ = \beta_-$ , with normalization of concentration, time and length  $\Delta c = c_-^{(0)} - c_+^{(0)}$  and  $\tau = w^2/D_+$ ,  $w = 6\beta_+\gamma/\Delta c$ .

$$(\delta c_+, \delta c_-, \delta R)^T = \sum_i \epsilon_i (c_i^+, c_i^-, R_i)^T e^{\mu_i t}. \quad (\text{E.31})$$

### E.5.3 Perturbation of a cylinder

In the cylindrical case, the eigenfunctions can be chosen as

$$\begin{pmatrix} \delta c_+ \\ \delta c_- \\ \delta R \end{pmatrix} = \sum_{nlm} \epsilon_{nlm} \begin{pmatrix} P_{nmq}^+(r) \Phi_m(\varphi) Z_q(z) \\ P_{nmq}^-(r) \Phi_m(\varphi) Z_q(z) \\ \bar{R} \cdot \Phi_m(\varphi) Z_q(z) \end{pmatrix} e^{\mu_{nmq} t}. \quad (\text{E.32})$$

A short derivation is shown in the Appendix. Here, the functions  $\Phi$  and  $Z$  can be expressed as

$$\Phi_m(\varphi) = \begin{cases} \sin(mc) \\ \cos(mc) \end{cases}, \quad Z_q(z) = \begin{cases} \sin(qz) \\ \cos(qz) \end{cases} \quad (\text{E.33})$$

with  $m \in \mathbb{Z}$  and  $q \in \mathbb{R}$ . The angular function  $\Phi_m(\varphi)$  needs two parts to account for the same deformation, but in different directions in Cartesian coordinates. Since the angle  $\varphi$  lies between 0 and  $2\pi$ , we only find integer valued modes. For the length-function  $Z_q(z)$ , the two possibilities differentiate between deformations that have a maximum or a minimum at  $z = 0$ . The cylinder in our discussion is infinite in the  $z$ -direction, therefore  $q$  is continuous.

The radial solutions are slightly more complicated, and can be expressed as

$$P_{nmq}^\pm(r) = A_{nmq}^\pm I_m(\lambda_{nmq}^\pm r) + B_{nmq}^\pm K_m(\lambda_{nmq}^\pm r) \quad (\text{E.34})$$

with

$$\lambda_{nmq\pm}^2 = \frac{k_\pm + \mu_{nmq}}{D_\pm} + q^2 \in \mathbb{C}, \quad (\text{E.35})$$

where  $I_m$  and  $K_m$  denote modified Bessel functions of first and second order. Together, they are a complete set of basis-functions, and also the radial solutions of the modified Bessel equation, which we get from Eq. (E.28) with the ansatz of Eq. (E.32). The value of  $\mu_{nmq}$  enters  $\lambda_{nmq}^\pm$ . It will be determined by the radial equation. The index  $n$  simply numbers different solutions for  $\mu$  of the radial equation. In the case of an unstable shape,  $\mu > 0$ , we find  $\lambda^2 > 0$  in the cylinder and outside. For  $\lambda^2 < 0$ ,  $\lambda$  is imaginary, and the solutions can alternatively be expressed by the Bessel functions  $J_m$  and  $Y_m$ .

The coefficients  $A$  and  $B$  are determined by the boundary conditions. For  $\lambda_{nmq\pm}^2 > 0$ , the modified Bessel functions  $I_m$  diverge for large  $\lambda_\pm r$ , and the functions  $K_m$  diverge for vanishing  $\lambda_\pm r$ , we know  $A^+ = 0$  and  $B^- = 0$ . We find for the boundary conditions of the concentration field, Eq. (E.30),

$$P_{nmq}^\pm(\bar{R}) = a_{mq}^\pm \quad (\text{E.36})$$



with

$$a_{mq}^{\pm} = \gamma\beta_{\pm}h_{mq} - \bar{c}'(\bar{R}_{\pm}) \cdot \bar{R} \quad (\text{E.37})$$

and curvature term

$$h_{mq} = \frac{m^2 + \bar{R}^2 q^2 - 1}{2\bar{R}}. \quad (\text{E.38})$$

This determines the remaining two coefficients,

$$A^- = a_{mq}^-/I_m(\lambda_{nmq}^- \bar{R}) \quad (\text{E.39})$$

$$B^+ = a_{mq}^+/K_m(\lambda_{nmq}^+ \bar{R}). \quad (\text{E.40})$$

Inserting Eq. (E.32) into the equation that describes the interface movement, Eq. (E.29), it becomes

$$\begin{aligned} (c_-^{(0)} - c_+^{(0)})\mu_{nmq} = & D_+ \bar{c}_+''(\bar{R}) - D_- \bar{c}_-''(\bar{R}) \\ & + \frac{D_+}{\bar{R}} P'_{nmq+}(\bar{R}) - \frac{D_-}{\bar{R}} P'_{nmq-}(\bar{R}) \end{aligned} \quad (\text{E.41})$$

This is an implicit equation to determine the growth rate of perturbation modes  $\mu_{nl}$  (this is also the eigenvalue). The equation is implicit, because the eigenfunctions  $P_{nmq}^{\pm}$  depend on  $\mu_{nmq}$  via  $\lambda_{nmq}^{\pm}$ , see Eq. (E.35).

In Fig. E.3 the largest eigenvalues of different deformations are shown. In panel A, the instability of the  $l = 1$  mode is shown as a function of the wavevector  $q$  for different stationary radii (along one of the lines in Fig. 6.7A). At  $q = 0$  we see that the eigenvalue is zero, so translations of the whole cylinder have a marginal stability. Depending on the stationary radius, this is the maximal eigenvalue, and larger wavevectors are stable ( $R = 2$ ), or the eigenvalue has a maximum at a larger  $q_{max} > 0$ , so that the cylinder is unstable with respect to a deformation with mode  $m = 1$  and the respective wavevector. For a change in volume,  $m = 0$  and  $q = 0$ , we find the same result as for the spherical case: the smaller stationary radius for one fixed set of parameter values is unstable, the larger one is stable. For  $q > 0$ , there can, however, be a  $q_{max}$  where the size is unstable with respect to the  $m = 0$  mode. Since this corresponds to oscillations of droplet volume along the cylinder axis, we may expect this to lead to a split of the shape into single droplets in the full nonlinear dynamics. For  $m \geq 2$ , the initial value for  $q = 0$ , as well as the slope and the existence of a maximum with  $q_{max} \neq 0$  depends on parameter values.

## E.6 Stationary disks in 2d

We now consider stationary disks in 2d, the equivalent of spherical droplets in two dimensions. The stationary radius and concentration field of such a round droplet is given by the same equations as for the droplet cylinder in 3d, as a cut through the cylinder with constant  $z$ , but with mean curvature  $H(\bar{R}) = 1/\bar{R}$ . The linear stability

analysis of a stationary disk is the same as for the cylinder for  $q = 0$ , with curvature term

$$h_{mq} = \frac{m^2 - 1}{\bar{R}}. \quad (\text{E.42})$$

The mode  $m$  describes deformations of the droplet disk, equivalent to mode  $l$  in spherical droplets. A sketch of a stationary disk and its deformations can be seen in Fig. 6.4 in the main text.

## Appendix F

### Stability analysis of chemically active droplets with hydrodynamic flows

---

In this appendix we derive the linear stability of spherical stationary droplets in the effective droplet model with hydrodynamic flows. The model is defined by Eq. (3.20) to (3.31) in chapter 3. We present the stationary state, the linear stability analysis and the scaling behavior of the stability for vanishing chemical reaction rates. A discussion of the results can be found in chapter 7.

#### F.1 Linear stability analysis with hydrodynamic flows

Here we derive stationary spherical states and their stability for the effective droplet model with hydrodynamic flows, Eq. (3.20) to (3.31).

##### F.1.1 Stationary state of a spherical active droplet

We first briefly discuss the stationary solutions of the effective droplet model. We consider states with spherical symmetry and without hydrodynamic flows  $\bar{\mathbf{v}} = 0$ , where the bar indicates a steady state value. In this case, the pressure is constant both inside and outside the droplet, with a pressure difference due to Laplace pressure between the inside and outside of the droplets,

$$\bar{p}_- = \bar{p}_+ + \frac{2\gamma}{R}. \quad (\text{F.1})$$

The steady state concentration profiles in the presence of chemical reactions are

given by

$$\bar{c}_+(r) = +\frac{\nu_+}{k_+} + c_+^{(0)} + A_+ k_0(r/l_+) \quad (\text{F.2})$$

$$\bar{c}_-(r) = -\frac{\nu_-}{k_-} + c_-^{(0)} + A_- i_0(r/l_-), \quad (\text{F.3})$$

where  $i_0(x) = 2 \sinh(x)/x$  and  $k_0(x) = e^{-x}/x$  denote modified spherical Bessel functions of order zero of the first and second kind, respectively. The characteristic length scales  $l_{\pm} = (D_{\pm}/k_{\pm})^{1/2}$  are set by reaction rate constants and diffusion coefficients. The parameters  $A_{\pm}$  are determined by the boundary condition at the droplet interface, Eq. (3.28)-(3.29),

$$A_+ = \left( \frac{\gamma\beta_+}{\bar{R}} - \frac{\nu_+}{k_+} \right) \frac{1}{k_0(\bar{R}/l_+)} \quad (\text{F.4})$$

$$A_- = \left( \frac{\gamma\beta_-}{\bar{R}} + \frac{\nu_-}{k_-} \right) \frac{1}{i_0(\bar{R}/l_-)}. \quad (\text{F.5})$$

Stationarity of the droplet radius  $\bar{R}$  implies

$$D_+ \bar{c}'_+(\bar{R}) = D_- \bar{c}'_-(\bar{R}), \quad (\text{F.6})$$

see Eq. (3.31). Note that this equation typically has zero, one or two solutions for a given set of parameters.

### F.1.2 Linearized dynamics

We introduce small perturbations to the spherically symmetric stationary state, with  $p = \bar{p} + \delta p$ ,  $\mathbf{v} = \delta \mathbf{v}$ ,  $c = \bar{c} + \delta c$  and  $R = \bar{R} + \delta R$  and write the dynamics of these perturbations to linear order. The linearized dynamics reads

$$\nabla \delta p = \eta_{\pm} \Delta \delta \mathbf{v} \quad (\text{F.7})$$

$$\nabla \cdot \delta \mathbf{v} = 0 \quad (\text{F.8})$$

$$\partial_t \delta c = -\delta v_r \bar{c}' + D_{\pm} \nabla^2 \delta c - k_{\pm} \delta c \quad (\text{F.9})$$

$$\begin{aligned} \partial_t \delta R = & \delta v_r(\bar{R}) + \frac{1}{\Delta c} [D_+ \bar{c}''_+(\bar{R}) - D_- \bar{c}''_-(\bar{R})] \delta R \\ & + \frac{1}{\Delta c} [D_+ \partial_r \delta c_+(\bar{R}) - D_- \partial_r \delta c_-(\bar{R})]. \end{aligned} \quad (\text{F.10})$$

Here  $\delta v_r$  denotes the radial part of the hydrodynamic velocity. With  $\delta c_-$  and  $\delta c_+$  we denote perturbations of the concentration field inside and outside the droplet. The same notation holds for the other fields. In this linear analysis, boundary conditions apply at the stationary radius  $\bar{R}$ ,

$$\delta c_{\pm}(\bar{R}) = \beta_{\pm} \gamma \delta H - \bar{c}'_{\pm}(\bar{R}) \delta R, \quad (\text{F.11})$$

with perturbation of the curvature  $\delta H = H(R) - H(\bar{R})$ .

The linearized dynamics can be decomposed in spherical harmonics, see Eq. (7.1) in chapter 7. The curvature perturbation then takes the form

$$\delta H = \sum_{nlm} \frac{h_l}{\bar{R}} \epsilon_{nlm} Y_{lm} , \quad (\text{F.12})$$

with  $h_l = (l^2 + l - 2)/2$ .

### F.1.3 Hydrodynamic eigenmodes of the linearized dynamics

We can expand the hydrodynamic eigenmodes using a basis of vector spherical harmonics, see Eq. (7.2) in chapter 7. The velocity boundary conditions Eq. (3.27) in chapter 3 for the mode amplitudes read

$$0 = v_{lm}^{r+}(\bar{R}) - v_{lm}^{r-}(\bar{R}) \quad (\text{F.13})$$

$$0 = v_{lm}^{(1)+}(\bar{R}) - v_{lm}^{(1)-}(\bar{R}) \quad (\text{F.14})$$

$$0 = v_{lm}^{(2)+}(\bar{R}) - v_{lm}^{(2)-}(\bar{R}) . \quad (\text{F.15})$$

The stress boundary conditions (see Eq. (3.25) and Eq. (3.26) in chapter 3) at the interface read

$$0 = 2\eta_+ (v_{lm}^{r+})'(\bar{R}) - p_{lm}^+(\bar{R}) - 2\eta_- (v_{lm}^{r-})'(\bar{R}) + p_{lm}^-(\bar{R}) - 2\gamma\epsilon_{lm} \frac{h_l}{\bar{R}} \quad (\text{F.16})$$

$$0 = \eta_+ \left[ (v_{lm}^{(1)+})'(\bar{R}) + \frac{v_{lm}^{r+}(\bar{R})}{\bar{R}} - \frac{v_{lm}^{(1)+}(\bar{R})}{\bar{R}} \right] \quad (\text{F.17})$$

$$- \eta_- \left[ (v_{lm}^{(1)-})'(\bar{R}) + \frac{v_{lm}^{r-}(\bar{R})}{\bar{R}} - \frac{v_{lm}^{(1)-}(\bar{R})}{\bar{R}} \right] \quad (\text{F.18})$$

$$0 = \eta_+ \left[ (v_{lm}^{(2)+})'(\bar{R}) - \frac{v_{lm}^{(2)+}(\bar{R})}{\bar{R}} \right] - \eta_- \left[ (v_{lm}^{(2)-})'(\bar{R}) - \frac{v_{lm}^{(2)-}(\bar{R})}{\bar{R}} \right] . \quad (\text{F.19})$$

We solve the radial profiles of the modes with a polynomial ansatz and exclude functions that diverge for  $r \rightarrow 0$  or  $r \rightarrow \infty$  inside and outside the droplet, respectively. The pressure is then given by

$$p_{lm}^-(r) = \gamma f_A \left( \frac{r}{\bar{R}} \right)^{l+1} \quad (\text{F.20})$$

$$p_{lm}^+(r) = -\gamma f_B \left( \frac{r}{\bar{R}} \right)^{-l} . \quad (\text{F.21})$$

For the hydrodynamic flow velocity we obtain

$$v_{lm}^{r-}(r) = \frac{\gamma}{\eta_-} \left[ f_{C1} \left( \frac{r}{\bar{R}} \right)^{l+1} - f_{C3} \left( \frac{r}{\bar{R}} \right)^{l-1} \right] \quad (\text{F.22})$$

$$v_{lm}^{(1)-}(r) = \frac{\gamma}{\eta_-} \left[ \frac{l+3}{l(l+1)} f_{C1} \left( \frac{r}{\bar{R}} \right)^{l+1} - \frac{l+1}{l(l+1)} f_{C3} \left( \frac{r}{\bar{R}} \right)^{l-1} \right] \quad (\text{F.23})$$

$$v_{lm}^{(2)-}(r) = 0 \quad (\text{F.24})$$

and

$$v_{lm}^{r+}(r) = \frac{\gamma}{\eta_-} \left[ -f_{C2} \left( \frac{r}{R} \right)^{-l} + f_{C4} \left( \frac{r}{R} \right)^{-l-2} \right] \quad (\text{F.25})$$

$$v_{lm}^{(1)+}(r) = \frac{\gamma}{\eta_-} \left[ \frac{l-2}{l(l+1)} f_{C2} \left( \frac{r}{R} \right)^{-l} - \frac{1}{l+1} f_{C4} \left( \frac{r}{R} \right)^{-l-2} \right] \quad (\text{F.26})$$

$$v_{lm}^{(2)+}(r) = 0. \quad (\text{F.27})$$

Here, we have defined

$$f_A = \frac{(l-1)(l+1)(l+2)(2l+3)}{\Delta(2l^2+4l) + (2l^2+4l+3)} \quad (\text{F.28})$$

$$f_B = \frac{l(l-1)(l+2)(2l-1)}{(2l^2+1) + (2l^2-2)/\Delta} \quad (\text{F.29})$$

$$f_{C1} = \frac{1}{2} \frac{l(l-1)(l+1)(l+2)}{\Delta(2l^2+4l) + (2l^2+4l+3)} \quad (\text{F.30})$$

$$f_{C2} = \frac{1}{2} \frac{l(l-1)(l+1)(l+2)}{\Delta(2l^2+1) + (2l^2-2)} \quad (\text{F.31})$$

$$f_{C3} = \frac{1}{2} \frac{l(l-1)(l+1)(l+2)(\Delta(2l^2+4l+3) + (2l^2+4l))}{(\Delta(2l^2+1) + (2l^2-2))(\Delta(2l^2+4l) + (2l^2+4l+3))} \quad (\text{F.32})$$

$$f_{C4} = \frac{1}{2} \frac{l(l-1)(l+1)(l+2)(\Delta(2l^2-2) + (2l^2+1))}{(\Delta(2l^2+1) + (2l^2-2))(\Delta(2l^2+4l) + (2l^2+4l+3))} \quad (\text{F.33})$$

where  $\Delta = \eta_+/\eta_-$  denotes the ratio of the viscosities inside and outside the droplet.

#### F.1.4 Concentration eigenmodes

The equation for the radial part of the concentration eigenmode is

$$\frac{1}{D_{\pm}} v_l^r(r) \bar{c}'(r) = \left[ \frac{1}{r^2} \frac{d}{dr} r^2 \frac{d}{dr} - \lambda_{nl}^{\pm 2} - \frac{l(l+1)}{r^2} \right] c_{nl}(r) \quad (\text{F.34})$$

with

$$\lambda_{nl}^{\pm 2} = (k_{\pm} + \mu_{nl})/D_{\pm}. \quad (\text{F.35})$$

The boundary conditions at  $\bar{R}$  are

$$c_{nl}(\bar{R}_{\pm}) = \gamma \beta_{\pm} \frac{h_l}{\bar{R}} - \bar{R} \bar{c}'(\bar{R}_{\pm}). \quad (\text{F.36})$$

The left-hand side of Eq. (F.34) constitutes an inhomogeneity

$$f_l^{\pm}(r) = -\frac{1}{D_{\pm}} v_l^r(r) \bar{c}'(r). \quad (\text{F.37})$$

The solution  $c_{nl}^{\pm}(r)$  of the inhomogeneous equation (F.34) that satisfies the boundary condition Eq. (F.36) can be constructed from a particular solution  $c_{nl,p}^{\pm}(r)$  of the

inhomogeneous equation to which solutions  $c_{nl,h}^\pm(r)$  of the homogeneous equation with  $f_l^\pm = 0$  are added to satisfy the boundary conditions, Eq. (F.36). This can be expressed as

$$c_{nl}^-(r) = \alpha_{nl}^- c_{nl,h}^-(r) + c_{nl,p}^-(r) \quad (\text{F.38})$$

$$c_{nl}^+(r) = \alpha_{nl}^+ c_{nl,h}^+(r) + c_{nl,p}^+(r), \quad (\text{F.39})$$

where the coefficients  $\alpha_\pm$  read

$$\alpha_{nl}^\pm = \frac{a_l^\pm - c_{nl,p}^\pm(\bar{R})}{c_{nl,h}^\pm(\bar{R})}, \quad (\text{F.40})$$

with  $a_l^\pm = c_{nl}^\pm(\bar{R})$ .

We are especially interested in the case of unstable modes with  $\mu_{nl} > 0$ . Therefore we focus on the solution of equation (F.34) for  $\lambda_{nl}^{\pm 2} > 0$  and  $k_\pm > 0$ . In this case, the homogeneous equation with  $f_l^\pm = 0$  is a modified Helmholtz equation which is solved by modified spherical Bessel functions,  $c_{nl,h}^-(r) = i_l(\lambda_{nl}^- r)$  and  $c_{nl,h}^+(r) = k_l(\lambda_{nl}^+ r)$ , where  $i_l$  and  $k_l$  denote the modified spherical Bessel functions of first and second order, respectively. The particular solution of the inhomogeneous equation can be obtained by a Green's function approach,

$$c_{l,p}^-(r) = \lambda_{nl}^- k_l(\lambda_{nl}^- r) \int_0^r [i_l(\lambda_{nl}^- r_2) f_l^-(r_2) r_2^2] dr_2 \quad (\text{F.41})$$

$$+ \lambda_{nl}^- i_l(\lambda_{nl}^- r) \int_r^{\bar{R}} [k_l(\lambda_{nl}^- r_2) f_l^-(r_2) r_2^2] dr_2$$

$$c_{l,p}^+(r) = \lambda_{nl}^+ k_l(\lambda_{nl}^+ r) \int_{\bar{R}}^r [i_l(\lambda_{nl}^+ r_2) f_l^+(r_2) r_2^2] dr_2 \quad (\text{F.42})$$

$$+ \lambda_{nl}^+ i_l(\lambda_{nl}^+ r) \int_r^\infty [k_l(\lambda_{nl}^+ r_2) f_l^+(r_2) r_2^2] dr_2,$$

with the radial part of the inhomogeneity  $f_l^\pm(r)$  given by Eq. (F.37). The explicit calculation of these functions has to be handled with care, since the functions  $k_l$  and  $i_l$  have divergences for large and small arguments  $r$  that cancel in the final result but can still lead to numerical difficulties when evaluated directly.

The derivative of the concentration profile at  $\bar{R}$  can be expressed as

$$c'_{nl}(\bar{R}_-) = \frac{a_l^-}{\bar{R}} g_{l,i}(\lambda_{nl}^- \bar{R}) + \frac{c_{l,p}^-(\bar{R})}{\bar{R}} \cdot [g_{l,k}(\lambda_{nl}^- \bar{R}) - g_{l,i}(\lambda_{nl}^- \bar{R})] \quad (\text{F.43})$$

$$c'_{nl}(\bar{R}_+) = \frac{a_l^+}{\bar{R}} g_{l,k}(\lambda_{nl}^+ \bar{R}) + \frac{c_{l,p}^+(\bar{R})}{\bar{R}} \cdot [g_{l,i}(\lambda_{nl}^+ \bar{R}) - g_{l,k}(\lambda_{nl}^+ \bar{R})] \quad (\text{F.44})$$

with

$$g_{l,i}(x) = \frac{x i'_l(x)}{i_l(x)} \quad (\text{F.45})$$

$$g_{l,k}(x) = \frac{x k'_l(x)}{k_l(x)}. \quad (\text{F.46})$$

Using the equation for the shape perturbations (F.10), and using Eqns (F.43) and (F.44), we obtain Eq. (7.3) in chapter 7. This equation determines the eigenvalue  $\mu_{nlm}$  of the hydrodynamic modes.

## F.2 Scaling relations in the limit of small reaction fluxes

In the limit of small chemical reaction fluxes  $s_{\pm}$  we obtain simple scaling expressions for stationary radii and their shape instability conditions. Here we discuss the stationary radius in the limit of small chemical reaction amplitude  $A = \nu_- \tau / \Delta c$  while keeping the ratios  $\nu_- / (k_- \Delta c)$  and  $k_+ / k_-$  of reaction parameters fixed. Here we present the method and discuss the results.

### F.2.1 Stationary radius

The stationary radius does not contain hydrodynamic flows, so that the results in Section 4.4 without hydrodynamic flows hold.

### F.2.2 Shape instability

We now discuss scaling relations for the onset of instability in the  $(A, \hat{\epsilon})$  plane in the limit of small  $A$ , which give the trends shown as dashed lines in Fig. 7.2D-F. We use the scaling of the stationary radius  $\bar{R} = \bar{R}_s$  close to  $\epsilon_0$  with  $\hat{R} = \bar{R} A^{1/3} / w$ ,  $\hat{\epsilon} = \epsilon A^{-1/3}$  and  $\hat{l}_{\pm} = l_{\pm} A^{1/2}$  in Eq. (7.3) to obtain

$$\hat{\mu}_{nlm} = -\frac{d_l A^{-2/3}}{\hat{R}} \frac{1}{F} + \frac{2}{3}(l-1) - \frac{D_+ (l-1) g_l}{D_- \hat{R}^3} + O(A^{1/6}) \quad (\text{F.47})$$

where  $\hat{\mu}_{nlm} = \mu_{nlm} \tau / A$  and  $\hat{R}$  is related to  $\hat{\epsilon}$  by Eq. (4.21). Here,  $d_l = f_{C3} - f_{C1}$ , where  $f_{C1}$  and  $f_{C3}$  are defined in Eq. (F.33) and

$$g_l = \frac{h_l(l+1) + \frac{D_- \beta_-}{D_+ \beta_+} h_l l}{l-1} \quad (\text{F.48})$$

with  $h_l = (l^2 + l - 2)/2$ . For large mode index  $l$ ,

$$d_l = \frac{l}{2(\eta_+ / \eta_- + 1)} + O(1/l). \quad (\text{F.49})$$

We now consider conditions for which  $\mu_{nlm} = 0$  for small  $A$  and the mode  $(n, l, m)$  becomes unstable. Using (4.21) in (F.47), we find a relation between  $\hat{\epsilon}$  and  $\hat{R}$  at the onset of instability  $\mu_{nlm} = 0$ ,

$$\hat{\epsilon} = \frac{d_l}{2(l-1)} \frac{1}{\hat{F}} \hat{R} + \left( \frac{1}{6} + \frac{D_+}{D_-} \frac{1}{2} g_l \right) \hat{R}^{-1} + O(A^{1/6}). \quad (\text{F.50})$$

This curve captures the scaling behavior of the onset of instability for different parameters in the  $\bar{R} - \epsilon$  plane, corresponding to the red dotted line in Fig. 7.2A-C.



We now focus on finding the scaling relations for the onset of stability of the stationary radius as function of  $A$ ,  $\epsilon$  and  $F$ , as shown in Fig. 7.2D-F. At this onset, both (F.50) and (4.21) need to be satisfied. We use both equations to eliminate  $\hat{R}$ . We find a crossover regime with relations  $A^* \sim F^{-3/2}$  between the region where hydrodynamic flows are relevant ( $A < A^*$ ) and where they can be neglected ( $A > A^*$ ). For  $A > A^*$  we find for  $\mu_{nlm} = 0$  as relation between  $A$  and  $\epsilon$

$$A \simeq 54 \frac{gl}{(1 + \frac{1}{2}gl)^3} \epsilon^3. \quad (\text{F.51})$$

For  $A < A^*$  we find

$$A \simeq \frac{1}{3} \left( \frac{2(l-1)}{d_l} \right)^2 \epsilon^{-1} F^{-2}. \quad (\text{F.52})$$

In Fig. 7.2D-F, the dashed lines indicate these two scaling solutions in the limit  $A \rightarrow 0$  and  $F \rightarrow \infty$  for  $l = 2$ , which we find to be the first mode to become unstable. We find that the general trends of the stability diagram are captured well, with small deviations from the full solution of Eq. (7.3) for small  $\epsilon$ , and larger deviations in the regime close to  $\epsilon_\infty$  where the scaling of the stationary radius  $\bar{R}_s \propto A^{-1/3}$  breaks down.

### F.2.3 Details on scaling analysis with hydrodynamic effects

With hydrodynamic effects included, the equation for the eigenvalues is

$$\Delta c \mu_{nl} = \frac{\Delta c}{\bar{R}} v_l^r(\bar{R}) + D_+ \bar{c}''(\bar{R}_+) - D_- \bar{c}''(\bar{R}_-) + \frac{D_+}{\bar{R}} c'_{nl}(\bar{R}_+) - \frac{D_-}{\bar{R}} c'_{nl}(\bar{R}_-). \quad (\text{F.53})$$

with

$$c'_{nl}(\bar{R}_-) = \frac{a_l^-}{\bar{R}} g_{l,i}(\lambda_- \bar{R}) + \frac{c_{lm,p}^-(\bar{R})}{\bar{R}} \cdot [g_{l,k}(\lambda_- \bar{R}) - g_{l,i}(\lambda_- \bar{R})] \quad (\text{F.54})$$

$$c'_{nl}(\bar{R}_+) = \frac{a_l^+}{\bar{R}} g_{l,k}(\lambda_+ \bar{R}) + \frac{c_{lm,p}^+(\bar{R})}{\bar{R}} \cdot [g_{l,i}(\lambda_+ \bar{R}) - g_{l,k}(\lambda_+ \bar{R})], \quad (\text{F.55})$$

and

$$g_{l,i}(x) = \frac{x i'_l(x)}{i_l(x)} \quad (\text{F.56})$$

$$g_{l,k}(x) = \frac{x k'_l(x)}{k_l(x)}. \quad (\text{F.57})$$

The first term is

$$\frac{\Delta c}{\bar{R}} v_l^r(\bar{R}) \approx -\frac{\gamma}{\eta_-} \frac{\Delta c}{\bar{R}} d_l \quad (\text{F.58})$$

which scales with  $A^a$  at the stationary radius, and a function  $d_l$  that only depends on  $\Delta = \eta_+/\eta_-$  and mode  $l$ . This function can be approximated by its limit for large modes  $l$ ,

$$d_l \approx \frac{l}{2(\Delta + 1)} \quad (\text{F.59})$$

This approximation works rather well even for  $l = 2$ .

The full hydrodynamic velocity is (derived via Stokes equation, see separate document)

$$v_l^{r+}(r) = -\frac{\gamma}{\eta_-} f_{C2} R^l r^{-l} + \frac{\gamma}{\eta_-} f_{C4} R^{l+2} r^{-l-2} \quad (\text{F.60})$$

$$v_l^{r-}(r) = \frac{\gamma}{\eta_-} f_{C1} R^{-l-1} r^{l+1} - \frac{\gamma}{\eta_-} f_{C3} R^{-l+1} r^{l-1}. \quad (\text{F.61})$$

The particular solutions for the concentration field, with inhomogeneity  $f_l^\pm(r) = -\frac{1}{D_\pm} v_l^{r\pm}(r) \bar{c}'_\pm(r)$ , can be found via a Greens ansatz as

$$c_{nl,p}^-(R) = \lambda_- k_l(\lambda_- R) \int_0^R i_l(\lambda_- r) f_l^-(r) r^2 dr \quad (\text{F.62})$$

$$c_{nl,p}^+(R) = \lambda_+ i_l(\lambda_+ R) \int_R^\infty k_l(\lambda_+ r) f_l^+(r) r^2 dr. \quad (\text{F.63})$$

For  $A \rightarrow 0$ , and  $R \ll l_\pm$ , we can express the modified spherical Bessel functions  $i_l(x)$  and  $k_l(x)$  by it's lowest orders for  $x \rightarrow 0$ ,

$$i_l(x) \approx \frac{x^l}{1 \cdot 3 \cdot 5 \cdot \dots \cdot (2l + 1)} \quad (\text{F.64})$$

$$k_l(x) \approx \frac{1 \cdot 3 \cdot 5 \cdot \dots \cdot (2l - 1)}{x^{l+1}} \quad (\text{F.65})$$

For the particular solution inside the droplet, we find that it is independent of the reaction amplitude  $A$ ,

$$c_{nl,p}^-(\bar{R}) \approx \frac{\gamma}{\eta_-} \frac{\nu_-}{3D_- k_-} \frac{1}{2l(2l + 1)} \left( \frac{f_{C3}}{2l + 3} - \frac{f_{C1}}{2l + 5} \right) \frac{R_0^3}{l_-^2}. \quad (\text{F.66})$$

This contributes the following term to Eq. (7.3):

$$-\frac{D_-}{\bar{R}} \frac{c_{lm,p}^-(\bar{R})}{\bar{R}} \cdot [g_{l,k}(\lambda_- \bar{R}) - g_{l,i}(\lambda_- \bar{R})] \approx \frac{\gamma}{\eta_-} \frac{\nu_-}{3k_-} \frac{2l - 1}{2l(2l + 1)} \left( \frac{f_{C1}}{2l + 5} - \frac{f_{C3}}{2l + 3} \right) \frac{R}{l_-^2} \quad (\text{F.67})$$

which goes with  $A^{2/3}$ , and therefore converges to 0 faster than the  $v^r$ -term in the limit  $A \rightarrow 0$ .

For the particular solution outside the droplet, the calculation is a bit more involved, because in the integral both small and large values for  $x$  occur. For this, we use a series expansion for  $k_l(x)$  (see Abramowitz et al. (1965)),

$$k_l(x) = 2R(l + 1/2, x)e^{-x} \quad (\text{F.68})$$

$$R(l + 1/2, x) = \sum_{k=0}^l (l + 1/2, k)(2x)^{-k} \quad (\text{F.69})$$

$$= 1 + \frac{(l + 1)!}{1!\Gamma(l)}(2x)^{-1} + \frac{(l + 2)!}{2!\Gamma(l - 1)}(2x)^{-2} + \dots \quad (\text{F.70})$$

This expansion, and the explicit form for  $\bar{c}$  yields terms  $\int e^{-2x} x^k$ . These are solved by  $-2^{-k-1}\Gamma(k + 1, 2x)$ , where  $\Gamma$  denotes the (incomplete) gamma function. Expanding the Gamma function as a series,

$$\Gamma(-n, x) = \frac{(-1)^n}{n!} \left[ E_1(x) - e^{-x} \sum_{j=0}^{n-1} \frac{(-1)^j j!}{x^{j+1}} \right] \quad (\text{F.71})$$

with exponential integral

$$E_1(x) = -\gamma - \ln x - \sum_{k=1}^{\infty} \frac{(-x)^k}{k \cdot k!}, \quad (\text{F.72})$$

we find a solution of the integrals in terms of sums of exponential and (rational) polynomial terms.

Keeping only the relevant terms (or  $R/l_+ \ll 1$ ), we arrive at

$$c_{nl,p}^+(\bar{R}) \approx \frac{\gamma}{\eta_-} \frac{1}{D_+} \frac{1}{1 \cdot 3 \cdot 5 \cdot \dots \cdot (2l + 1)} \frac{(2l)!}{l!} \left( \frac{2^{-l-2}}{l} f_{C2} - \frac{2^{-l+2}}{l-1} f_{C4} \right) l_+ \frac{R}{l_+} \left( \frac{\beta_+ \gamma}{R} - \Delta c \epsilon \right) \quad (\text{F.73})$$

which is independent of  $A$ , similar to  $c_{nl,p}^+(\bar{R})$ .

Comparison with Eq. (F.58) shows that the respective terms of the particular solutions in Eq. (F.53) have the same linear dependency on  $\gamma/\eta_-$ , but a larger dependency on  $A$ , and do therefore not contribute in the limit  $A \rightarrow 0$ . This is nice, since we would expect from physical considerations that for smaller reactions rates, the concentration field has smaller gradients, so that the advection of the field with the hydrodynamic flow plays a smaller role. Note however, that for intermediate values, it vanishes slower than the effects in Eq. (7.3), so that it can play a role for intermediate hydrodynamic influence, given by  $F = \gamma/\eta_- \cdot \tau/w$  (where  $w$  and  $\tau$  are relevant length- and timescales that are independent of  $A$ ).

Thus, combining the hydrodynamic term Eq. (F.58) with our results from Eq. (7.3), we find that for  $A \rightarrow 0$ , the hydrodynamic flow dominates, which stabilizes the droplet. The scaling of the growth rate with the reaction amplitude is due to the fact that we are considering stationary droplet sizes.

Including the hydrodynamic flow into Eq. (7.3) that describes the instability of the stationary droplet radius, we can express the onset of instability  $\mu_l = 0$  as

$$\epsilon_0(R_0) = \frac{1}{D_+ 2(l-1)} \left( R_0 F_0 \frac{w}{\tau} d_l + \frac{\beta_+ \gamma D_+}{R_0 \Delta c} f_l \right) \quad (\text{F.74})$$

with  $f_l = 2(l-1) + h_l(l+1) + h_l l \frac{D_- \beta_-}{D_+ \beta_+}$ . The minimum of this function can be found as

$$R_0^{*2} = \frac{1}{F_0 \frac{\tau}{w}} \frac{\beta_+ \gamma D_+}{\Delta c} \frac{f_l}{d_l} \quad (\text{F.75})$$

Since we are considering the stability of stationary radii, this needs to be equated to the expressions for the stationary radius, which gives a value for  $F_0$  at which the hydrodynamic effects start to dominate the droplet stability.

We can again find the limit of the eigenvalue for large stationary radii, where the first order perturbation is the hydrodynamic term (for large enough  $F_0$ ,

$$\mu \approx \frac{2}{3}(l-1) \frac{\nu_-}{\Delta c} - \frac{1}{R_0} F_0 \frac{w}{\tau} d_l - \frac{D_+ \beta_+ \gamma}{R_0^3 \Delta c} g_l \quad (\text{F.76})$$

with  $g_l = \frac{D_+}{D_-} h_l(l+1) + \frac{\beta_-}{\beta_+} h_l l$ . For large  $F_0$ , we can calculate an alternative equation for the stationary radii at which the instability develops  $\mu = 0$  (ignoring the last term), and equate it to the reformulation of Eq.(70) (again, ignoring the last term). We find the scaling behavior of the region of instability that is influenced mainly by the hydrodynamic flows

$$\epsilon_0 \approx \left( F_0 \frac{w}{\tau} \frac{d_l}{2(l-1)} \right)^2 3 \frac{\Delta c}{\nu_- D_+} \quad (\text{F.77})$$

or, returning to the non-rescaled form,  $\epsilon = \epsilon_0 A^{1/3}$  etc.,

$$\epsilon \approx F^2 A^{-1} \left( \frac{w}{\tau} \frac{d_l}{2(l-1)} \right)^2 3 \frac{\Delta c}{\nu_- D_+} \quad (\text{F.78})$$

For the other limit,  $F_0$  small, we recover the non-hydrodynamic scaling behavior. The transition is given by Eq. (F.75).

# Appendix G

## Parameter examples

---

### G.1 Chemical turnover time of stationary droplets

To facilitate the estimation of parameters, we define the droplet turnover time as the time after which the droplet material has been replaced on average. Consequently, the turnover time  $t_R$  is given by the total amount  $N$  of droplet material in the droplet, divided by the integrated flux  $J$  with which droplet material is turned into component  $A$  by the reaction  $B \rightarrow A$ ,

$$t_R = \frac{N}{J} . \quad (\text{G.1})$$

Here,  $N$  is given by

$$N = \int_V c_-(\mathbf{r}) dV , \quad (\text{G.2})$$

where  $c_-(\mathbf{r})$  is the concentration field of droplet material inside the droplet, and  $V$  is the droplet volume. In the stationary state, the reaction flux  $J$  is equal to the integrated outflux of droplet material across the droplet interface, which is given by

$$J = - \oint_S j_-(R) dA , \quad (\text{G.3})$$

where  $j_-(R)$  is the diffusion flux of droplet material normal to the droplet surface  $S$ .

In a stationary state,  $j_-(R)$  is given by Eq. (C.4) and  $c_-(\mathbf{r})$  by Eq. (C.1). We then have

$$N = \frac{4}{3} \pi R^3 \left( c_-^{(0)} - \frac{\nu_-}{k_-} \right) + 4\pi R l_-^2 \left( \frac{\nu_-}{k_-} + \frac{\gamma \beta_-}{R} \right) \left( \frac{R}{l_-} \coth \frac{R}{l_-} - 1 \right) \quad (\text{G.4})$$

$$J = 4\pi R D_- \left( \frac{\gamma \beta_-}{R} + \frac{\nu_-}{k_-} \right) \left( \frac{R}{l_-} \coth \frac{R}{l_-} - 1 \right) . \quad (\text{G.5})$$

Therefore, the turnover time of a stationary droplet is given by

$$t_R = \frac{c_-^{(0)} - \frac{\nu_-}{k_-}}{\nu_- + k_- \frac{\gamma\beta_-}{R}} \cdot \frac{\frac{1}{3} \left(\frac{R}{l_-}\right)^2}{\frac{R}{l_-} \coth \frac{R}{l_-} - 1} + \frac{1}{k_-}. \quad (\text{G.6})$$

In the limit of  $R \ll l_-$  and  $\gamma\beta_-/(c_-^{(0)} - c_+^{(0)}) \ll R$ , we find

$$t_R \approx \frac{c_-^{(0)}}{\nu_-}. \quad (\text{G.7})$$

## G.2 Examples of parameter values for dividing droplets without hydrodynamics

In Table G.1, we provide five examples of parameter values for which droplets become unstable. The corresponding stationary radii are shown in Fig. G.1 as a function of the supersaturation. The turnover time  $t_R$  is defined in G.1. Case I is based on the properties of colloidal droplets or liquid protein phases with low interfacial tension, Brangwynne et al. (2009); Li et al. (2012); Safran (1994). We find that droplet division at sizes of several micrometers could be realized experimentally, see Fig. G.1 and Table G.1. In case I the division radius is  $R_{div} \approx 3 \mu\text{m}$ . Case II is based on the properties of water/oil interfaces, see Safran (1994); Peters and Arabali (2013); Page et al. (2000); Atkins and de Paula (2010). This example shows that even for these larger interfacial tensions as compared to case I, droplets can still have a division radius of the order of micrometers. Case III shows the effect of different diffusion constants and length-scales inside and outside the droplet, with division radii again in the micrometer range. Cases IV and V explore parameter regimes for which dividing droplets are larger. Case IV is based on case I, but with a longer turnover time. This leads to an increased division radius of  $10 \mu\text{m}$ . Case V is an example for division at even larger radii with  $R_{div} \approx 140 \mu\text{m}$ . To obtain this droplet size, large diffusion constants  $D$  are required, and the interfacial width  $w$  and the turnover time  $t_R$  also have to be large. This can be understood by considering Eq. (4.31), which implies that for  $R \ll l_{\pm}$ , the division radius scales as  $R_{div} \sim (Dwt_R)^{1/3}$ .

Our analysis thus shows that dividing droplets with sizes of several micrometers could be achieved experimentally. Simple choices of realistic parameter values typically lead to such droplet sizes. However, larger droplets from 100 micrometers to millimeters may turn out to be more difficult to achieve. To obtain such droplets in case V we had to choose large diffusion coefficients and slow reaction rates. We therefore propose that dividing active droplets as presented in this work provide simple models of micrometer sized protocells.

## G.3 Estimation of the influence of hydrodynamic flows

Here we estimate the hydrodynamic parameter for two physical phase-separating systems to understand the importance of hydrodynamic flows on the droplet division

## G.3. Estimation of the influence of hydrodynamic flows

Quantity	Unit	Case I	Case II	Case III	Case IV	Case V
$D_-$	$\mu\text{m}^2/\text{s}$	10	10	1	10	1000
$D_+$	$\mu\text{m}^2/\text{s}$	10	10	100	10	1000
$w$	nm	10	1	10	10	100
$\gamma$	mN/m	$10^{-3}$	10	$10^{-3}$	$10^{-3}$	10
$\beta_- = \frac{w\Delta c}{6\gamma}$	$\text{M}\cdot\text{m}^2/\text{N}$	$2 \cdot 10^{-4}$	$2 \cdot 10^{-8}$	$2 \cdot 10^{-4}$	$2 \cdot 10^{-4}$	$1.7 \cdot 10^{-6}$
$\beta_+ = \frac{w\Delta c}{6\gamma}$	$\text{M}\cdot\text{m}^2/\text{N}$	$2 \cdot 10^{-4}$	$2 \cdot 10^{-8}$	$2 \cdot 10^{-4}$	$2 \cdot 10^{-4}$	$1.7 \cdot 10^{-6}$
$c_-^{(0)}$	mM	100	$10^3$	100	100	$10^3$
$c_+^{(0)}$	mM	1	$10^{-3}$	1	1	$10^{-3}$
$t_R$	s	100	100	10	4000	$10^4$ ( $\approx 3$ h)
$l_-$	mm	0.1	5	0.1	0.1	5
$l_+$	mm	0.1	5	0.01	0.1	5
$\nu_- = \frac{c_-^{(0)}}{t_R}$	mM/s	1	10	10	$2.5 \cdot 10^{-2}$	0.1
$\nu_+ = \epsilon\Delta ck_+$	nM/s	200	0.3	$2 \cdot 10^5$	100	30
$k_- = \frac{D_-}{l_-^2}$	$1/\text{s}$	$10^{-3}$	$4 \cdot 10^{-7}$	$10^{-4}$	$10^{-3}$	$4 \cdot 10^{-5}$
$k_+ = \frac{D_+}{l_+^2}$	$1/\text{s}$	$10^{-3}$	$4 \cdot 10^{-7}$	1	$10^{-3}$	$4 \cdot 10^{-5}$
$\bar{R}_s$ using Eq. (4.13)	$\mu\text{m}$	3	1	3	10	140
$\bar{R}_c$ using Eq. (4.13)	$\mu\text{m}$	0.7	0.2	0.7	1.7	20
$R_{div} = \bar{R}_s$	$\mu\text{m}$	3	1	3	10	140
$\epsilon_{div}$		$2 \cdot 10^{-3}$	$8 \cdot 10^{-4}$	$2 \cdot 10^{-3}$	$10^{-3}$	$8 \cdot 10^{-4}$
$k_+\tau_0$		$10^{-8}$	$4 \cdot 10^{-13}$	$10^{-5}$	$10^{-8}$	$5 \cdot 10^{-10}$
$k_-\tau_0$		$10^{-8}$	$4 \cdot 10^{-13}$	$10^{-9}$	$10^{-8}$	$5 \cdot 10^{-10}$
$\nu_+\tau_0/\Delta c$		$2 \cdot 10^{-11}$	$3 \cdot 10^{-17}$	$2 \cdot 10^{-9}$	$10^{-11}$	$3 \cdot 10^{-13}$
$\nu_-\tau_0/\Delta c$		$10^{-7}$	$10^{-9}$	$10^{-7}$	$2.5 \cdot 10^{-9}$	$10^{-9}$
$c_+^{(0)}/\Delta c$		0.01	$10^{-6}$	0.01	0.01	$10^{-6}$
$\beta_+/\beta_-$		1	1	1	1	1
$D_-/D_+$		1	1	0.01	1	1
$\Delta c = c_-^{(0)} - c_+^{(0)}$	mM	99	$10^3$	99	99	$10^3$
$w$	nm	10	1	10	10	100
$\tau_0 = w^2/D_+$	$\mu\text{s}$	10	0.1	1	10	10

Table G.1: Examples for parameter values of the effective model for five different cases. Both dimensional and dimensionless parameters are shown. Our choice of parameters that are related to phase separation ( $D_{\pm}$ ,  $w$ ,  $\gamma$ , and  $c_{\pm}^{(0)}$ ) is based on measured values in liquid protein phases, Brangwynne et al. (2009); Li et al. (2012); Safran (1994), (cases I, III and IV) and in water/oil interfaces, Safran (1994); Peters and Arabali (2013); Page et al. (2000); Atkins and de Paula (2010) (case II). Case V explores extreme parameter ranges to create large droplet radii. The parameters describing chemical reaction rates can vary widely depending on concentration levels and specific reactions considered, Atkins and de Paula (2010). The reaction rates  $k_{\pm}$  and  $\nu_{\pm}$  are related to elasticity coefficients, Kacser et al. (1973), for which only very few measured values have been reported. Instead of specifying  $k_{\pm}$  and  $\nu_{\pm}$  directly, we therefore choose experimentally relevant turnover times  $t_R$ , Brangwynne et al. (2009), and length-scales  $l_{\pm}$  that are larger than resulting droplet radii such that the droplets are approximately homogeneous. The remaining parameters ( $\beta_{\pm}$ ,  $\nu_{\pm}$ , and  $k_{\pm}$ ) can be determined using the expressions given in the first column of the Table. The supersaturation  $\epsilon_{div}$  at which the stationary radius  $\bar{R}_s$  becomes unstable,  $\mu_{12} = 0$ , is obtained by linear stability analysis.

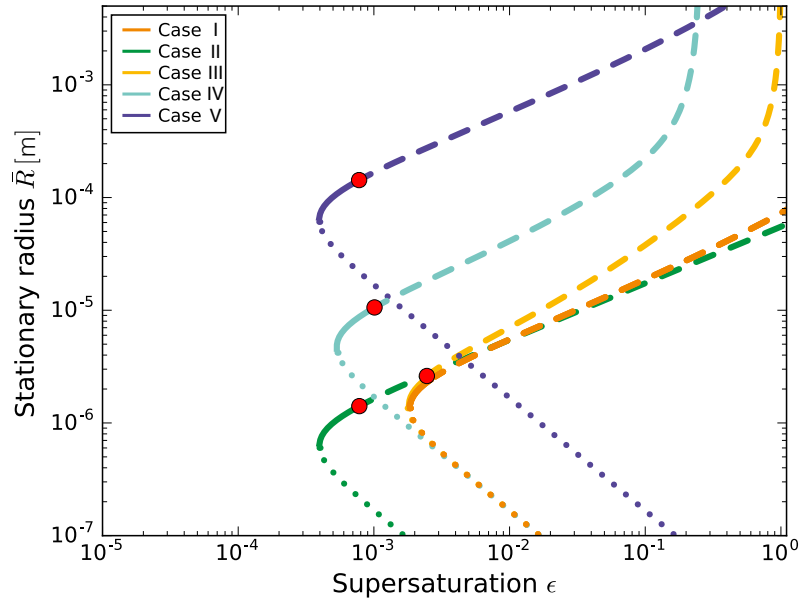


FIGURE G.1: Stationary radius  $\bar{R}$  as a function of the supersaturation  $\epsilon$ . The curves correspond to the five parameter sets given in Table G.1, and are calculated using Eq. (4.4). Dotted lines indicate an unstable droplet size ( $l = 0$  mode) and dashed lines indicate a shape instability ( $l = 2$  mode), see Eq. (4.13). Stable droplets are shown as solid lines. The red dots show the onset of the shape instability. We report the respective stationary radii and supersaturations in Table G.1.

in experimental systems. We discuss two cases, water-oil phase separation, and soft colloidal systems (such as protein-RNA phase-separation in cells). We have already estimated parameter values for both systems without the influence of hydrodynamic flows, where we found that droplet division should be possible for realistic values of chemical reaction rates in both systems, and that corresponding stationary radii would have sizes of a few micrometers. Here we estimate the value of the dimensionless viscosity  $F$  for water-oil and soft colloidal systems, and compare them to the analytical phase diagrams presented in Fig. 7.2.

To calculate the hydrodynamic parameter  $F$  for experimental systems, we need an estimation of the diffusion coefficient of the droplet material  $D_+$  outside the droplet, of the interfacial width  $w$ , of the surface tension  $\gamma$  and of the viscosity  $\eta_-$  inside the droplet. For water-oil systems, the interfacial width is of the order of  $w \approx 1nm$  and the diffusion constant is  $D_+ \approx 10^{-9}m^2/s$ . We can estimate the surface tension as  $\gamma \approx 10^{-2}N/m$ , and the viscosity  $\eta_- \approx 10^{-3}(N \cdot s)/m^2$ , Safran (1994); Haynes (2014). With these values, we find  $F \approx 0.1$ . In this case droplet division is strongly suppressed, see Fig. 7.2. For soft colloidal systems, we estimate  $w \approx 10nm$ ,  $D_+ \approx$



$10^{-10}m^2/s$  and  $\gamma \approx 10^{-6}N/m$ , Safran (1994); Brangwynne et al. (2009). The value of  $F$  depends on the viscosity of the droplet. For values  $\eta_- \approx 10^{-3}(N \cdot s)/m^2$ ,  $F \approx 10$ , and for  $\eta_- \approx 1 - 10(N \cdot s)/m^2$ , we have  $F \approx 10^4$ . In both cases droplet division is possible, but more easy to achieve for larger  $F$ . We convert  $A^*$  to the reaction rate  $\nu_-$  inside the droplet using the droplet concentration given in the previous section.

We can use the scaling analysis with hydrodynamic flows, Appendix F.2, to estimate the instability of the concrete parameter examples discussed previously under the influence of hydrodynamic flows. In these scaling equations, the ratios  $\eta_+/\eta_-$  and  $D_-\beta_-/(D_+\beta_+)$  enter the calculation of  $A^*$  and  $\epsilon^*$  but we find that they do not lead to relevant changes in the results. The scaling analysis thus yields results very similar to the estimation using Fig. 7.2.



## Bibliography

---

- Milton Abramowitz, Irene A Stegun, and David Miller. Handbook of Mathematical Functions With Formulas, Graphs and Mathematical Tables (National Bureau of Standards Applied Mathematics Series No. 55). *Journal of Applied Mechanics*, 32(1):239, 1965. doi: 10.1115/1.3625776. URL <http://appliedmechanics.asmedigitalcollection.asme.org/article.aspx?articleid=1396937>.
- Bruce Alberts, Dennis Bray, Karen Hopkin, Alexander D Johnson, Julian Lewis, Martin Raff, Keith Roberts, and Peter Walter. *Essential Cell Biology*. Garland Science, 2013. ISBN 0815344554.
- Meghan Andes-Koback and Christine D Keating. Complete Budding and Asymmetric Division of Primitive Model Cells To Produce Daughter Vesicles with Different Interior and Membrane Compositions. *Journal of the American Chemical Society*, 133(24):9545–9555, 2011. doi: 10.1021/ja202406v. URL <https://pubs.acs.org/doi/10.1021/ja202406v>.
- U Ascher, S Ruuth, and R Spiteri. *Implicit-Explicit Runge-Kutta Methods for Time-Dependent Partial Differential Equations*, 1997.
- P Atkins and J de Paula. *Atkins' Physical Chemistry*. OUP Oxford, 2010. ISBN 9780199543373. URL <https://books.google.de/books?id=BV6cAQAQBAJ>.
- P W Atkins. *Physical Chemistry*. Oxford University Press, Oxford, 1994.
- William M Aumiller and Christine D Keating. Phosphorylation-mediated RNA/peptide complex coacervation as a model for intracellular liquid organelles. *Nature Chemistry*, 8(2):129–137, feb 2016. doi: 10.1038/nchem.2414. URL <http://dx.doi.org/10.1038/nchem.2414>.

- Pascale Angelica Bachmann, Pier Luigi Luisi, and Jacques Lang. Autocatalytic self-replicating micelles as models for prebiotic structures. *Nature*, 357(6373):57–59, may 1992. doi: 10.1038/357057a0. URL <http://dx.doi.org/10.1038/357057a0>.
- Salman F. Banani, Hyun O. Lee, Anthony A. Hyman, and Michael K. Rosen. Biomolecular condensates: organizers of cellular biochemistry. *Nature Reviews Molecular Cell Biology*, 18(5):285–298, may 2017. doi: 10.1038/nrm.2017.7. URL <http://dx.doi.org/10.1038/nrm.2017.7>.
- John A Baross and Sarah E Hoffman. Submarine hydrothermal vents and associated gradient environments as sites for the origin and evolution of life. *Origins of Life and Evolution of the Biosphere*, 15(4):327–345, dec 1985. doi: 10.1007/BF01808177. URL <http://dx.doi.org/10.1007/BF01808177>.
- R G Barrera, G A Estevez, and J Giraldo. Vector spherical harmonics and their application to magnetostatics. *European Journal of Physics*, 6(4):287–294, oct 1985. doi: 10.1088/0143-0807/6/4/014. URL <http://stacks.iop.org/0143-0807/6/i=4/a=014?key=crossref.3ddea36749b1b2b1e7c999596f2b68d8>.
- George Keith Batchelor. *An Introduction to Fluid Dynamics*. Cambridge University Press, 2000.
- Tobias Baumgart, Samuel T. Hess, and Watt W. Webb. Imaging coexisting fluid domains in biomembrane models coupling curvature and line tension. *Nature*, 425(6960):821–824, oct 2003. doi: 10.1038/nature02013. URL <http://www.nature.com/articles/nature02013>.
- Clifford P. Brangwynne, Christian R. Eckmann, D S Courson, A Rybarska, Carsten Hoege, Jöbin Gharakhani, F. Julicher, and Anthony A Hyman. Germline P Granules Are Liquid Droplets That Localize by Controlled Dissolution/Condensation. *Science*, 324(5935):1729–1732, jun 2009. doi: 10.1126/science.1172046. URL <http://www.sciencemag.org/cgi/doi/10.1126/science.1172046>.
- A.J. Bray. Theory of phase-ordering kinetics. *Advances in Physics*, 43(3):357–459, jun 1994. doi: 10.1080/00018739400101505. URL <http://www.tandfonline.com/doi/abs/10.1080/00018739400101505>.
- Dawn J Brooks, Jacques R Fresco, Arthur M Lesk, and Mona Singh. Evolution of Amino Acid Frequencies in Proteins Over Deep Time: Inferred Order of Introduction of Amino Acids into the Genetic Code. *Molecular Biology and Evolution*, 19(10):1645–1655, oct 2002. doi: 10.1093/oxfordjournals.molbev.a003988. URL <http://academic.oup.com/mbe/article/19/10/1645/1258758>.
- Kevin P. Browne, David A. Walker, Kyle J. M. Bishop, and Bartosz A. Grzybowski. Self-Division of Macroscopic Droplets: Partitioning of Nanosized Cargo into Nanoscale Micelles. *Angewandte Chemie*, 122(38):6908–6911, sep 2010. doi: 10.1002/ange.201002551. URL <http://doi.wiley.com/10.1002/ange.201002551>.

- John W Cahn and John E Hilliard. Free Energy of a Nonuniform System. I. Interfacial Free Energy. *The Journal of Chemical Physics*, 28(2):258–267, feb 1958. doi: 10.1063/1.1744102. URL <http://aip.scitation.org/doi/10.1063/1.1744102>.
- Daniele Carati and René Lefever. Chemical freezing of phase separation in immiscible binary mixtures. *Physical Review E*, 56(3):3127–3136, sep 1997. doi: 10.1103/PhysRevE.56.3127. URL <https://link.aps.org/doi/10.1103/PhysRevE.56.3127>.
- M E Cates. Complex fluids: the physics of emulsions. *Soft Interfaces: Lecture Notes of the Les Houches Summer School: Volume 98, July 2012*, 98:317, 2012.
- Subrahmanyan Chandrasekhar. *Hydrodynamic and hydromagnetic stability*. Dover Publications, Inc., New York, 1981.
- C.-M. Chen, P. G. Higgs, and F. C. MacKintosh. Theory of Fission for Two-Component Lipid Vesicles. *Physical Review Letters*, 79(8):1579–1582, aug 1997. doi: 10.1103/PhysRevLett.79.1579. URL <https://link.aps.org/doi/10.1103/PhysRevLett.79.1579>.
- L.Q. Chen and Jie Shen. Applications of semi-implicit Fourier-spectral method to phase field equations. *Computer Physics Communications*, 108(2-3):147–158, feb 1998. doi: 10.1016/S0010-4655(97)00115-X. URL <http://www.sciencedirect.com/science/article/pii/S001046559700115X>.
- J J Christensen, K Elder, and H C Fogedby. Phase segregation dynamics of a chemically reactive binary mixture. *Phys. Rev. E*, 54(3):R2212—R2215, 1996. doi: 10.1103/PhysRevE.54.R2212. URL <http://pre.aps.org/abstract/PRE/v54/i3/pR2212{31}>.
- Peter Constantin, Todd F. Dupont, Raymond E. Goldstein, Leo P. Kadanoff, Michael J. Shelley, and Su-Min Zhou. Droplet breakup in a model of the Hele-Shaw cell. *Physical Review E*, 47(6):4169–4181, jun 1993. doi: 10.1103/PhysRevE.47.4169. URL <https://link.aps.org/doi/10.1103/PhysRevE.47.4169>.
- John Crank. *Free and moving boundary problems*. Clarendon Press, 1987. ISBN 0198533705, 9780198533702. URL <http://books.google.com/books?id=wTB4AsVvQDsc&printsec=frontcover>.
- Vittorio Cristini and John Lowengrub. Three-dimensional crystal growth—II: non-linear simulation and control of the Mullins–Sekerka instability. *Journal of Crystal Growth*, 266(4):552–567, jun 2004. doi: 10.1016/j.jcrysgro.2004.02.115. URL <https://linkinghub.elsevier.com/retrieve/pii/S002202480400346X>.
- John Crosby, Tom Treadwell, Michelle Hammerton, Konstantinos Vasilakis, Matthew P. Crump, David S. Williams, and Stephen Mann. Stabilization and enhanced reactivity of actinorhodin polyketide synthase minimal complex in polymer–nucleotide coacervate droplets. *Chemical Communications*, 48(97):11832, 2012. doi: 10.1039/c2cc36533b. URL <http://xlink.rsc.org/?DOI=c2cc36533b>.

- Michael Cross and Henry Greenside. *Pattern Formation and Dynamics in Nonequilibrium Systems*. Cambridge University Press, Cambridge, 2009. ISBN 9780511627200. doi: 10.1017/CBO9780511627200. URL <http://books.google.com/books?id=TjK7PQAACA&printsec=frontcover>{%}5Cnpapers2://publication/uuid/3146CF37-2E58-4773-9068-4C68D2A79F79.
- Stephen H Davis. *Theory of solidification*. Cambridge University Press, 2001.
- Sybrén Ruurds De Groot and Peter Mazur. *Non-equilibrium thermodynamics*. Dover Publications, Inc., New York, 2011.
- Graham R Dennis, Joseph J Hope, and Mattias T Johnsson. XMDS2: Fast, scalable simulation of coupled stochastic partial differential equations. *Computer Physics Communications*, 184(1):201–208, jan 2013. doi: 10.1016/j.cpc.2012.08.016. URL <https://linkinghub.elsevier.com/retrieve/pii/S0010465512002822>.
- I Derényi and I Lagzi. Fatty acid droplet self-division driven by a chemical reaction. *Phys. Chem. Chem. Phys.*, 16(10):4639–4641, jan 2014. doi: 10.1039/C3CP54676D. URL <http://xlink.rsc.org/?DOI=C3CP54676D>.
- Rashmi C Desai and Raymond Kapral. *Dynamics of Self-organized and Self-assembled Structures*. Cambridge University Press, 2009.
- H.G. Döbereiner, J. Käs, D. Noppl, I. Sprenger, and E. Sackmann. Budding and fission of vesicles. *Biophysical Journal*, 65(4):1396–1403, oct 1993. doi: 10.1016/S0006-3495(93)81203-7. URL <https://linkinghub.elsevier.com/retrieve/pii/S0006349593812037>.
- Nobuhide Doi, Koichi Kakukawa, Yuko Oishi, and Hiroshi Yanagawa. High solubility of random-sequence proteins consisting of five kinds of primitive amino acids. *Protein Engineering, Design and Selection*, 18(6):279–284, jun 2005. doi: 10.1093/protein/gzi034. URL <http://academic.oup.com/peds/article/18/6/279/1510755/High-solubility-of-randomsequence-proteins>.
- Björn Drobot, Juan M. Iglesias-Artola, Kristian Le Vay, Viktoria Mayr, Mrityunjay Kar, Moritz Kreysing, Hannes Mutschler, and T-Y. Dora Tang. Compartmentalised RNA catalysis in membrane-free coacervate protocells. *Nature Communications*, 9(1):3643, dec 2018. doi: 10.1038/s41467-018-06072-w. URL <http://www.nature.com/articles/s41467-018-06072-w>.
- Jens Eggers. Nonlinear dynamics and breakup of free-surface flows. *Reviews of Modern Physics*, 69(3):865–930, 1997. doi: 10.1103/RevModPhys.69.865.
- Shana Elbaum-Garfinkle, Younghoon Kim, Krzysztof Szczepaniak, Carlos Chih-Hsiung Chen, Christian R. Eckmann, Sua Myong, and Clifford P. Brangwynne. The disordered P granule protein LAF-1 drives phase separation into droplets

- with tunable viscosity and dynamics. *Proceedings of the National Academy of Sciences*, 112(23):201504822, 2015. doi: 10.1073/pnas.1504822112. URL <http://www.pnas.org/lookup/doi/10.1073/pnas.1504822112>.
- Martha J Fedor and James R Williamson. The catalytic diversity of RNAs. *Nat. Rev. Mol. Cell. Biol.*, 6(5):399–412, may 2005. doi: 10.1038/nrm1647.
- Marina Feric, Nilesh Vaidya, Tyler S Harmon, Diana M Mitrea, Lian Zhu, Tiffany M Richardson, Richard W Kriwacki, Rohit V Pappu, and Clifford P Brangwynne. Coexisting Liquid Phases Underlie Nucleolar Subcompartments. *Cell*, 165(7):1686–1697, 2016. doi: <https://doi.org/10.1016/j.cell.2016.04.047>. URL <http://www.sciencedirect.com/science/article/pii/S0092867416304925>.
- Paul I J Flory. Thermodynamics of High Polymer Solutions. *The Journal of Chemical Physics*, 10(51):51–61, 1942. doi: 10.1146/annurev.pc.02.100151.002123.
- S W Fox. The evolutionary significance of phase-separated microsystems. *Orig. Life*, 7(1):49–68, jan 1976.
- Erica A. Frankel, Philip C. Bevilacqua, and Christine D. Keating. Polyamine/Nucleotide Coacervates Provide Strong Compartmentalization of Mg<sup>2+</sup>, Nucleotides, and RNA. *Langmuir*, 32(8):2041–2049, 2016. doi: 10.1021/acs.langmuir.5b04462.
- A. Gierer and H. Meinhardt. A theory of biological pattern formation. *Kybernetik*, 12(1):30–39, 1972. doi: 10.1007/BF00289234. URL <http://www.springerlink.com/index/t541854v22417131.pdf>.
- Walter Gilbert. Origin of life: The RNA world. *Nature*, 319(6055), 1986.
- Luca Giomi and Antonio DeSimone. Spontaneous division and motility in active nematic droplets. *Phys. Rev. Lett.*, 112(14):147802, 2014. URL <http://eutils.ncbi.nlm.nih.gov/entrez/eutils/efetch.fcgi?dbfrom=pubmed&id=24766017&retmode=ref&cmd=prlinks>.
- Sharon C Glotzer, D Stauffer, and N Jan. Monte Carlo simulations of phase separation in chemically reactive binary mixtures. *Phys. Rev. Lett.*, 72(26):4109–4112, 1994. URL [http://prl.aps.org/abstract/PRL/v72/i26/p4109\\_f1](http://prl.aps.org/abstract/PRL/v72/i26/p4109_f1).
- Jeremy B A Green and James Sharpe. Positional information and reaction-diffusion: two big ideas in developmental biology combine. *Development (Cambridge, England)*, 142(7):1203–1211, 2015. doi: 10.1242/dev.114991. URL <http://dev.biologists.org/content/142/7/1203.full>.
- Shani Guttman, Zvi Sapir, Moty Schultz, Alexander V. Butenko, Benjamin M. Ocko, Moshe Deutsch, and Eli Sloutskin. How faceted liquid droplets grow tails. *Proceedings of the National Academy of Sciences*, page 201515614, 2016. doi:

- 10.1073/pnas.1515614113. URL <http://www.pnas.org/lookup/doi/10.1073/pnas.1515614113>.
- John Burdon Sanderson Haldane. The origin of life. *The Rationalist Annual*, 148:3–10, 1929. URL <http://www.sciencedirect.com/science/article/pii/S001282529900015X>.
- M M Hanczyc. Metabolism and motility in prebiotic structures. *Philos. Trans. R. Soc. Lond., B, Biol. Sci.*, 366(1580):2885–2893, 2011. doi: 10.1098/rstb.2011.0141. URL <http://eutils.ncbi.nlm.nih.gov/entrez/eutils/elink.fcgi?dbfrom=pubmed&id=21930579&retmode=ref&cmd=prlinks>.
- M M Hanczyc and J W Szostak. Replicating vesicles as models of primitive cell growth and division. *Curr. Opin. Chem. Biol.*, 8(6):660–664, 2004. doi: 10.1016/j.cbpa.2004.10.002. URL <http://eutils.ncbi.nlm.nih.gov/entrez/eutils/elink.fcgi?dbfrom=pubmed&id=15556412&retmode=ref&cmd=prlinks>.
- William M Haynes. *CRC handbook of chemistry and physics*. CRC press, 2014.
- Stephan Herminghaus, Corinna C Maass, Carsten Krüger, Shashi Thutupalli, Lucas Goehring, and Christian Bahr. Interfacial mechanisms in active emulsions. *Soft matter*, 10(36):7008–22, 2014. doi: 10.1039/c4sm00550c. URL <http://pubs.rsc.org/en/content/articlehtml/2014/sm/c4sm00550c>.
- Paul G Higgs and Niles Lehman. The {RNA} World: molecular cooperation at the origins of life. *Nat. Rev. Genet.*, 16(1):7–17, jan 2015. doi: 10.1038/nrg3841. URL <http://dx.doi.org/10.1038/nrg3841>.
- Maurice L. Huggins. Some Properties of Solutions of Long-chain Compounds. *J. Phys. Chem.*, 46(1):151–158, 1942. doi: 10.1021/j150415a018. URL <http://pubs.acs.org/doi/abs/10.1021/j150415a018>.
- Anthony A Hyman, Christoph A Weber, and Frank Jülicher. Liquid-liquid phase separation in biology. *Annu. Rev. Cell Dev. Biol.*, 30(1):39–58, 2014. doi: 10.1146/annurev-cellbio-100913-013325. URL <http://www.annualreviews.org/doi/abs/10.1146/annurev-cellbio-100913-013325>.
- William M Jacobs and Daan Frenkel. Phase Transitions in Biological Systems with Many Components. *Biophysj*, 112(4):683–691, 2017. doi: 10.1016/j.bpj.2016.10.043. URL <http://dx.doi.org/10.1016/j.bpj.2016.10.043>.
- H O Johansson, G Karlström, F Tjerneld, and C a Haynes. Driving forces for phase separation and partitioning in aqueous two-phase systems. *Journal of chromatography. B, Biomedical sciences and applications*, 711(1-2):3–17, 1998. doi: 10.1016/S0378-4347(97)00585-9. URL <http://www.ncbi.nlm.nih.gov/pubmed/9699970>.



- Frank Jülicher, Stephan W Grill, and Guillaume Salbreux. Hydrodynamic theory of active matter. *Reports on Progress in Physics*, 81(7):076601, jul 2018. doi: 10.1088/1361-6633/aab6bb. URL <http://stacks.iop.org/0034-4885/81/i=7/a=076601?key=crossref.54b1ff7d6fa0c8207d74f7041b8f02b8>.
- H Kacser, , and JA34 Burns. The control of flux. In *Symp. Soc. Exp. Biol.*, volume 27, pages 65–104, 1973.
- Eric Karsenti. Self-organization in cell biology: a brief history. *Nature Reviews Molecular Cell Biology*, 9(3):255–262, mar 2008. doi: 10.1038/nrm2357. URL <http://www.nature.com/articles/nrm2357>.
- Andrew H. Knoll and Martin A. Nowak. The timetable of evolution. *Science Advances*, 3(5):1–14, 2017. doi: 10.1126/sciadv.1603076.
- Ryo Kobayashi. Modeling and numerical simulations of dendritic crystal growth. *Physica D: Nonlinear Phenomena*, 63(3-4):410–423, 1993. doi: 10.1016/0167-2789(93)90120-P.
- Shogo Koga, David S Williams, Adam W Perriman, and Stephen Mann. Peptide–nucleotide microdroplets as a step towards a membrane–free protocell model. *Nature Chemistry*, 3(9):720–724, 2011. doi: 10.1038/nchem.1110. URL <http://dx.doi.org/10.1038/nchem.1110>.
- Dilip Kondepudi and Ilya Prigogine. *Modern thermodynamics: from heat engines to dissipative structures*. John Wiley & Sons, 2014.
- Moritz Kreysing, Lorenz Keil, Simon Lanzmich, and Dieter Braun. Heat flux across an open pore enables the continuous replication and selection of oligonucleotides towards increasing length. *Nature Chemistry*, 7(3):203–208, 2015. doi: 10.1038/nchem.2155. URL <http://www.ncbi.nlm.nih.gov/pubmed/25698328>{%}35Cn<http://dx.doi.org/10.1038/nchem.2155>.
- K. Kruse, J. F. Joanny, F. Jülicher, J Prost, and K Sekimoto. Asters, Vortices, and Rotating Spirals in Active Gels of Polar Filaments. *Physical Review Letters*, 92(7): 1–4, 2004. doi: 10.1103/PhysRevLett.92.078101.
- Sławomir Lach, Seok Min Yoon, and Bartosz A. Grzybowski. Tactic, reactive, and functional droplets outside of equilibrium. *Chem. Soc. Rev.*, 65:1392–1399, 2016. doi: 10.1039/C6CS00242K. URL <http://xlink.rsc.org/?DOI=C6CS00242K>.
- J S Langer. Instabilities and pattern formation in crystal growth. *Reviews of Modern Physics*, 52(1):1–28, 1980. doi: 10.1103/RevModPhys.52.1. URL <http://link.aps.org/doi/10.1103/RevModPhys.52.1>.
- Kathryn A. Lanier and Loren Dean Williams. The Origin of Life: Models and Data. *Journal of Molecular Evolution*, 84(2-3):85–92, 2017. doi: 10.1007/s00239-017-9783-y.

- Mei Li, Xin Huang, T. Y Dora Tang, and Stephen Mann. Synthetic cellularity based on non-lipid micro-compartments and protocell models, 2014. URL <http://dx.doi.org/10.1016/j.cbpa.2014.05.018>.
- Pilong Li, Sudeep Banjade, Hui-Chun Cheng, Soyeon Kim, Baoyu Chen, Liang Guo, Marc Llaguno, Javoris V Hollingsworth, David S King, Salman F Banani, Paul S Russo, Qiu-Xing Jiang, B Tracy Nixon, and Michael K Rosen. Phase transitions in the assembly of multivalent signalling proteins. *Nature*, 483(7389): 336–340, 2012. doi: 10.1038/nature10879. URL <http://www.nature.com/nature/journal/v483/n7389/full/nature10879.html>.
- I.M. M Lifshitz and V.V. V Slyozov. The kinetics of precipitation from supersaturated solid solutions. *J. Phys. Chem. Solids*, 19(1-2):35–50, 1961. doi: 10.1016/0022-3697(61)90054-3. URL <http://linkinghub.elsevier.com/retrieve/pii/0022369761900543>.
- Yuan Lin, David S.W. Protter, Michael K. Rosen, and Roy Parker. Formation and Maturation of Phase-Separated Liquid Droplets by RNA-Binding Proteins. *Molecular Cell*, 60(2):208–219, oct 2015. doi: 10.1016/j.molcel.2015.08.018. URL <http://dx.doi.org/10.1016/j.molcel.2015.08.018>.
- Corinna C. Maass, Carsten Krüger, Stephan Herminghaus, and Christian Bahr. Swimming Droplets. *Annual Review of Condensed Matter Physics*, 7(1):annurev-conmatphys-031115-011517, 2016. doi: 10.1146/annurev-conmatphys-031115-011517. URL <http://www.annualreviews.org/doi/10.1146/annurev-conmatphys-031115-011517>.
- Javier Macía and Ricard V Solé. Synthetic Turing protocells: vesicle self-reproduction through symmetry-breaking instabilities. *Philos. Trans. R. Soc. Lond. B*, 362(1486):1821–1829, oct 2007. doi: 10.1098/rstb.2007.2074. URL <http://rstb.royalsocietypublishing.org/cgi/doi/10.1098/rstb.2007.2074>.
- S Marchi, W F Bottke, L. T. Elkins-Tanton, M Bierhaus, K Wuennemann, A Morbidelli, and D A Kring. Widespread mixing and burial of Earth’s Hadean crust by asteroid impacts. *Nature*, 511(7511):578–582, 2014. doi: 10.1038/nature13539. URL <http://dx.doi.org/10.1038/nature13539>.
- William F Martin. Hydrogen, metals, bifurcating electrons, and proton gradients: the early evolution of biological energy conservation. *FEBS Lett.*, 586(5):485–493, mar 2012. doi: 10.1016/j.febslet.2011.09.031.
- William F Martin, Filipa L Sousa, and Nick Lane. Evolution. Energy at life’s origin. *Science*, 344(6188):1092–1093, jun 2014. doi: 10.1126/science.1251653.
- C. B. Mast, S. Schink, U. Gerland, and D. Braun. Escalation of polymerization in a thermal gradient. *Proceedings of the National Academy of Sciences*, 110(20):8030–8035, 2013. doi: 10.1073/pnas.1303222110. URL <http://www.pnas.org/cgi/doi/10.1073/pnas.1303222110>.

- H. Meinhardt. Pattern formation in biology: a comparison of models and experiments. *Rep. Prog. Phys.*, 55(6):797–849, 1992. doi: 10.1088/0034-4885/55/6/003. URL <http://iopscience.iop.org/0034-4885/55/6/003>.
- Amandine Molliex, Jamshid Temirov, Jihun Lee, Maura Coughlin, Anderson P Kanagaraj, Hong Joo Kim, Tanja Mittag, and J Paul Taylor. Phase Separation by Low Complexity Domains Promotes Stress Granule Assembly and Drives Pathological Fibrillization Article Phase Separation by Low Complexity Domains Promotes Stress Granule Assembly and Drives Pathological Fibrillization. *Cell*, 163(1):123–133, 2015. doi: 10.1016/j.cell.2015.09.015. URL <http://dx.doi.org/10.1016/j.cell.2015.09.015>.
- Matthias Morasch, Dieter Braun, and Christof B. Mast. Heat-Flow-Driven Oligonucleotide Gelation Separates Single-Base Differences. *Angewandte Chemie – International Edition*, pages 6788–6791, 2016. doi: 10.1002/anie.201601886.
- William W Mullins and Robert F Sekerka. Morphological Stability of a Particle Growing by Diffusion or Heat Flow. *J. Appl. Phys.*, 34(2):323–329, 1963. doi: 10.1063/1.1702607. URL <http://scitation.aip.org/content/aip/journal/jap/34/2/10.1063/1.1702607>.
- Giovanni Murtas. Early self-reproduction, the emergence of division mechanisms in protocells. *Mol. BioSyst.*, 9(2):195–204, 2013. doi: 10.1039/C2MB25375E. URL <http://xlink.rsc.org/?DOI=C2MB25375Ehttp://eutils.ncbi.nlm.nih.gov/entrez/eutils/elink.fcgi?dbfrom=pubmed&id=23232904&retmode=ref&cmd=prlinks>.
- Karina K Nakashima, Jochem F Baaij, and Evan Spruijt. Reversible generation of coacervate droplets in an enzymatic network. *Soft Matter*, 14(3):361–367, 2018. doi: 10.1039/C7SM01897E. URL <http://pubs.rsc.org/en/content/articlepdf/2017/sm/c7sm01897ehttp://xlink.rsc.org/?DOI=C7SM01897E>.
- Allen P. Nutman, Vickie C. Bennett, Clark R. L. Friend, Martin J. Van Kranendonk, and Allan R. Chivas. Rapid emergence of life shown by discovery of 3,700-million-year-old microbial structures. *Nature*, pages 1–12, 2016. doi: 10.1038/nature19355. URL <http://www.nature.com/doi/finder/10.1038/nature19355>.
- Aleksandr Ivanovich Oparin. Origin of Life. *Izd.Moskovhii RabochiI*, 1924.
- Aleksandr Ivanovich Oparin. *Origin of Life*. Dover Publications, Inc., New York, 1952.
- Wilhelm Ostwald. Studien über die Bildung und Umwandlung fester Körper. *Z. Phys. Chem*, 22(3):289–330, 1897.
- Cheryl A. Page, James S. Bonner, Peggy L. Sumner, and Robin L. Autenrieth. Solubility of petroleum hydrocarbons in oil/water systems. *Marine Chemistry*, 70(1-3): 79–87, 2000. doi: 10.1016/S0304-4203(00)00016-5.

- A Z Patashinski, R Orlik, K Paclawski, M A Ratner, and B A Grzybowski. The unstable and expanding interface between reacting liquids: Theoretical interpretation of negative surface tension. *Soft Matter*, 8(5):1601–1608, 2012. URL <http://pubs.rsc.org/en/content/articlehtml/2012/sm/c1sm06590d>.
- Avinash Patel, Hyun O Lee, Louise Jawerth, Shovamayee Maharana, Marcus Jahnelt, Marco Y Hein, Stoyno Stoynov, Julia Mahamid, Shambaditya Saha, Titus M Franzmann, Andrej Pozniakovski, Ina Poser, Nicola Maghelli, Loic A Royer, Martin Weigert, Eugene W Myers, Stephan Grill, David Drechsel, Anthony A Hyman, and Simon Alberti. A Liquid-to-Solid Phase Transition of the ALS Protein FUS Accelerated by Disease Mutation. *Cell*, 162(5):1066–1077, 2015. doi: <https://doi.org/10.1016/j.cell.2015.07.047>. URL <http://www.sciencedirect.com/science/article/pii/S0092867415009630>.
- Joseph D Paulsen, Rémi Carmigniani, Anerudh Kannan, Justin C Burton, and Sidney R Nagel. Coalescence of bubbles and drops in an outer fluid. *Nature Communications*, 5:3182, 2014. doi: 10.1038/ncomms4182. URL <http://www.ncbi.nlm.nih.gov/pubmed/24458225> <http://www.nature.com/doi/10.1038/ncomms4182>.
- Ben K. D. Pearce, Ralph E. Pudritz, Dmitry A. Semenov, and Thomas K. Henning. Origin of the RNA world: The fate of nucleobases in warm little ponds. *Proceedings of the National Academy of Sciences*, 114(43):11327–11332, oct 2017. doi: 10.1073/pnas.1710339114. URL <http://www.pnas.org/lookup/doi/10.1073/pnas.1710339114>.
- F. Peters and D. Arabali. Interfacial tension between oil and water measured with a modified contour method. *Colloids and Surfaces A: Physicochemical and Engineering Aspects*, 426:1–5, 2013. doi: 10.1016/j.colsurfa.2013.03.010. URL <http://dx.doi.org/10.1016/j.colsurfa.2013.03.010>.
- Matthew W. Powner, Béatrice Gerland, and John D. Sutherland. Synthesis of activated pyrimidine ribonucleotides in prebiotically plausible conditions. *Nature*, 459(7244):239–242, 2009. doi: 10.1038/nature08013. URL <http://www.nature.com/doi/10.1038/nature08013>.
- Ilya Prigogine, Gregoire Nicolis, and Agnes Babloyantz. Thermodynamics of evolution. *Physics Today*, 25(11):23–28, nov 1972. doi: 10.1063/1.3071090. URL <http://physicstoday.scitation.org/doi/10.1063/1.3071090>.
- S. Puri and H. L. Frisch. Segregation dynamics of binary mixtures with simple chemical reactions. *Journal of Physics A: General Physics*, 27(18):6027–6038, 1994. doi: 10.1088/0305-4470/27/18/013.
- Christopher V Rao, Denise M Wolf, and Adam P Arkin. Control, exploitation and tolerance of intracellular noise. *Nature*, 420(6912):231–237, 2002. doi: 10.1038/nature01258. URL [http://sfx.mpg.de/sfx/\\_local?id=doi:10.1038/nature01258](http://sfx.mpg.de/sfx/_local?id=doi:10.1038/nature01258).

- Riccardo Rao and Massimiliano Esposito. Nonequilibrium Thermodynamics of Chemical Reaction Networks: Wisdom from Stochastic Thermodynamics. *arXiv*, 041064:19, 2016. doi: 10.1103/PhysRevX.6.041064. URL <http://arxiv.org/abs/1602.07257>.
- Lord Rayleigh. On the instability of jets. *Proceedings of the London Mathematical Society*, 10:4–13, 1878. doi: 10.1112/plms/s1-10.1.4.
- Lord Rayleigh. On the instability of a cylinder of viscous liquid under capillary force. *The London, Edinburgh, and Dublin Philosophical Magazine and Journal of Science*, 34(207):145–154, 1892. doi: 10.1080/14786430601019433. URL <http://www.tandfonline.com/doi/abs/10.1080/14786449208620301>.
- Benedikt Rieß, Caren Wanzke, Marta Tena-Solsona, Raphael K. Grötsch, Chandan Maity, and Job Boekhoven. Dissipative assemblies that inhibit their deactivation. *Soft Matter*, 14(23):4852–4859, 2018. doi: 10.1039/C8SM00822A. URL <http://xlink.rsc.org/?DOI=C8SM00822A>.
- Samuel A Safran. *Statistical thermodynamics of surfaces, interfaces, and membranes*, volume 90. Perseus Books, 1994.
- Shambaditya Saha, Christoph A Weber, Marco Nusch, Omar Adame-Arana, Carsten Hoege, Marco Y Hein, Erin Osborne-Nishimura, Julia Mahamid, Marcus Jahnel, Louise Jawerth, Andrej Pozniakovski, Christian R Eckmann, Frank Jülicher, Anthony A Hyman, Frank Jü, Anthony A Hyman, Omar Adame-Arana, Carsten Hoege, Marco Y Hein, Erin Osborne-Nishimura, Julia Mahamid, Marcus Jahnel, Louise Jawerth, and Andrej Pozniakovski. Polar Positioning of Phase-Separated Liquid Compartments in Cells Regulated by an mRNA Competition Mechanism. *Cell*, 166(6):1–13, 2016. doi: 10.1016/j.cell.2016.08.006. URL <http://dx.doi.org/10.1016/j.cell.2016.08.006>.
- Richard P Sear and JoséA Cuesta. Instabilities in complex mixtures with a large number of components. *Phys. Rev. Lett.*, 91(24):245701—245701/4, 2003. URL <http://eutils.ncbi.nlm.nih.gov/entrez/eutils/efetch.fcgi?dbfrom=pubmed&id=14683134&retmode=ref&cmd=prlinks>.
- Rabea Seyboldt and Frank Jülicher. Role of hydrodynamic flows in chemically driven droplet division. *New Journal of Physics*, 20(10):105010, nov 2018. doi: 10.1088/1367-2630/aae735. URL <https://doi.org/10.1088/1367-2630/aae735>.
- Yongdae Shin and Clifford P. Brangwynne. Liquid phase condensation in cell physiology and disease. *Science*, 357(6357), 2017. doi: 10.1126/science.aaf4382.
- Ekaterina Sokolova, Evan Spruijt, Maike M K Hansen, Emilien Dubuc, Joost Groen, Venkatachalam Chokkalingam, Aigars Piruska, Hans A Heus, and Wilhelm T S Huck. Enhanced transcription rates in membrane-free protocells formed by coacervation of cell lysate. *Proc. Natl. Acad. Sci. USA*, 110(29):11692–11697, 2013.

- doi: 10.1073/pnas.1222321110. URL <http://www.pnas.org/cgi/doi/10.1073/pnas.1222321110>.
- Helen Song, Delai L. Chen, and Rustem F. Ismagilov. Reactions in droplets in microfluidic channels. *Angewandte Chemie – International Edition*, 45(44):7336–7356, 2006. doi: 10.1002/anie.200601554.
- J. Stefan. Über die Theorie der Eisbildung, insbesondere über die Eisbildung im Polarmeere. *Annalen der Physik*, 278(2):269–286, 1891. doi: 10.1002/andp.18912780206.
- J Stenesh. *Biochemistry*. Springer US, 2013. ISBN 9781475794298. URL <https://books.google.de/books?id=UI7gBwAAQBAJ>.
- J W Szostak, D P Bartel, and P L Luisi. Synthesizing life. *Nature*, 409(6818):387–390, 2001. doi: 10.1038/35053176. URL <http://eutils.ncbi.nlm.nih.gov/entrez/eutils/eflink.fcgi?dbfrom=pubmed&id=11201752&retmode=ref&cmd=prlinks>.
- Dora T.-Y. Tang, Dirk van Swaay, Andrew DeMello, J L Ross Anderson, and Stephen Mann. In vitro gene expression within membrane-free coacervate protocells. *Chem. Commun.*, 51(57):11429–11432, 2015. doi: 10.1039/C5CC04220H. URL <http://dx.doi.org/10.1039/C5CC04220H>.
- T-Y. Dora Tang, C Rohaida Che Hak, Alexander J Thompson, Marina K Kuimova, D S Williams, Adam W Perriman, and Stephen Mann. Fatty acid membrane assembly on coacervate microdroplets as a step towards a hybrid protocell model. *Nature chemistry*, 6(6):527–33, 2014. doi: 10.1038/nchem.1921. URL <http://dx.doi.org/10.1038/nchem.1921>.
- P Taylor. Ostwald ripening in emulsions. *Adv. Colloid Interface Sci.*, 75(2):107–163, 1998. doi: 10.1016/S0001-8686(98)00035-9. URL <http://linkinghub.elsevier.com/retrieve/pii/S0001868698000359>.
- E. Tjhung, D. Marenduzzo, and M. E. Cates. Spontaneous symmetry breaking in active droplets provides a generic route to motility. *Proceedings of the National Academy of Sciences*, 109(31):12381–12386, 2012. doi: 10.1073/pnas.1200843109.
- J Toner, Y H Tu, and S Ramaswamy. Hydrodynamics and phases of flocks. *Ann. Phys.*, 318(1):170–244, 2005. doi: 10.1016/j.aop.2005.04.011. URL <http://www.sciencedirect.com/science/article/pii/S0003491605000540>.
- A. M. Turing. The chemical basis of morphogenesis. *Phil. Trans. R. Soc. London*, 237(1-2):37–72, 1952. doi: 10.1007/BF02459572. URL <http://rspb.royalsocietypublishing.org/content/237/641/37.short>.
- P J Unrau and D P Bartel. RNA-catalysed nucleotide synthesis. *Nature*, 395(6699):260–263, sep 1998. doi: 10.1038/26193.

- Gang Wan, Brandon D Fields, George Spracklin, Aditi Shukla, Carolyn M Phillips, and Scott Kennedy. Spatiotemporal regulation of liquid-like condensates in epigenetic inheritance. *Nature*, 2018. doi: 10.1038/s41586-018-0132-0. URL <http://dx.doi.org/10.1038/s41586-018-0132-0><http://www.nature.com/articles/s41586-018-0132-0>.
- Christoph A Weber, Chiu Fan Lee, and Frank Jülicher. Droplet ripening in concentration gradients. *New Journal of Physics*, 19(5):53021, may 2017. doi: 10.1088/1367-2630/aa6b84. URL <https://doi.org/10.1088/1367-2630/aa6b84>.
- Stephanie C. C Weber and Clifford P. P Brangwynne. Getting RNA and Protein in Phase. *Cell*, 149(6):1188–1191, 2012. doi: 10.1016/j.cell.2012.05.022. URL <http://www.sciencedirect.com/science/article/pii/S0092867412006344>.
- Madeline C Weiss, Filipa L Sousa, Natalia Mrnjavac, Sinje Neukirchen, Mayo Roettger, Shijulal Nelson-Sathi, and William F Martin. The physiology and habitat of the last universal common ancestor. *Nature Microbiology*, 1(9):16116, sep 2016. doi: 10.1038/nmicrobiol.2016.116. URL <http://dx.doi.org/10.1038/nmicrobiol.2016.116>.
- C R Woese, O Kandler, and M L Wheelis. Towards a natural system of organisms: proposal for the domains Archaea, Bacteria, and Eucarya. *Proc. Natl. Acad. Sci. USA*, 87(12):4576, jun 1990.
- Jianfeng Xu, Nicholas Green, Clémentine Gibard, Ramanarayanan Krishnamurthy, and John Sutherland. Prebiotic Phosphorylation of 2-Thiouridine Provides Either Nucleotides or DNA Building Blocks via Photoreduction. *Nature Chemistry*, xx, 2019. doi: 10.1038/s41557-019-0225-x.
- Zhijie Yang, Jingjing Wei, Yaroslav I. Sobolev, and Bartosz A. Grzybowski. Systems of mechanized and reactive droplets powered by multi-responsive surfactants. *Nature*, pages 1–6, 2018. doi: 10.1038/nature25137. URL <http://www.nature.com/doi-finder/10.1038/nature25137>.
- Lauren D Zarzar, Vishnu Sresht, Ellen M Sletten, Julia a Kalow, Daniel Blankschtein, and Timothy M Swager. Dynamically reconfigurable complex emulsions via tunable interfacial tensions. *Nature*, 518(7540):520–4, 2015. doi: 10.1038/nature14168. URL <http://www.ncbi.nlm.nih.gov/pubmed/25719669>.
- Ou-Yang Zhong-can and W Helfrich. Instability and deformation of a spherical vesicle by pressure. *Phys. Rev. Lett.*, 59(21):2486–2488, nov 1987.
- David Zwicker. *Physical Description of Centrosomes as Active Droplets*. PhD thesis, Technische Universität Dresden, 2013.

David Zwicker, Markus Decker, Steffen Jaensch, Anthony A Hyman, and Frank Jülicher. Centrosomes are autocatalytic droplets of pericentriolar material organized by centrioles. *Proc. Natl. Acad. Sci. USA*, 111(26):E2636–45, jul 2014. doi: 10.1073/pnas.1404855111. URL <http://www.ncbi.nlm.nih.gov/pubmed/24979791>.

David Zwicker, Anthony A. Hyman, and Frank Jülicher. Suppression of Ostwald ripening in active emulsions. *Phys. Rev. E*, 92(1):012317, 2015. doi: 10.1103/PhysRevE.92.012317. URL <http://link.aps.org/doi/10.1103/PhysRevE.92.012317>.

David Zwicker, Rabea Seyboldt, Christoph A Weber, Anthony A Hyman, and Frank Jülicher. Growth and division of active droplets provides a model for protocells. *Nature Physics*, 13(4):408–413, apr 2017. doi: 10.1038/nphys3984. URL <http://www.nature.com/articles/nphys3984>.





## Acknowledgments

First and foremost I want to thank my supervisor Frank Jülicher for his guidance and advice, the possibility to visit exciting conferences and summer schools, for many interesting discussions and for teaching me that asking questions in talks is not annoying or embarrassing, but can yield exciting new knowledge. I also want to thank him for giving me the chance to work on the most exciting PhD project that ever was, including both beautiful nonequilibrium physics and deep questions about the origin of life on Earth. I could not have wished for a more exciting topic. My deepest thanks also go to Dora Tang, who gave me the chance to try my hand at experimental work.

I also want to thank the group of postdocs and PhD students at PKS, CBG and CSBD. Especially I want to thank Tyler Harmon, Suropriya Saha, Lennart Hilbert and Christoph Weber for stimulating discussions about droplets and physics in general.

I want to thank my family, especially my mother, who listened to hours of enthusiastic, but often confused talk about all aspects of my PhD project, and encouraged me especially during the writing process. Lastly, I want to thank my quasi-adoptive family, Fam. Biemann. Knowing that you care about me and my project means so much to me.

RABEA SEYBOLDT  
Dresden  
April 2019



## Versicherung

Hiermit versichere ich, dass ich die vorliegende Arbeit ohne unzulässige Hilfe Dritter und ohne Benutzung anderer als der angegebenen Hilfsmittel angefertigt habe; die aus fremden Quellen direkt oder indirekt übernommenen Gedanken sind als solche kenntlich gemacht. Die Arbeit wurde bisher weder im Inland noch im Ausland in gleicher oder ähnlicher Form einer anderen Prüfungsbehörde vorgelegt.

Die Dissertation wurde am Max-Planck-Institut für Physik komplexer Systeme unter wissenschaftlicher Betreuung von Prof. Dr. Frank Jülicher angefertigt. Frühere Promotionsverfahren haben nicht stattgefunden.

Ich erkenne die Promotionsordnung des Fachbereichs Mathematik und Naturwissenschaften der Technischen Universität Dresden an.